

The application of Cu(I) phenanthroline dyes in DSCs with optimized I⁻/I₃⁻ and Co(II/III) electrolytes

Inauguraldissertation

ZUR
Erlangung der Würde eines Doktors der Philosophie
vorgelegt der
Philosophisch-Naturwissenschaftlichen Fakultät
der Universität Basel

VON

Sebastian O. FÜRER
aus Basel-Stadt

Basel, 2016

Originaldokument gespeichert auf dem Dokumentenserver der Universität Basel
edoc.unibas.ch



Dieses Werk ist unter dem Vertrag „Creative Commons Namensnennung-Keine kommerzielle Nutzung-Keine Bearbeitung 3.0 Schweiz“ (CC BY-NC-ND 3.0 CH) lizenziert.

Die vollständige Lizenz kann unter
creativecommons.org/licenses/by-nc-nd/3.0/ch/
eingesehen werden

Genehmigt von der Philosophisch-Naturwissenschaftlichen Fakultät
auf Antrag von

Prof. Dr. Edwin C. Constable und Prof. Dr. Oliver S. Wenger

Basel, den 19.05.2015

Prof. Dr. Jörg Schibler
Dekan

Acknowledgments

First of all, I would like to thank my supervisors Prof. Dr. Edwin C. Constable and Prof. Dr. Catherine E. Housecroft for giving me the opportunity to do my PhD in their group on this very exciting topic. Over the last four years they were always here to help whenever I had a problem occurring. I am also thankful to them for the freedom they gave me in my researches. In particular I want to thank Catherine for the immense support during the last two months in which I was writing my thesis.

Furthermore I want to thank Prof. Dr. Oliver S. Wenger for being my co-examiner and co-referee.

I am very thankful to Prof. Dr. Catherine E. Housecroft and Dr. Collin Morris for proof-reading my thesis. I thank Niels Burzan, Lukas Troxler, Laura Luu, Tatjana Kosmalski and Fabienne Thommen for their contributions to this work as part of their “Wahlpraktikum”.

Dr. Thilo Glatzel, Dr. Gino Günzburger and Rés Jöhr are acknowledged for their help with solar cell measurements, troubleshooting and fruitful discussions. Dr. Nik Hostettler, Cathrin Ertl, Dr. Roche Walliser and Dr. Colin Martin are thanked for recording NMR-measurements. Dr. Sven Brauchli, Dr. Collin Morris, Frederik Malzner, Dr. Gabriel Schneider and Dr. Niamh Murray are acknowledged for recording ESI-MS spectra. Dr. Collin Morris is acknowledged for the LC-MS measurements and Dr. Steffen Müller and Max Klein for MALDI-TOF measurements. I thank Dr. Jennifer Zampese and Dr. Markus Neuburger for X-ray diffraction and Sylvie Mittelheisser and Werner Kirsch for elemental analysis. Heinz Nadig is acknowledged for HRMS measurements. Dr. Ewald Schönhofer and Lieselotte Siegfried are acknowledged for preparation of TiO₂ pastes. I thank Dr. Ewald Schönhofer for optimizing the screen-printing process and a lot of more optimizations he has achieved in our attempts to reach the new N719 champion reference cell. The team of Dr. Daniel Häussinger is acknowledged for the NMR support.

Beatrice Erismann is thanked for all her support with administrative problems and her patience with all the missing LILO sheets. Furthermore I thank Markus Hauri for supplying us with chemicals and the technical staff for all their support and keeping the building running.

I want to thank all current and former members of the Constable/Housecroft group for the nice working atmosphere and the good time I had with you all. In particular I want to thank Dr. Sven Brauchli, Dr. Andreas Bünzli, Annika Büttner, Dr. Nik Hostettler, Dr. Peter Kopecky, Dr. Colin Martin, Dr. Collin Morris, Dr. Ewald Schönhofer, Dr. Jonas Schönle, Dr. Iain Wright for the

good time we had together in and outside the lab and for their friendship. I want to thank Dr. Iain Wright for enthusiastic late night discussions about research and science in general.

Furthermore I want to thank my family and friends for their constant support outside of the lab. I am gratefully thankful to my parents and my sister for all of their support and help throughout my life and for always encouraging me to follow my passion.

For Financial support, the European Research Council (Advanced grant 267816 LiLo), the Swiss National Science Foundation and the University of Basel are acknowledged.

Table of Contents

1	ABSTRACT	1
2	ABBREVIATIONS	3
3	INTRODUCTION	6
3.1	Motivation	6
3.2	Photovoltaic Technologies	9
3.3	Dye Sensitized Solar Cells	9
3.3.1	Design and Working-Principle of n-type Dye Sensitized Solar Cells	10
3.3.2	Components of DSCs	12
3.3.2.1	Semiconductor	12
3.3.2.2	Dyes	14
3.3.2.2.1	Ruthenium (II) Dyes	15
3.3.2.2.2	Copper(I) Complexes	16
3.3.2.2.3	Donor- π -Bridge-Acceptor Dyes	18
3.3.2.3	Electrolyte	19
4	MATERIALS AND METHODS	24
4.1	General Materials	24
4.2	Materials for the Dye Sensitized Solar Cells	24
4.2.1	Working Electrode	24
4.2.2	Doctor Blading	24
4.2.3	Screen Printing	24
4.2.4	Counter Electrode	25
4.2.5	Cell Assembly	25
4.2.6	Electrolyte	26
4.3	General Methods for Characterization and Analysis of the Synthetic Work	26
4.4	Characterisation of the Dye Sensitized Solar Cells	27
4.4.1	Cell Masking	27
4.4.2	Sun Simulator	27
4.4.3	Current Density to Voltage (J/V) Measurements	28
4.4.4	Dark Current Measurements	29
4.4.5	Long Term Measurements	29
4.4.6	Incident Photon to Current Efficiency	30
4.4.7	Voltage-Decay Measurements	31
5	SYNTHESIS	32
5.1	Aim and Target Molecules	32
5.2	Anchoring Ligands	34
5.3	Ligand Synthesis	36
5.4	Complex Synthesis	46

6	CHARACTERISATION	51
6.1	UV-Vis Spectroscopy	51
6.2	Cyclic Voltammetry	54
6.3	Crystallographic Data	58
7	STATE OF THE ART DYE SENSITIZED SOLAR CELLS	61
7.1	Introduction	61
7.2	From Partially to Completely Sealed DSCs	62
7.3	Optimization of Completely Sealed DSCs	65
7.3.1	Improvement of the Measuring Setup	65
7.3.2	Optimization of the I ⁻ /I ₃ ⁻ Electrolyte	66
7.3.3	Optimization of the Counter Electrode	67
7.3.4	Optimization of the TiO ₂ Layer Thickness	68
7.3.5	Optimization of the Distance between the Working and the Counter Electrode	70
7.3.6	Activation and Cleaning with UV-Ozone Treatment	72
7.3.7	J/V Measurements over Time	73
7.3.8	Conclusion of the Optimizations of Doctor-Bladed DSCs	74
7.4	DSCs from Screen Printed TiO ₂ Electrodes	74
7.4.1	Fabrication of DSCs under Inert Conditions	75
7.4.2	Application of a Scattering Layer	77
7.5	Masking of the DSCs	80
7.6	Conclusions	83
8	ANCHORING LIGANDS	84
9	PHENANTHROLINE BASED COPPER DYES	91
9.1	Investigation of Different 2,9-Dimethylphenanthroline Ancillary Ligands	91
9.2	Stepwise assembly	100
10	OPTIMIZATION OF THE I⁻/I₃⁻ ELECTROLYTE FOR THE PERFORMANCE OF COPPER(I) DYES IN DSCS	106
10.1	Screening of I ⁻ /I ₃ ⁻ electrolytes	107
10.2	Optimization of the I ⁻ /I ₃ ⁻ electrolyte for [Cu(15)(ALP1)] ⁺ sensitized solar cells	112
11	CO(II/III) ELECTROLYTES FOR CU(I) SENSITIZED SOLAR CELLS	119
11.1	Optimization of the TiO ₂ working electrode for DSCs incorporating [Co(bpy) ₃][PF ₆] _{2/3} electrolytes	120
11.2	DSCs Containing [Cu(13)(ALP1)] ⁺ or [Cu(15)(ALP1)] ⁺ Dyes with [Co(bpy) ₃][PF ₆] _{2/3} Electrolyte	124

11.2.1	Comparison of [Cu(13)(ALP1)] ⁺ and [Cu(15)(ALP1)] ⁺ Sensitized Solar Cells	124
11.2.2	Silane Additives as a Recombination Blocking Layer	129
11.3	Influence of the Counterion of the Co(II/III) Electrolyte on the DSC Performance	132
12	EXPERIMENTAL PART	134
12.1	Anchoring Ligands	134
12.1.1	(1 <i>E</i> ,5 <i>E</i>)-1,6-Di(furan-2-yl)hexa-1,5-diene-3,4-dione (2)	134
12.1.2	1 <i>E</i> ,5 <i>E</i> -1,6-Di(2-furyl)hexa-1,5-diene-3,4-dione	134
12.1.3	6,6'-Dimethyl-2,2'-bipyridine-4,4'-dicarboxylic acid (ALC)	135
12.1.4	Tetraethyl 6,6'-dimethyl-2,2'-bipyridine-4,4'-diyl diphosphonate (4)	136
12.1.5	tetraethyl ((6,6'-dimethyl-[2,2'-bipyridine]-4,4'-diyl)bis(4,1-phenylene))bis(phosphonate) (5)	136
12.1.6	(6,6'-dimethyl-[2,2'-bipyridine]-4,4'-diyl)diphosphonic acid (ALP)	137
12.1.7	((6,6'-dimethyl-[2,2'-bipyridine]-4,4'-diyl)bis(4,1-phenylene))diphosphonic acid (ALP1)	138
12.1.8	ALP1 TBA	139
12.2	Ligand Synthesis	139
12.2.1	2,9-Dimethyl-1,10-phenanthroline-5,6-dione (1)	139
12.2.2	4-bromo- <i>N,N</i> -bis(4-methoxyphenyl)aniline (2)	140
12.2.3	Di-4-anisyl-4-bromophenylamine (3)	141
12.2.4	4-(6,9-dimethyl-1 <i>H</i> -imidazo[4,5- <i>f</i>][1,10]phenanthrolin-2-yl)- <i>N,N</i> -bis(4-methoxyphenyl)aniline (4)	142
12.2.5	2-(4-bromophenyl)-6,9-dimethyl-1 <i>H</i> -imidazo[4,5- <i>f</i>][1,10]phenanthroline (5)	143
12.2.6	2-(4-bromophenyl)-6,9-dimethyl-1-octyl-1 <i>H</i> -imidazo[4,5- <i>f</i>][1,10]phenanthroline (6)	144
12.2.7	1-bromo-4-butoxybenzene (7)	145
12.2.8	1-bromo-4-(dodecyloxy)benzene (8)	145
12.2.9	4-butoxyaniline (9)	146
12.2.10	4-dodecyloxyaniline (10)	146
12.2.11	Bis(4-butoxyphenyl)amine (11)	147
12.2.12	Bis(4-dodecyloxyphenyl)amine (12)	148
12.2.13	4-(6,9-dimethyl-1-octyl-1 <i>H</i> -imidazo[4,5- <i>f</i>][1,10]phenanthrolin-2-yl)- <i>N,N</i> -diphenylaniline (13)	148
12.2.14	4-(6,9-dimethyl-1-octyl-1 <i>H</i> -imidazo[4,5- <i>f</i>][1,10]phenanthrolin-2-yl)- <i>N,N</i> -bis(4-methoxyphenyl)aniline (14)	149
12.2.15	4-butoxy- <i>N</i> -(4-butoxyphenyl)- <i>N</i> -(4-(6,9-dimethyl-1-octyl-1 <i>H</i> -imidazo[4,5- <i>f</i>][1,10]phenanthrolin-2-yl)phenyl)aniline (15)	150
12.2.16	2-(4-(9 <i>H</i> -carbazol-9-yl)phenyl)-6,9-dimethyl-1-octyl-1 <i>H</i> -imidazo[4,5- <i>f</i>][1,10]phenanthroline (17)	151
12.2.17	5-(9 <i>H</i> -carbazol-9-yl)thiophene-2-carbaldehyde (18)	152
12.2.18	2-(4-(9 <i>H</i> -carbazol-9-yl)phenyl)-6,9-dimethyl-1 <i>H</i> -imidazo[4,5- <i>f</i>][1,10]phenanthroline (19)	153
12.2.19	1,10-phenanthroline-5,6-dione (20)	154
12.2.20	2-(4-bromophenyl)-1 <i>H</i> -imidazo[4,5- <i>f</i>][1,10]phenanthroline (21)	154
12.2.21	2-(4-bromophenyl)-1-octyl-1 <i>H</i> -imidazo[4,5- <i>f</i>][1,10]phenanthroline (22)	155
12.2.22	4-butoxy- <i>N</i> -(4-butoxyphenyl)- <i>N</i> -(4-(1-octyl-1 <i>H</i> -imidazo[4,5- <i>f</i>][1,10]phenanthrolin-2-yl)phenyl)aniline (23)	156
12.2.23	5,5'-((1,2-phenylenebis(azanediyl))bis(ethan-1-yl-1-ylidene))bis(2,2-dimethyl-1,3-dioxane-4,6-dione) (25)	157
12.2.24	2,9-dimethyl-1,10-phenanthroline-4,7(1 <i>H</i> ,10 <i>H</i>)-dione (26)	157
12.2.25	4,7-dichloro-2,9-dimethyl-1,10-phenanthroline (27)	158

12.2.26	4,4'-(2,9-dimethyl-1,10-phenanthroline-4,7-diyl)bis(<i>N,N</i> -diphenylaniline) (28)	159
12.3	Copper Complex Synthesis	160
12.3.1	[Cu(5) ₂][PF ₆]	160
12.3.2	[Cu(6) ₂][PF ₆]	161
12.3.3	[Cu(13) ₂][PF ₆]	162
12.3.4	[Cu(14) ₂][PF ₆]	163
12.3.5	[Cu(15) ₂][PF ₆]	164
12.3.6	[Cu(17) ₂][PF ₆]	165
12.3.7	[Cu(28) ₂][PF ₆]	166
13	CONCLUSION	167
14	REFERENCES	170

1 Abstract

The world faces an energy and climate crisis. After an unprecedented worldwide increase in energy consumption, which has largely been based on the use of fossil fuels, mankind is challenged by global warming and its consequences. The demand for renewable energy has focused our attention on capturing the inexhaustible solar energy. Photovoltaic (PV) devices based on silicon have been and remain the most popular choice. However, the high purity demands of this technique are a drawback for cheap energy production from solar power. Dye sensitized solar cells (DSCs) are a valuable alternative for low-cost PVs since the separation of light-harvesting and charge transport implicates less stringent purity demands of the built-in compositions. Replacing rare ruthenium used in Grätzel-type n-type DSCs by more Earth-abundant and sustainable metals is a goal of our research group. This thesis describes the use of heteroleptic Cu(I) dyes using phenanthroline ancillary ligands to harvest light.

Chapter 1 gives a short overview of the current energy problems and outlines the current status of the literature relevant to this thesis.

Chapter 2 describes the methods for the characterization of the investigated dyes and their application in dye sensitized solar cells (DSCs).

Chapter 3 shows the synthesis and characterization of ligands and of copper(I) complexes designed for application in DSCs.

Chapter 4 compares the performances of DSCs containing *heteroleptic* Cu(I) complexes made from $[\text{Cu}(\mathbf{13})_2][\text{PF}_6]$ (ligand **13** contains a peripheral hole-transporting NPh_2 group) and four different anchoring ligands with carboxylic acid (**ALC1**) or phosphonic acid (**ALP**, **ALP1** and **ALP1 TBA**) anchors.

Chapter 5 investigates the differences between *heteroleptic* Cu(I) dyes from several phenanthroline based ancillary ligands in combination with anchoring ligand **ALP1**.

Chapter 6 deals with the optimization of Γ^-/I_3^- electrolytes for $[\text{Cu}(\mathbf{15})(\text{ALP1})]^+$ sensitized solar cells (ligand **15** contains a peripheral hole-transporting domain related to that in ligand **13**).

Chapter 7 shows the incorporation of $[\text{Co}(\text{bpy})_3][\text{PF}_6]_{2/3}$ electrolyte in DSCs using $[\text{Cu}(\mathbf{13})(\text{ALP1})]^+$ and $[\text{Cu}(\mathbf{15})(\text{ALP1})]^+$ sensitizers.

Chapter 8 lists the experimental details.

Chapter 9 concludes the work and gives an outlook for future work.

Parts of the work in this thesis (including syntheses of ligands) have been published as follows:

Hole-transport functionalized copper(I) dye sensitized solar cells

B. Bozic-Weber, S. Y. Brauchli, E. C. Constable, S. O. Furer, C. E. Housecroft and I. A. Wright

Phys. Chem. Chem. Phys., 2013, **15**, 4500-4504.

Improving the photoresponse of copper(I) dyes in dye-sensitized solar cells by tuning ancillary and anchoring ligand modules

B. Bozic-Weber, S. Y. Brauchli, E. C. Constable, S. O. Furer, C. E. Housecroft, F. J. Malzner, I. A. Wright and J. A. Zampese

Dalton Trans., 2013, **42**, 12293–12308.

Copper(I) dye-sensitized solar cells with $[\text{Co}(\text{bpy})_3]^{2+/3+}$ electrolyte

B. Bozic-Weber, E. C. Constable, S. O. Furer, C. E. Housecroft, L. J. Troxler and J. A. Zampese

Chem. Commun., 2013, **49**, 7222-7224.

Alkyl chain-functionalized hole-transporting domains in zinc(II) dye-sensitized solar cells

N. Hostettler, S. O. Furer, B. Bozic-Weber, E. C. Constable and C. E. Housecroft

Dyes and Pigments, 2015, **116**, 124–130.

2 Abbreviations

APCE	Absorbed photon to current efficiency
APTES	3-(aminopropyl)triethoxysilane
AR5	Fifth Assessment Report
AZA	2-azaadamantan- <i>N</i> -oxyl
BMII	1-Butyl-3-methylimidazolium iodide
Btu	British thermal unit
CdTe	Cadmium telluride
CH ₂ Cl ₂	Dichloromethane
CIGS	Copper indium gallium selenide
ClO ₄	Perchlorate
Cs ₂ CO ₃	Caesium carbonate
CV	Cyclic voltammogram
dbbip	2,6-Bis(1'-butylbenzimidazol-2'-yl)pyridine
DFT	Density functional theory
DMII	1,3-Dimethylimidazolium iodide
DMPI	1,2-Dimethyl-3-propylimidazolium iodide
DMSO	Dimethyl sulfoxide
DSC	Dye sensitized solar cell
DTB	4,4'- <i>Di-tert</i> -butyl-2,2'-bipyridine
EQE	External quantum efficiency
EtOH	Ethanol
EU	European Union
eV	Electron volt
<i>ff</i>	Fill factor
FTO	Fluor-doped tin oxide
GaAs	Gallium arsenide
GNCS	Guanidinium thiocyanate
GPC	Gel permeable chromatography
HOMO	Highest occupied molecular orbital
HPLC	High-performance liquid chromatography
IPCC	Intergovernmental Panel on Climate Change
IPCE	Incident photon to current efficiency

IQE	Internal quantum efficiency
J/V	Current density/voltage
J_{MP}	Current density at the maximum power point
J_{SC}	Short-circuit current density
LUMO	Lowest unoccupied molecular orbital
MALDI-TOF	Matrix-assisted laser desorption ionization – time of flight
MBI	1-methylbenzimidazole
MeOH	Methanol
MLCT	Metal to ligand charge transfer
MO	Molecular orbital
MPN	3-methoxypropionitrile
Mtoe	Million tonnes oil equivalent
N719	di-tetrabutylammonium cis-bis(isothiocyanato) bis(2,2'-bipyridyl-4,4'-dicarboxylato)ruthenium(II)
Nb ₂ O ₅	Niobium pentoxide
NBB	<i>n</i> -butylbenimidazole
NCS	Thiocyanate
NHE	Standard hydrogen electrode
NIR	Near infrared
OCVD	Open circuit voltage decay
OECD	Organization for Economic Cooperation and Development
PCE	Power conversion efficiency
<i>phen</i>	Phenanthroline
P _{Max}	Maximum power point
PV	Photovoltaic
SnO ₂	Tin dioxide
TBA	Tetrabutly ammonium
TBP	4- <i>tert</i> -butyl pyridine
<i>t</i> BuOH	<i>tert</i> -butanol
TCO	Transparent conductive oxide
TEMPO	2,2,6,6-tetramethyl-1-piperidinyloxy
TiCl ₄	Titanium tetrachloride
TiO ₂	Titanium dioxide
TMAS	Trimethylammoniumpropyltrimethoxysilane

UVO	Ultraviolet ozone
V_{MP}	Voltage at the maximum power point
VN	Valeronitrile
V_{OC}	Open circuit potential

3 Introduction

3.1 Motivation

One of the most challenging problems of human kind is the increasing energy consumption and its environmental consequences; this is mainly due to the excessive consumption of fossil fuels, which are non-sustainable energy sources. The world's energy consumption was approximately 524 quadrillion Btu (Btu = British thermal unit ≈ 1055.06 J) in 2011 and is expected to increase up to 820 quadrillion Btu by 2040. This development is driven by the increase in population and economic growth, particularly in Asia, with emerging economies in China and India. Figure 1 shows the expected rise in total energy consumption over the next 25 years.

A significant increase in energy demand is predicted, especially in the non-OECD Asian countries (including China and India; OECD = Organization for Economic Cooperation and Development) with an annual expected increase of 2.5%. Considering the total worldwide energy consumption by fuel, (Figure 2) it is evident that the largest part of the consumed energy originates from fossil fuels. Only 2.2% of the worldwide energy consumption in 2013 was from renewable energies, 6.7% from hydroelectric and 4.4% from nuclear power. This combines for a total of 13.3% of the total energy consumption that arose from CO₂ neutral energy sources. There is a unanimous understanding in the scientific community that this development with the associated emission of CO₂ as the dominant greenhouse gas has led to global warming and climate change.¹

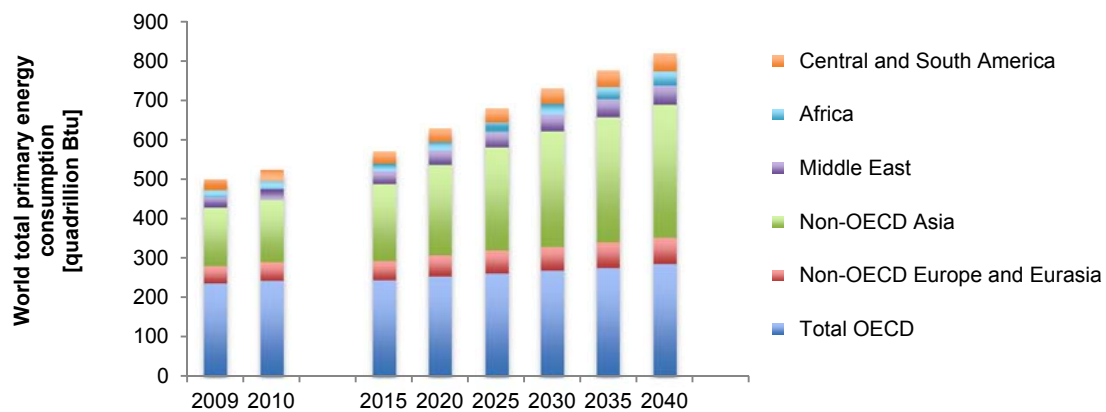


Figure 1 World total primary energy consumption 2009-2040; history (2009-2010) and prediction (2015-2040).

The Fifth Assessment Report (AR5)¹ of the Intergovernmental Panel on Climate Change (IPCC) clearly shows the unequivocal warming of the climate system and changes over the last decades that are unprecedented over the previous decades to millennia.

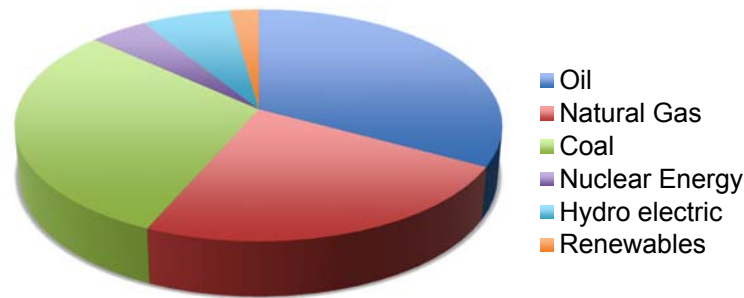


Figure 2 Worldwide total primary energy consumption by fuel in 2013 in Mtoe (Million tonnes oil equivalent).

Figure 3a shows the annual global combined land and ocean surface temperatures observed between 1850-2005.¹ An increase of 0.85 °C was observed over this period with each of the last three decades being successively warmer than any preceding decade since 1850. This led to melting of the Greenland and Arctic ice sheets and continuous shrinking of the glaciers in the last decades. Together with the ocean thermal expansion, this led to a rise in the sea level rate (Figure 3b). The atmospheric concentrations of CO₂, CH₄, and N₂O have increased by about 40%, 150% and 20%, respectively, with respect to pre-industrial levels and reached concentrations unprecedented in at least the last 800,000 years (Figure 3c). The increase in CO₂ concentration is attributed primarily to fossil fuel emissions and secondarily to net land use change emissions (Figure 3d). Absorption of about 30% of the emitted anthropogenic CO₂ caused a decrease in the pH level of surface water by 0.1 since the beginning of the industrial era. According to AR5, it is extremely likely that human influence has been the dominant cause of the observed warming since the mid-20th century. The anthropogenic increase in greenhouse gas concentrations is believed to be the main reason for global warming over the last decades. By 2100, an increase in global surface temperature of more than 1.5 °C with respect to 1850-1900 was calculated for all realistic scenarios. If the increase in greenhouse gas concentration is not drastically reduced, the rise in temperature will become greater than 1.5 °C. However, even 1.5 °C will have a dramatic impact on our climate with an increase in extreme weather conditions and a dramatic consequence for population at the coastal lines.

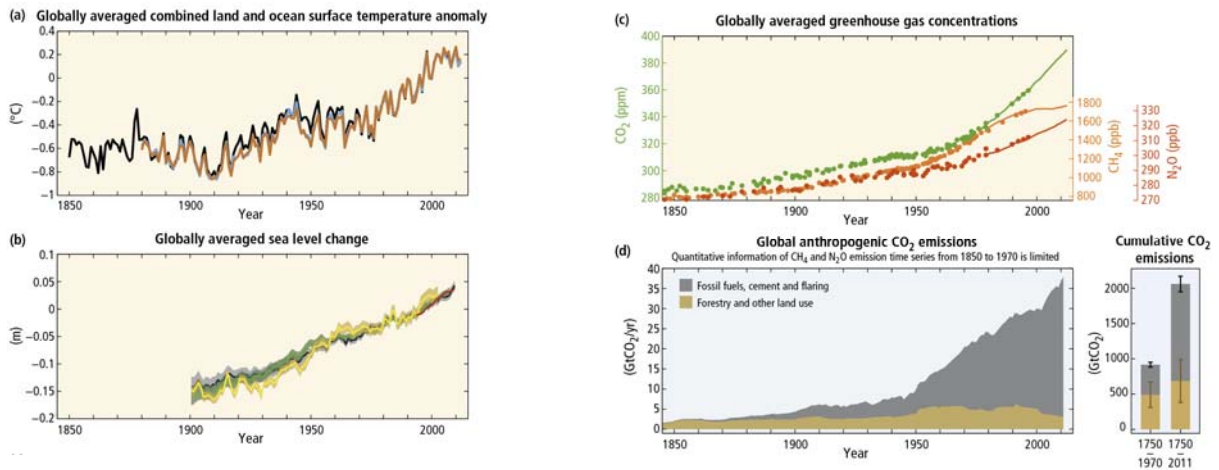


Figure 3 Global increase in combined land and ocean surface temperatures (a), sea level change (b), greenhouse gas concentrations (c), and anthropogenic CO₂ emissions between 1850-2005.¹

Therefore, a rapid change of climate politics and a fast reorientation towards renewable energy sources are vital for decreasing man-made greenhouse emissions. In 2011, the Federal Council and Parliament decided that Switzerland should withdraw from the use of nuclear energy on a step-by-step basis. On the basis of this and further decisions of the Swiss Parliament, the Federal Council outlined an energy policy (Energy Strategy 2050) that focuses on the consistent exploitation of the existing energy efficiency potential and on the balanced utilisation of the potentials of hydropower and new renewable energy sources.² In 2007, the leaders of the European Union set the energy targets of the EU for the year 2020, which were enacted in 2009 through the 2020 energy package.³ This package is a set of binding legislations of the European Union, which aims to ensure the EU achieves its climate and energy targets by 2020. The three key targets of this strategy are (i) the reduction of greenhouse gas emissions by 20% with respect to 1990 levels, (ii) increasing the share of the energy consumption in the EU from renewables by 20% and (iii) an improvement of the EU's energy efficiency by 20%. The energy roadmap by 2050 goes even further, but presently it is not obligatory.

Following these political guidelines, development of energy production from renewable sources must have top priority. Since the energy of the solar flux striking the Earth in one hour is equal to the yearly energy demand of mankind, conversion of solar into electrical energy seems to be the obvious choice for future energy supply from renewable sources. For this, maximally efficient photoconversion by cheap solar cells is requested. Dye sensitized solar cells (DSCs) have an enormous potential for future commercial low-cost solar energy production and are considered to be one of the key techniques in the future.

3.2 Photovoltaic Technologies

Solar cells, or photovoltaic cells (PV), are electrical devices that use the photovoltaic effect to convert the energy of light into electricity. The photovoltaic effect was discovered by Edmund Bequerel in 1839 who found that current passed between two Pt-electrodes immersed in an electrolyte media in the presence of sunlight.⁴ A century later, in 1954, *Chapin et al.* presented the first crystalline silicon solar cell at the Bell Lab with a published efficiency of 6%.⁵ These so called 'first-generation solar cells' based on silicon are still the conventional solar cells of today. These cells are based on single junction devices and have a so-called Shockley-Queisser limit of 31%, which assumes that absorption of an individual photon results in the formation of a single electron-hole pair with loss of all energy in excess of the energy gap as heat.⁶ Certified efficiencies of first generation solar cells up to 25% have been reported.⁷ Today, the PV market is dominated by first generation solar cells with China being the world leader in producing crystalline silicon based PVs. The main drawback of this type of solar cell is their high production and environmental costs and the energy payback time, which is estimated to be between 0.75 and 2.5 years.^{5,6,8} Second generation solar cells are based on thin film technologies that allow for fabrication of flexible solar cells and ease of manufacturing which lowers the production costs. Typical components in second generation PVs are gallium arsenide (GaAs), cadmium telluride (CdTe) or copper indium gallium selenide (CIGS). However, due to the rare abundance of these materials, the cost reduction and scale up of the production are limited. The efficiencies are comparable to first generation PVs with certified reported efficiencies of 28.8% for GaAs PVs, 21.0% for CdTe PVs and 20.5% CIGS PVs. Third generation solar cells are hybrid film solar cells and are meant to overcome the Shockley-Queisser limit, have lower processing costs, a minor environmental impact and shorter energy payback times.⁶ Several types of solar cells are included in the third generation family and show remarkable, but still lower, efficiencies than first and second generation PVs. Typical examples are dye sensitized solar cells (DSCs, with efficiencies up to 11.9%⁷), organic solar cells (11.0%⁷) or more recently, perovskite solar cells (20.1%⁷).

3.3 Dye Sensitized Solar Cells

In the 1970s, sensitization of wide band gap metal oxide semiconductors was an active area of research with splitting of water into its elements being the main goal of these studies.^{9,10} By sensitization of colloidal anatase particles with a ruthenium(II) dye, *Desilvestro et al.* achieved a significant increase in light harvesting with respect to previous studies on planar electrodes

and reached a conversion efficiency of 1.5% with their solar cell.¹¹ The key breakthrough was reported by *O'Regan* and *Grätzel* in 1991 with the first dye sensitized solar cell (DSC) that was a viable alternative to conventional silicon solar cells due to a remarkable power conversion efficiency of 7.1-7.9%.¹² These DSCs were comprised of nanoporous TiO₂ films sensitized with a ruthenium(II) charge-transfer dye and the I⁻/I₃⁻ redox couple as electrolyte. In contrast to silicon solar cells, light harvesting and charge generation are separated from charge carrier transport in DSCs. This leads to reduced purity demands of the applied materials, a main factor for the high material costs and long energy payback times of silicon solar cells.^{5,13} In general, n-type DSCs consist of a wide-band gap semiconductor, typically TiO₂, sensitized with a light-absorbing dye. After optical excitation, electrons are injected from the excited state of the dye into the conduction band of the semiconductor and a redox couple in the electrolyte regenerates the oxidized dye to its ground state. In addition to possible low-cost production, DSCs offer several advantages over conventional silicon solar cells. They have minor environmental impact, shorter payback times,⁵ and superior performance under diffuse light and at low light intensities, presumably due to the nanoporous surface of the semiconductor.¹² In contrast to silicon solar cells, the efficiency of DSCs may be enhanced by an increase in temperature from 20 °C and 60 °C, which is well within their operating temperature range.^{14,15} In combination with flexible conducting plastic-film substrates,^{16,17} the cost and weight can also be further reduced. Their flexibility in shape, colour, and transparency allows for new design applications and high performance at low light intensities is important for indoor applications. Since the fundamental findings of *O'Regan* and *Grätzel* in 1991, the research field of DSCs has attracted widespread interest within the international academic research community leading to more than five articles being published each day.⁵ With a growing interest from industry, certified record efficiencies of 11.9% in single cells (Sharp), 10.0% in submodules (Fujikura) and 8.8% in minimodules (Sharp, 26 serial cells) have been achieved.

3.3.1 Design and Working-Principle of n-type Dye Sensitized Solar Cells

Figure 4 shows the general working principle of an n-type dye-sensitized solar cell. A mesoporous layer of TiO₂ nanoparticles on a glass substrate coated with a transparent conductive oxide (TCO) layer makes up the photoanode. Typically, fluorine-doped tin oxide (FTO) is used as the TCO layer. The thickness of the mesoporous TiO₂ layer is usually around 10-15 µm. A charge-transfer dye is adsorbed onto the nanoparticles to harvest incident sunlight and inject electrons into the semiconductor. The counter electrode is a TCO coated glass substrate coated with a fine layer of a catalyst, typically Pt, for the regeneration of the redox

couple in the electrolyte solution. Both electrodes are placed on top of one another in a sandwich-type arrangement and the space between them is filled with an electrolyte containing a suitable redox couple to reduce the oxidized dye after electron injection. Figure 5 shows a simplified electron level diagram for a DSC containing a ruthenium(II) sensitizer and an I^-/I_3^- electrolyte and indicates the relevant electron transfer processes. Upon irradiation, the excited dye injects an electron into the semiconductor and is reduced by the electrolyte. The injected electron is transported through the semiconductor layer to the TCO-anode, which is connected through an outer circuit to the cathode. The oxidized electrolyte species is reduced at the counter electrode to complete the electrical cycle. The maximum voltage generated under illumination corresponds to the energy difference of the redox potential of the electrolyte and the Fermi level of the semiconductor (more details about the characteristic parameters of DSCs are described in 4.4.3). Overall, the cell ideally converts light into electrical power without any permanent chemical transformation.^{6,18}

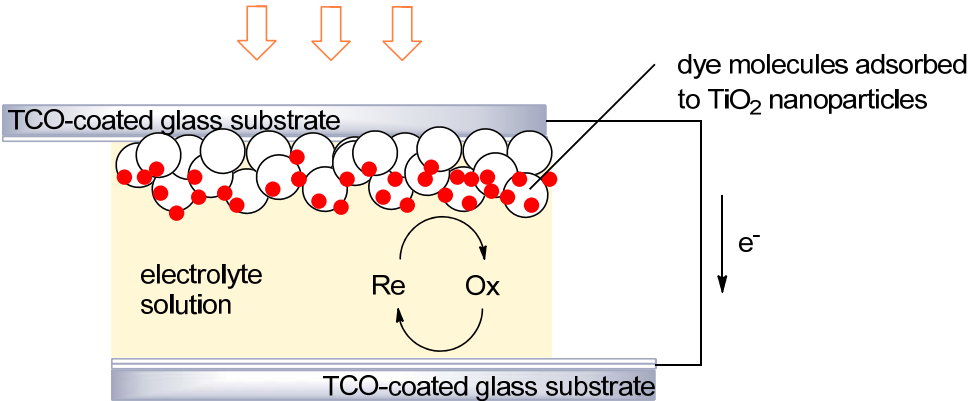


Figure 4 Schematic working principle of an n-type dye-sensitized solar cell.

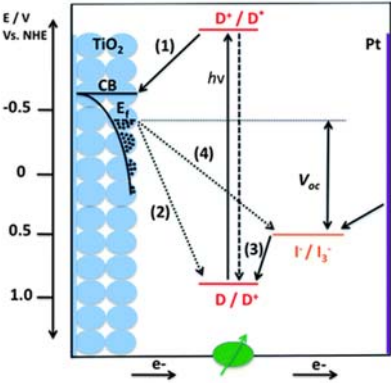


Figure 5: Energy level diagram for a DSC with the basic electron transfer processes indicated by numbers (1–4). The potentials for a DSC based on

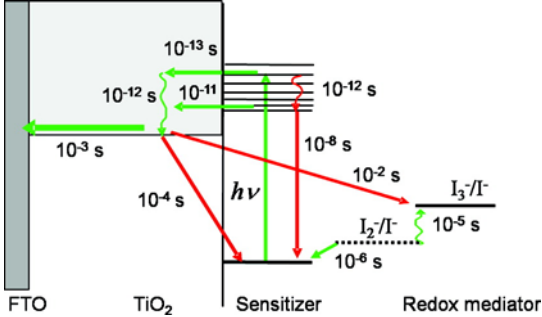


Figure 6: Overview of processes and typical time constants under working conditions (1 sun) in a Ru-dye-sensitized solar cell with I^-/I_3^- electrolyte.

the N3 dye, TiO₂, and the I⁻/I₃⁻ redox couple are shown.¹⁹

Recombination processes are indicated by red arrows.

Figure 6 shows the basic electron transfer processes occurring in a DSC. Photoexcitation of the dye upon irradiation is followed by an electron injection from the excited state of the dye into the TiO₂ conduction band (1). As indicated in Figure 6, this process typically happens in the picosecond regime, which is several orders of magnitude faster than the emission decay to the ground state. Possible loss mechanisms in DSCs are the recombination of electrons in the semiconductor with oxidized dye or electrolyte species (reactions 2 and 4 in Figure 5, respectively). However, recombination loss by reaction 2 from electrons in the semiconductor back to the oxidized dye (D⁺) is less pronounced in DSCs as this reaction path is significantly slower than the dye regeneration by the electrolyte species (3). A more dominant recombination process is the reduction of oxidized electrolyte species by electrons in the TiO₂ layer (4). With an I⁻/I₃⁻ electrolyte it is commonly thought that the recombination proceeds mainly via the reduction of I₂, rather than I₃⁻.²⁰ By replacing the I⁻/I₃⁻ redox couple with Co^{2+/3+}, the recombination kinetics of this reaction are significantly faster and initially lowered the performance of these electrolytes (cf. section 3.3.2.3).^{21–23}

3.3.2 Components of DSCs

As discussed above, DSCs consist of several components and those that are most easily modified (i.e. the semiconductor, the dye and the electrolyte) are discussed here in more detail. For a highly efficient solar cell a proper interplay of the different components is of crucial importance. However, all components affect each other and it is likely that an improvement in one component may be non-beneficial to another. Careful interpretation of results is therefore important and a more detailed understanding of the processes happening in DSCs is required.

3.3.2.1 Semiconductor

As mentioned above, the use of mesoporous TiO₂ electrodes rather than flat-surface bulk material electrodes was one of the main reasons for the boost in conversion efficiency in the 1991 published work of *O'Regan and Grätzel*.¹² The increase in surface area on going from a flat-surface (planar) to a mesoporous electrode is typically about a factor of 1000.⁶ By far the most often used semiconductor to date is TiO₂, but others such as ZnO, SnO₂ and Nb₂O₅ have been investigated. However, the most efficient solar cells so far are based on TiO₂. Titanium dioxide is environmentally friendly due to its non-toxicity and stability. Even today it is used in a wide variety of applications such as white paints, in self-cleaning materials, sunscreens,

toothpastes and even as a food additive (E171).⁶ TiO₂ exists naturally in three crystalline forms, namely rutile, anatase and brookite, of which rutile is the most thermodynamically stable form and brookite is difficult to prepare in pure form.²⁴ In DSCs, anatase is the preferred form due to its larger bandgap and higher conduction band edge with respect to rutile (Figure 7) whereby higher open circuit voltages (V_{oc}) can be reached in DSCs.

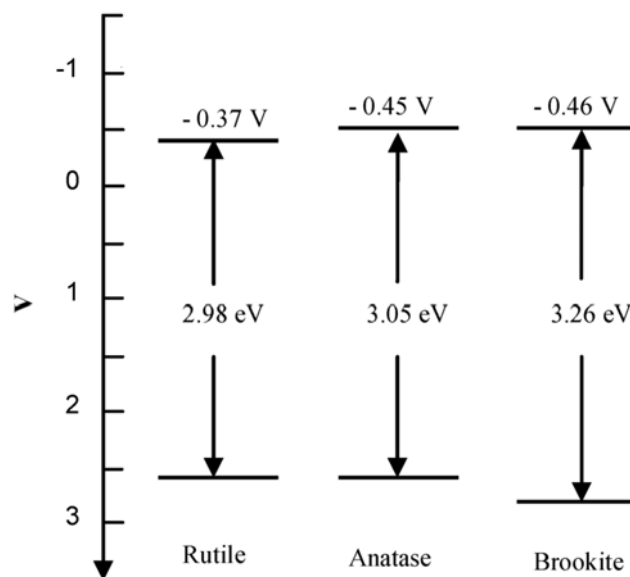


Figure 7 Bandgaps of the three naturally occurring crystalline forms of TiO₂ at pH 7 vs. NHE.²⁴

TiO₂ nanoparticles can be synthesized by hydrolysis of titanium(IV) alkoxides through acid or basic catalysis in an excess of water and are formulated in a paste with polymer additives. By varying the polymer concentration, the porosity of the final nanoporous surface can be altered; ideally it should be between 50 and 60%.²⁵ However, today many different pastes are commercially available. TiO₂ electrodes are usually prepared from colloidal nanoparticle pastes by doctor blading or screen printing followed by sintering at about 450 °C (cf. 4.2.1). TiO₂ films in state-of-the-art TiO₂ electrodes usually consist of four parts. The FTO coated glass is coated with a TiO₂ sublayer ~50 nm in thickness, usually deposited by aqueous TiCl₄ treatment or sputtering and spray-pyrolysis of precursor solutions. This fine layer is meant to suppress recombination by preventing a direct contact of the electrolyte and the FTO glass. On top of this, a 10-15 μm light absorption layer from ~20 nm TiO₂ nanoparticles is doctor bladed or screen-printed. This layer provides the large surface area for sensitization of the dye and transports the electrons from the dye to the FTO anode. Usually, a scattering layer ~3 μm in thickness consisting of 200-400 nm nanoparticles is printed on top. This allows for back-scattering of the incident light to improve the light harvesting efficiency of the dye. A fourth

layer is added by treatment of the electrode in an aqueous TiCl_4 layer and allows for fine tuning of the surface area and porosity.²⁶

3.3.2.2 Dyes

Due to the 3.2 eV bandgap, anatase TiO_2 only absorbs about 3% of the air mass 1.5 solar spectrum (Figure 8) and hence needs to be sensitized by an appropriate charge-transfer dye to harvest a larger spectral distribution of light.¹⁰ This makes the dye one of the key components of DSCs and consequently has to fulfill some necessary requirements. (i) The main characteristic of a dye is its absorption, which ideally covers the whole solar spectrum with the red and the near infrared (NIR) part being particularly important due to the increased photon flux of the sun in this region (Figure 8). (ii) The dye needs to bind efficiently to the semiconductor surface, which is commonly achieved by acid anchors such as CO_2H , $\text{P}(\text{O})(\text{OH})_2$ or cyanoacrylic acids (typically in organic dyes). (iii) For an efficient electron injection from the dye to the semiconductor, the excited state level of the dye should be sufficiently higher than the conduction band edge of the semiconductor. (iv) The HOMO level should be more positive than the redox potential of the electrolyte to allow for efficient regeneration of the dye molecules.⁶ (v) Finally, the dye should have a high stability under working conditions to allow for a long lifetime of the device ($\sim 10^8$ excitation cycles for a 20-year service life).²⁷

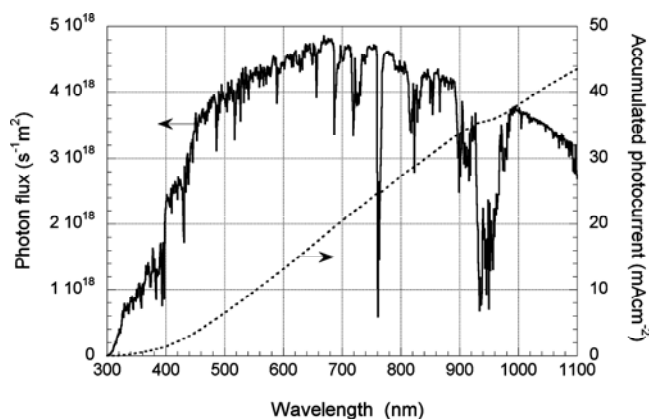


Figure 8 Photon flux of the AM 1.5 G spectrum at 1000 W m^{-2} and calculated accumulated photocurrent (dotted line).⁶

Thousands of different dyes have been implemented into DSCs over the last decades and they can be roughly classified into two groups: metal-organic complexes and metal-free organic dyes. In the context of this thesis, a short overview of three different classes of dyes will be given here: ruthenium(II) dyes, copper(I) dyes and donor- π -bridge-acceptor dyes.

3.3.2.2.1 Ruthenium (II) Dyes

Based on the initial success of ruthenium(II) sensitizers, these types of dyes have been intensively investigated and were only recently displaced as the best performing class of dyes in DSCs.¹³ Their broad absorption spectra, suitable energy levels of the excited and ground states combined with their relatively long excited-state lifetimes and good chemical stability made these metal complexes the photosensitizers of choice for the last two decades.⁶ Ruthenium dyes were first used for sensitization of TiO₂ single crystals in 1979.⁹ Also in the breakthrough report of *O'Regan* and *Grätzel* from 1991, the remarkable overall efficiency of 7.1-7.9% was achieved using a ruthenium(II) dye.¹² Some of the best performing Ru(II) dyes are shown in Figure 9 and were all developed by the group of *Grätzel*. With the dyes labelled as N3, black dye (N749) and N719 efficiencies over 10% were obtained and a maximum efficiency of 11.2% was reached with an N719 sensitized solar cell.²⁸ To date, N719 is one of the most investigated and established dyes and is commonly used as a reference dye in the DSC community (as in this thesis). Figure 10 shows the external quantum efficiency (EQE) of N3 and the black dye on TiO₂ and illustrates the extraordinary quantum efficiencies of these dyes over the entire visible range of the solar spectrum into the NIR. However, in recent years only little improvement was achieved with ruthenium(II) dyes. Assuming a lowest loss-in-potential of 750 mV for the ruthenium complex/iodide system, *Snaitth* estimated the maximum efficiency for these cells to be 13.8%.^{29,30} With measured efficiencies of up to 11.2% for these systems, the optimizations are already close to this estimated maximum limit. However, changing the ruthenium complex/iodide system by, for example, exchange of the electrolyte system to cobalt(II/III) electrolytes has not yet resulted in improved efficiencies. Nonetheless, efficiencies comparable to those achieved with I⁻/I₃⁻ electrolytes have been reached.^{31,32} Recent research on Ru(II) dyes focuses on the long-term stability of the devices, which is achieved by introducing alkyl chains³³ (as in Z907, Figure 9) or by designing thiocyanate free Ru(II) dyes (NCS is thought to be the most sensitive part of Ru(II) dyes).³⁴⁻³⁶

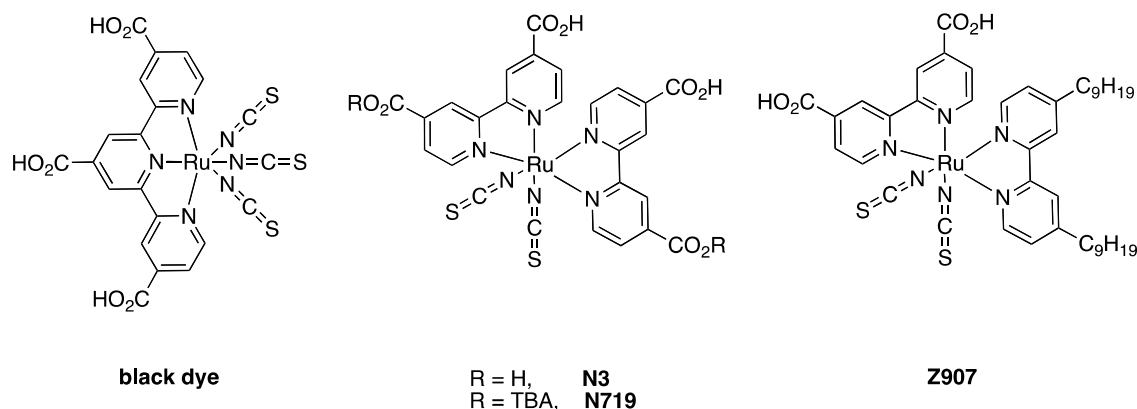


Figure 9 Examples of well performing ruthenium(II) dyes including the widely used reference dye N719. TBA = tetrabutyl ammonium

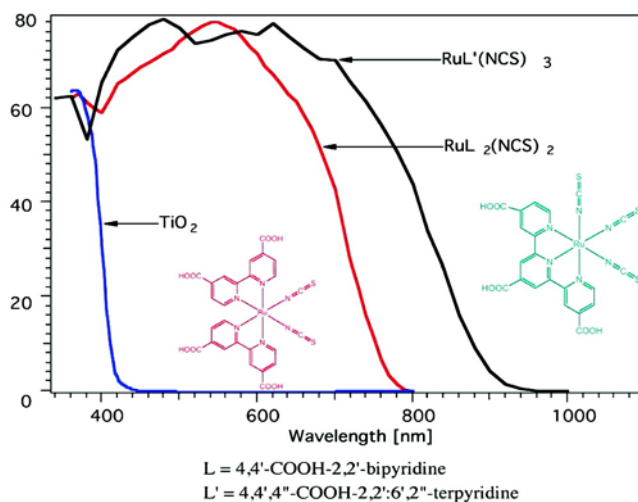


Figure 10 External quantum efficiency (EQE) of N3 (red line) and the black dye (N749, black line) as a function of wavelength.³⁷

A main disadvantage of ruthenium dyes is the toxicity and the rare abundance, and consequently high production costs, of ruthenium and for DSCs from these dyes. These are highly unfavorable characteristics for future large-scale energy production and, therefore, more abundant, cheaper, and sustainable alternatives are required.

3.3.2.2.2 Copper(I) Complexes

Since this thesis concerns the incorporation of copper(I) complexes in DSCs, they are discussed here in more detail. To date, Cu(I) complexes have not been as rigorously investigated as ruthenium(II) complexes for use in DSCs. However, the urgent need for more sustainable and cheaper components in DSCs have made them a hot research topic in recent years. Due to their

similar photophysical properties to Ru(II) complexes^{38,39}, they were applied in DSCs in 1991 by *Sauvage and co-workers*⁴⁰ and later by *Sakaki et al.*⁴¹ After first reports with *homoleptic* Cu(I) and efficiencies up to 2.3% (unmasked cells),⁴² our group has recently introduced a new *on-surface* strategy for the assembly of *heteroleptic* copper(I) bisdiimine complexes that has been successfully implemented for a wide range of different copper(I) dyes.^{43–46} For this, an anchoring ligand is first adsorbed onto the semiconductor surface, which subsequently undergoes a ligand exchange with a *homoleptic* Cu(I) dye (for more detail consult Chapter 8). This powerful method enables the screening of a large number of Cu(I) dyes without the need for isolation, giving access to an exciting new field of *heteroleptic* Cu(I) dyes. Such complexes cannot usually (but see below) be synthesized in solution since rapid ligand exchange of Cu(I) dyes leads to statistical mixtures of *homoleptic* and *heteroleptic* Cu(I) dyes.⁴⁷ Maximum power conversion efficiencies of 3.77% in unmasked⁴⁴ and 3.16% in masked DSCs⁴⁸ were obtained with *heteroleptic* Cu(I) dyes synthesized according to this strategy (Figure 11). The success of this method has inspired other groups to synthesize *heteroleptic* Cu(I) dyes following this procedure. However, the efficiencies obtained by DSCs with ancillary ligands used by the groups of *Robertson*⁴⁹ (Figure 12) and *Elliott*⁵⁰ (Figure 13) have not yet been very promising.

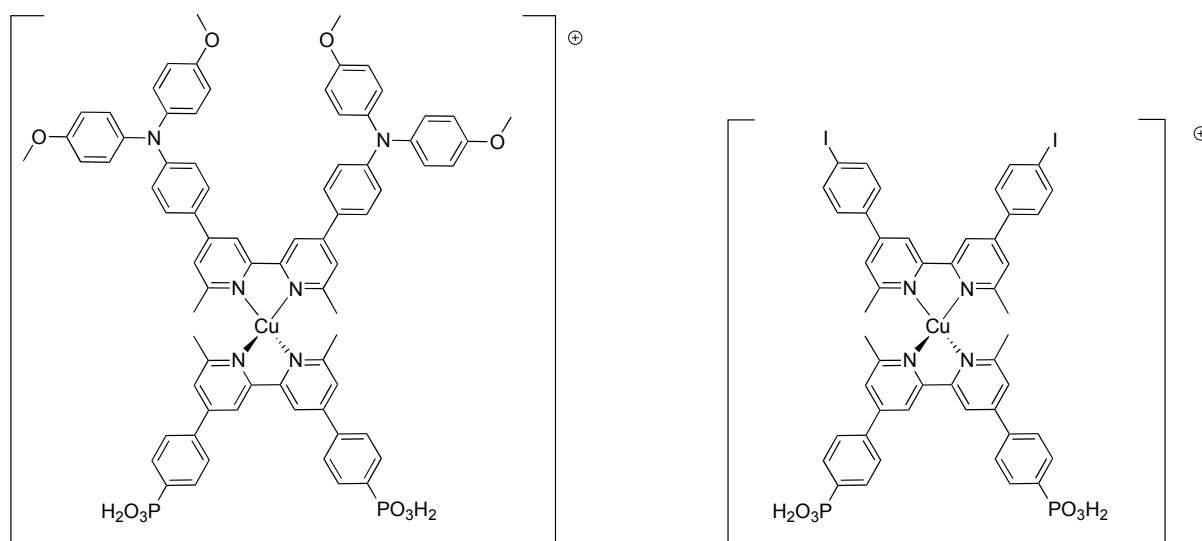
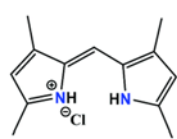
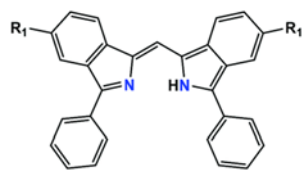


Figure 11 *Heteroleptic* Cu(I) dyes prepared by the described *on-surface* method leading to efficiencies in DSC of 3.77% in unmasked cells (left)⁴⁴ and 3.16% with masked cells (right).⁴⁸



HL1.HCl



R₁ = H HL2
= CF₃ HL3

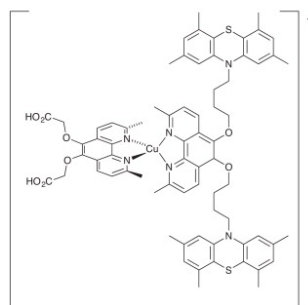


Figure 13 Cu(I) complex prepared after the on-surface synthesis and investigated by the group of Elliott.⁵⁰

Figure 12 Ancillary ligands used for the on-surface synthesis of Cu(I) complexes with 4,4'-dicarboxylic acid-6,6'-dimethyl-2,2'-bipyridine as anchoring ligand by the group of Robertson.⁴⁹

A different concept is adopted by the group of *Odobel*,^{51,52} following the HETPHEN strategy of *Schmittel*,⁵³ using highly sterically demanding diimine ligands, such as 2,9-dimesityl-1,10-phenanthroline to synthesize heteroleptic copper(bisdiimine) complexes that are stable with respect to ligand dissociation. The Cu(I) complexes shown in Figure 14 show conversion efficiencies up to 4.66% and are the most efficient Cu(I) dye sensitized solar cells to date.

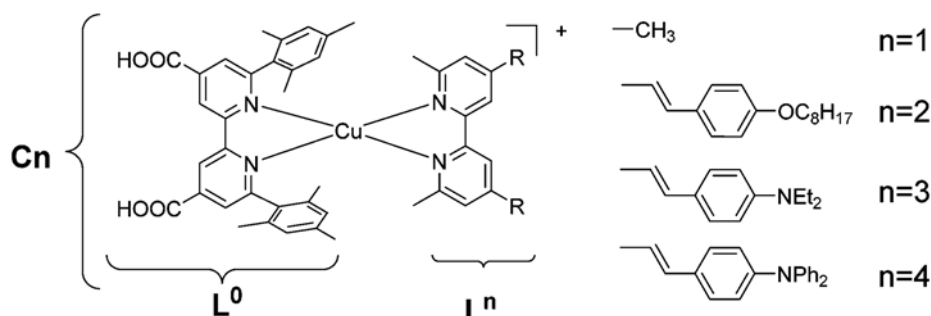


Figure 14 Investigated Cu(I) complexes by the group of *Odobel* showing a maximum conversion efficiency of 4.66% for C3 in combination with the coadsorbant cheno (see Figure 93)⁵²

3.3.2.2.3 Donor- π -Bridge-Acceptor Dyes

Another very successful class of dyes are donor- π -bridge-acceptor dyes. Organic dyes have shown low conversion efficiencies for a long time due to poor absorption in the red and stability issues. However, the concept of donor- π -bridge-acceptor allowed for tuning of the redox and absorption properties by adjusting the different units leading to improved efficiencies in recent years. Common donor groups such as arylamines and cyanoacrylates are usually chosen as the anchoring group. The π -bridge often consists of at least one thiophene unit. Molecular orbital (MO) calculations have shown that the highest-occupied molecular orbital (HOMO) of these dyes is located on the arylamine unit while the lowest-

unoccupied molecular orbital (LUMO) is centred on the cyanoacrylate anchoring group.⁵⁴ A typical example of this class of dye is shown in Figure 15a with a dye reported by *Feldt et al.*²² A maximum efficiency of 6.7% at 1000 W m⁻² was reported for this dye using a [Co(bpy)₃]^{2+/3+} electrolyte. The combined optimization of dye and electrolyte in this publication was a milestone in the development of high-performance DSCs containing cobalt(II/III) electrolyte (as discussed later).

The highest efficiency reported for a DSC to date was achieved with a donor- π -bridge-acceptor zinc porphyrin sensitizer.¹³ Based on the results obtained with the organic dye by *Feldt et al.*, long-chain alkoxy groups were attached to efficiently suppress interfacial back electron-transfer reactions. This allowed for the use of a [Co(bpy)₃]^{2+/3+} electrolyte with a subsequent higher V_{oc} . A diarylamine group attached to the porphyrin acts as a donor group and an ethynylbenzoic acid moiety serves as an acceptor anchoring group. After optimization of the DSC, a record efficiency of 12.3% was achieved.

However, a downside of these organic dyes is their long-term stability. In particular the synthesis of the zinc-porphyrin dyes is very challenging and may hinder this class of dyes from successful commercialization.

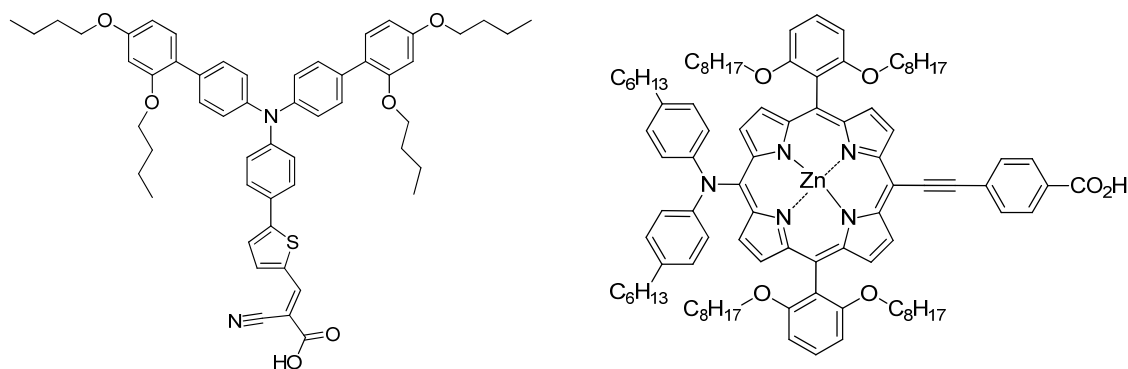


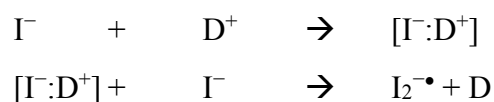
Figure 15: a) Typical example of a donor- π -bridge-acceptor dye with a reported efficiency of 6.7% in combination with a [Co(bpy)₃]^{2+/3+} electrolyte.²² b) The best performing dye in a DSC to date with a reported maximum efficiency of 12.1%.¹³

3.3.2.3 Electrolyte

The electrolyte is one of the key components of DSCs and has a substantial impact on the conversion efficiency of a solar cell since it influences all of the characteristic parameters. There are several requirements an electrolyte must fulfil for its efficient performance in DSCs⁵: (i)

The electrolyte needs to efficiently transport the charge carriers between the two electrodes and must rapidly reduce the oxidized dye to its ground state. (ii) Fast diffusion of the charge carriers and good interfacial contact with the mesoporous semiconductor and the counter electrode are required. (iii) The electrolyte must be chemically, thermally, optically and electrochemically stable and not cause desorption or degradation of the dye. (iv) The electrolyte should not absorb light in the visible range.

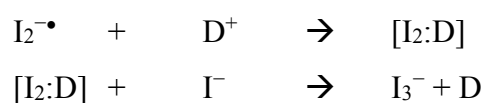
For about 20 years, the I^-/I_3^- redox couple was used almost exclusively as the electrolyte in DSC's. Until recently, only DSCs incorporating the I^-/I_3^- electrolyte achieved efficiencies beyond 10%. The superior performance was mainly attributed to the slow recombination kinetics, the very fast dye regeneration, and the favourable penetration of the nanoporous semiconductor.⁵⁵ The mechanism of the reduction of dye cations D^+ is still under discussion. However, the first two steps appear to work as shown in the following two reactions:



While the first step is fast the second one is rate limiting due to its dependence on the interaction of a second I^- with a $[I^-:D^+]$ -complex. Dissociation of $I_2^{\bullet-}$ immediately occurs when a second I^- interacts with the $[I^-:D^+]$ -complex. The spectroscopic detection of the $I_2^{\bullet-}$ anion radical supports this hypothesis. Finally, I^- and I_3^- are formed by disproportionation of two $I_2^{\bullet-}$:^{56,57}



For the dyes N3/N719, I^- has been shown to be bound to the sulfur atom of the thiocyanate ligand of the intermediate complex. In this case, the Ru(III) centre is reduced to Ru(II) and the complex is better written as $[I:D]$.⁵⁸ However, the nature of intermediate complexes for thiocyanate-free dyes is unknown. More recently, an alternative mechanism was reported in which the $I_2^{\bullet-}$ radical reduces a second D^+ to form a $[I_2:D]$ complex, which interacts with another I^- and the subsequent complex then dissociates to give I_3^- .⁵⁹



Despite the widespread use of the I^-/I_3^- redox couple, it does not fulfill all of the requirements described above for an ideal electrolyte. On the contrary, there are numerous negative features of this redox couple that limit the improvement and commercial application of DSCs. (i) I^-/I_3^- has a relatively high overpotential for dye regeneration and this limits the photovoltage. (ii) I_3^- absorbs light in the visible range resulting in a loss in photocurrent.⁵⁷ (iii) The I^-/I_3^- redox couple is reactive towards most metals and sealing materials leading to substantial stability problems especially in scale up.²²

A few alternative redox couples to the I^-/I_3^- system have been investigated. A common feature of all alternative electrolyte systems is the increased recombination rate with respect to the I^-/I_3^- electrolyte. Nevertheless some promising results have been presented. In 2010, *Marsan et al.* reported a disulfide/thiolate redox couple that yielded an efficiency of 6.4% under full sunlight with Z907 sensitized solar cells.⁶⁰ The redox couple (Figure 16) consists of a 5-mercapto-1-methyltetrazole ion and its dimer and has a comparable redox potential to I^-/I_3^- with 0.49 V vs. NHE. In comparison to I^-/I_3^- , this redox couple is non-corrosive and does not absorb in the visible spectrum. These properties together with the good performance makes it a valuable alternative to I^-/I_3^- . *Daeneke et al.* presented a ferrocene/ferrocenium (Fc/Fc^+) electrolyte in 2011 that yielded a remarkable efficiency of 7.5% in combination with an organic donor-acceptor sensitizer. Due to a better match of the redox potential of Fc/Fc^+ with the ground state energy of the dye, the performance was superior to I^-/I_3^- under comparable conditions.⁶¹ However, for high efficiencies exclusion of oxygen during the electrolyte preparation and cell construction was of vital importance, which is a significant hindrance for future commercialisation. Further reports concentrated on the use of radical ions such as TEMPO (2,2,6,6-tetramethyl-1-piperidinyloxy)^{62,63} or AZA (2-azaadamantan-*N*-oxyl)⁶² with remarkable efficiencies of up to 8.6%.

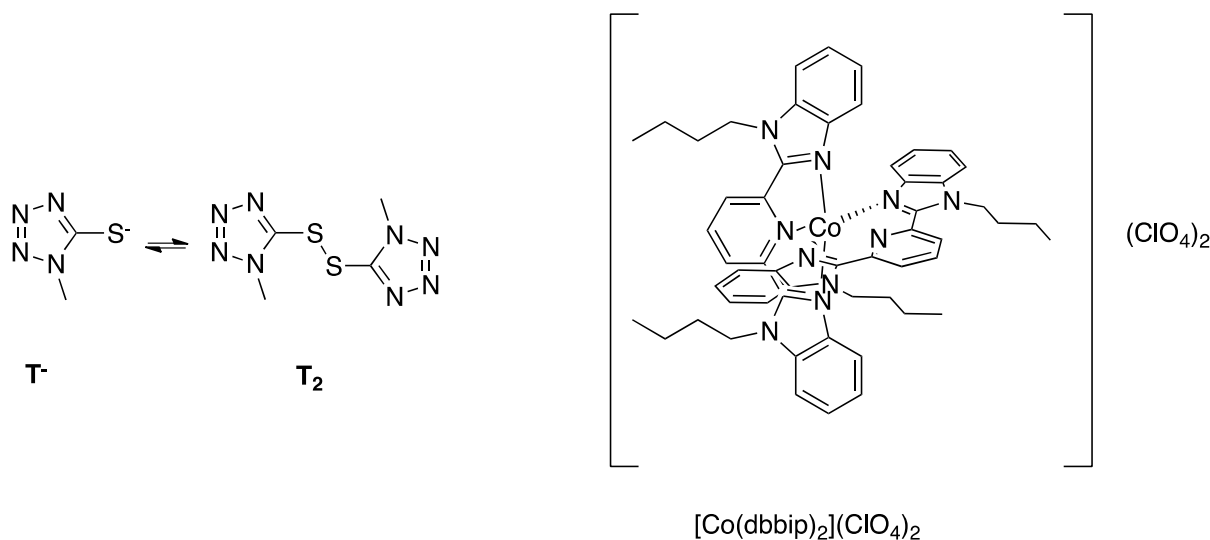


Figure 16: Two iodine free electrolytes: the disulfide/thiolate redox couple (a) and the cobalt complex $[\text{Co}(\text{dbbip})_2](\text{ClO}_4)_2$ (b).

The most investigated, and also the best performing, alternative redox couple are cobalt(II/III) complexes. Cobalt complexes have been recognized as potential alternative mediators for DSCs for over a decade. A main advantage of these redox shuttles is the tunability of their redox potential, which allows for a better adjustment to the dye ground state potential. Thereby, the overpotential loss in the regeneration step of the dye can be reduced resulting in higher photovoltages and consequently increased conversion efficiencies.^{30,64} Another attractive feature of cobalt(II/III) polypyridyl complex redox shuttles is their reduced competitive visible light absorption with respect to the I^-/I_3^- redox couple. Additionally, cobalt(II/III) complexes are non-corrosive, facilitating the production of large-area DSCs and increasing their lifetime.⁶⁵ Promising early results were obtained by *Nusbaumer* in 2001 by using the $[\text{Co}(\text{dbbip})_2](\text{ClO}_4)_2$ redox couple (with $\text{dbbip} = 2,6\text{-bis}(1'\text{-butylbenzimidazol-2}'\text{-yl})\text{pyridine}$, Figure 16). A power conversion efficiency of 2.2% at full sunlight was reached in combination with a ruthenium(II) dye and with an illumination at 10% light intensity of one sun, the efficiency was raised to 5.2%. This dependence of the power conversion efficiency on the incident light intensity was attributed to mass transport limitations of the electrolyte.⁶⁶ Two years later and after optimization of the TiO_2 -film thickness, the counter electrode, the mediator concentration and incorporation of a sterically more demanding ruthenium(II) sensitizer an overall efficiency for the same redox couple of 4% was reported.⁶⁷ However, despite these optimizations, a dependence of the efficiency from 1 sun to lower illumination intensities was still observed.⁶⁷ *Sapp et al.* screened a variety of cobalt(II/III) complexes and found

$\text{Co}(\text{DTB})_3^{2+/3+}$ (with DTB = 4,4'-di-*tert*-butyl-2,2'-bipyridine) to perform best in DSCs and achieved 80% of the performance of a comparable DSC based on an I^-/I_3^- electrolyte.⁶⁸ Later, *Nelson et al.* found the diffusion rate of $\text{Co}(\text{DTB})_3^{2+/3+}$ through typical titania films in DSCs to be an order of magnitude slower than I_3^- .⁶⁹ *Klahr* and *Hamann* found that the main limitations of cobalt bipyridyl redox shuttles are recombination and mass transport of the oxidized species through the nanoparticle photoelectrode. However, recombination loss could be reduced by coating the photoanode with an ultrathin Al_2O_3 blocking layer.⁷⁰ A breakthrough was achieved by the work of *Feldt et al.*²² with the introduction of bulky alkoxy chains at the dye molecule (Figure 15 a) rather than at the Co-complex itself. With this, recombination could be reduced without increasing the mass transport of the cobalt redox shuttle. Furthermore, the previously obtained limitations for cobalt electrolytes were further reduced by incorporation of thin-film TiO_2 films enabled by the use of high extinction coefficient dyes. This resulted in a power conversion efficiency of 6.7% using a $[\text{Co}(\text{bpy})_3]^{2+/3+}$ electrolyte.²² These results were the basis for a landmark paper by *Yella et al.* in 2011 who combined an optimized donor- π -bridge-acceptor zinc porphyrin dye (Figure 15 b) with a $[\text{Co}(\text{bpy})_3]^{2+/3+}$ electrolyte to obtain a DSC with a record conversion efficiency of over 12%.¹³ This achievement represents a paradigm shift, since it was the first time that Ru(II) sensitizers were outperformed by a different class of dyes while simultaneously achieving a higher DSC performance with an electrolyte other than I^-/I_3^- . Key for this achievement was the simultaneous optimization of dye, electrolyte and semiconductor characteristics. An important factor for the improved efficiency when using a Co(II/III) electrolyte (that was only briefly mentioned in the supplementary data) was the careful tuning of the mesoporous TiO_2 film for this electrolyte species. In 2012, *Tsao et al.* presented a method of tuning the four characteristic properties of TiO_2 films, namely film thickness, porosity, particle and pore size. This allows for the preparation of thicker TiO_2 films with increased porosity and pore size for the successful implementation in DSCs containing Co(II/III) electrolytes and was achieved by varying the TiCl_4 concentration in the post-treatment step.²⁶

4 Materials and Methods

4.1 General Materials

MiliQ water and HPLC grade solvents were used exclusively for cleaning of electrodes and to prepare dye and electrolyte solutions.

4.2 Materials for the Dye Sensitized Solar Cells

4.2.1 Working Electrode

The working electrodes were either self-printed or purchased from Solaronix (ref. 74991).

4.2.2 Doctor Blading

FTO coated glass (TC022-7, 7 Ω /sq, 2.2 mm, Solaronix) was cut into pieces of 2x1.6 cm and 2x0.9 cm, respectively, was sonicated in a 2% aqueous surfactant solution (Sonoswiss cleaner, SW-C L2) for 7-10 min. and was rinsed with water. After sonicating the glasses in acetone and EtOH for 7-10 min. each, they were dried in a stream of N₂. A thin layer of TiO₂ was adsorbed by dipping the glasses into a 40 mM aqueous solution of TiCl₄ for 30 min. The electrodes were rinsed with water and EtOH and dried in a stream of N₂. The electrodes were then covered by two parallel layers of adhesive tape (Scotch™ Magic™ 3M) leaving a free area of 0.5x0.9 cm, and a colloidal paste of TiO₂ (nanoxide T, Solaronix, 15-20 nm particle size) was spread over the electrode to fill the area. The electrodes were left to dry in air at room temperature for 15 min. until the plates were completely transparent. Then they were sintered at 450 °C for 30 min. in an oven. After cooling down to room temperature they were post-treated by dipping the glasses into a 40 mM aqueous solution of TiCl₄ for 30 min. The electrodes were rinsed with water and EtOH and were dried in a stream of N₂. Finally they were sintered again at 450 °C for 30 min. in an oven.

4.2.3 Screen Printing

The screen printing method was done following a modified literature procedure.⁷¹

For the self-printed electrodes, fluorine doped tin oxide (FTO) glass plates (TC022-7, 7 Ω /sq, 2.2 mm, Solaronix) with a thickness of 2.2 mm and a sheet resistance of 7 Ω /sq were sonicated in a 2% aqueous surfactant solution (Sonoswiss cleaner, SW-C L2) for 15 min. After rinsing with water and EtOH they were dried in a stream of N₂ and were further cleaned by ultraviolet ozone treatment using a UVO-Cleaner® 42 from Jelight Company, Inc. A thin layer of TiO₂

was adsorbed by dipping the glasses into a 40 mM aqueous solution of TiCl_4 for 30 min. The electrodes were rinsed with water and EtOH and dried in a stream of N_2 . A layer of TiO_2 -paste (DSL 90-T or 18NRT, Dyesol) with an average particle size of ~ 20 nm was screen printed (90T mesh size, Serilith AG, Switzerland) onto the glass plates. The printed electrodes were kept in an EtOH chamber for 1.5 min, and 3 min for the following printing cycles, to reduce surface irregularities of the printed layer followed by drying for 6 min at 125°C on a heating plate. The printing cycle was repeated 2 or 3 times and a final TiO_2 scattering layer with an average particle size 150-200 nm (WER2-O, dyesol) was printed on top. The electrodes were gradually heated at 75°C for 30 min, at 135°C for 15 min, at 325°C for 5 min, at 375°C for 5 min, at 450°C for 15 min and at 500°C for 15 min in an oven (Nabertherm N 15/65HA). After the final sintering, the thickness of the TiO_2 layer was 12-15 μm (measured with Tencor Alpha-Step 500 profilometer).

4.2.4 Counter Electrode

The counter electrodes were either self-printed or purchased from Solaronix (ref. 74991). Self-made counter electrodes were prepared from an FTO glass plate (TC022-7, $7\ \Omega/\text{sq}$, 2.2 mm, Solaronix) with a previously drilled hole. The electrodes were heated for 15 min at 500°C on a heating plate, washed with water and a 0.1 M HCl solution in EtOH and sonicated in acetone for 15 min. The electrodes were dried on a heating plate at 500°C for 15 min. After cooling to room temperature, the Pt catalyst was deposited on the FTO glass plates by coating the surface with 2 aliquots of a 25.0 μL solution of a platinum precursor in propanol (Platisol T, Solaronix) and was activated by heating on a heating plate at 500°C for 15 min.

4.2.5 Cell Assembly

The two electrodes were assembled using a thermoplast hot-melt sealing foil (Solaronix, Meltonix 1170-25, 1170-60 and 1170-100 Series; 25, 60 and 100 μm , respectively) and heating the cell via the counter electrode with a soldering iron at 200 - 250°C while pressing together the two electrodes. The tip of the soldering iron was modified by a square hole with the size of the active area of the cell to avoid degradation or desorption of the anchored dye by heat. After sealing the electrodes, the cell was evacuated and flushed with N_2 three times and the electrolyte was filled in through the pre-drilled hole in the counter electrode by vacuum back filling. The hole was sealed using sealing foil and a covering glass. To improve the contact for the measurements silver paint was added on the side of each electrode.

4.2.6 Electrolyte

Investigating the influence of changing the electrolyte is a main part of this work and is therefore described in the respective chapters (Chapter 10 and Chapter 11).

An I^-/I_3^- -mediator was used as a reference electrolyte and was composed of LiI (0.1 mol dm^{-3}), I_2 (0.05 mol dm^{-3}), 1-methylbenzimidazole (0.5 mol dm^{-3}) and 1-butyl-3-methylimidazolium iodide (0.6 mol dm^{-3}) in 3-methoxypropionitrile.

4.3 General Methods for Characterization and Analysis of the Synthetic Work

^1H and ^{13}C NMR spectra were recorded on a Bruker Avance III-500 or 400 MHz NMR spectrometer; chemical shifts were referenced to residual solvent peaks with respect to $\delta(\text{TMS}) = 0$ ppm. Solution absorption spectra were recorded on a Perkin Elmer Lambda 25 spectrometer and an Agilent Cary5000 UV-Vis-NIR spectrophotometer. Solid state absorption spectra of TiO_2 electrodes were measured on an Agilent Cary5000 UV-Vis-NIR spectrophotometer using commercial TiO_2 -electrodes (Solaronix, Ref. 74111) without a scattering layer. FT-IR spectra were collected using a Perkin Elmer Spectrum Two with UATR for solid samples. MALDI-TOF and electrospray ionization (ESI) mass spectra were recorded on Bruker esquire 3000^{plus} and Bruker Daltonics Inc. microflex instruments, respectively; LC-ESI-MS mass spectra used a combination of Shimadzu (LC) and Bruker AmaZon X instruments. High resolution MS were measured on a Bruker maXis 4G instrument. Elemental analyses were measured on a Leco CHN-900 microanalyser. Crystallographic data were collected on a Bruker-Nonius Kappa APEX diffractometer with data reduction, solution and refinement using the programs APEX2, SIR92,⁷² and CRYSTALS,⁷³ Structures were analysed using Mercury v. 3.5.^{74,75}

4.4 Characterisation of the Dye Sensitized Solar Cells

4.4.1 Cell Masking

For the J/V measurements the cells were measured with a sun simulator after prior calibration with a silicon solar cell. Dye sensitized solar cells are more efficient at converting diffuse light into electricity than silicon solar cells, which are by far more efficient at converting light shining perpendicular onto the cell. Additionally, the architecture of DSCs with, in this case, 2 mm thick glass can lead to scattered and reflected light leading to an overestimating of the incident light (Figure 17a). *Snaith*⁷⁶ and *Schmidt-Mende*⁷⁷ have discussed the inconsistency of solar cell measurements due to unmasked cells in the literature. *Snaith*⁷⁸, *Grätzel*⁷⁹, and *Han*⁸⁰ have pointed out how to overcome the overestimation of the incident light by different ways of masking the cells. Therefore we have developed an easy and reproducible protocol (see Section 7.5) to fully mask our cells. Figure 17c shows the final masking procedure that was used for most of the DSCs discussed in this work. A copper sheet with a defined aperture (average area of 0.06012 cm² with a standard deviation of 1%) was placed on top of the cell to have a defined irradiated area of the cell. The irradiated area was smaller than the complete active area of the electrode of 0.288 and 0.36 cm², respectively. A complete masking of the edges and side of the cell was achieved using a black tape.

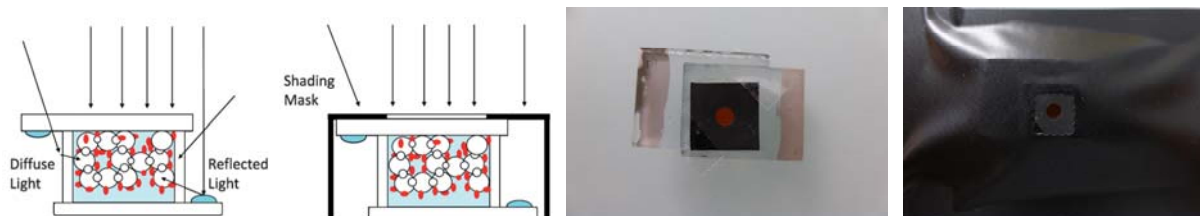


Figure 17 Reflected and scattered light leading to an overestimating of the incident light in an unmasked cell (left) and a masked cell (right). b) Copper sheet top mask with the aperture for a defined irradiated area. c) Fully masked cell

4.4.2 Sun Simulator

J/V measurements were performed using a SolarSim 150 (Solaronix) equipped with a Philips MSR 200 HR 1CT (Philips MSR 200 HR 928097905114) and two Xenon bulbs (Osram HLX 64623 XENOPHOT) previously calibrated with a Si-reference cell to 1000 Wm⁻² (1 sun). The cells were kept at a constant temperature of 25 °C and were measured by applying an external voltage by a Keithley 2400 source meter. ReRa Tracer 1.0 and 2.0, respectively, (ReRa Systems

NL) was used for controlling the source meter as well as collecting and analyzing the measured data.

4.4.3 Current Density to Voltage (J/V) Measurements

The most important characteristic of a solar cell is its power conversion efficiency η . This is the efficiency of the conversion of incident light into electricity. It is dependent on the intensity of the incoming light as well as on the irradiated active area of the solar cell. The maximum power point (P_{\max}) of the cell is reached when the product of the current density and the potential reaches its maximum.

$$P_{\max} = |V \cdot J|_{\max} \quad (1)$$

The respective potential and current at P_{\max} are called V_{MP} and J_{MP} , respectively.

η can be determined by current density to voltage (J/V) measurements under illumination and is defined by

$$\eta = \frac{|V \cdot J|_{\max}}{P_{\text{In}}} = \frac{J_{\text{SC}} \cdot V_{\text{OC}} \cdot ff}{P_{\text{In}}} \quad (2)$$

with P_{in} as the power density of the incident light, V as the applied voltage, and J as the current density.⁶ The maximum current density that the solar cell can reach is the short circuit current density J_{SC} at short circuit conditions. The maximum potential of the cell is at open circuit conditions and is called the open circuit potential V_{OC} . Graphically, the J_{SC} is the interception of the J/V -curve at $V=0$ and V_{OC} the interception of the curve at $J=0$ (Figure 18). The fill factor (ff) is the ratio of the inner rectangle and the outer rectangle and has a value from 0 to 1. The ff describes the shape of the curve and is an indicator for how efficient the solar cell is in its working range. Mathematically, the ff is defined as

$$ff = \frac{V_{\text{MP}} J_{\text{MP}}}{V_{\text{OC}} J_{\text{SC}}} \quad (3)$$

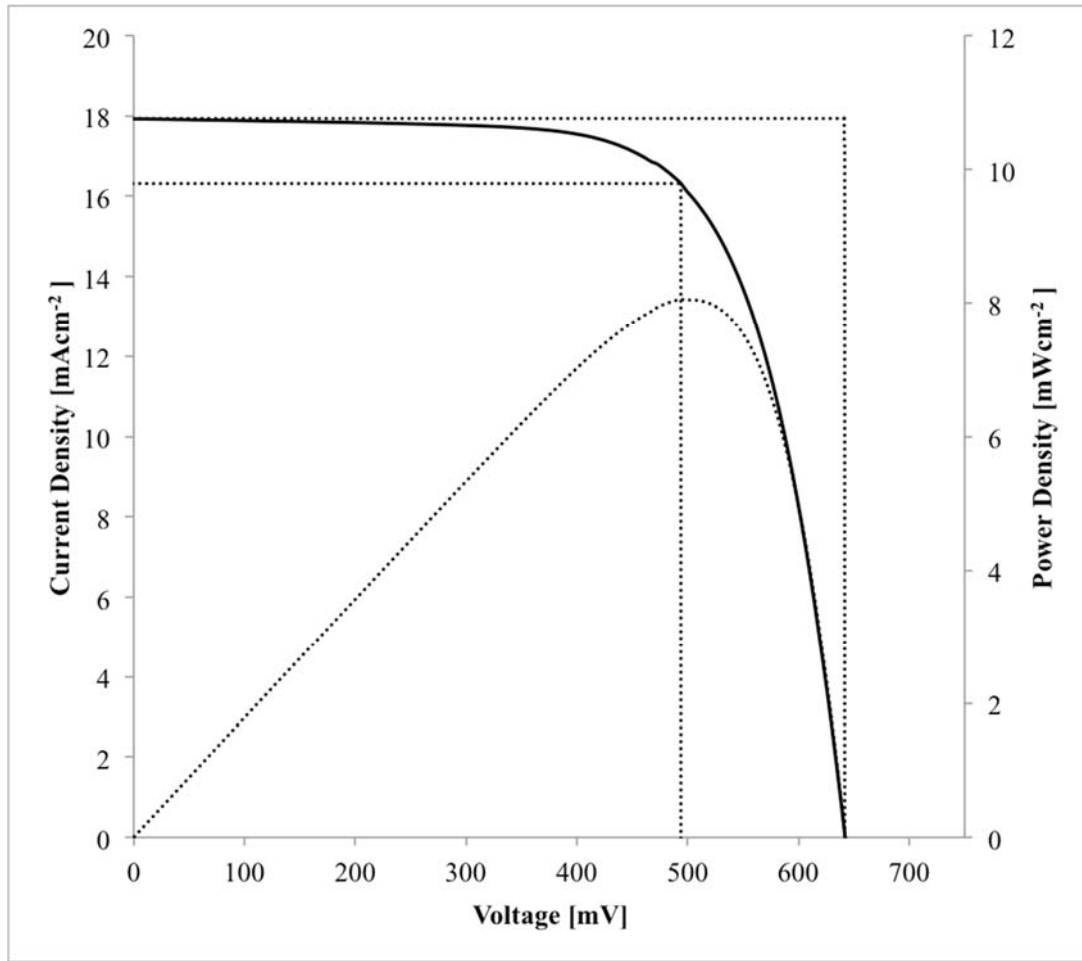


Figure 19: A typical J/V curve of a N719 cell measured in our lab under the described conditions. The outer rectangle is defined by the V_{OC} and J_{SC} and the inner one by V_{MP} and J_{MP} . The quotient of the two gives the ff .

4.4.4 Dark Current Measurements

Measuring a J/V curve in the dark gives the dark current of a cell. The dark current is voltage dependent and is directly related to the recombination process (process 2 and 4 in Figure 5) and the V_{OC} of a cell.⁸¹ Dark current measurements were collected under the same conditions as the illuminated J/V curves but in the dark. To suppress surrounding background light the cells were completely covered by a black tape.

4.4.5 Long Term Measurements

To test the long term stability of different cells measurements were made over a period of up to 95 h under constant irradiation at 1000 Wm^{-2} and at a constant temperature of $25 \text{ }^\circ\text{C}$. A homemade source meter (prepared by the workshop in the Department of Physics) was

controlled via a *LabView* interface programmed by *Dr. Gino Günzburger* to measure J/V curves every 5 minutes.

4.4.6 Incident Photon to Current Efficiency

The incident photon to current efficiency (IPCE) or external quantum efficiency shows the spectral response of a solar cell. It is measured by recording the current output while shining monochromatic light onto the cell at short circuit conditions. Chopping the monochromatic light source allows the use of a white light bias light to run the measurement under real operational conditions. IPCE or EQE is defined as

$$EQE(\lambda) = 1240 \cdot \frac{J_{sc}(\lambda) [\text{Acm}^{-2}]}{\lambda [\text{nm}] \cdot P_{in}(\lambda) [\text{Wcm}^{-2}]} \quad (4)$$

where 1240 is a correction factor from eV to nm. Integration over the whole EQE spectra results in the I_{sc} (Equation (5))

$$I_{sc} = \int_0^{\infty} EQE(\lambda) \cdot I_s(\lambda) d\lambda \quad (5)$$

If only the adsorbed light is taken into account it is defined as the internal quantum efficiency (IQE) or absorbed photon to current efficiency (APCE). For this reflection and transmission of the light source have to be subtracted from P_{in} . In this work only EQE was measured as the reflection and transmission should be very similar between different cells that were produced in the same way or are from the same commercial source. Therefore we expect no difference in the relative trends between different cells from their EQEs and IQEs, respectively.

The quantum efficiency measurements were performed on a Spe-Quest quantum efficiency setup from Rera Systems (Netherlands) equipped with a 100 W halogen lamp (QTH) and a lambda 300 grating monochromator from Lot Oriel. The monochromatic light was modulated to 3Hz using a chopper wheel from ThorLabs. The cell response was amplified with a large dynamic range IV converter from CVI Melles Griot and then measured with a SR830 DSP Lock-In amplifier from Stanford Research.

4.4.7 Voltage-Decay Measurements

Open circuit voltage decay (OCVD) was measured after the simple method developed by *Zaban, Greenshtein and Bisquert* in 2003.⁸² The electron lifetime as a function of voltage can be calculated from this V_{OC} vs. time data by

$$\tau_n = -\frac{k_{BT}}{e} \left(\frac{dV_{OC}}{dt} \right)^{-1} \quad (6)$$

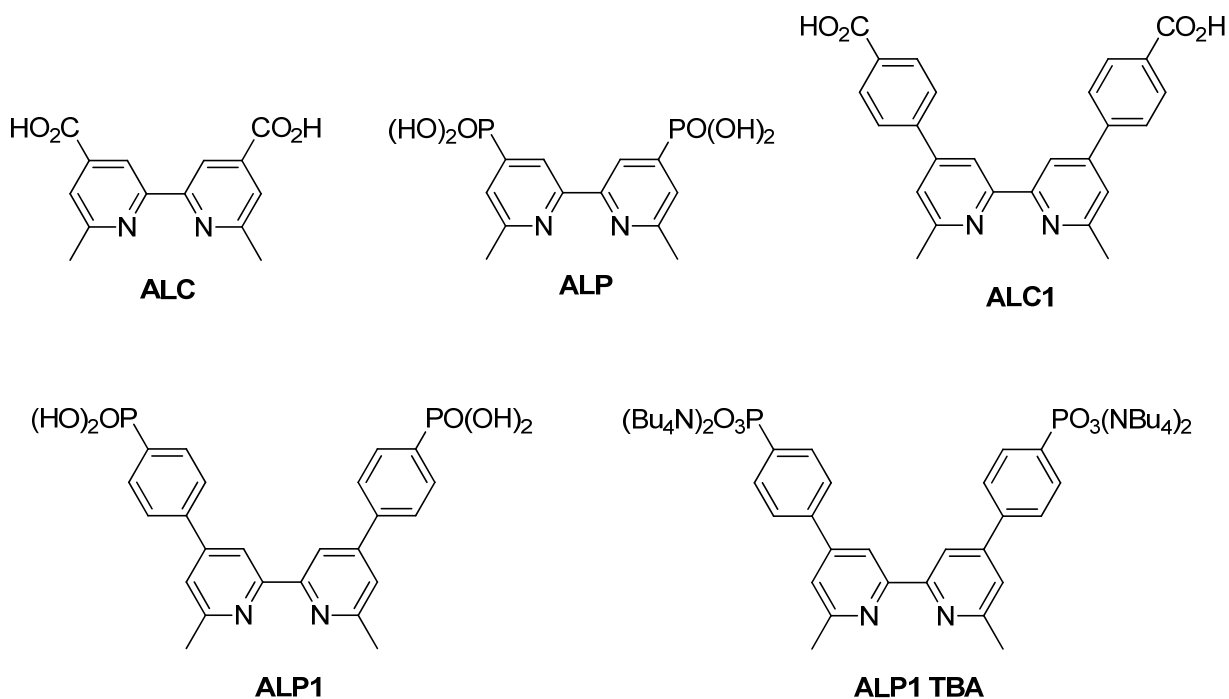
where k_{BT} is the thermal energy and e is the elementary charge.⁸²

The cells were irradiated with a sun simulator (LOT Quantum Design LS0811) equipped with a shutter and connected to a Keithley 2400 source meter for at least 15 s and the shutter was closed to collect the decay of the V_{OC} over time. To reduce light pollution from the background, the cells were further covered after closing the shutter. The sun simulator was controlled via a *LabView* interface programed by *Rés Jöhr*. Later measurements in this thesis were run on a Modulab XM electrochemical system.

5 Synthesis

5.1 Aim and Target Molecules

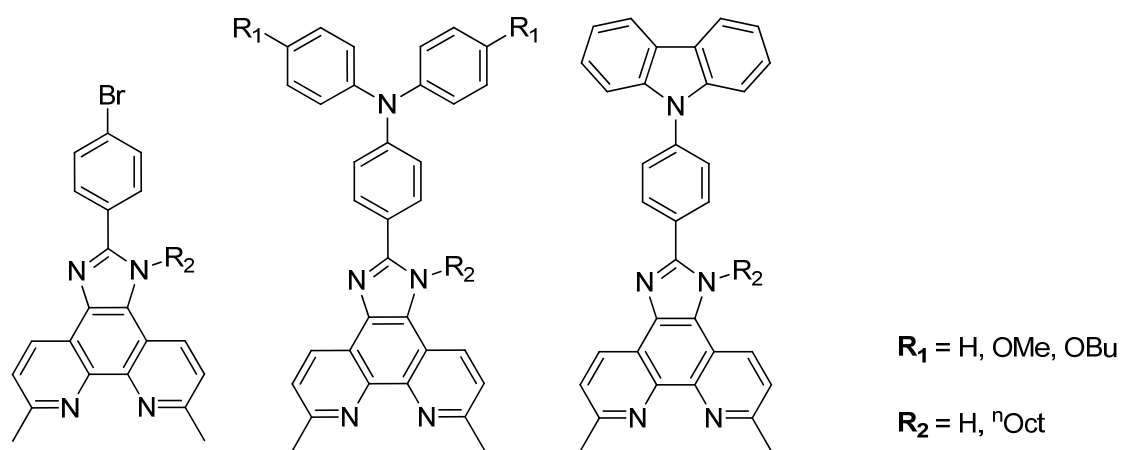
Before the start of this thesis work, several anchoring ligands had been developed by our group for the synthesis of *heteroleptic* copper complexes on TiO₂ surfaces of which mainly two, **ALC1** and **ALP**, turned out to be promising candidates in DSCs.¹⁸ In the current work, introduction of a phenyl spacer to **ALC** as well as changing the carboxylic acid to a phosphonic acid anchor proved to be beneficial concerning the solar cell efficiency. Capitalizing on these results **ALP1** was synthesized as the logical combination of the benefits of **ALC1** and **ALP**, respectively (Scheme 1). Due to the poor solubility of **ALP1** in solvents other than DMSO and a potential stronger binding and electron injection on TiO₂, the corresponding tetrakis(tetra-*n*-butyl)ammonium salt **ALP1 TBA** was synthesized.



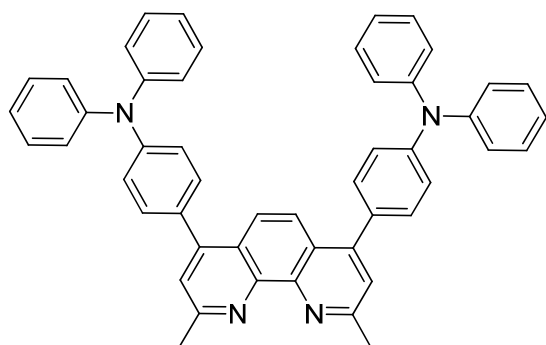
Scheme 1 Anchoring Ligands.

The second part of this chapter describes the syntheses of 2,9-dimethyl-1,10-phenanthroline based ancillary ligands of the type I and II (Scheme 2). Type I ligands are 5,6-imidazole-substituted 2,9-dimethyl-1,10-phenanthrolines which differ in their donating group, which is either a diaryl unit or a 9*H*-carbazole. Furthermore, different *para*-alkoxy groups were attached to the diaryl unit in order to increase both solubility and donating character. The alkylation of

the imidazole nitrogen was meant to decrease aggregation between dye molecules on the TiO₂ surface as well as reducing electron recombination with the electrolyte as has been shown for alkyl-tailed organic dyes in DSCs.²² Alkylation of the imidazole also avoids problems with possible protonation issues of the imidazole ring and increases the solubility of the molecules.



Type I



Type II

Scheme 2 Two types of 2,9-dimethyl-1,10-phenanthroline based ancillary ligands were synthesized. Type I ligands are 5,6-imidazole-substituted 2,9-dimethyl-1,10-phenanthrolines and type II are 4,7-substituted 2,9-dimethyl-1,10-phenanthrolines.

Finally, the 2,9-dimethyl-1,10-phenanthroline unit was substituted in the 4- and 7-positions (Type II ligands) to tune the electronic properties while also increasing the electronic absorption by simultaneous introduction of two donating groups.

Using the new ancillary ligands, the *homoleptic* Cu(I) complexes were synthesized from two equivalents of the ligand with one equivalent of [Cu(MeCN)₄][PF₆].

Finally, the *homoleptic* complexes were used for the *in situ* synthesis of *heteroleptic* complexes on TiO₂ surfaces by ligand exchange with bound anchoring ligands (see Chapter 9).

5.2 Anchoring Ligands

ALC was synthesized by the method of *Kröhnke* following a previously reported procedure (Figure 20).⁴² The method of *Kröhnke* is a widely used method for the synthesis of substituted pyridines as well as bi-, ter-, and oligopyridines starting from pyridinium salts and α,β -unsaturated diketones in the presence of ammonium acetate.⁸³ Its variability and simplicity as well as the cheap starting materials are thereby the most important advantages of this method.

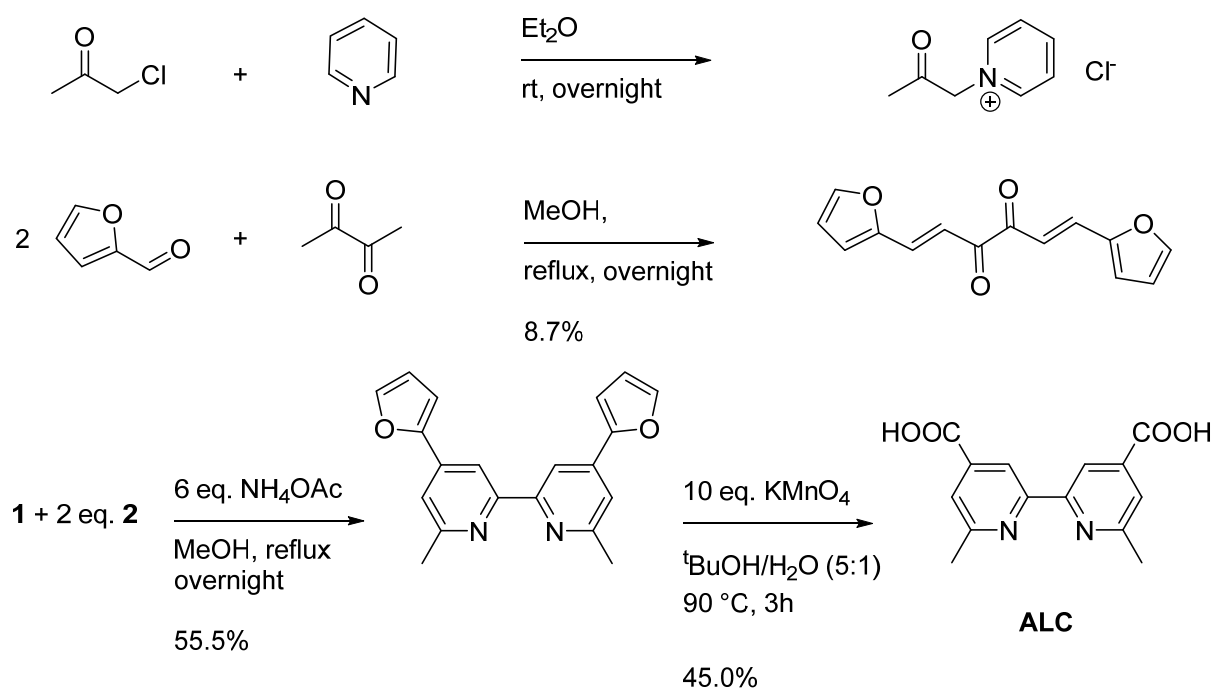


Figure 20 Synthesis of anchoring ligand **ALC**.

Figure 20 shows the synthetic pathway towards the synthesis of **ALC** starting from chloroacetone and pyridine which form 1-acetylpyridinium chloride, a so-called Kröhnke salt, in diethyl ether overnight. *Aldol condensation* of 2 equivalents of 2-furaldehyde with 2,3-butanedione leads to (1*E*,5*E*)-1,6-Di(2-furyl)hexa-1,5-diene-3,4-dione. This reacts with the pyridinium salt in two consequent *Michael* additions to a 1,5-diketone intermediate which undergoes a ring closure in the presence of NH₄OAc to form the 4,4'-di(2-furyl)-6,6'-dimethyl-2,2'-bipyridine in moderate yields. Oxidation to the carboxylic acid by an excess of KMnO₄ yields anchoring ligand **ALC**.

The phosphonic acid anchoring ligands **ALP** and **ALP1** were synthesized starting from the respective dibromo-functionalized 2,2'-bipyridines (Figure 21). By treating with diethyl phosphite in the presence of a catalytic amount of Pd(PPh₃)₄ and Cs₂CO₃ as a base in the microwave reactor for 20 minutes, the phosphonic esters were obtained in moderate to good yields. Deprotection to the phosphonic acids by bromotrimethylsilane was carried out in CH₂Cl₂. **ALP1** precipitates out of solution in MeOH as a white solid. A solution of **ALP** in MeOH was treated with a mild aqueous HCl solution to obtain a white precipitate upon cooling with an ice bath.

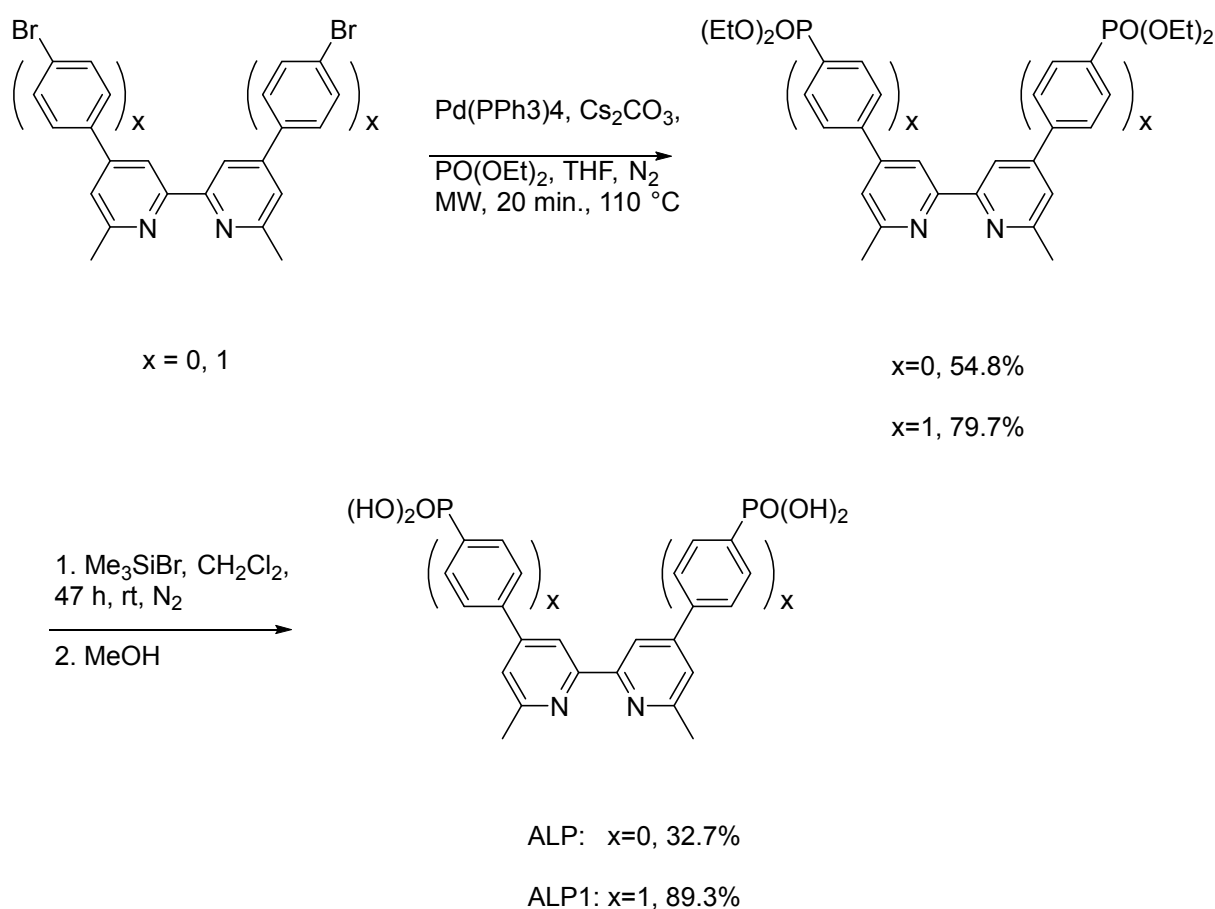


Figure 21 Synthesis of the phosphonic acid anchoring ligands **ALP** and **ALP1**

Due to its poor solubility in solvents other than DMSO, the N^nBu_4 salt of **ALP1** was synthesized as shown in Figure 22. For this, **ALP1** was suspended in EtOH and a solution of TBAOH in water was added until everything had dissolved.

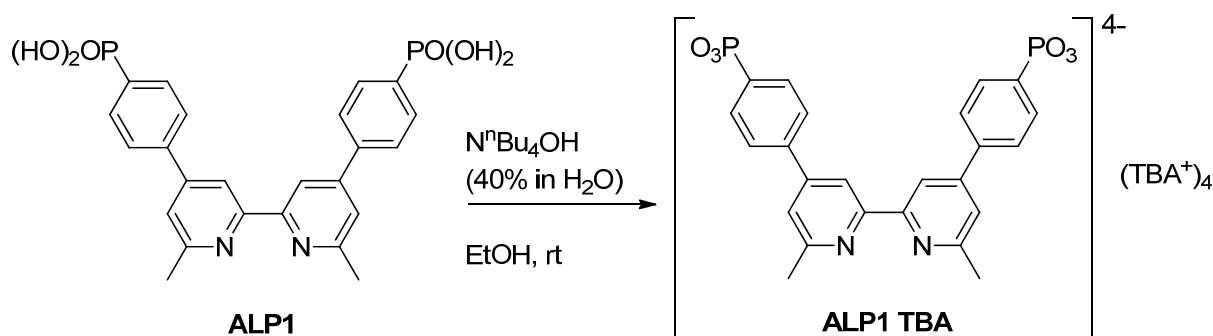


Figure 22 Synthesis of the tetrakis-*n*-butyl ammonium salt of ALP1.

5.3 Ligand Synthesis

2,9-Dimethyl-1,10-phenanthroline-5,6-dione (**1**) was synthesized by oxidation of 2,9-dimethyl-1,10-phenanthroline using KBr, H₂SO₄ and HNO₃ and refluxing for 3h adapting a literature procedure for the non-methylate phenanthroline analogue.⁸⁴ Bromide is first oxidized to bromine to enable the oxidation of the phenanthroline unit to occur. Neutralization with NaOH resulted in the product with impurities and after crystallization from EtOH and CHCl₃ the product was only obtained in low yields. Therefore, the milder method of *Sun et al.*⁸⁵ was applied which uses KBrO₃ as an oxidizing agent in a 60% aqueous solution of H₂SO₄ at room temperature to obtain the product in good yields. A beneficial aspect of this method is its facility for scale up (up to 10 g of starting material was synthesized).

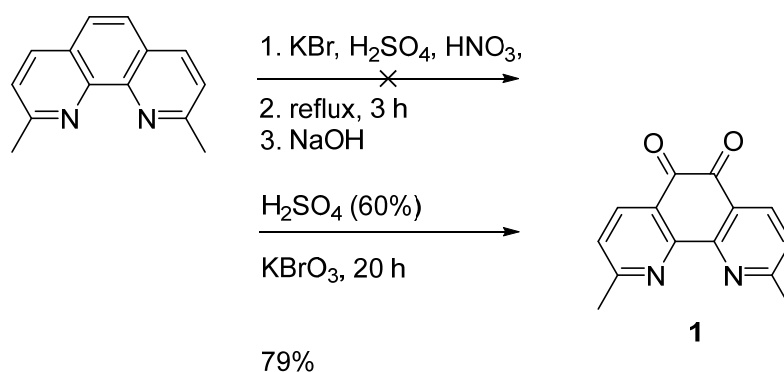


Figure 23 Synthesis of 2,9-dimethyl-1,10-phenanthroline-5,6-dione.

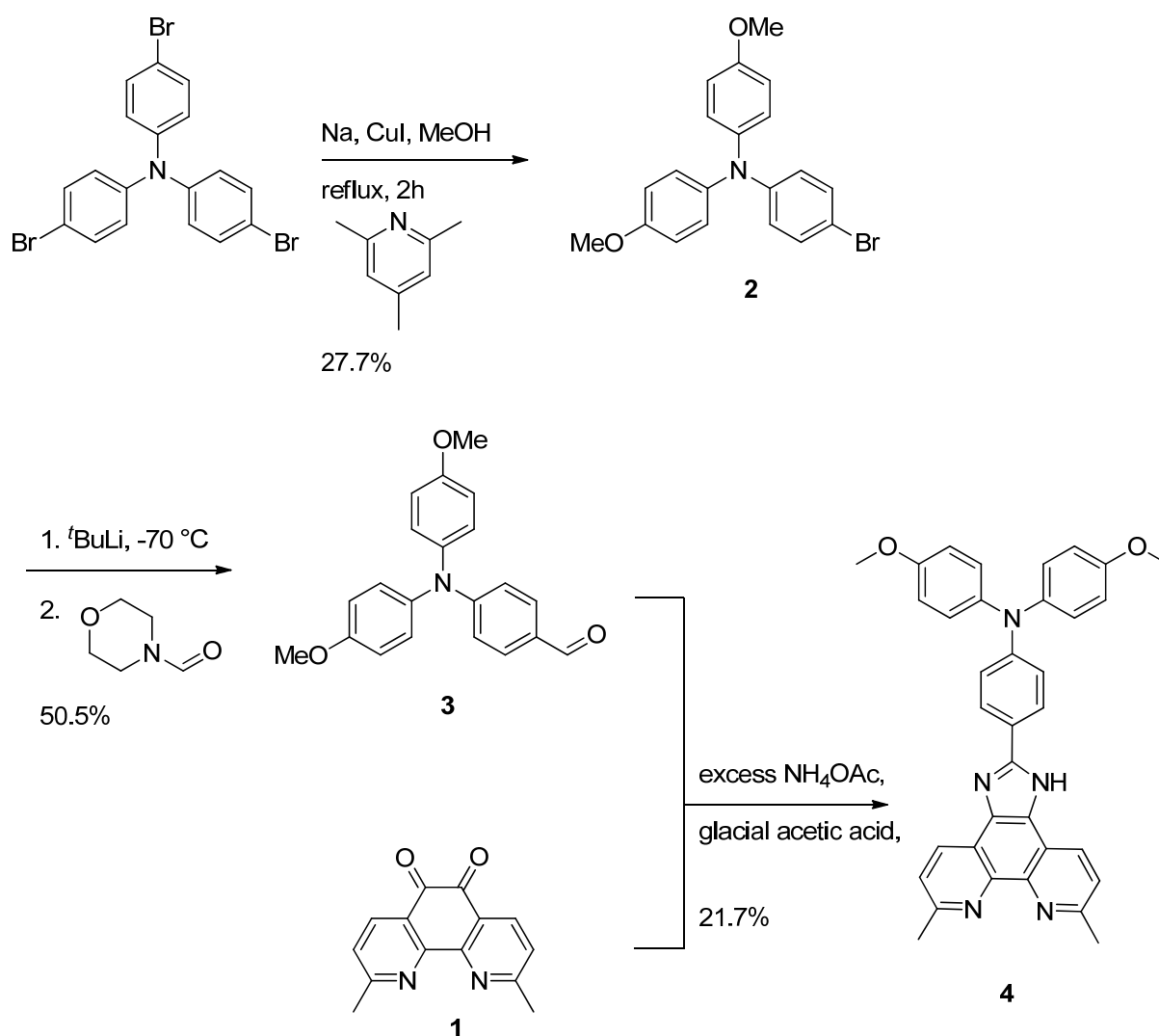


Figure 24 Method I for the synthesis of the imidazole derivatives.

From **1**, **4** can be obtained by reacting with 4-(bis(4-methoxyphenyl)amino)benzaldehyde (**3**) in the presence of NH₄OAc in glacial acetic acid. **3** was synthesized from tris(4-bromophenyl)amine with CuI and Na in methanol followed by introduction of the aldehyde by treating with 4-formylmorpholine and ^tBuLi. The statistical nature of the first reaction leads to poor selectivity as the mono- and trismethoxylated side products are obtained as well. Combined with the low yield of the imidazole formation to **4**, the overall yield is very low. This motivated us to change the synthetic route to a second method starting from 4-bromobenzaldehyde and consequent coupling of the donor group by a *Hartwig-Buchwald* coupling. The variability of this synthetic route is very advantageous allowing for couplings with different amines and thereby introduction of a wide variety of donor groups from substituted amines to carbazoles or thiazines.

Starting from **1**, 4-bromobenzaldehyde was introduced in the presence of NH₄OAc in glacial acetic acid. Unfortunately the product could not be isolated as a clean product. Neither column chromatography on silica or alumina, nor recrystallization led to a clean product. It was expected that the tendency for protonation of the imidazole was the problem. Careful neutralization with continuous cooling with an ice-bath or workup under slightly acidic or basic conditions did not lead to an improved result. To avoid potential problems with water, NH₄OAc was stored in a desiccator for several days and glacial acetic acid was freshly recrystallized but with no impact on the result of the experiment. Also using the slightly impure product without further purification for the next step led to the same purification problems in the following reaction.

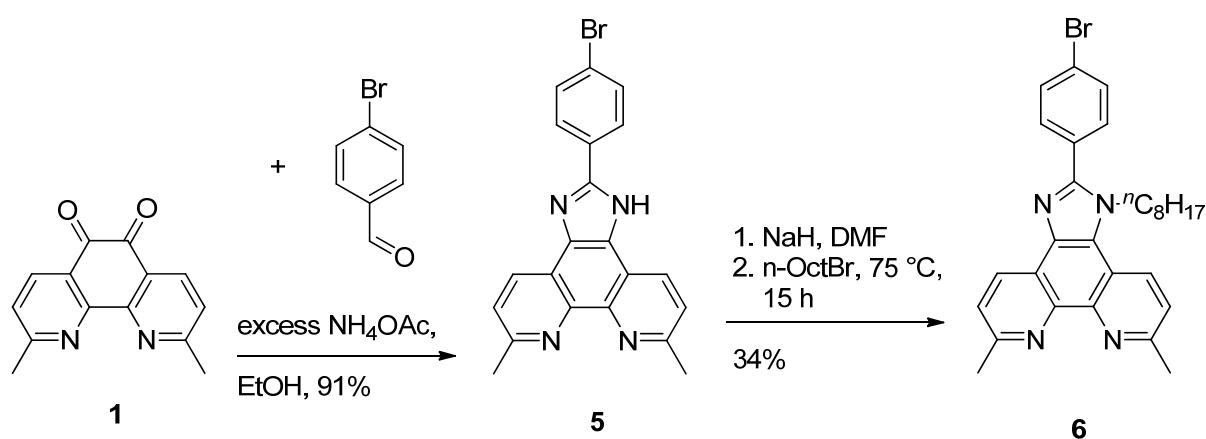


Figure 25 Optimized reaction conditions leading to the synthesis of **6**.

Finally, changing the solvent from glacial acetic acid to ethanol and working under inert atmosphere lead to the product in good yields (91%). The *n*-octyl chain was introduced at the imidazole nitrogen after deprotonation in DMF with NaH under an atmosphere of N₂. The product could be isolated by column chromatography on alumina followed by recrystallization from a toluene:ethyl acetate mixture (1:3). Attempts to improve the initial low yields by the addition of 15-crown-6 to the reaction mixture were unsuccessful. Increase in the reaction temperature from 80 °C to 150 °C led to an approximate doubling in the yield, still reaching only 8 %. By reduction of the reaction time to 4 h, the yield could be increased dramatically up to 34%, which provided enough material to go on with the next steps (

Table 1).

Temperature	Time	Yield
80 °C	72 h	4 %
150 °C	72 h	8 %
85 °C	4 h	34 %

Table 1 Optimization of the reaction conditions for the alkylation of **5** to compound **6**.

In the next step the donating groups were attached on the backbone of the 2,9-dimethyl-phenanthroline ligands by palladium catalyzed *Hartwig-Buchwald* couplings. Diphenylamine, bis(4-methoxyphenyl)amine and 9H-carbazole were available commercially. Diarylamine **11** and **12** were synthesized starting from 4-bromophenol and treating with the respective bromoalkane under basic conditions in acetone to yield 4-bromo-alkoxybenzene derivatives **7** and **8**. Starting from 4-acetamidophenol the respective alkylated amidophenols **9** and **10** were synthesized in a similar fashion. Diarylamines **11** and **12** were obtained from a copper catalyzed reaction of **7** and **9** or **8** and **10**, respectively, in DMSO under basic conditions following an adapted literature procedure.⁸⁶

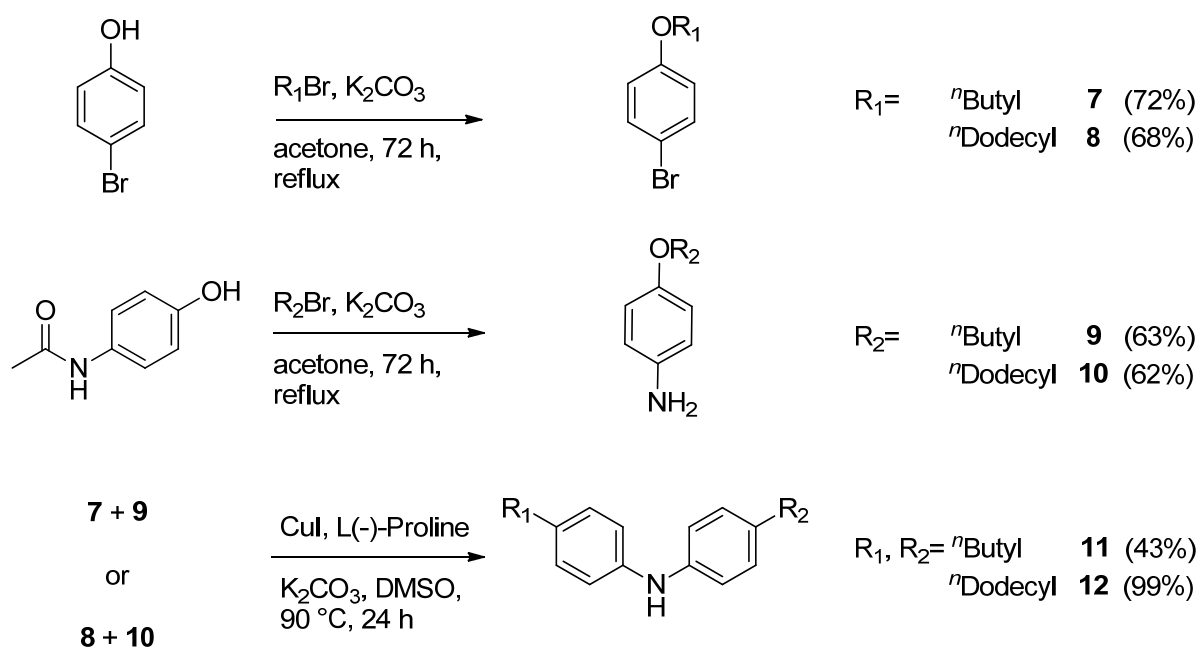


Figure 26 Synthesis of the diarylamines **11** and **12**.

Synthesis of ligands **13-17** turned out to be more challenging than expected with the workup of these types of reactions being difficult. The main problem turned out to be the separation of the starting material and the product. While the amines were removed easily from the reaction mixture, purification using column chromatography showed the respective product either did not move at all or with the same R_f values as **6**, independent on the polarity of the used solvent mixtures. Addition of weak bases such as triethylamine did not help either. Therefore the only solution was to consume **6** completely by using an excess of the particular amine and adjusting the reaction conditions. This strategy worked well for **13** and **15** with 1.1 and 1.5 eq. of the amine, respectively, catalyzed by $\text{Pd}(\text{dba})_2$ with NaOtBu as a base in 52% and 51% yield, respectively. Compounds **14**, **16** and **17** turned out to be more challenging.

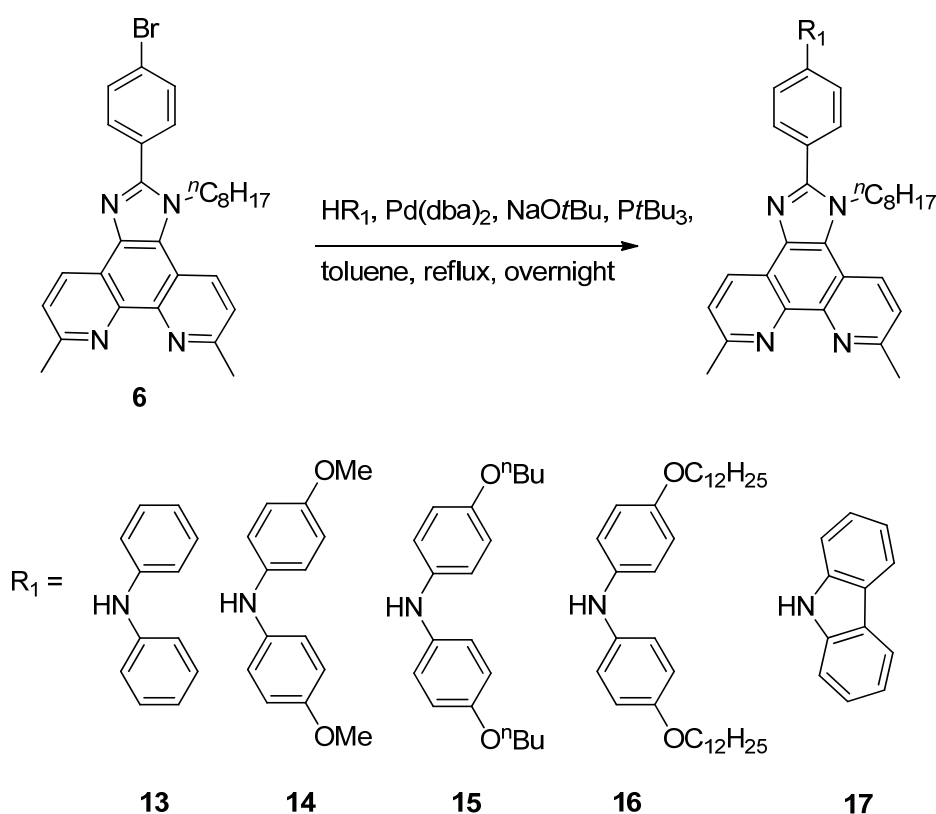


Figure 27 Hartwig-Buchwald couplings to the final ligands.

With **6** not being separable from the products, the reaction progress could not be followed by TLC. However, using $^1\text{H-NMR}$ spectroscopy, compound **6** can easily be distinguished from the products as demonstrated in the example of **14** in Figure 28. The primary CH_2 signal of the n -alkyl chain is shifted downfield from δ 4.54 to 4.59 ppm in the product making distinction between a 1:1 reaction mixture and the product possible. The shift of this peak seems to be

independent of possible protonation states and further has the advantage of being clearly separated from other product signals or solvent peaks. The shift is seen in all compounds **13-17** and is for some of the ligands even more pronounced in MeCN.

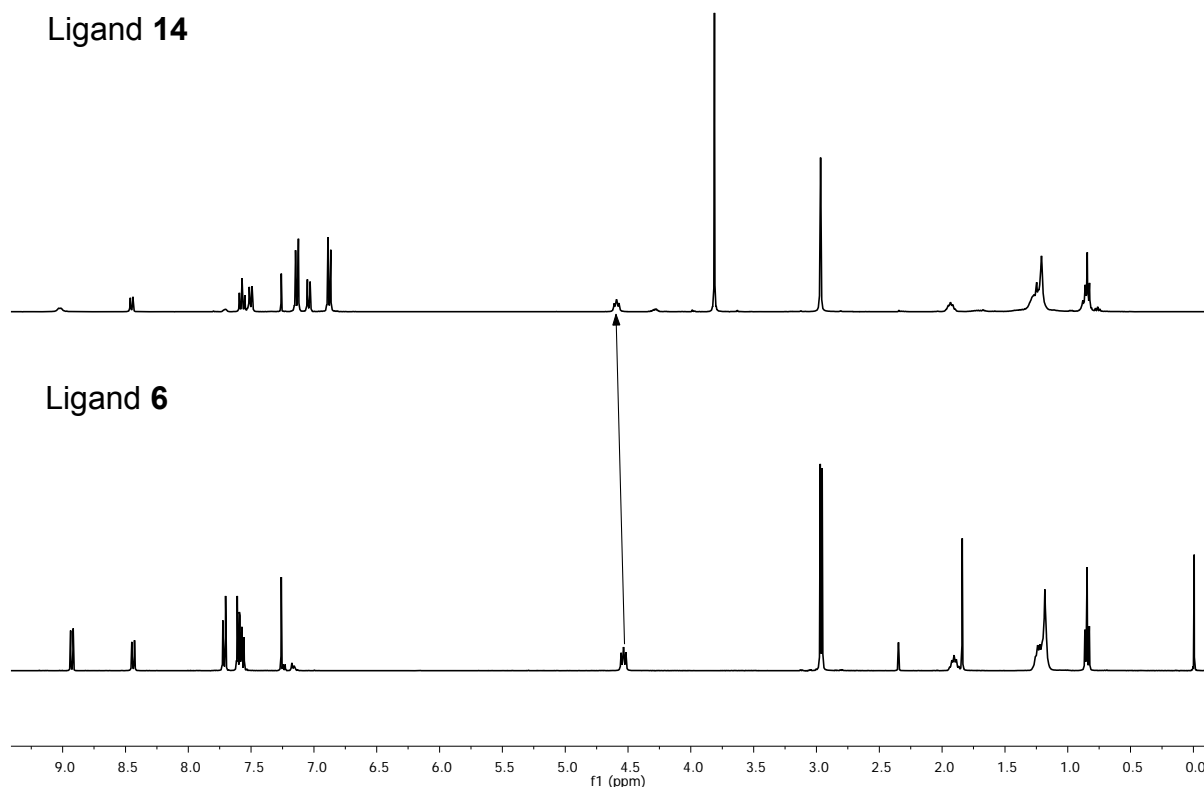


Figure 28 Downfield shift of the N-CH₂ from compound **6** to **14** after coupling with bis(methoxyphenyl)amine.

Table 2 shows the tested reaction conditions for the synthesis of ligand **14**. Due to the low yield with classical *Hartwig-Buchwald* conditions, the reaction time was increased which improved the yield dramatically. By changing the catalyst from Pd(dba)₂ to Pd(PPh₃)₄, an even higher yield was achieved. However, if Pd(OAc)₂ is used as the catalyst only a poor conversion is obtained. Heating the reaction mixture with a microwave reactor gave no noticeable conversion in 20 min. of reaction time using the Pd(dba)₂ catalyst. In contrast, a yield of 67% could be reached with Pd(PPh₃)₄, which is nearly as good as with reflux conditions but within a much shorter reaction time. An alternative route in which the *Hartwig-Buchwald* coupling occurs prior to the alkylation of NH was discarded after poor yields in the first step.

As discussed above, the workup turned out to be the crucial challenge for all of these reactions. Compound **14** could not be isolated in useful amounts and purity for use in solar cells. Even if **6** was consumed completely by using Pd(PPh₃)₄ as a catalyst, the product was contaminated

with PPh₃ and OPPh₃. However the successful synthesis of the product could be confirmed by ESI-MS, ¹H-NMR spectroscopy and a crystal structure.

Reaction Time	6 (eq.)	Reagents and Conditions	Catalyst	Yield
24 h	1.1	2.5 eq. NaOtBu 100 °C, toluene	Pd(dba) ₂ + P ^t Bu ₃ (5 mol%)	4 %
72 h	1.1	2.5 eq. NaOtBu 100 °C, toluene	Pd(dba) ₂ + P ^t Bu ₃ (5 mol%)	38 %
24 h	1.1	2.5 eq. NaOtBu 100 °C, toluene	Pd(PPh ₃) ₄	79% + PPh ₃
24 h	1.1	2.5 eq. Cs ₂ CO ₃ 100 °C, toluene	Pd(OAc) ₂ + P ^t Bu ₃	Mixture
20 min.*	5.0	2.5 eq. NaOtBu 100 °C, toluene	Pd(PPh ₃) ₄	67% + PPh ₃
20 min.*	5.0	2.5 eq. NaOtBu 100 °C, toluene	Pd(dba) ₂ + P ^t Bu ₃ (5 mol%)	-

Table 2 Tested reaction conditions for the synthesis of 14. *reaction done in a microwave reactor

Synthesis of compound **16** was tried with similar conditions as for **14**. However, neither the classical conditions using Pd(dba)₂ nor in a microwave reactor with Pd(PPh₃)₄ led to any product. Adding more of the catalyst to the reaction mixture after 24 h of reaction time did not improve the result nor did an increase in reaction time to 5 days. It is possible that the C₁₂-chain is too sterically hindered to allow the Pd-catalyst to work.

Insertion of a 9H-carbazole as the donor group to yield **17** also turned out to be rather difficult. Reaction with Pd(PPh₃)₄ in toluene in the microwave reactor for 20 min. did not yield any product at 110 °C or 130 °C. Elongating the reaction time to 100 min. did not lead to any improvement either. Therefore it was decided to synthesize the 4-(9H-carbazol-9-yl)benzaldehyde **18** and react it directly with the neocuproine-dione **1** followed by alkylation (Figure 29). Compound **18** was synthesized following a literature procedure⁸⁷ in an *Ullmann* type reaction in good yields to obtain the product as a pale-yellow solid. Ring closure to the imidazole followed by alkylation with ⁿOctBr worked in moderate yields.

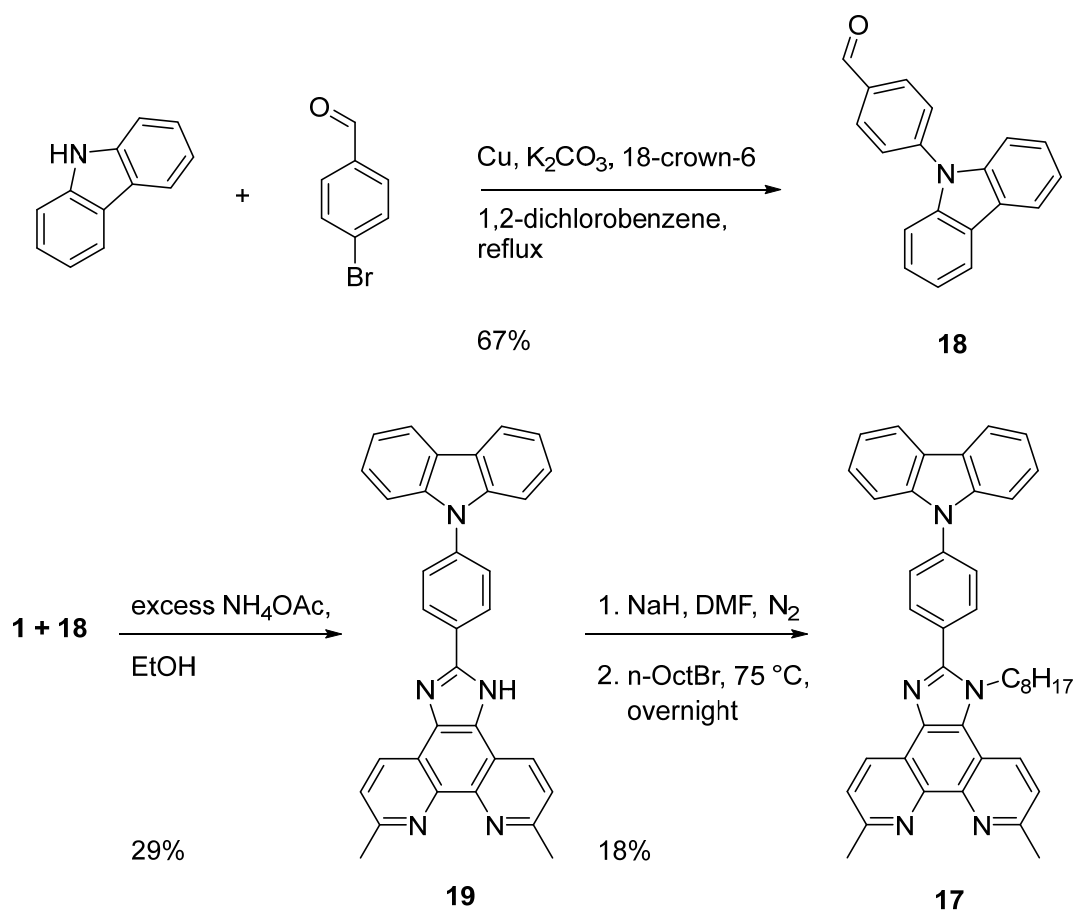


Figure 29 Alternative route for the synthesis of **17**.

In order to investigate the necessity of having methyl groups in the 2 and 9 positions of the 1,10-phenanthroline for the stability of the copper(I) complex and its performance in DSCs, attempts were made to synthesize the phenanthroline analogues of **15** and **17**. It was expected that these syntheses should produce less problems as similar compounds are published in the literature.⁸⁸ For this, 1,10-phenanthroline was oxidized to 1,10-phenanthroline-5,6-dione **20** using the same procedure as described above.⁸⁵ The synthesis of the respective imidazole was done in glacial acetic acid following a literature procedure⁸⁸ which worked in good yields in contrast to the neocuproine equivalent discussed above. Alkylation was done as above and the reaction proceeded with comparable yields. Coupling of **22** with diarylamine **11** to **23** was repeated several times but the same purification problems as with the methylated analogue occurred. Compound **22** could not be separated from **23** by column chromatography on silica, alumina or basic alumina. Therefore gel permeable chromatography (GPC) was tried which showed promising results in a qualitative experiment but did not work in a quantitative one. With every cycle, the bands became broader, leading again to the assumption that sensitivity to protonation seems to be the problem with these types of ligands. Coupling the amine directly

to **21** did not yield any product at all. Changing the reaction time from 24h to 48h or even 6d did not improve the yield. Finally, the best results were obtained by using a 5-fold excess of the amine. By running the $^1\text{H-NMR}$ spectrum in acetone instead of CDCl_3 , a better resolved spectrum was obtained, most likely due to the protic nature of chloroform.

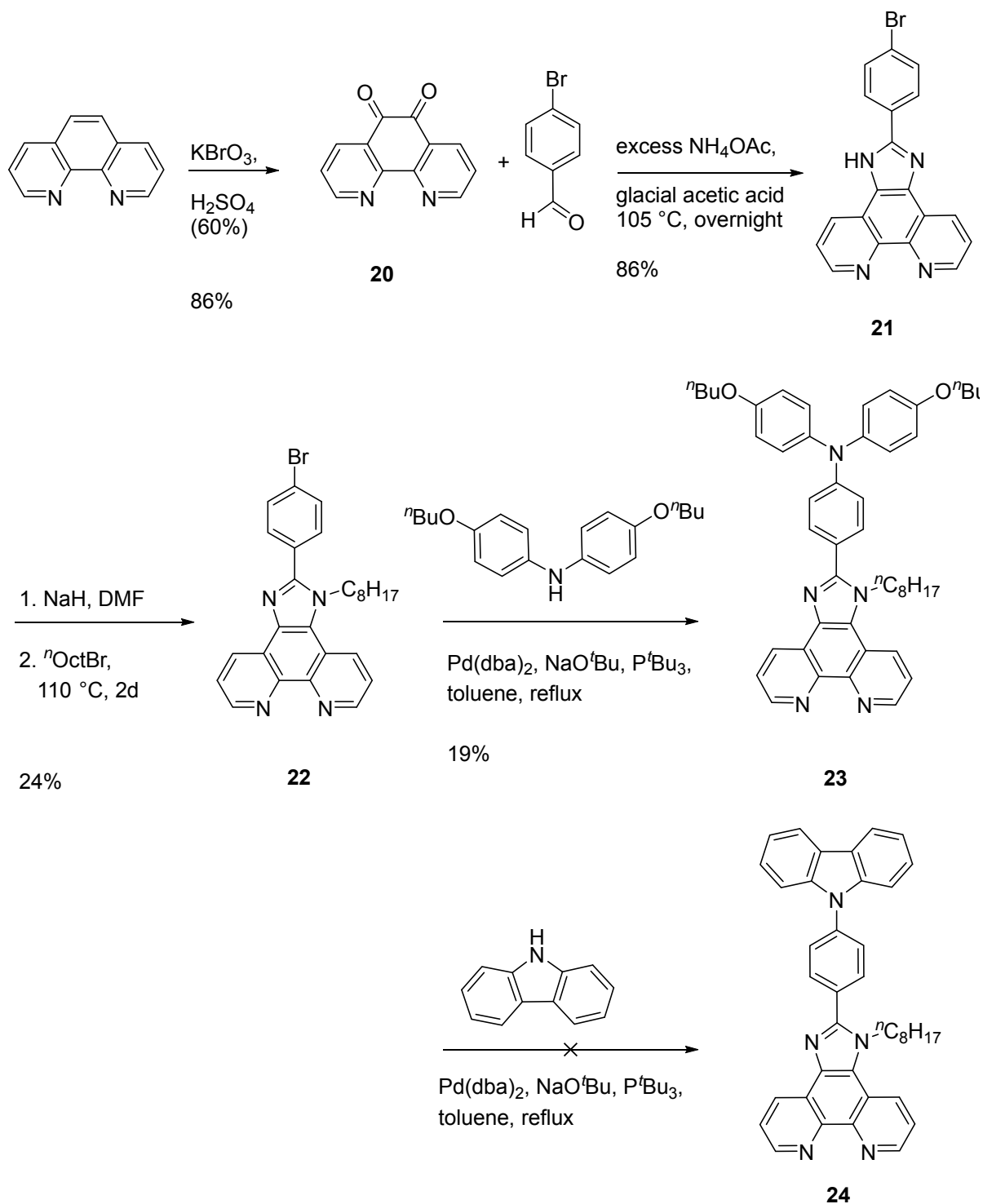


Figure 30 Synthetic pathway for the 1,10-phenanthroline equivalents **21**, **23** and **24**.

The synthesis of **24** was not successful under these conditions either and could not be synthesized. However, since **23** showed only poor performances in solar cell experiments, this synthesis was not investigated further.

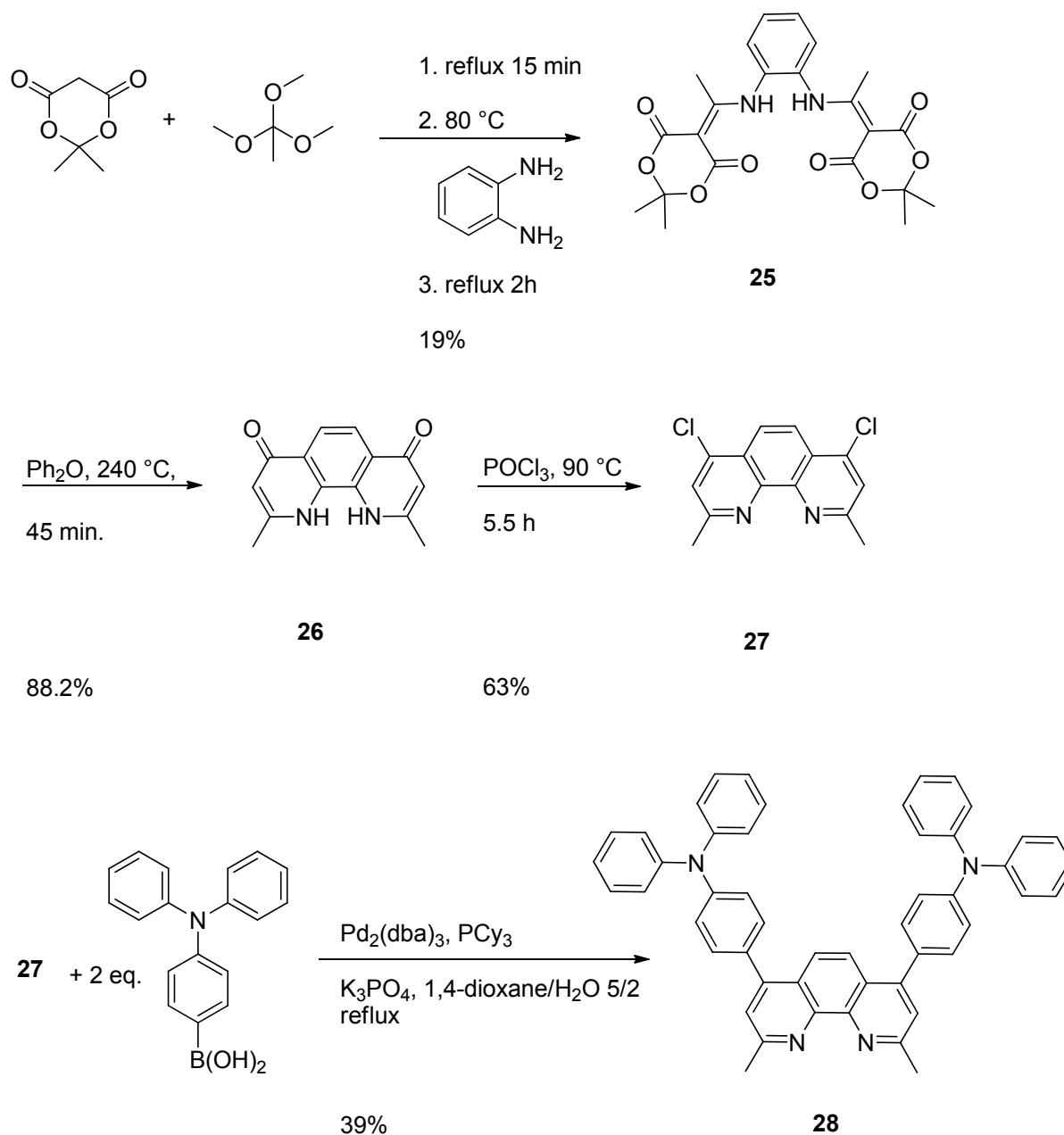


Figure 31 Synthetic pathway towards compound **28**.

By going from 5,6-substituted 2,9-dimethyl-1,10-phenanthrolines to 4,7-substituted ones, the syntheses and purifications appeared to be more trivial. For the synthesis of **28**, 2,2-dimethyl-1,3-dioxane-4,6-dione was refluxed with ortho-phenylenediamine in trimethyl orthoacetate to yield **25** as a white solid. After decarboxylation in diphenyl ether, 2,9-dimethyl-1,10-

phenanthroline-4,7-dione (**26**) was obtained as a white solid in good yields. Chlorination occurred upon treatment with POCl₃ at 90 °C for 5.5 h. The chloro groups in the 4,7-positions of 1,10-phenanthroline allow for *Suzuki* couplings with respective donors. Consequently **28** was obtained by coupling **27** with 4-(diphenylamino)phenylboronic acid in moderate yields.

5.4 Complex Synthesis

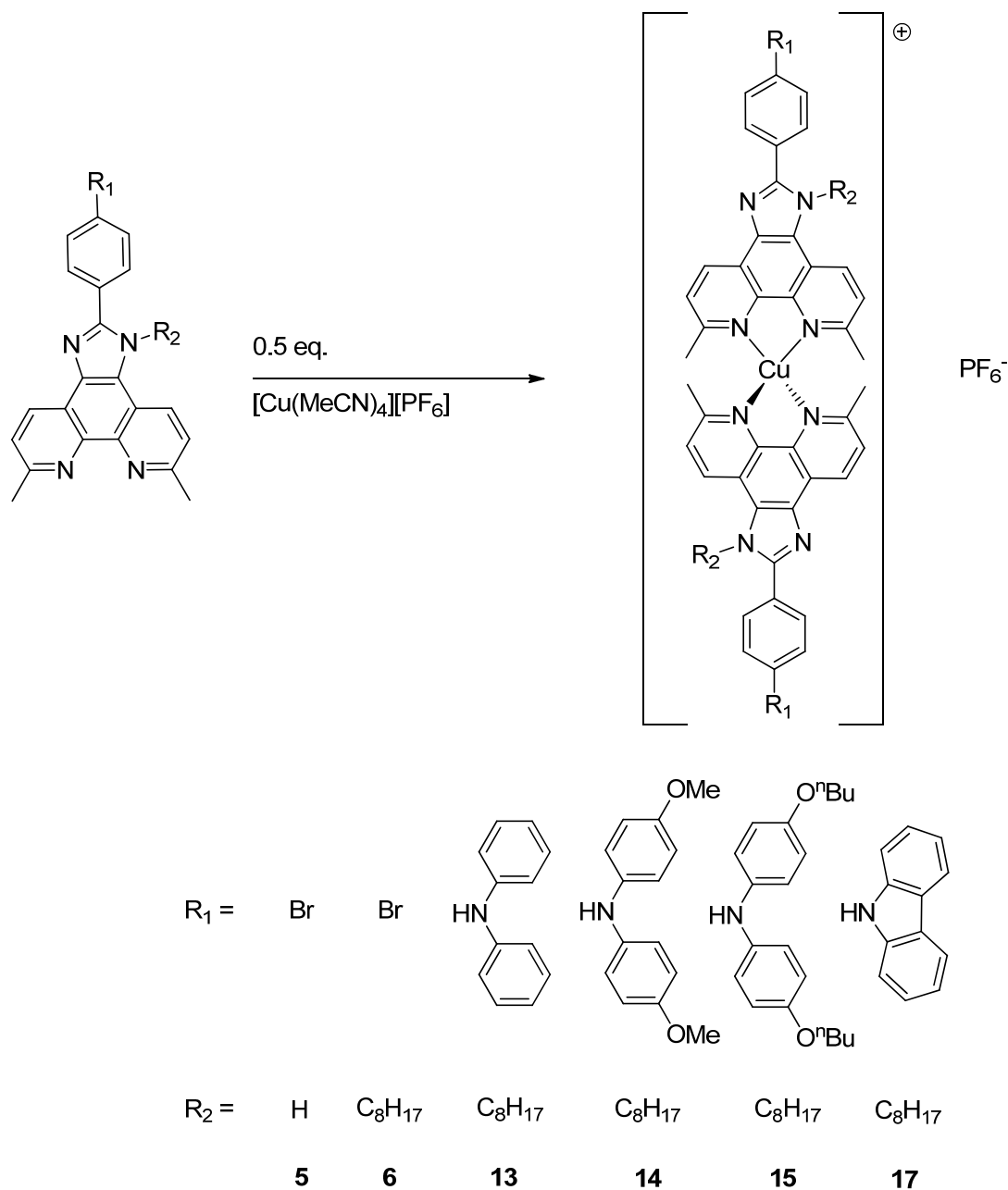


Figure 32 Synthesis of the Cu(I)-complexes with 5,6-substituted phenanthroline ligands.

The copper(I) complexes were synthesized by dropwise addition of an acetonitrile solution of [Cu(MeCN)₄][PF₆] to a solution of the particular ligand in chloroform or dichloromethane.

Because these complexes could not be precipitated by addition of diethyl ether, they were purified by column chromatography on alumina or silica to yield the products as red solids. Synthesis of a homoleptic Cu(I) complex of **23** was not possible due to the missing steric protection of the copper(I) centre. Substituents adjacent to the N,N'-donor set prevent tetrahedral copper(I) converting to square-planar copper(II); in the absence of such substituents, the copper(I) complex is easily oxidized to the corresponding copper(II) species.

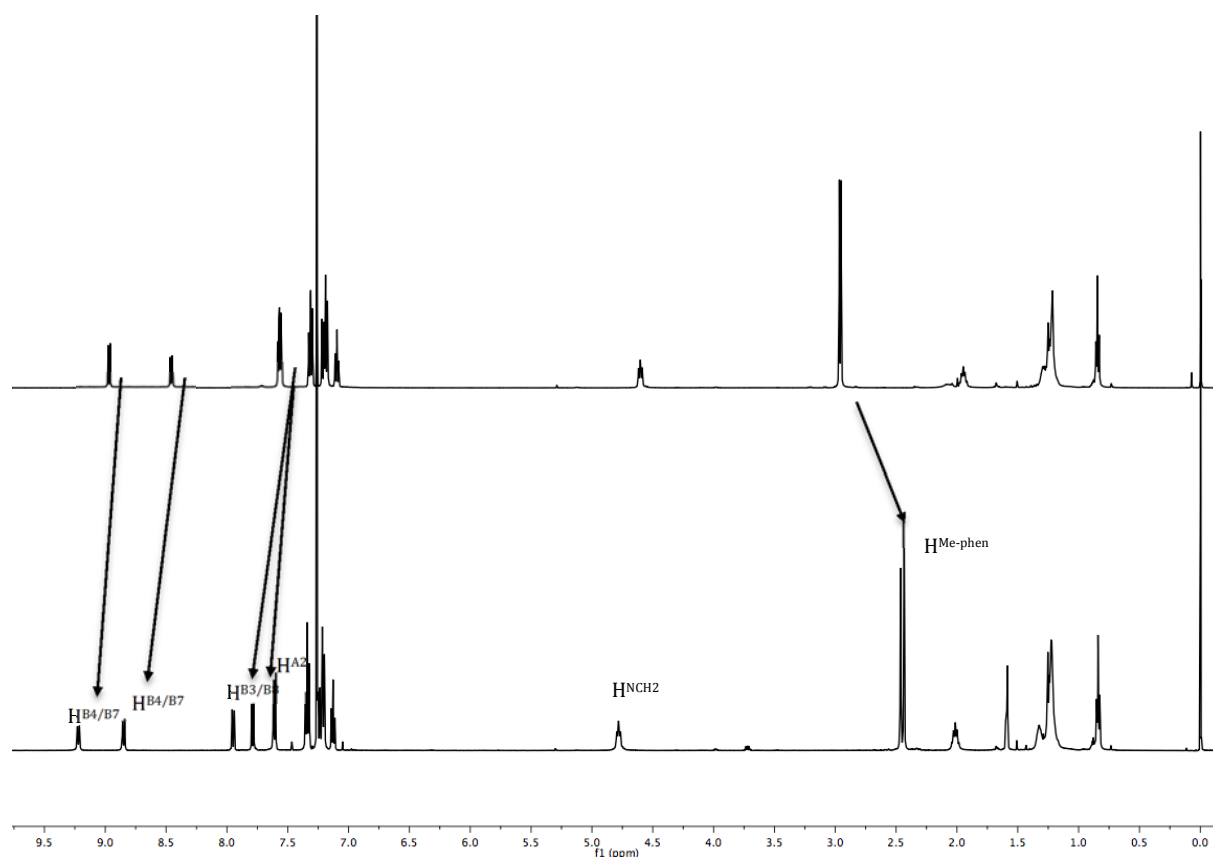


Figure 33 Comparison of the $^1\text{H-NMR}$ spectra of the free ligand **13** (above) and $[\text{Cu}(\mathbf{13})_2][\text{PF}_6]$ in CDCl_3 .

Figure 33 shows as a representative example a comparison of the $^1\text{H-NMR}$ spectra of the free ligand **13** and its copper complex $[\text{Cu}(\mathbf{13})_2][\text{PF}_6]$ in CDCl_3 . Upon complexation, the protons that are close to the coordinating nitrogens of the phenanthroline are shifted with respect to the free ligand. The 4 protons $\text{H}^{\text{B}3/\text{B}8}$ which overlap with the $\text{H}^{\text{A}2}$ signal in the free ligand are shifted downfield and become clearly distinguishable. The same is observed for protons $\text{H}^{\text{B}4/\text{B}7}$. The methyl groups in the 2 and 9 positions of the phenanthroline unit are high-field shifted. The NCH_2 -proton of the imidazole chain is slightly shifted towards low-field with all the other protons not really affected upon coordination.

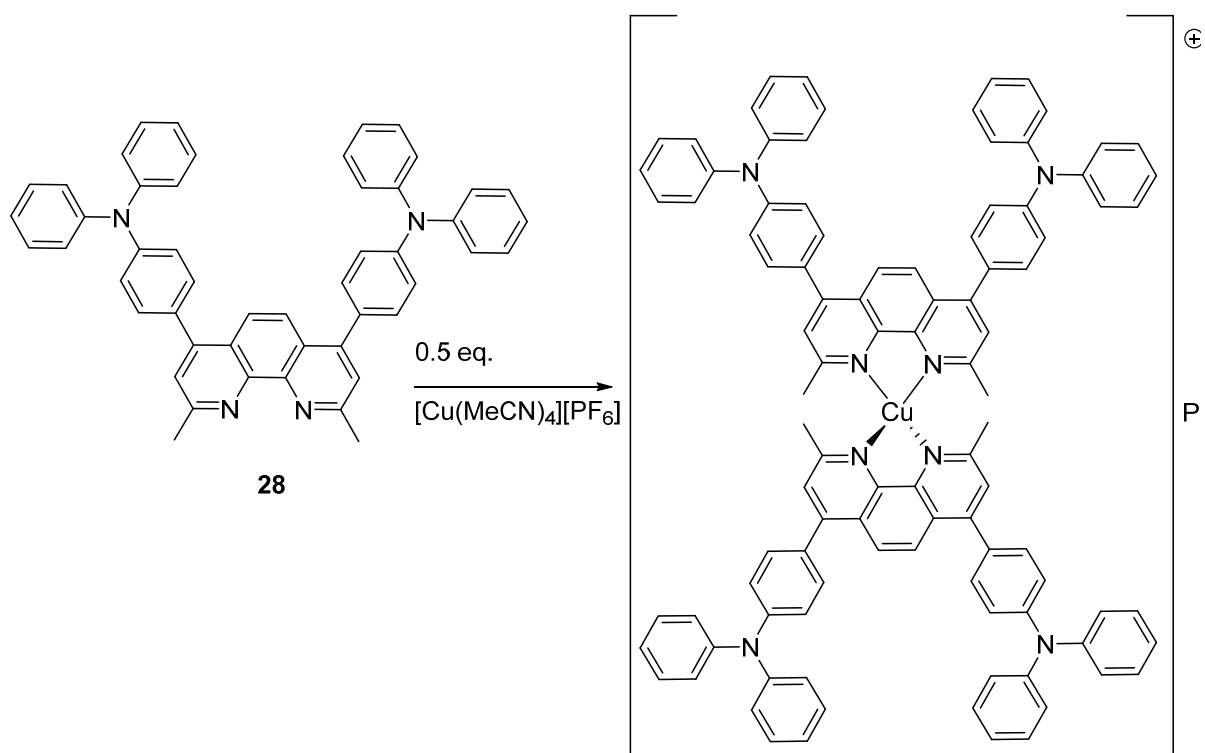


Figure 34 Synthesis of the Cu(I)-complex with the 4,7-substituted phenanthroline Ligand **28**.

[Cu(**28**)₂][PF₆] was synthesized as the other complexes described before by mixing two equivalents of the ligand with one equivalent of [Cu(MeCN)₄][PF₆] to get an immediate colour change to dark red. This complex was purified by removing the solvent and washing with water and filtering the complex. The complex was obtained as a red solid.

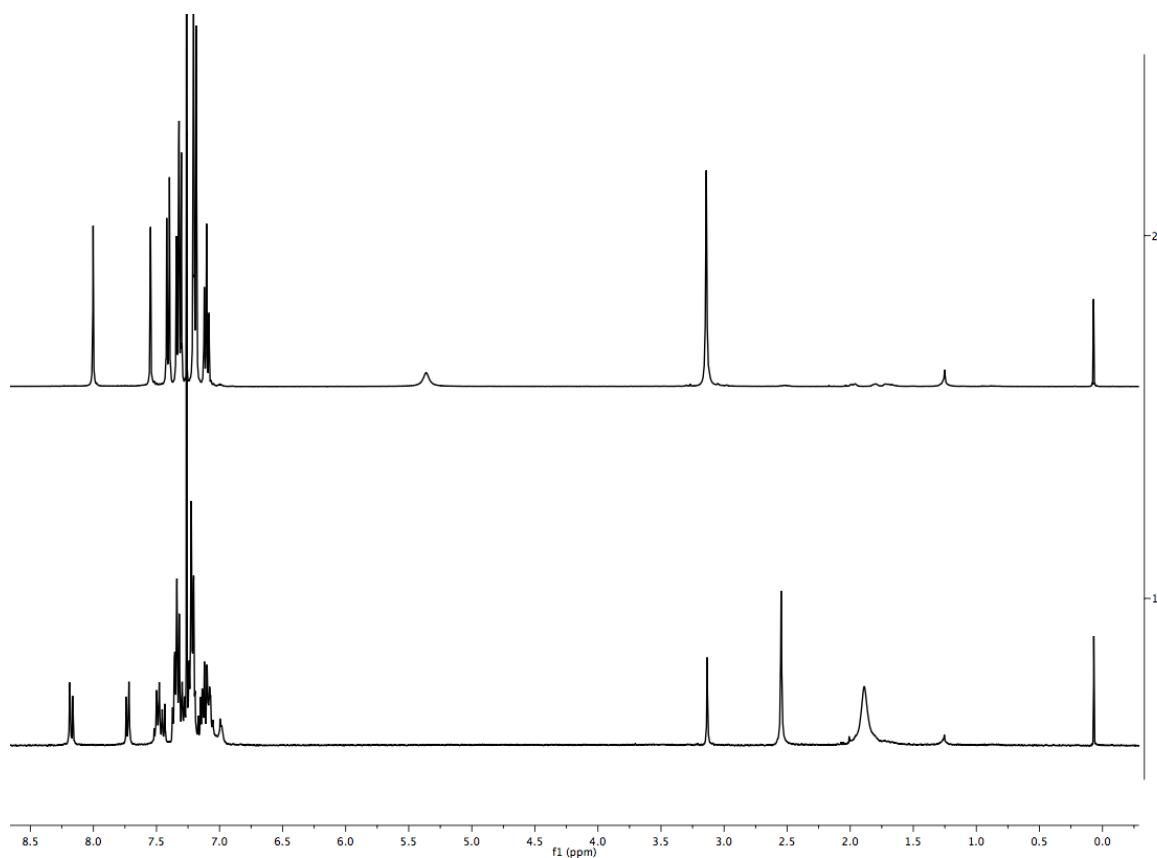


Figure 35 Comparison of the $^1\text{H-NMR}$ spectra of the free ligand **28 (above) and $[\text{Cu}(\mathbf{28})_2][\text{PF}_6]$ in CDCl_3 .**

Figure 35 compares $^1\text{H-NMR}$ spectra of ligand **28** (top spectra) with its copper complex $[\text{Cu}(\mathbf{28})_2][\text{PF}_6]$ in CDCl_3 . Again the methyl peak is shifted towards higher field upon coordination to the copper centre. In the aromatic region the splitting of the peaks gets more complex compared to the free ligand with protons $\text{H}^{\text{B4/B7}}$ shifted further low-field. The complexity of the splitting in the aromatic region strongly depends on the solvent in which it is measured and seems to correlate with the protic nature of the used solvents (Figure 36).

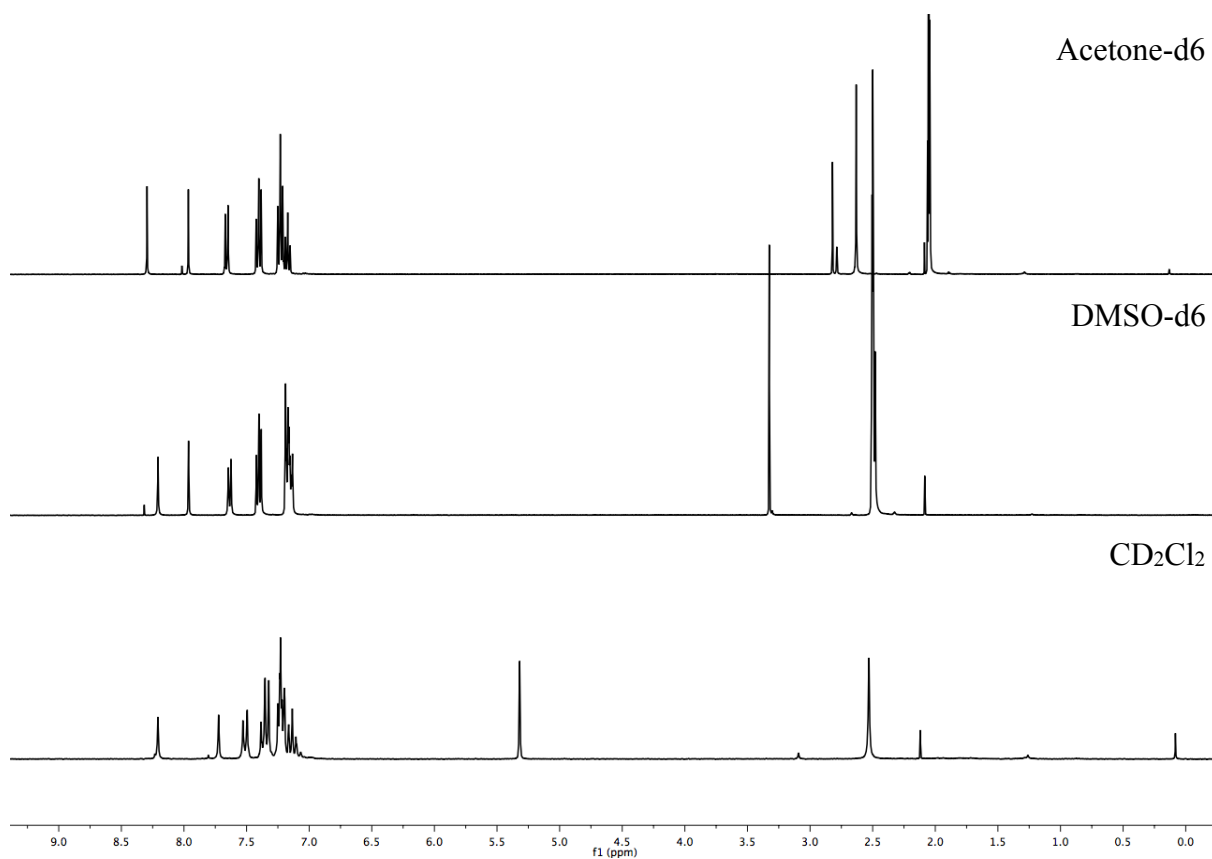


Figure 36 ¹H-NMR spectra of [Cu(28)₂][PF₆] in acetone (top), DMSO (middle) and CH₂Cl₂.

All ligands and complexes used for DSCs have been fully characterized (cf Chapter 12). It is worth mentioning that all 2,9-dimethyl-1,10-phenanthroline copper complexes could not be detected by ESI-MS if dissolved in MeCN but mass spectra were obtained using MeOH solutions of the complexes.

6 Characterisation

6.1 UV-Vis Spectroscopy

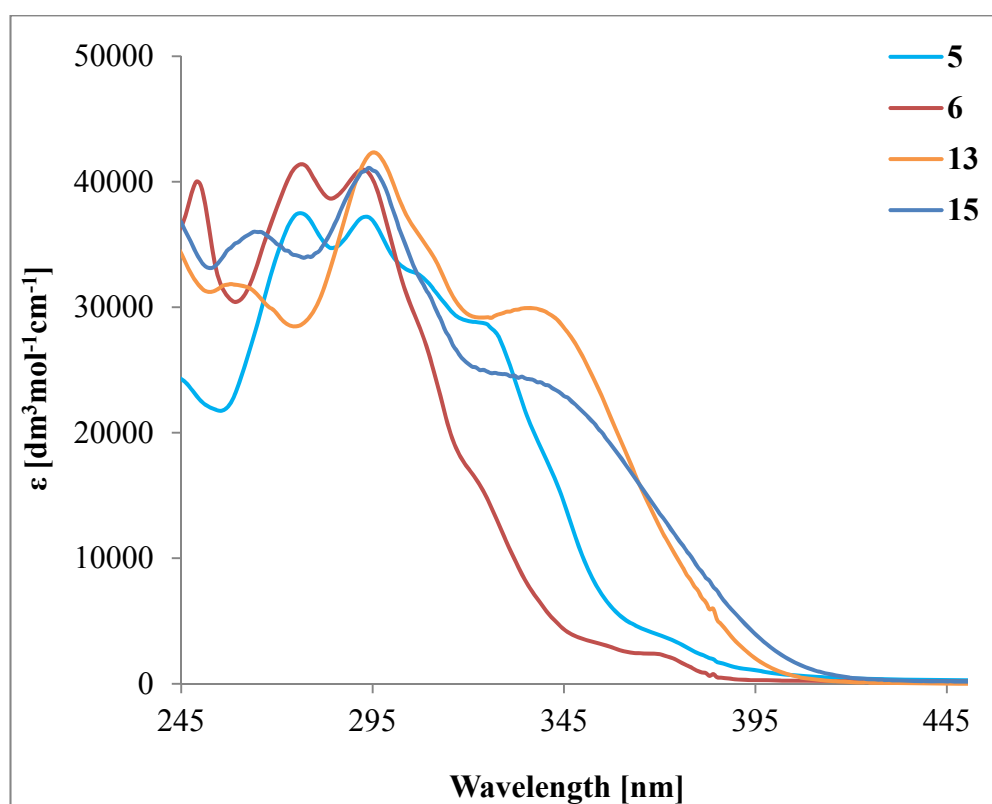


Figure 37 UV-Vis absorption spectra of compounds **5** in MeOH and **6**, **13** and **15** in CH₂Cl₂ ($c=1 \times 10^{-5}$ M).

Figure 37 shows the absorption spectra of compounds **5**, **6**, **13**, and **15** with absorption maxima around $40000 \text{ dm}^3 \text{ mol}^{-1} \text{ cm}^{-1}$. All compounds absorb in the UV region of the spectral range and can be assigned to spin allowed $\pi^* \leftarrow \pi$ and $\pi^* \leftarrow n$ transitions. The bromo compounds **5** and **6** show two maxima with λ_{max} at 276 and ≈ 293 nm, with **6** having a third λ_{max} at a shorter wavelength. By insertion of a diaryl amine donor group onto the imidazole and extension of the aromatic system, a broader absorption to longer wavelengths is obtained (ligand **13**). Introduction of *n*-butoxy chains on the diaryl amine moiety lowers the intensity of the shoulder around 350 nm but the absorption tails further out into the red region.

The absorption spectrum of **23** is slightly blue-shifted with respect to its 2,9-methylated analogue **15** (Figure 38). Compound **17** shows an intense λ_{max} at 297 nm, characteristic of the carbazole unit. Triphenylamine substitution at the 4 and 7 positions of 1,10-phenanthroline in compound **28** leads to an intense λ_{max} at 297 nm and two shoulders at ≈ 360 nm and ≈ 500 nm tailoring out into the visible part of the spectrum. Table 3 lists the absorption maxima and corresponding extinction coefficients of the compounds.

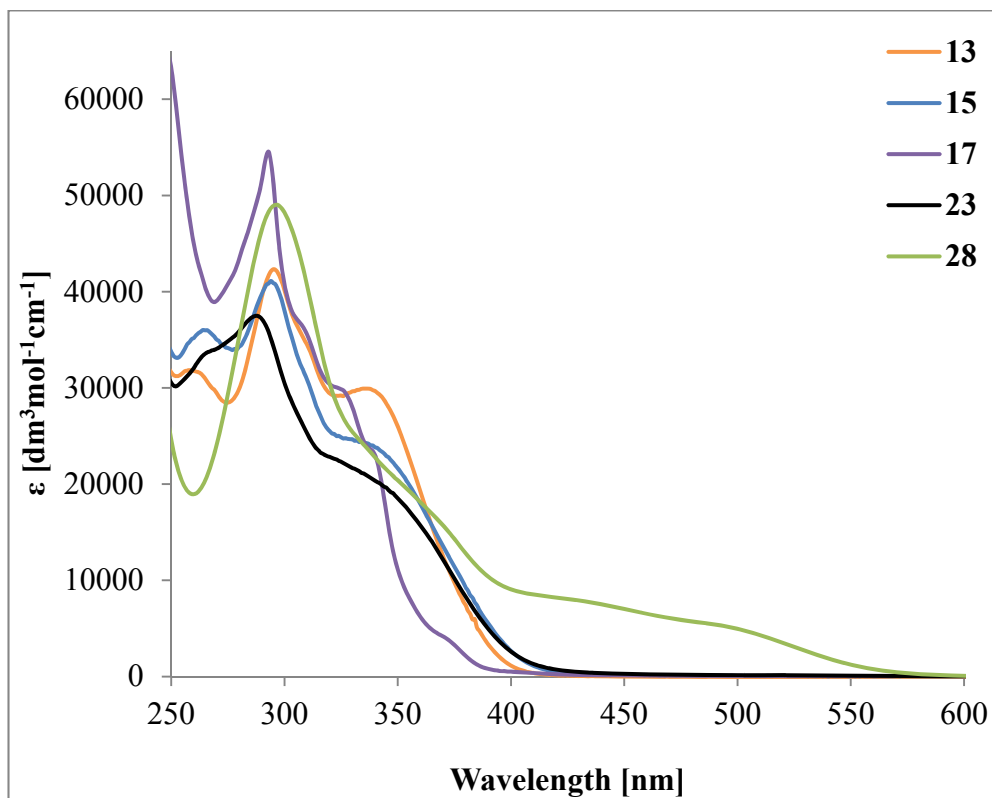


Figure 38 UV-Vis absorption spectra of ligands 13, 15, 17, 23 and 28 in CH₂Cl₂ (c=1x10⁻⁵ M).

Absorption Maxima of the Ligands		
Ligand	$\lambda_{\text{max}}[\text{nm}]\epsilon[\text{dm}^3 \text{mol}^{-1} \text{cm}^{-1} 10^3]$	Solvent
5	276 (37206), 293 (37206), 306 (32759 (sh)), 324 (28719 (sh))	MeOH
6	249 (40012), 276 (41374), 292 (40956), 370 (2377 (sh))	CH ₂ Cl ₂
13	258 (31845), 295 (42326), 335 (29925)	CH ₂ Cl ₂
15	267 (35714), 296 (40675), 341 (23758 (sh))	CH ₂ Cl ₂
17	297 (55012), 310 (35513 (sh)), 325 (29857 (sh)), 340 (23014), 370 (4169 (sh))	CH ₂ Cl ₂
23	283 (37489), 349 (18740 (sh))	CH ₂ Cl ₂
28	297 (49018), 360 (18121 (sh)), 500 (4955 (sh))	CH ₂ Cl ₂

Table 3 Absorption maxima of compounds 5, 6, 13, 15, 17 and 23.

Figure 39 compares the absorption spectra of the copper complexes measured in CH₂Cl₂ with the detailed absorption maxima listed in Table 4. The absorption in the UV region is comparable with the ligand absorptions. An additional absorption is shown for all complexes around 470-

485 nm arising from metal-to-ligand charge-transfer (MLCT) transitions. The additional diaryl moiety as a donating group on the back of the imidazole in $[\text{Cu}(\mathbf{13})_2][\text{PF}_6]$ compared to $[\text{Cu}(\mathbf{6})_2][\text{PF}_6]$ did not have a significant effect on the absorption spectra. Neither a change in intensity nor energy of the MLCT was observed. On the contrary, the introduction of the *n*-butoxy substituent on the diarylamine in $[\text{Cu}(\mathbf{15})_2][\text{PF}_6]$ leads to a slight blue shift of the MLCT-band with respect to its non-alkylated analogue $[\text{Cu}(\mathbf{13})_2][\text{PF}_6]$. Changing the donor group from diphenylamine to carbazole leads to a red shift of the MLCT with a similar value as the bromo analogue. In conclusion, substitution at the back of the imidazole does not have a strong effect on the MLCT band of the Cu-complexes.

Changing the substitution pattern from the 5,6-positions of neocuproine to the 4,7-positions leads to a more intense and broader MLCT band with a slight red shift compared to the other copper complexes.

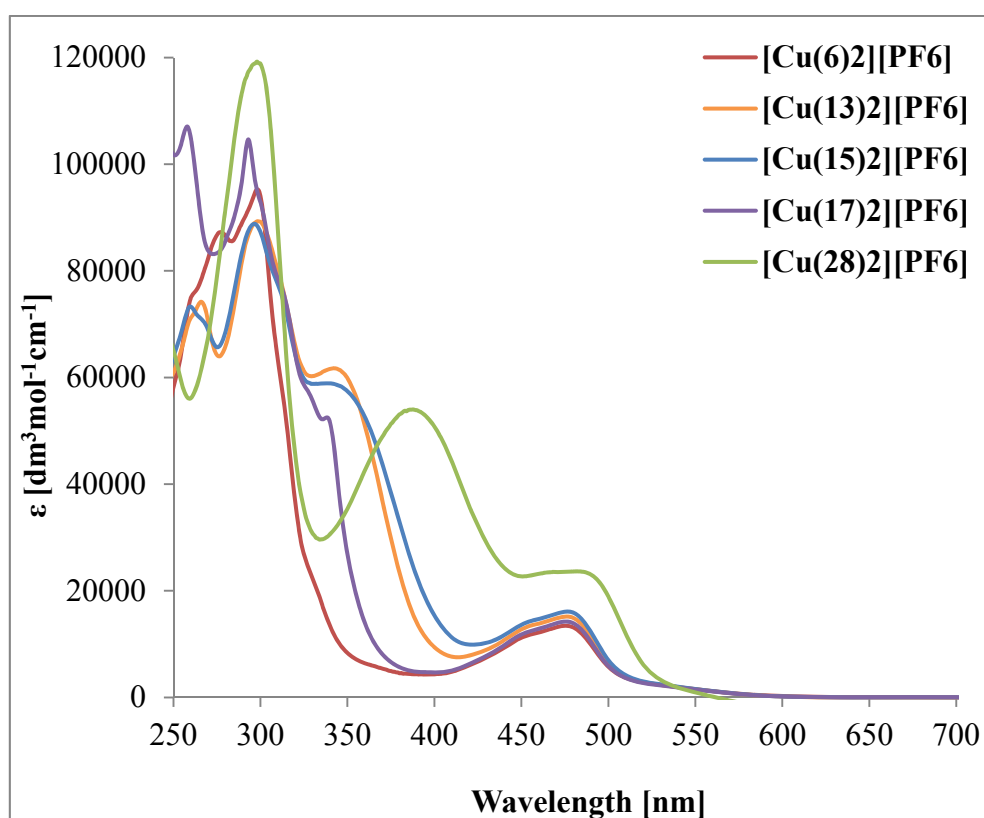


Figure 39 UV-Vis absorption spectra of the *homoleptic* copper(I) complexes of ligands 6, 13, 15, 17 and 28 in CH_2Cl_2 ($c = 1 \times 10^{-5} \text{ M}$).

Absorption Maxima of the Complexes		
	$\lambda_{\max}[\text{nm}] \ \epsilon[\text{dm}^3 \text{mol}^{-1} \text{cm}^{-1}]$	Solvent
[Cu(6) ₂][PF ₆]	282 (87245), 304 (95258), 482 (13427)	CH ₂ Cl ₂
[Cu(13) ₂][PF ₆]	266 (74200), 299 (89274), 342 (61731), 476 (15156)	CH ₂ Cl ₂
[Cu(15) ₂][PF ₆]	256 (73281), 292 (88786), 342 (58653 (sh)), 469 (16112)	CH ₂ Cl ₂
[Cu(17) ₂][PF ₆]	262 (106422), 298 (104318), 338 (52880), 482 (14477)	CH ₂ Cl ₂
[Cu(28) ₂][PF ₆]	300 (119226), 391 (53988), 486 (23643 (sh))	CH ₂ Cl ₂

Table 4 Absorption maxima of the copper complexes of ligands **6**, **13**, **15**, **17** and **28**.

6.2 Cyclic Voltammetry

The electrochemical properties of all the copper complexes were studied by cyclic voltammetry in CH₂Cl₂ to avoid potential interaction of coordinating solvents such as acetonitrile. Glassy carbon was used as the working electrode, platinum as the counter electrode and silver was used as a pseudo-reference. All redox potentials are shown with respect to Fc/Fc⁺ which was used as an internal reference. [NⁿBu₄][PF₆] was used as supporting electrolyte for the measurement. Table 5 summarizes the redox potentials of the *homoleptic* copper complexes of ligands **6**, **13** and **28**.

Electrochemical Data of the Complexes			
	$E^{1/2}_{\text{ox}} [\text{V}]$ ($E_{\text{pc}} - E_{\text{pa}} [\text{mV}]$)	$E^{1/2}_{\text{ox}} [\text{V}]$	$E^{1/2}_{\text{ox}} [\text{V}]$
[Cu(6) ₂][PF ₆]	+0.42 (32)		
[Cu(13) ₂][PF ₆]	+0.42 (29)	+0.63 (78)	
[Cu(28) ₂][PF ₆]	+0.32 (105)	+0.41 (109)	+0.61 (221)

Table 5 Electrochemical data measured by cyclic voltammetry with respect to Fc/Fc⁺ measured in degassed CH₂Cl₂ with [nBu₄N][PF₆] as electrolyte.

Figure 40a shows the cyclic voltammogram of the simplest copper complex of the series. A reversible oxidation process of the Cu(I) centre occurs at +0.42 V, which is close to the reported value of +0.50 V by Eggleston et al. for 2,9-dimethyl-1,10-phenanthroline,⁸⁹ and shows that the 4-bromophenyl groups in the 5,6-positions of the phenanthroline unit have no significant influence on the redox potential of the copper centre. The cyclic voltammogram of [Cu(**13**)₂][PF₆] is shown in Figure 40b for a CV window up to +1.8 V and in Figure 40c for a

CV window run only up to +1.3 V. The smaller CV window allows one to distinguish between the oxidation of the Cu(I) centre and the diphenyl amine unit.

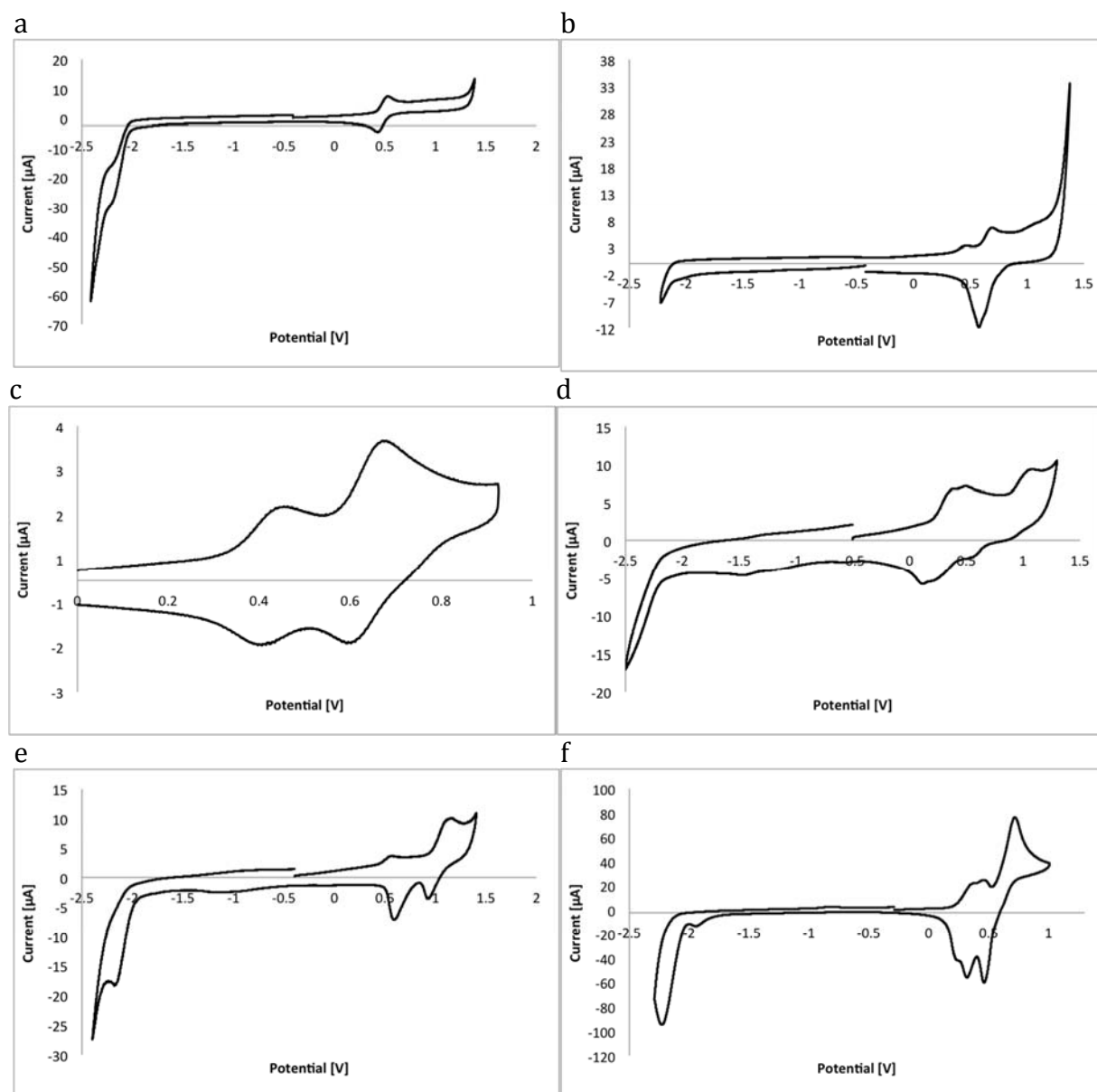


Figure 40 Cyclic voltammograms of the copper complexes measured in 0.1 M $^n\text{Bu}_4\text{N}^+[\text{PF}_6]^-$ in degassed CH_2Cl_2 with respect to Fc/Fc^+ . a) $[\text{Cu}(\mathbf{6})_2][\text{PF}_6]$, b) $[\text{Cu}(\mathbf{13})_2][\text{PF}_6]$ up to 1.8 V, c) $[\text{Cu}(\mathbf{13})_2][\text{PF}_6]$ up to 1.3 V, d) $[\text{Cu}(\mathbf{15})_2][\text{PF}_6]$, e) $[\text{Cu}(\mathbf{17})_2][\text{PF}_6]$, f) $[\text{Cu}(\mathbf{28})_2][\text{PF}_6]$.

The cyclic voltammograms of $[\text{Cu}(\mathbf{15})_2][\text{PF}_6]$, $[\text{Cu}(\mathbf{17})_2][\text{PF}_6]$ and $[\text{Cu}(\mathbf{28})_2][\text{PF}_6]$ are rather complex. While for the 4,7-substituted complex $[\text{Cu}(\mathbf{28})_2][\text{PF}_6]$ the oxidation processes can be distinguished if the CV window is only run up to +1.3 V, this is not the case for $[\text{Cu}(\mathbf{15})_2][\text{PF}_6]$ and $[\text{Cu}(\mathbf{17})_2][\text{PF}_6]$. The oxidation of the diaryl unit coincides with the oxidation of Cu(I) due to low lying energy levels. The oxidations at +0.41 V and +0.61 V in $[\text{Cu}(\mathbf{28})_2][\text{PF}_6]$ are assigned to the oxidation processes of the two diaryl amine units. The second oxidation is

similar to the redox potential of the oxidation in $[\text{Cu}(\mathbf{13})_2][\text{PF}_6]$ which has only one diaryl amine unit attached to the 5- and 6-positions of the phenanthroline unit. The complexes, in particular $[\text{Cu}(\mathbf{28})_2][\text{PF}_6]$, strongly adsorb on the electrodes during the measurements and for this reason, only the first scan cycles were used.

To investigate the origin of the interference of the oxidation of the donor group and the Cu(I) center in $[\text{Cu}(\mathbf{15})_2][\text{PF}_6]$ and $[\text{Cu}(\mathbf{17})_2][\text{PF}_6]$, respectively, the characters of molecular orbitals in the HOMO manifold of the ground state complexes were calculated for the two complexes. Ground state density functional theory (DFT) calculations were performed by *Prof. Dr. Catherine E. Housecroft* using Spartan 14 (v. 1.1.8)¹ at the B3LYP level with a 6-31G* basis set in vacuum. Initial structure minimization was carried out at a molecular mechanics or PM3 level.

Figure 41 shows the DFT calculations of the HOMO and LUMO manifolds of $[\text{Cu}(\mathbf{15})_2][\text{PF}_6]$. The LUMO manifold consists of two MOs very close in energy; effectively a degenerate pair with the MO character localized on the *phen* unit and small contribution from the Cu atom.

The HOMO and HOMO–1 are also close in energy and are localized on the donating $(\text{MeOC}_6\text{H}_4)_2\text{N}(\text{C}_6\text{H}_4)$ units. The next two orbitals in the HOMO manifold are centred on copper, and the two filled MOs just below are localized on the $(\text{MeOC}_6\text{H}_4)_2\text{N}$ units.

Figure 42 shows the calculated HOMO and LUMO manifolds from DFT calculations of $[\text{Cu}(\mathbf{15})_2][\text{PF}_6]$. The LUMO and LUMO+1 are very close in energy and have the same orbital characteristics localised on the *phen* units with a small contribution from copper. The HOMO and HOMO–1 are also close to being degenerate and are localised on the donating carbazole domain. The next two orbitals in the HOMO manifold are centred on the carbazole units and the two filled MOs just below these are copper-centred.

In summary, the LUMO/LUMO+1 manifold is localized on the *phen* unit with some contribution from the copper center in both complexes. On the contrary, the HOMO/HOMO–1 manifold is localized on the respective donating group.

¹ Spartan '14, Wavefunction, Inc., Irvine, CA 92612.

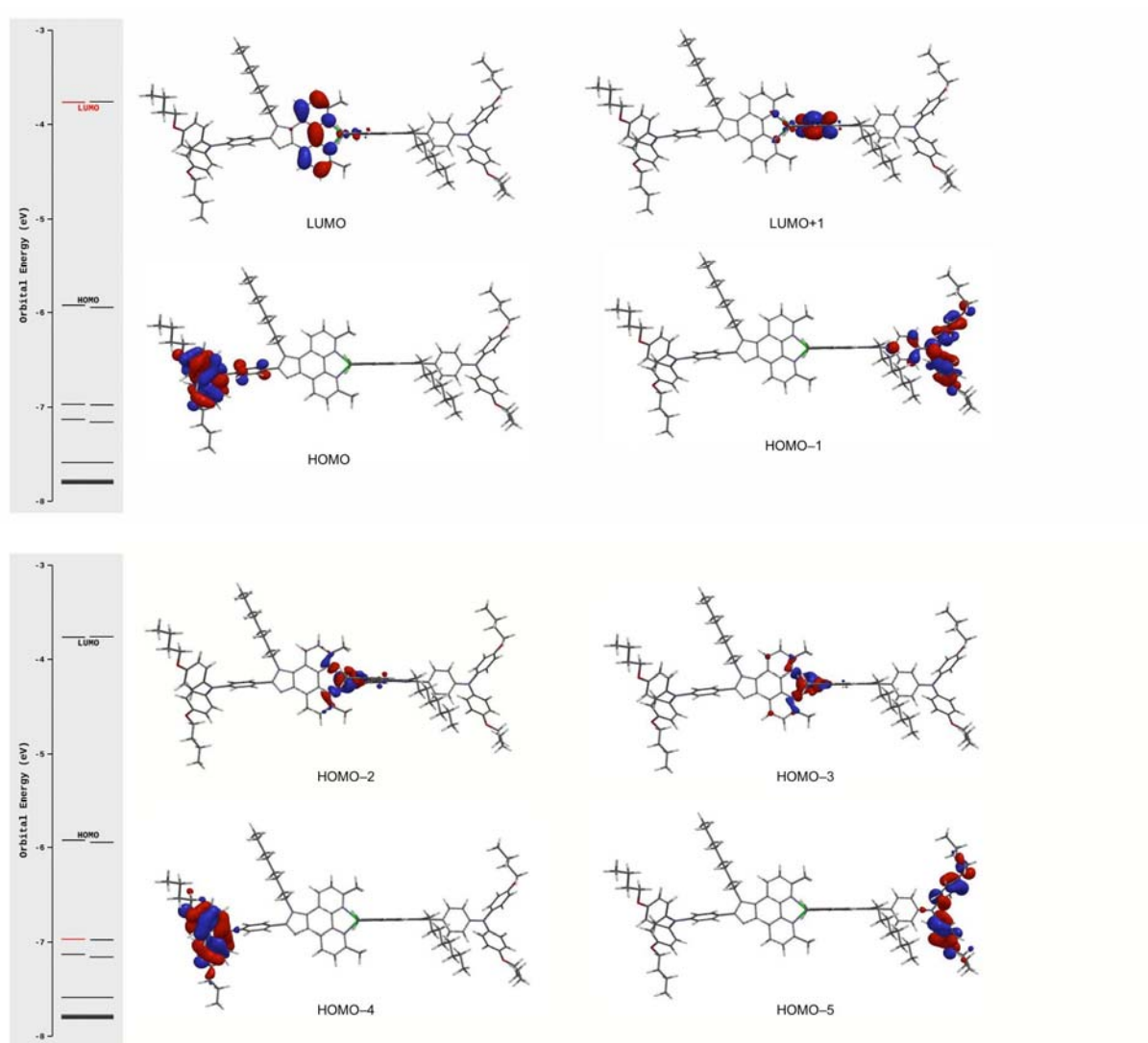


Figure 41 Results of ground state DFT calculations of $[\text{Cu}(\text{15})_2][\text{PF}_6]$ at the B3LYP level with a 6-31G* basis set in vacuum.

With respect to the CV measurements, it can be pointed out that the HOMO manifold possesses localized character on either the peripheral groups or the copper in both complexes. Oxidation therefore involves oxidation of these domains and several oxidation processes at potentials not too far apart are consistent with the DFT calculations. It is important to note that with the basis set used (6-31G*) on all atoms, the precise energies of the MOs are not to be relied upon, although the orbital compositions are valid.⁹⁰

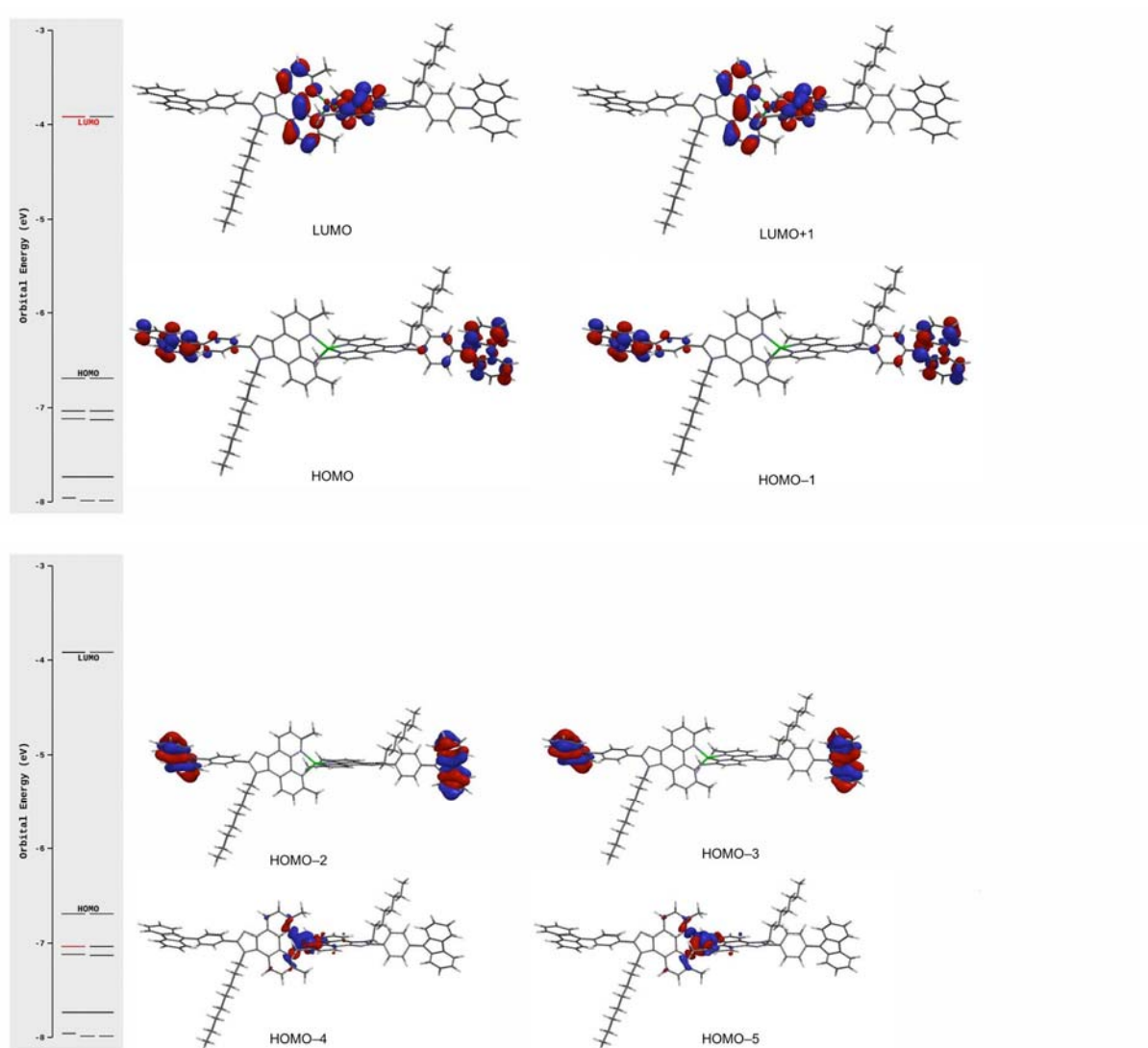


Figure 42 DFT calculations of $[\text{Cu}(\mathbf{17})_2][\text{PF}_6]$ at the B3LYP level with a 6-31G* basis set in vacuum.

6.3 Crystallographic Data

Single crystals of **6** were grown from a toluene-ethyl acetate solution and crystallize in the monoclinic space group $P2_1/c$ with an R factor of 5.02%. Figure 43 shows the crystal structure of ligand **6**. The aryl group is twisted by 58.6° with respect to the imidazole plane allowing for $\text{CH}\cdots\pi$ and $\text{Br}\cdots\text{CH}$ interactions with the tilted alkyl chain. Interaction of the C8-chain with the bromophenyl moiety is facilitated through an unusual angle of 100.9° between a plane through N4-C24 and a plane through C24-C29. This is close to a right angle and is quite unusual for an alkyl chain and indicates the strong interaction with the bromophenyl moiety. The distance $\text{C29H29}\cdots\text{Br1}$ is 3.12 Å which is close to the sum of the van der Waals radii of 3.05 Å⁹¹ and the closest $\text{CH}\cdots\pi$ contacts are 3.20 and 3.30 Å. The molecules π -stack between the

phen groups, which leads to packing between centrosymmetric pairs. The distance between the least squares plane through the phenanthrolines is 3.35 Å.

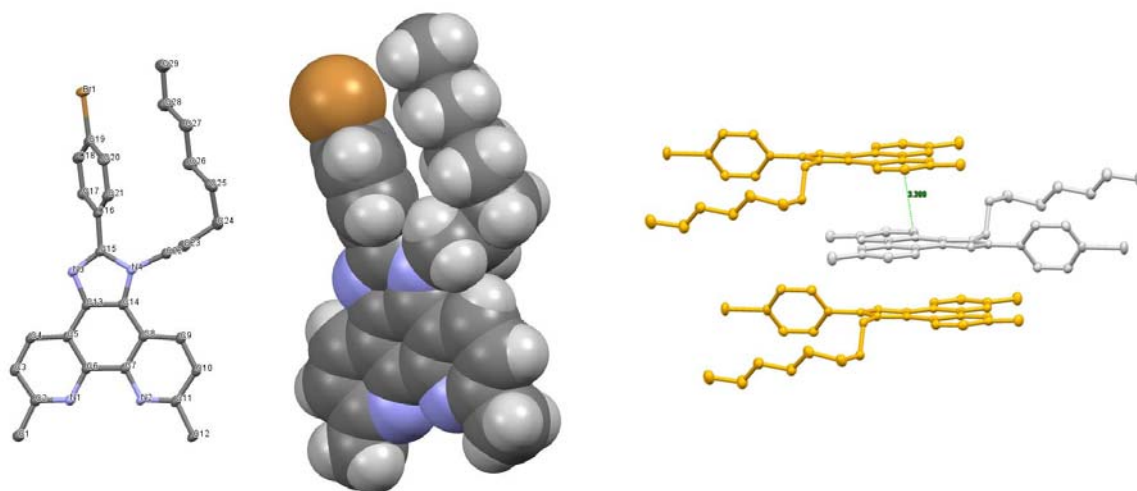


Figure 43 Crystal structure of ligand 6 with ellipsoids plotted at 50% probability and hydrogens omitted for clarity (left) and the spacefilled structure in the middle which shows the van der Waals interaction of the alkyl chain with the bromophenyl unit. On the right, the π -stacking between the phenanthroline unit is shown.

Figure 44 shows the crystal structure of 17, which crystallizes in the triclinic space group P-1. Similar to the structure of 6 the aryl group is twisted by 53.4° with respect to the imidazole plane. The angle between the carbazole unit and the phenyl spacer is 55.6° . The angle between a plane through N3, C34 and C35 and a plane through C35-C41 is 80.0° which is even smaller than the 100.9° in ligand 6 and allows for an interaction with the phenyl spacer and the carbazole. The C41H $\cdots\pi$ interaction with the carbazole unit is as close as 2.97 Å while the closest interactions with the phenyl spacer are 3.04 Å and 2.98 Å. The molecules form layers by π -stacking a carbazole unit over a phenanthroline unit with a distance of 3.45 Å from the centroid of the phenanthroline unit to the least squares plane through the carbazole unit and an angle of 7.6° between the least square planes. With the alkyl chain lying on one side of the molecule, the other side interacts with a second sheet by π -stacking between two phenanthroline units with a distance between the least squares planes of 3.34 Å. The double sheet consists of carbazole-phenanthroline-phenanthroline-carbazole interactions and is shown in Figure 44.

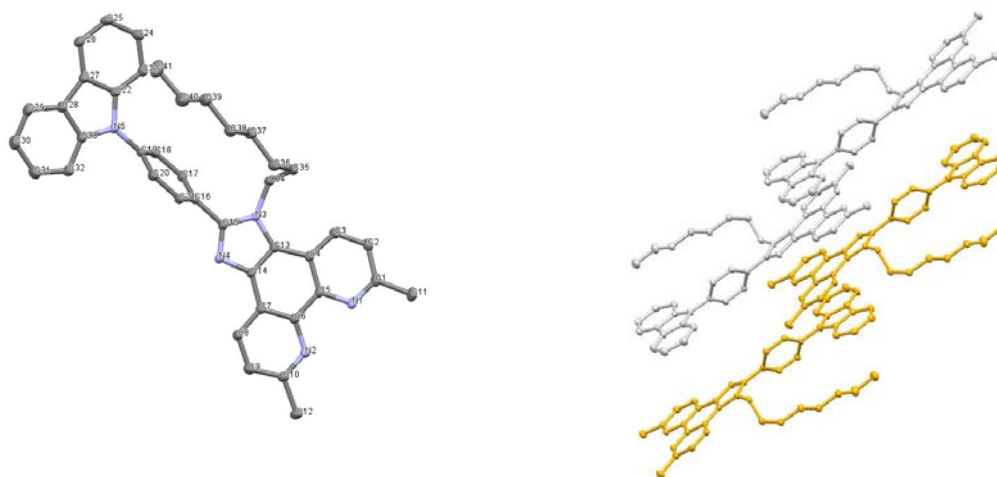


Figure 44 Crystal structure of ligand 17 with ellipsoids plotted at 50% probability and hydrogens omitted for clarity (left). Double sheet with π -stacking in the order carbazole-phenanthroline-phenanthroline-carbazole (right).

Ligand **14** crystallizes in the space group $P2_1/c$. In contrast to the two structures discussed above, the alkyl chain points away from the molecule in this case. This allows for van der Waals interactions between two molecules as shown in Figure 46. The connecting aryl ring is twisted by 43.2° out of the imidazole plane while the two 4-methoxy-phenyls are twisted by 63.1° and 65.3° with respect to the phenyl spacer. Due to this twisting, no close packing by π -stacking is possible and the molecules mainly interact by van der Waals forces.

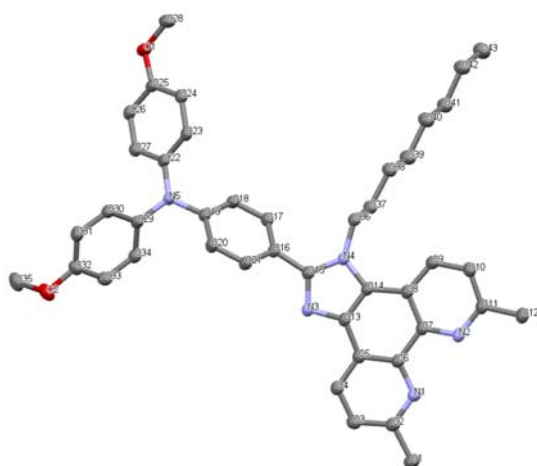


Figure 45 Crystal structure of ligand 14 with ellipsoids plotted at 50% probability and hydrogens omitted for clarity.

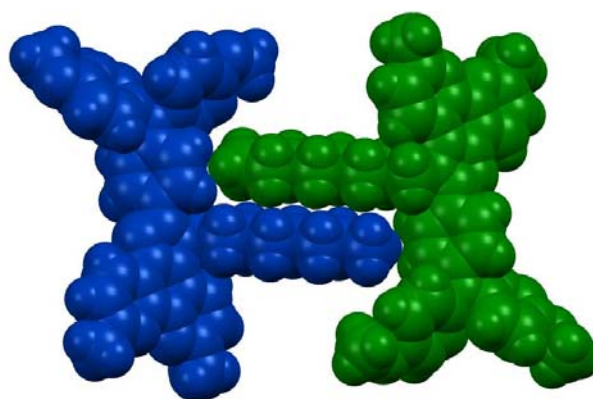


Figure 46 Van der Waals interactions between the alkyl chains in the crystal structure of ligand 14.

7 State of the Art Dye Sensitized Solar Cells

7.1 Introduction

Prior to the start of this research project, partially sealed dye sensitized solar cells were state of the art in our research group.^{92,42} These cells have obvious disadvantages with only being stable for a short time period due to solvent evaporation and undesirable interactions with oxygen and water. Hence, improvement of the fabrication and measurement of DSCs played a major role, particularly in the early stages, in the research for this thesis. With DSCs being a complex interplay of electrochemical reactions, physical processes and diffusion charge-carrying processes, many factors can be optimized. Changes of single components of solar cells such as the dye, the semiconductor, the electrolyte or the counter electrode can lead to enhanced solar cell performances. Modification of both the fabrication of DSCs and the measuring set up can further improve the result.

Although there are many descriptions of the construction and fabrication of DSCs in the literature, with the reports from the group of *Grätzel*^{6,71} probably being the most established ones, these are optimized for the specific equipment and dyes used and often lack details that are crucial for the development of efficient DSCs. However, it is of crucial importance to have valid, comparable and reproducible results of the measured solar cells. Therefore a significant amount of time was initially invested in this doctoral work to develop and optimize a reproducible standard protocol for the fabrication and measurement of DSCs in our laboratory. The ruthenium dye N719 (Figure 47), developed by the group of *Grätzel*, is the commonly accepted reference dye in the DSC community with a reported maximum efficiency of 10.1%.⁷¹ For this reason, we first established a well performing N719 reference cell.

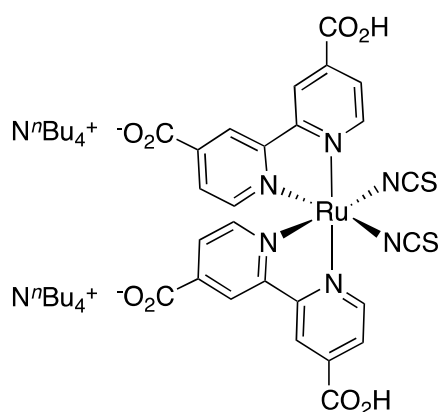


Figure 47 The ruthenium dye N719 commonly used as a reference dye in the DSC community.

In this chapter the development from partially to completely sealed solar cells is shown, followed by the improvements achieved by varying several parameters in the fabrication of completely sealed, doctor-bladed DSCs. After presenting the results with screen printed DSCs the development of the masking protocol is described.

7.2 From Partially to Completely Sealed DSCs

As mentioned above the fabrication of DSCs in this thesis started from so-called partially sealed cells for which the working electrode was made by the doctor blading technique (see 4.2.2). “Partially sealed” in this context means that the working and counter electrodes were assembled with a sealing foil but the cells were not completely sealed. The electrolyte was filled in by adding a drop between the electrodes to moisten the DSC interior by capillary forces. The advantage of this method is its simplicity as it only requires TiO₂-paste, FTO-coated glass, scotch tape and a heating plate for the production of the working electrodes. The technique also allows for the fast production of working electrodes with TiO₂ thicknesses of several μm and, in contrast to fully sealed cells, there is no need for a vacuum pump or N₂ gas for the vacuum back filling of the electrolyte. However, the main disadvantage of partially sealed cells (which are sometimes referred to as "open cells") is the fast evaporation of electrolyte and hence the short timescale over which the cells can be measured. Furthermore, the presence of oxygen and water means that side reactions within the cell such as undesired oxidations are more likely. For this reason, completely sealed DSCs were produced by punching a hole into the scotch tape to have a defined round aperture with a diameter of 0.65 cm. With this technique a sealing foil, which was used to assemble the electrodes, could be adhered around the hole to completely close the cell. The electrolyte was filled in by vacuum back filling via a small hole in the counter electrode, which was completely sealed with a sealing foil and a covering glass to obtain a completely sealed cell (see 4.2.5).

Figure 48 shows the comparison of the performance of partially sealed and completely sealed cells sensitized with N719 and an I⁻/I₃⁻ electrolyte, which was labelled standard II and consists of 0.1 M LiI, 0.05 M I₂, 0.5 M 1-methylbenzimidazole (MBI) and 0.6 M 1-butyl-3-methylimidazolium iodide (BMII) in 3-methoxypropionitrile. In Table 6 the detailed photovoltaic parameters of the two cells are listed. The overall efficiency of the N719 reference cell could be increased dramatically from 2.18 % to 4.75%. Despite the lower V_{oc} in the completely sealed versus partially sealed cell, η is improved because of an increase in both current density and fill factor.

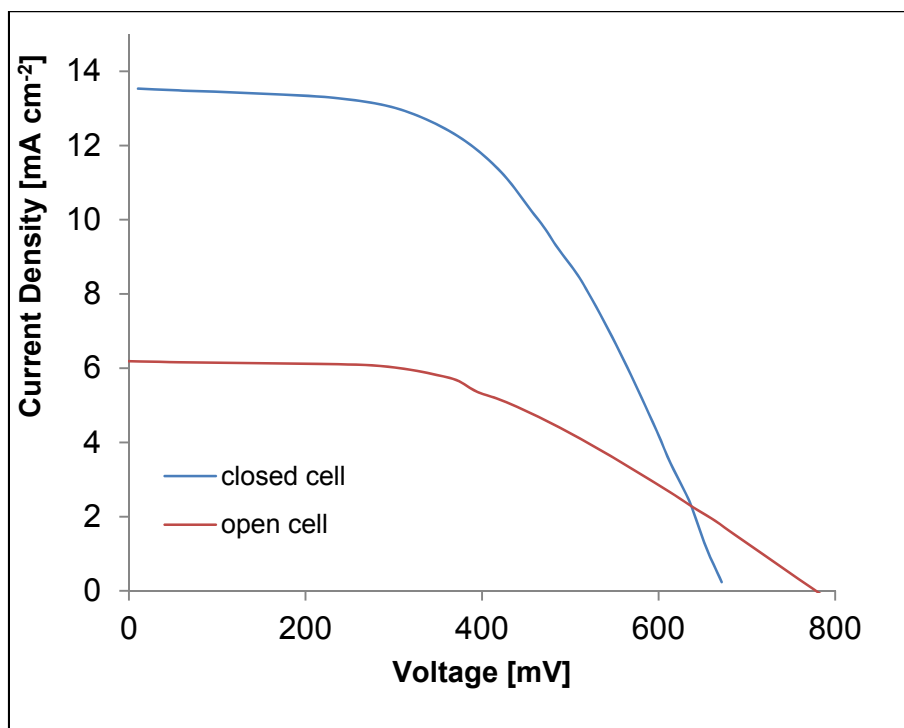


Figure 48 Comparison of a completely and a partially sealed cell. Both cells are sensitized with N719 and are filled with Standard II electrolyte consisting of 0.1 M LiI, 0.05 M I₂, 0.5 M MBI and 0.6 M BMII IN 3-methoxypropionitrile. The cells were measured on the day of assembly.

	partially sealed cells	completely sealed cells
Voc [mV]	798	671
Jsc [mA cm ⁻²]	6.18	13.53
ff [%]	44.2	52.3
η [%]	2.18	4.75

Table 6 Detailed photovoltaic parameters for the partially and completely sealed cells in Figure 48.

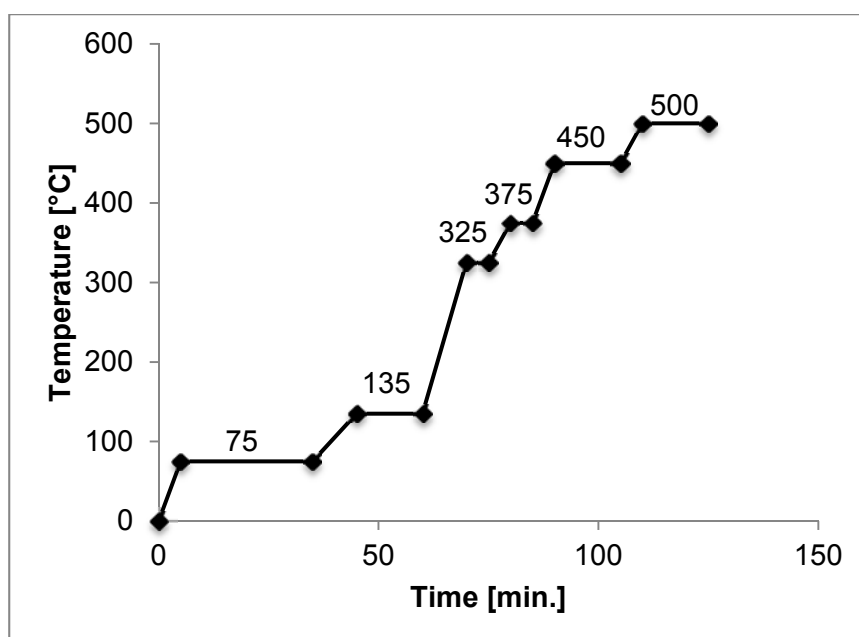


Figure 49 Heating protocol for sintering of TiO₂ electrodes.

One reason for this improvement is the enhanced stability of the cell because the electrolyte cannot evaporate as the DSC is completely sealed. Provided they are correctly sealed, there should be no leakage or evaporation of the electrolyte. This leads to constant conditions over the measuring time with no variation in the concentration of the electrolyte. Furthermore no undesired side reactions with oxygen or water are possible due to the inert atmosphere in the cells.

However, another innovation on going from partly to completely sealed DCS was a change in TiO₂ paste. For the completely sealed cells TiO₂ pastes initially prepared by *Dr. Ewald Schönhofer* were used. In his doctoral studies, he investigated the influence of the TiO₂ paste on the performance of N719 reference cells.⁹³ The homemade paste was prepared by an adapted method of *Grätzel*⁹⁴ and lead to enhanced efficiencies as reported by our group.⁹⁰ Furthermore a different sintering program for the paste with several heating steps was applied to reduce the formation of cracks in the TiO₂. The use of multiple heating ramps allows for slower heating to the maximum temperature and enables the mild combustion of organic additives and residues without destroying the TiO₂ layer. A heating protocol after *Krüger*⁹⁵ (Figure 49) was applied which slowly heats the electrodes over a period of 2 hours up to 500 °C. It is important to let the electrodes slowly cool down to room temperature to avoid cracks formed by temperature differences. Additionally, the cleaning protocol of the FTO coated glass was changed. The glass was cleaned by sonicating in a 2% aqueous surfactant solution, acetone, and ethanol for 7 minutes each followed by drying in N₂.

In summary, these adaptations were expected to have a strong impact on the improvement in current density and efficiency of the completely sealed cells with respect to partially sealed cells. Finally, there is also a difference in the active area with the partially sealed cells having a TiO_2 area of 0.45 cm^2 and the completely sealed cell a round area of 0.33 cm^2 which may have an influence on the performance.

7.3 Optimization of Completely Sealed DSCs

To improve the efficiency of the N719 reference cell, several parameters for the construction of the solar cell and its measurement can be optimized. In this section, these optimizations are outlined. At first, the optimization of the measurement setup is discussed. In the second part of this chapter, the optimization of the DSC fabrication is discussed. The influence of the electrolyte, the thickness of the TiO_2 layers, the distance between the working and the counter electrode and the method of counter electrode fabrication will be outlined.

7.3.1 Improvement of the Measuring Setup

Comparison of the data in Table 6 with literature values⁷¹ shows that the ff is the parameter that can be improved the most. A low ff indicates a high resistance within the cell or a high resistance as a result of the way the DSC is connected into a circuit. A simple way to reduce the resistance at the contacts to the cell is to use the four-wire method to measure the J/V curves. For this, two pairs of leads are connected to the solar cell: with the first pair, a voltage is applied across the cell, and with the second pair, the voltage drop across the cell is measured. Using this method, the resistance of the wires and contacts can be compensated, which can reduce the contact resistances significantly. Figure 50 and Table 7 show the influence of a four-wire measurement compared to a two-wire one. By compensation of the lead resistance by the source meter, a more accurate measurement is achieved. The change of the measurement setup affects only the ff and, as a consequence, η is improved; V_{OC} and J_{SC} remain unchanged.

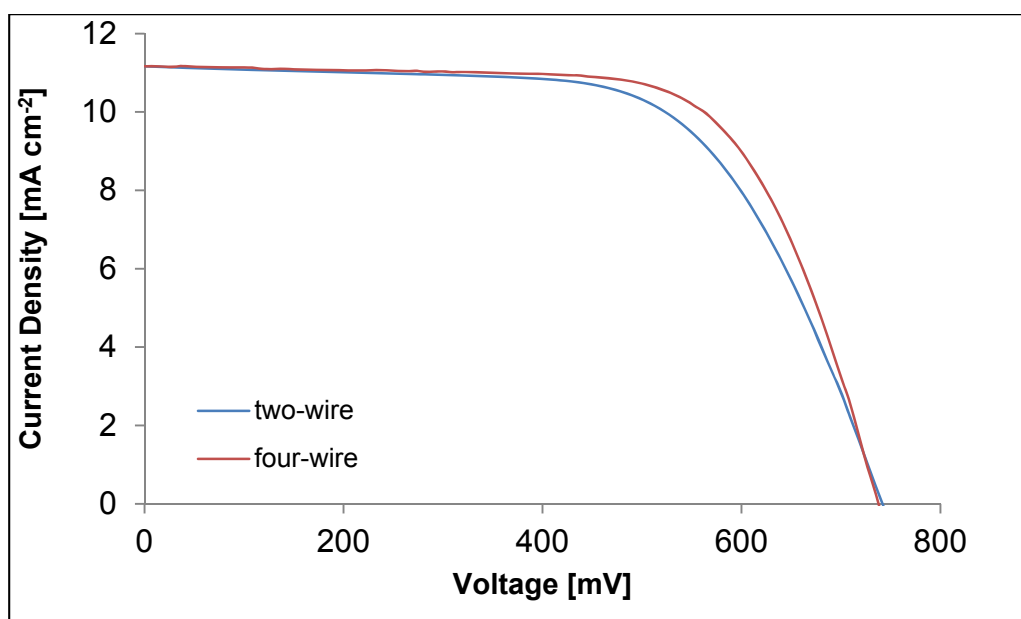


Figure 50 Influence of a 4-wire measurement versus a two-wire one on the J/V measurement of the same N719 sensitized solar cell on the same day.

	two-wire	four-wire
V_{oc} [mV]	736	736
J_{sc} [mA cm^{-2}]	11.17	11.17
ff [%]	63.7	68.4
η [%]	5.24	5.63

Table 7 Photovoltaic Parameters of the J/V measurements in Figure 50.

7.3.2 Optimization of the I^-/I_3^- Electrolyte

Subsequently, the influence of the electrolyte was investigated. The electrolyte plays a fundamental role in a DSC by regenerating the oxidized dye and by closing the electrical circuit through charge transport between the electrodes. With the I^-/I_3^- redox couple being by far the most established and successful mediator for DSCs, two I^-/I_3^- electrolytes of different compositions and concentrations were compared. Our previously used electrolyte consisting of 0.1 M LiI, 0.05 M I_2 , 0.5 M MBI and 0.6 M BMII in 3-methoxypropionitrile (called Standard II) was compared with an electrolyte consisting of 0.5 M LiI, 0.05 M I_2 and 0.5 M MBI in 3-methoxypropionitrile (called Standard I). Figure 51 and Table 8 clearly show that the Standard II electrolyte outperforms Standard I. Although with the Standard I electrolyte a higher V_{oc} of 690 mV compared to 663 mV with Standard II is reached, this is more than compensated for by the higher J_{sc} of 11.35 versus 8.88 mA cm^{-2} with Standard II versus Standard I electrolyte,

respectively. This leads to an efficiency of 4.89% with Standard II in comparison to 4.07% with Standard I. Consequently, DSCs were henceforth prepared with Standard II electrolyte.

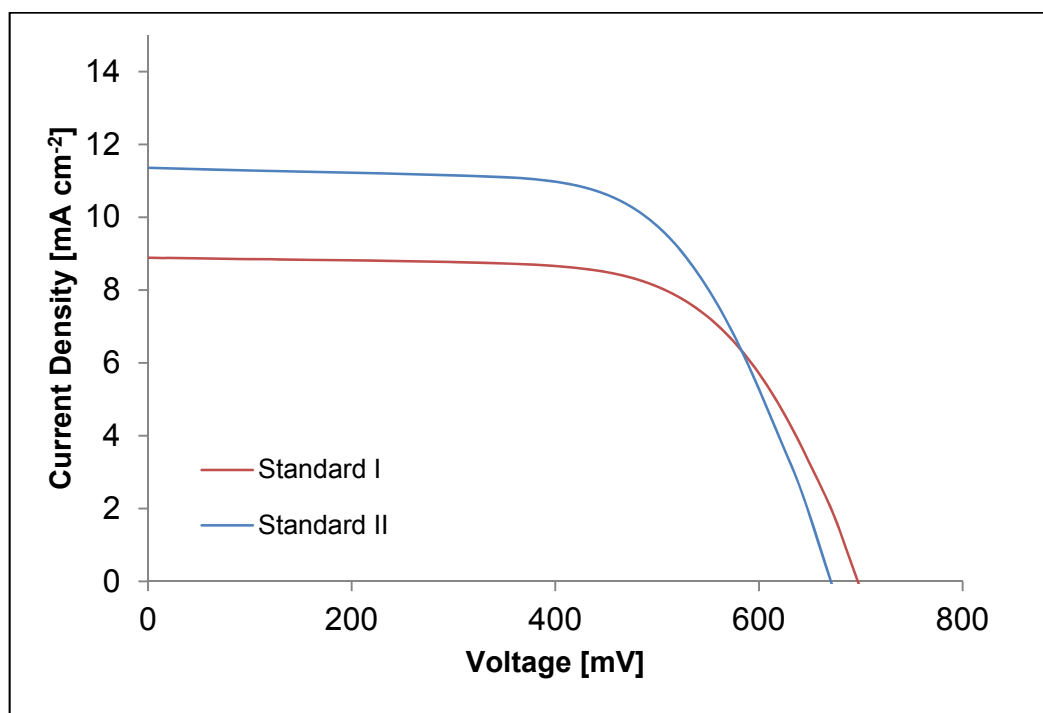


Figure 51 J/V curves of N719 sensitized solar cells filled with either Standard I or Standard II electrolyte.

	Standard I	Standard II
V_{oc} [mV]	690	663
J_{sc} [mA cm^{-2}]	8.88	11.35
ff [%]	66.4	65.0
η [%]	4.07	4.89

Table 8 Photovoltaic Parameters of the DSCs shown in Figure 51.

7.3.3 Optimization of the Counter Electrode

The next parameter that was changed in the fabrication of the DSCs was the counter electrode. The catalyst on the counter electrode plays an important role in the recovery of the electrolyte at the counter electrode and has therefore an important impact on the DSCs performance. The catalytic activity depends on the amount of catalyst adsorbed and the homogeneity of the layer. Therefore the influence of the application of the commercial Pt-precursor solution (Platisol-T) onto the glass electrode on the performance of the DSCs was investigated. There are two common techniques described in the literature: dropwise addition and spreading of the precursor solution with a paintbrush onto the FTO-coated glass. In both cases, the Pt is activated by heating the electrode to 450 °C for 15-20 min. Figure 52 and Table 9 show the comparison

of the two methods with the dropwise addition yielding a higher DSC performance. The dropwise addition method outperforms the paint-brush one by higher J_{sc} and ff , even though V_{oc} drops. The same trend is seen if Standard I electrolyte is used.

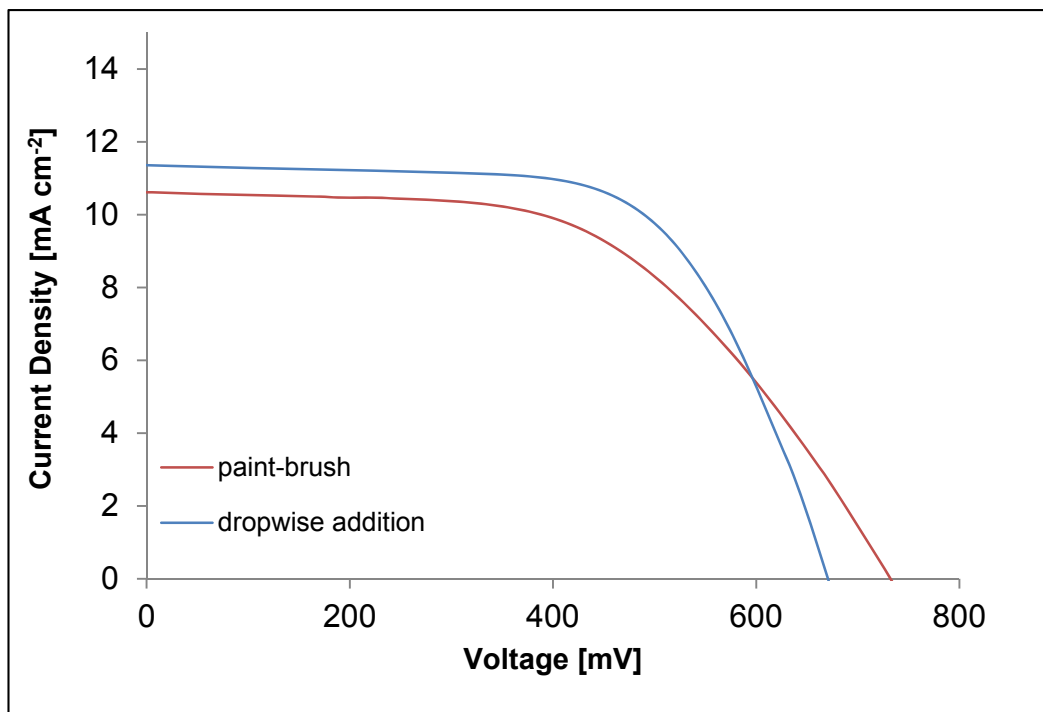


Figure 52 Comparison of DSCs with counter electrodes either prepared by dropwise addition or via a paint-brush of the Pt-precursor solution.

	paint-brush	dropwise addition
V_{oc} [mV]	727	663
J_{sc} [mA cm^{-2}]	10.61	11.35
ff [%]	54.5	65.0
η [%]	4.20	4.89

Table 9 Photovoltaic Parameters of the DSCs shown in Figure 52.

7.3.4 Optimization of the TiO_2 Layer Thickness

The thickness of the TiO_2 layer is another parameter in the fabrication process that can be changed to optimize the DSC efficiency. The thicker the layer, the more dye can be adsorbed which, in theory, should lead to higher current densities and performance. However, if the TiO_2 layer becomes too thick, side reactions such as recombination of electrons in the TiO_2 with the electrolyte become more important and reduce the solar cell's performance.^{96,97} In the literature, optimal thicknesses of 12-15 μm are reported.⁶

Hence, the impact of the thickness of the TiO₂-layer was investigated. By doctor blading one layer of TiO₂, a layer thickness of ~7 μm is obtained¹⁸ and two layers led to an approximate doubling of the thickness. However, the thickness obtained strongly depends on the paste used and the pressure applied while doctor blading. Two approaches to obtain a double layer were followed. First, a second layer of TiO₂ was doctor bladed on top of an air-dried first layer to sinter the double layer. The second approach was to doctor blade a second layer on top of a previously sintered layer. Unfortunately, in the latter approach, the second layer did not stick to the first and peeled off. Figure 53 shows the comparison of single versus double layer cells following the first approach. For consistency, duplicate cells were prepared and measured. The double layer DSCs clearly outperform the single layer ones. Table 10 shows that the increase in efficiency arises from an increase in current density, which is consistent with more dye being adsorbed on the semiconductor. However, although the TiO₂ layer thickness is approximately doubled, J_{SC} is only increased by 24%. This leads to the assumption that a thickness of the semiconductor is reached where side reactions are already playing a dominant role and limit the improvement of the cells. This is consistent with the best performing thicknesses of 12-15 μm reported in literature.^{6,96,97} Consequently, no further layers were applied.

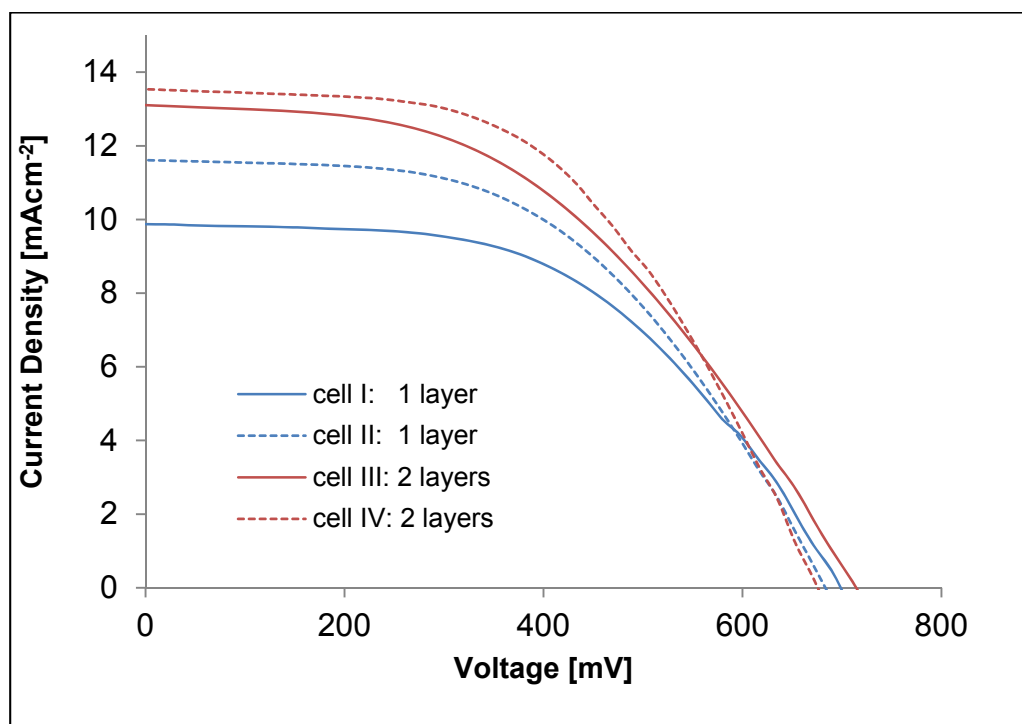


Figure 53 Comparison of DSCs with a single and a double layer of TiO₂, respectively. All cells were sensitized with N719 and were filled with Standard II electrolyte consisting of 0.1 M LiI, 0.05 M I₂, 0.5 M MBI and 0.6 M BMII IN 3-methoxypropionitrile. The cells were measured on the day of assembly.

	single layer		double layer	
	cell I	cell II	cell III	cell IV
V _{oc} [mV]	690	671	708	671
J _{sc} [mA cm ⁻²]	9.87	11.61	13.09	13.53
ff [%]	53.0	52.0	47.0	52.3
η [%]	3.61	4.06	4.36	4.75

Table 10 Detailed photovoltaic parameters for the partially and completely sealed cells in Figure 53.

7.3.5 Optimization of the Distance between the Working and the Counter Electrode

Another parameter to be investigated is the distance between the working and counter electrode. Hauch and Georg⁹⁸ showed that reducing the distance between the electrodes decreases the diffusion resistance and hence the overall DSC performance. In completely sealed cells, the sealing foil thickness defines the distance between the two electrodes and is therefore preferably as short as possible. Therefore, the influence of the sealing foil thickness on the DSC performance was investigated. Three sealing foil thicknesses 25, 60 and 100 μm were tested with the 60 μm foil being the thickness previously used in our DSC setups. Table 11 gives photovoltaic parameters for the partially and completely sealed cells, the J/V curves for which are shown in Figure 54. These data summarize the results of the DSCs assembled with different sealing foil thicknesses and 1 layer of TiO₂. Although the relative errors between duplicate cells are noticeable, a clear trend is evident with improving efficiencies going from thicker to thinner sealing foils. The improvement mainly arises from an increase in current density and an enhanced ff which is consistent with a reduced diffusion resistance. The solar cells with 25 μm sealing foil showed the best performances, agreeing well with the results of Hauch and Georg. The same trend was confirmed for DSCs with two layers of TiO₂. Figure 55 and Table 12 summarize the results of these measurements with the 25 μm sealing foil, again leading to the best results due to increased J_{sc} and ff. The low ff in all of these measurements may be related to the doctor blading technique. The need for an air drying step in the fabrication process to somehow stabilize the layer and the relatively large thickness of one TiO₂ layer may lead to cracks and irregularities in the TiO₂ layer. This increases the resistance within the cell and leads to a low ff.

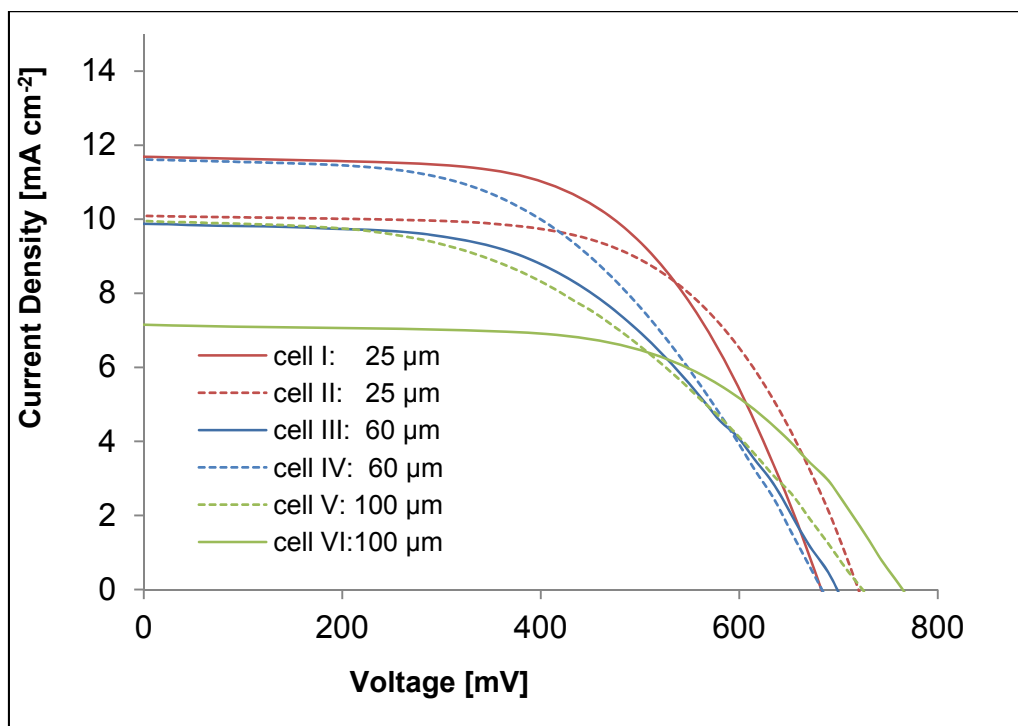


Figure 54 J/V curves for DSCs with 25, 60 and 100 μm sealing foil thickness, respectively. All cells consist of 1 layer of TiO_2 sensitized with N719 and were filled with Standard II electrolyte consisting of 0.1 M LiI, 0.05 M I_2 , 0.5 M MBI and 0.6 M BMII IN 3-methoxypropionitrile. The cells were measured on the day of assembly.

	25 μm		60 μm		100 μm	
	cell I	cell II	cell III	cell IV	cell V	cell VI
V_{oc} [mV]	671	708	690	671	708	763
J_{sc} [mA cm^{-2}]	11.68	10.09	9.87	11.61	9.94	7.14
ff [%]	60.4	62.5	53.0	52.0	48.2	60.2
η [%]	4.73	4.47	3.61	4.06	3.40	3.28

Table 11 Detailed photovoltaic parameters for the partially and completely sealed cells of Figure 54.

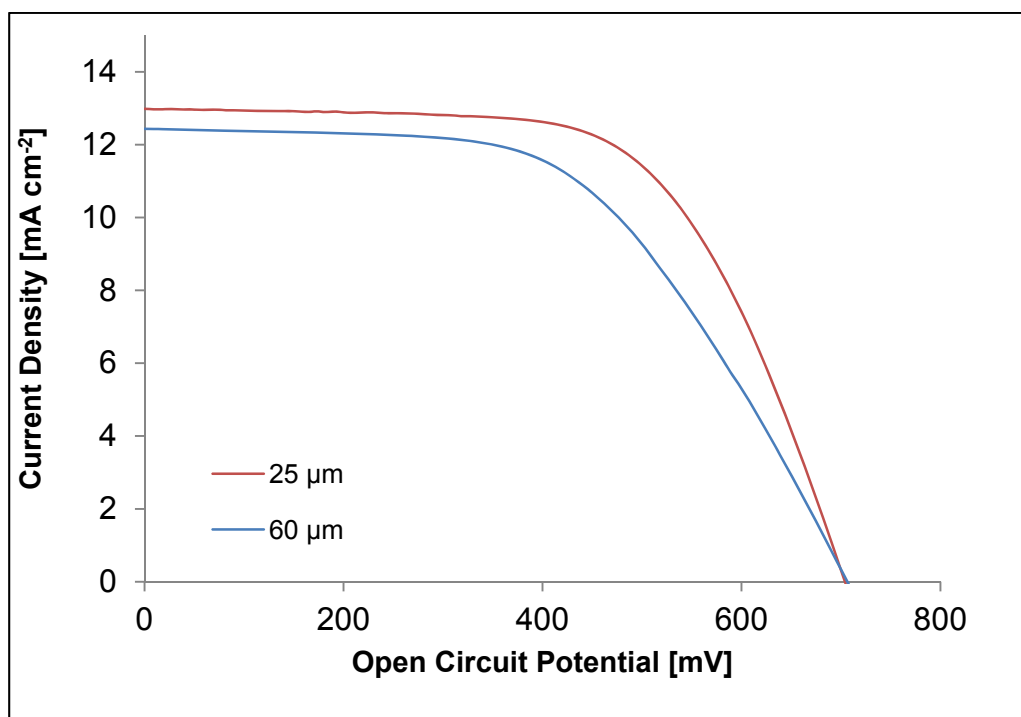


Figure 55 Comparison of DSCs with a double layer of TiO₂ a sealing foil thickness of 25 and 60 μm , respectively. All cells were sensitized with N719 and were filled with Standard II electrolyte consisting of 0.1 M LiI, 0.05 M I₂, 0.5 M MBI and 0.6 M BMII IN 3-methoxypropionitrile. The cells were measured on the day of assembly.

	25 μm	60 μm
V _{OC} [mV]	700	700
J _{sc} [mA cm ⁻²]	12.99	12.44
ff [%]	62.8	56.3
η [%]	5.71	4.90

Table 12 Detailed photovoltaic parameters of the two double TiO₂ layer cells shown in Figure 55.

7.3.6 Activation and Cleaning with UV-Ozone Treatment

The N719 reference cells could be further improved with an additional UV-ozone treatment step in the cleaning process of the electrodes. UV-O₃ treatment is an efficient method to remove organic residues and activate oxide surfaces. Figure 56 shows *J/V* curves of two N719 DSCs which were UV-O₃ treated prior to doctor blading of the TiO₂. The UV-O₃ treatment enhances the efficiency from 5.71% (Table 12) up to 6.58% (Table 13). Comparing the photovoltaic parameters of these cells in Table 13 with the results obtained without UV-O₃ treatment (Table 12, 25 μm cell) clearly shows that the enhancement arises from an increase in current density.

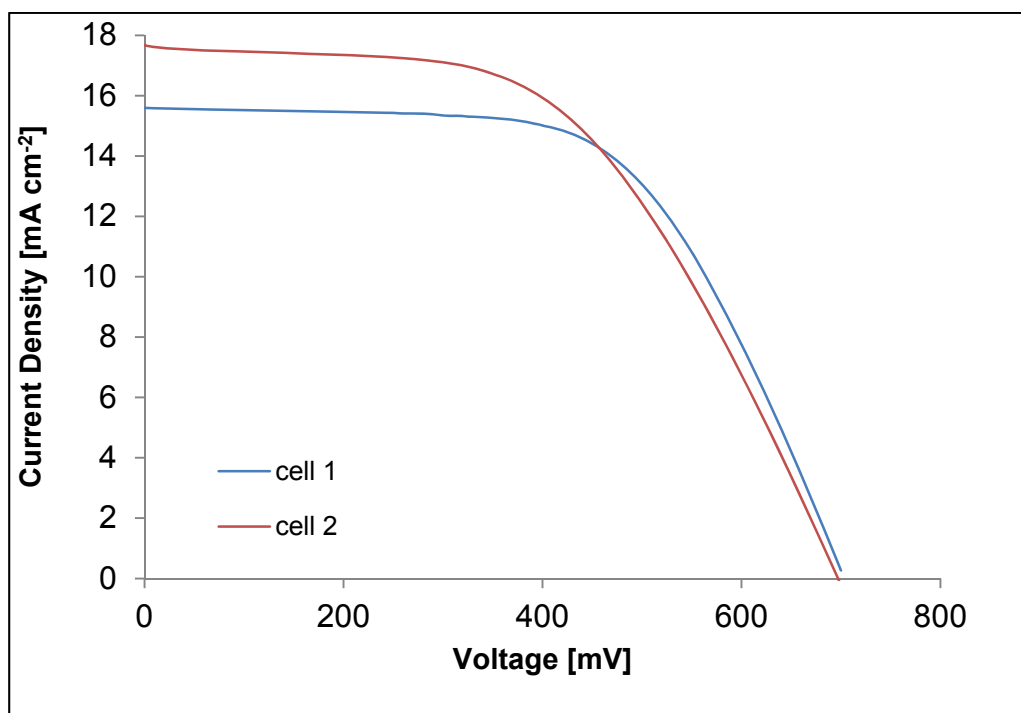


Figure 56 Optimized N719 reference cell with a doctor-bladed double layer of TiO₂ and a sealing foil thickness of 25 μm . All cells were sensitized with N719 and were filled with Standard II electrolyte consisting of 0.1 M LiI, 0.05 M I₂, 0.5 M MBI and 0.6 M BMII IN 3-methoxypropionitrile. The cells were measured on the day of assembly.

	cell 1	cell 2
V _{oc} [mV]	700	693
J _{sc} [mA cm ⁻²]	15.59	17.67
ff [%]	60.3	53.4
η [%]	6.58	6.54

Table 13 Detailed photovoltaic parameters of the optimized N719 reference cells shown in Figure 56.

7.3.7 J/V Measurements over Time

The complete sealing guarantees stable measuring conditions over several days to weeks, which had an important influence on our DSC performances as the solar cells turned out to improve over time, reaching a maximum efficiency approximately on the fifth day. Figure 57 shows the efficiency of an N719 sensitized solar cell over time. All three characteristic parameters used for the calculation of η , namely J_{sc} , V_{oc} and ff , improve over time and this leads to a relative increase in efficiency of 27% from day 1 to day 5. The first three data points are measured on day 1, the day of assembly, and show that the main improvement is obtained within the first 24 hours. From the fifth day, the efficiency of the cell is stable over a time period of at least two weeks. This improvement has been observed for several different dyes in our group.^{44,45,90} The

increase in efficiency is attributed to reorganization processes of the dye on the surface that minimize aggregation and other undesirable effects.

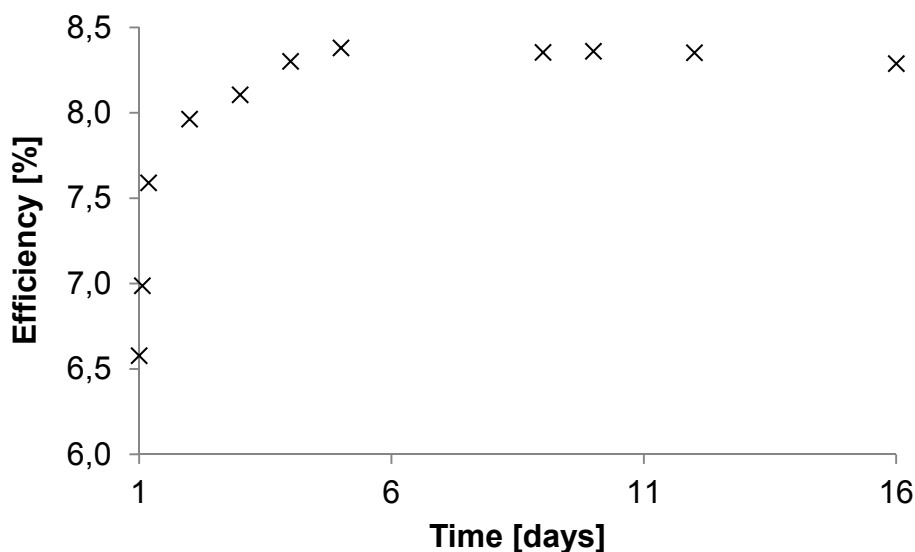


Figure 57 Efficiency over time of an optimized N719 reference cell (cell 1 Table 13). The second and third data points are measured 1.5 h and 4.5 h after the first one, respectively, on the day of assembly.

day	1	1+1.5h	1 +4.5 h	2	3	4	5	12	16
V_{oc} [mV]	700	708	716	737	755	771	777	780	784
J_{sc} [mA cm^{-2}]	15.59	15.41	16.68	16.78	17.07	16.98	17.29	17.52	17.50
ff [%]	60.3	64.1	63.5	64.4	62.9	63.4	62.3	61.1	60.4
η [%]	6.58	6.99	7.59	7.96	8.11	8.30	8.38	8.35	8.29

Table 14 Photovoltaic parameters of selected data points of Figure 57.

7.3.8 Conclusion of the Optimizations of Doctor-Bladed DSCs

In summary, the reference cell with dye N719 could be improved more than three-fold from 2.18% in partially sealed cells to 6.58% in completely sealed cells on the day of assembly. DSC performances were improved by reducing the thickness of the sealing foil to 25 μm , assembling a TiO_2 double layer and cleaning the FTO-coated glass plates by an UV- O_3 prior to doctor blading. The completely sealed DSCs show a significant increase over time (a so-called 'ripening effect') and reach a maximum efficiency of 8.38% on day 5 after assembly.

7.4 DSCs from Screen Printed TiO_2 Electrodes

Despite the successful optimization of the N719 reference cell, a main disadvantage of the doctor blading technique is with the reproducibility of the working electrode fabrication. The

thickness and uniformity of the TiO₂-layer strongly depends on the pressure applied while spreading the TiO₂-paste and is therefore highly dependent on the person producing the cell and the day it is produced. Furthermore, the thickness of a TiO₂ layer depends on the thickness of the scotch tape, which cannot be predetermined and whose consistency is unknown. Therefore a screen-printing method was applied which is the state-of-the-art technique for the production of TiO₂ electrodes for DSCs in research and industry and is described in Section 4.2.3. The main advantage of this method is its reproducibility and variability. By changing the TiO₂-paste, the mesh, and the printing cycles, the thickness as well as the particle and pore size can be adjusted for use with different dyes and electrolytes.

The optimized fabrication conditions developed for the completely sealed doctor bladed DSCs were also applied for the screen printed ones. Consequently, two aliquots of a 25 µL platinum precursor solution were used to prepare each counter electrode and the electrodes were assembled with a 25 µm thick sealing foil. Screen printing allows for a finer adjustment of the TiO₂ semiconductor thickness as each layer is approximately 2 µm. The optimized thickness for N719 sensitized solar cells was investigated by *Dr. Ewald Schönhofer* and was determined to be 7 screen printed layers of TiO₂.⁹³ Thereby, an approximate thickness of 12-14 µm is obtained, which is similar to the doctor bladed electrodes.

The efficiencies obtained with screen printed electrodes were similar to the optimized doctor bladed ones. However, the results are more reproducible and a higher quantity of electrodes can be fabricated. For the optimization of the N719 reference cell two more adjustments were investigated in this thesis. The first was the fabrication of DSCs under inert conditions in a glove box. The second was the application of a scattering layer to increase the absorption probability. These investigations are outlined in the next two sections.

7.4.1 Fabrication of DSCs under Inert Conditions

Impurities such as dust particles or water can lower the efficiency of a DSC by desorption or other undesirable reactions.^{33,99} For this reason a set of solar cells was prepared in a glove box. The electrodes were prepared as described previously but were transferred hot into the glove box after sintering. New dye solutions under inert conditions were prepared and the electrodes were sensitized and assembled in the glove box. After complete sealing the cells were measured under ambient conditions. Figure 58 and Table 15 compare *J/V* curves and the photovoltaic parameters of DSCs prepared in the glove box under inert conditions with DSCs prepared under ambient conditions. The DSC prepared under ambient conditions (cells 1 and 2) outperform the ones prepared under inert conditions (cells 3 and 4). The higher *J_{SC}* values in cells 3 and 4

indicate that either more dye has been adsorbed on the semiconductor under inert conditions or the adsorbed dye molecules were bound more strongly and hence inject electrons more efficiently. However, the cells prepared in the glove box lack high V_{OC} values and have lower ff . In summary, this leads to lower efficiencies of cells 3 and 4 with respect to cells 1 and 2 prepared under ambient conditions (Table 15). These results agree with an unpublished work of our group in collaboration with the group of *Dr. Thilo Glatzel*, in which the same trends were observed for DSCs sensitized with N719 and carotenoic acids, respectively, prepared under ambient and inert conditions.

The decrease in J_{SC} together with the increase in V_{OC} for the DSCs prepared under ambient conditions could indicate a dipole induced conduction band shift of the TiO_2 semiconductor. *Hao et al.* could show that in a set of three electrolytes with solvents of different dipole moments, V_{OC} linearly depends on the dipole moment of the solvent together with a contrary influence on the J_{SC} .¹⁰⁰ Similar effects were observed for electrolyte additives such as Li^{+101} and 4-*tert*-butylpyridine.¹⁰² Furthermore, *Redmond* and *Fitzmaurice* found that the flatband potential of polycrystalline TiO_2 is notably more positive for water and nonaqueous protic solvents with respect to nonaqueous aprotic solvents. This observation was explained with a proton adsorption-desorption equilibrium.¹⁰³ Although the TiO_2 electrodes were sensitized in a solution of N719 in ethanol for both inert and ambient conditions in our experiments, the significantly lower amount of water under inert conditions may lead to a similar conduction band shift. In addition, the low water content for the fabrication in the glove box may have an influence on the binding configuration of N719 as it was observed for other dyes. For instance, *Zhang et al.*¹⁰⁴ showed that the addition of a small amount of water to the electrolyte solution led to an improved efficiency in Eosin Y sensitized solar cells mainly by an improved V_{OC} . By spectroscopic and computational methods, they attributed the effect of the water to an improved binding of the dye to the TiO_2 surface through deprotonation of the carboxylic acid functionality and attachment of the dye through a bidentate binding mode. Moreover, *Tachibana et al.* compared N719 with its protonated analogue N3 and found that the protonation state the ruthenium dye has an important influence on the binding mode and hence the performance of the DSCs.¹⁰⁵

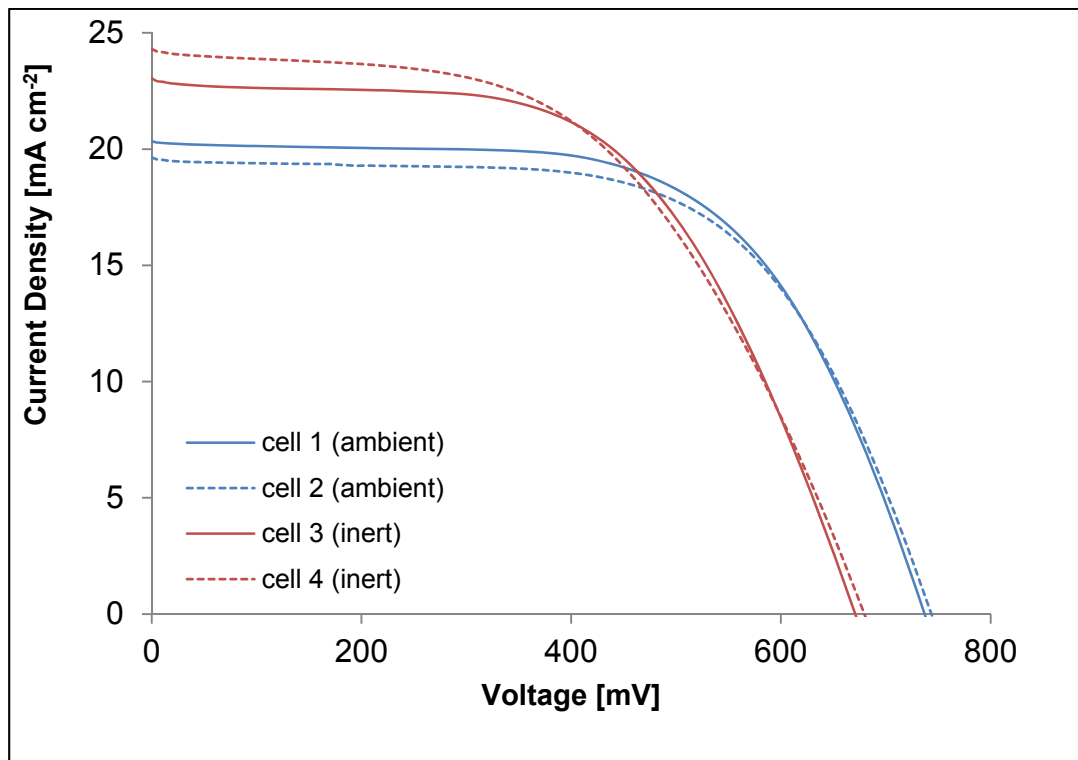


Figure 58 Comparison of DSCs prepared either under ambient (blue) or inert conditions (red).

	ambient		inert	
	cell 1	cell 2	cell 3	cell 4
V _{oc} [mV]	737	743	671	679
J _{sc} [mA cm ⁻²]	20.28	19.54	22.91	24.19
ff [%]	61.8	62.1	57.4	52.8
η [%]	9.24	9.02	8.83	8.67

Table 15 Photovoltaic Parameters of the DSCs shown in Figure 58.

7.4.2 Application of a Scattering Layer

A commonly used method to further improve the efficiency of DSCs is the use of a scattering layer. Like the normal semiconductor layer, the scattering layer consists of TiO₂ nanoparticles but of larger size, typically around 150-200 nm, and is applied on top of the normal TiO₂ layers. This allows backscattering of non-absorbed light and therefore increases the probability of light absorption if the cell is illuminated from the back (Figure 59). Figure 60 and

	no scattering layer		scattering layer	
	cell I	cell II	cell III	cell IV
V _{OC} [mV]	737	743	744	739
J _{SC} [mA cm ⁻²]	20.28	19.54	21.04	21.32
ff [%]	61.8	62.1	60.0	61.3

η [%]	9.24	9.02	9.39	9.66
------------	------	------	------	------

Table 16 compare DSCs with and without a scattering layer. As expected, the current density increases by addition of a scattering layer. The scattering layer is hardly colored when the electrode is soaked in the dye bath and leads to the assumption that the gain in current density arises mainly from the back scattering and not from an increased dye adsorption.

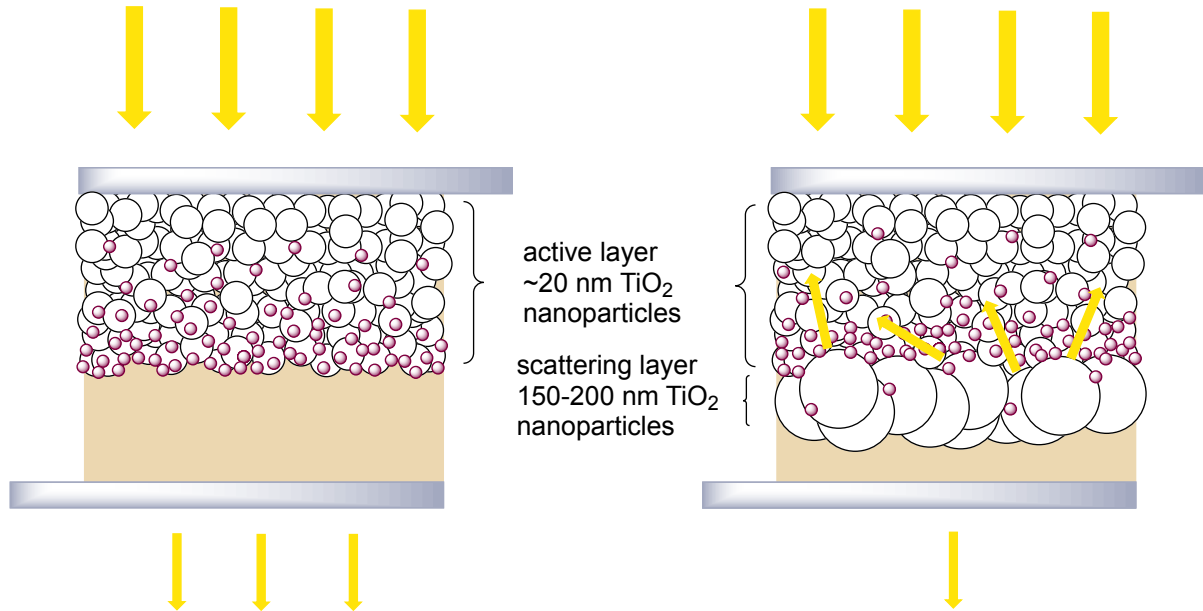


Figure 59 DSC without (left) and with (right) a scattering layer on top of the nanoporous active layer. Both the transparent active layer and the opaque scattering layer consist of TiO₂ nanoparticles with an average size of ~20 nm for the active and 150-200 nm for the scattering layer, respectively.

Figure 61 shows the efficiencies of four cells (two with and two without scattering latter) over time. As seen previously for doctor bladed cells, the screen printed DSCs improve over time as well. The maximum efficiency measured with these cells was 9.92% on day 8 for a DSC with a scattering layer and shows a relative increase in efficiency of 2.7% with respect to the day of assembly. Compared to the doctor bladed cells this improvement is only marginal. However, the doctor bladed DSCs already reach their maximum efficiency one day after assembly (i.e. on day 2), which is significantly faster than the doctor bladed cells (cf. Figure 57). The relative efficiencies between pairs of cells with and without a scattering layer do not change within a period of one week.

	no scattering layer		scattering layer	
	cell I	cell II	cell III	cell IV
Voc [mV]	737	743	744	739
Jsc [mA cm ⁻²]	20.28	19.54	21.04	21.32

ff [%]	61.8	62.1	60.0	61.3
η [%]	9.24	9.02	9.39	9.66

Table 16 Photovoltaic Parameters of the DSCs shown in Figure 60 on day of assembly.

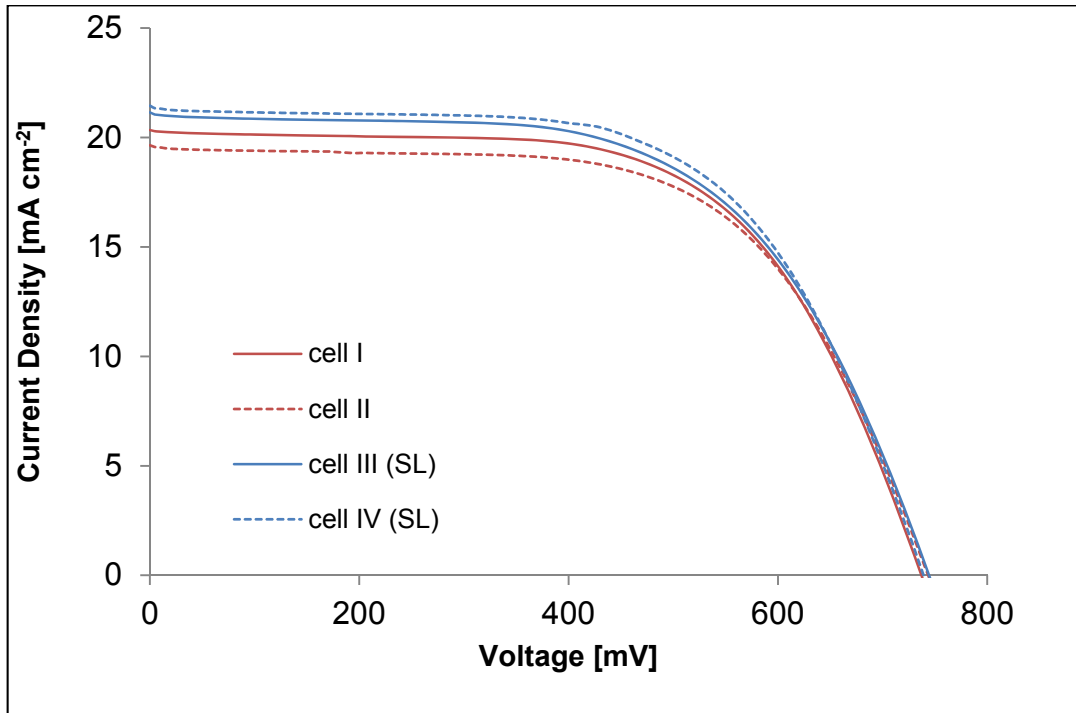


Figure 60 Comparison of J/V curves of DSCs with (blue lines) and without (red lines) scattering layer on day of assembly. The scattering layer only affects the current density with the other photovoltaic parameters being nearly unchanged.

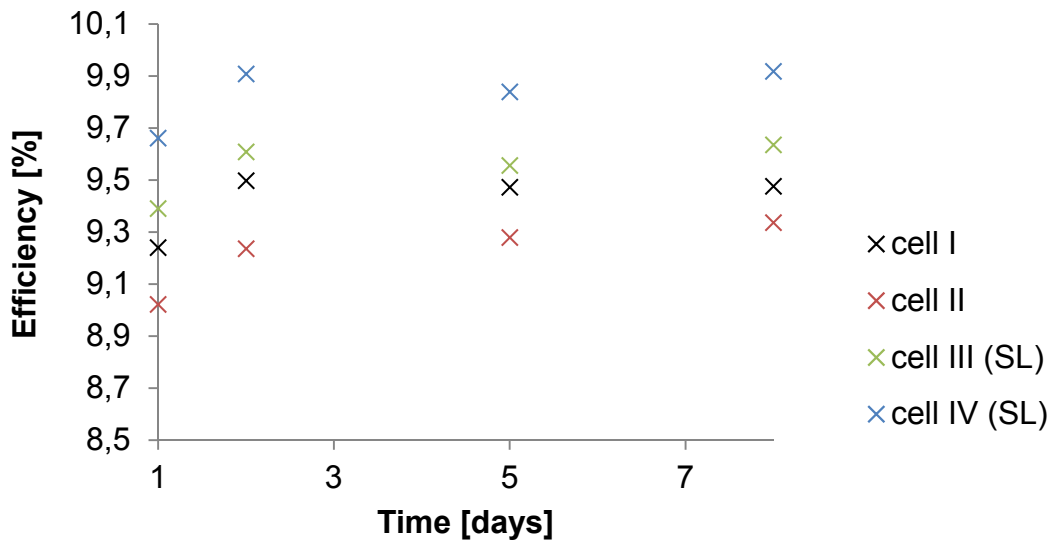


Figure 61 The efficiencies of the DSCs with and without scattering layer in Figure 59 versus time.

7.5 Masking of the DSCs

The last step in the development of a reproducible and consistent reference cell was masking of the DSCs to have a controlled measuring environment. As mentioned in earlier, DSCs are more efficient in converting diffuse light into electricity than silicon solar cells, which leads to an overestimation of the incident light through scattered and reflected light if the light source is calibrated with a silicon solar cell. *Snaith*⁷⁶ and *Schmidt-Mende*⁷⁷ have discussed the inconsistency of solar cell measurements due to unmasked cells in the literature.

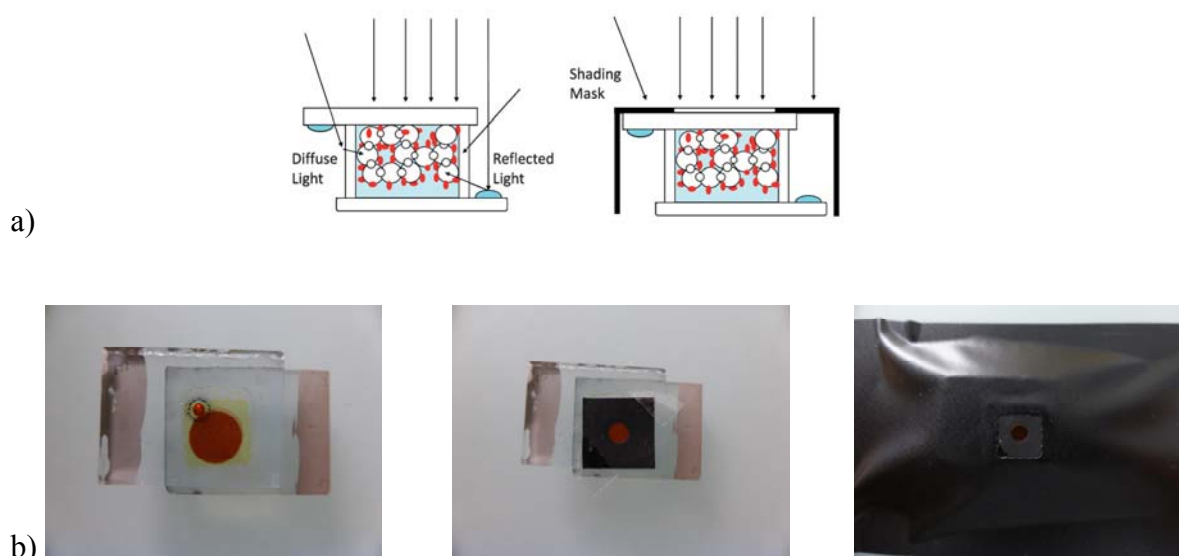


Figure 62 a) Reflected and scattered light leading to an overestimation of the incident light in an unmasked cell (left) and a masked cell (right). b) Copper sheet top mask with the aperture for a defined irradiated area (top) and fully masked cell (bottom).

In a first attempt, the scattered light from the sun simulator was decreased by equipping the inside of the sun simulator with a non-reflective black layer to overcome the overestimation of the incident light obtained. As a result, the scattered light could be reduced dramatically but this led to an intensity of the incident light below 1.0 sun. Therefore we decided to mask the solar cells to suppress diffuse light right on the DSCs. For this, the cells were completely masked, meaning the top and the edges of the cell were covered with a shading mask (Figure 62b). This blocks light from being reflected and scattered on the TiO₂ and glass surface and on the edges of the glass electrodes (Figure 62a). The illuminated area was defined with a defined circular aperture. *Ito et al.*⁷⁹ suggested using masks with an aperture slightly bigger than the active area. However, as *Yang et al.*⁸⁰ have already pointed out, this again could lead to an

overestimation of the incident light as the exact scattering on the edge of the surface area is unknown. An aperture with the same size as the active area is difficult to produce as the edges of the TiO₂ are not perfectly well-defined due to the nanoporous nature of the material. Therefore the aperture should ideally be smaller than the active area.^{78,80} Three different aperture sizes were prepared by punching a hole into a black piece of tape with diameters of 3, 4, and 5 mm. This leads to aperture sizes of 7.1, 12.6 and 19.6 mm². These masks were taped onto the working electrode with the aperture centred on the active area of the cell and the glass edges covered. A comparison of the efficiencies reached with the three aperture sizes is shown in Figure 63. The results are compared to unmasked cells for which the active area of 28.8 mm² was used to calculate the efficiencies. The four cells described in Figure 60 and Table 16 were measured again masked. All cells are 20-40% lower in efficiency after the mask has been applied; however the DSCs with the scattering layer were less affected than those without. Table 17 lists the photovoltaic parameters of the cells and illustrates that the loss in efficiency mainly arises from a drop in current density. The V_{OC} is only slightly reduced (<10%) and the ff is improved. This might be expected, as the resistance of the cell should be lowered with decreased current densities. From the three different masks the one with the smallest aperture, 7.1 mm², showed the highest efficiencies for all cells.

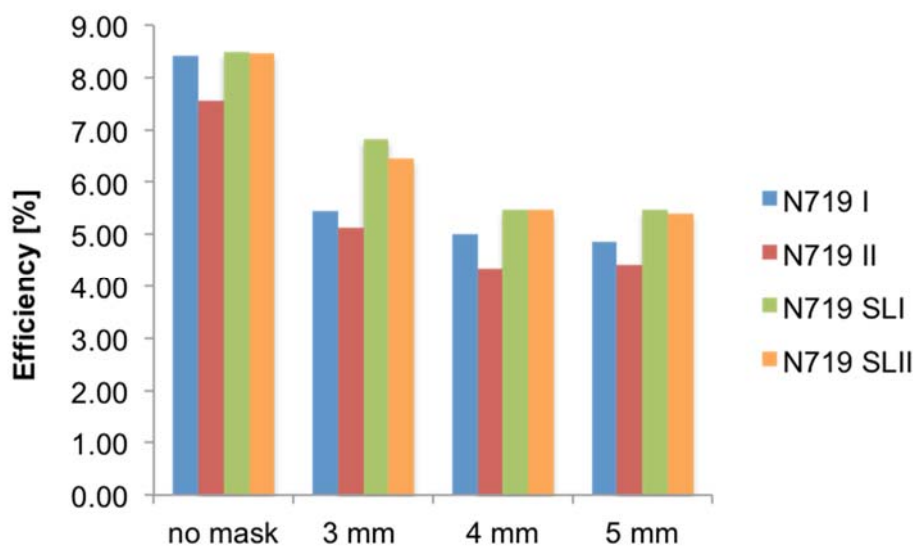


Figure 63 Comparison of the efficiencies of unmasked and masked DSCs. Round masks with three different diameters of 3, 4 and 5 mm were tested with the active TiO₂ area of the solar cell having a diameter of 6 mm.

For further measurements we used 1 cm² copper sheets of 0.1 mm thickness with a circular aperture to define the exact irradiated area. The copper sheets were coated with a black finish

to suppress backscattering of light within the cell on the inside of the copper sheet (Figure 62 b). The aperture size was measured by scanning and analyzing the aperture by *Dr. Ewald Schönhofer*⁹³ using the program *imageJ*¹⁰⁶ and was determined to have an average area of 6.012 mm² with a standard deviation of 1%.

Device	Size [mm²]	J_{sc} [mA cm⁻²]	V_{oc} [mV]	ff [%]	η [%]
cell I	28.8	16.99	758	65	8.41
	7.1	10.91	675	74	5.46
	12.6	9.95	690	73	5.01
	19.6	9.52	710	72	4.85
cell II	28.8	15.17	735	68	7.55
	7.1	10.17	662	76	5.13
	12.6	8.38	679	76	4.35
	19.6	8.62	695	74	4.42
cell III (+SL)	28.8	17.48	763	64	8.48
	7.1	13.43	689	74	6.82
	12.6	10.70	704	73	5.47
	19.6	10.72	724	70	5.46
cell IV (+SL)	28.8	17.11	765	65	8.47
	7.1	12.38	692	75	6.46
	12.6	10.37	707	74	5.46
	19.6	10.61	714	71	5.40

Table 17 Photovoltaic parameters for cells I-IV (see Figure 60) without mask and with masks with three different apertures.

7.6 Conclusions

In summary, the N719 reference cell could be improved from 2.18% in a partially sealed doctor bladed cell to 9.66% in a fully optimized, completely sealed, screen printed DSC. Due to the ripening effect in completely sealed DSCs this efficiency even improved to 9.92% on day 8. By complete masking of DSCs to overcome overestimation of the incident light, the efficiencies are reduced relatively by 20-40%.

As a short summary, the achievements of the overall optimization processes are listed.

- Completely sealed DSCs are superior to partially sealed DSCs. Furthermore, the complete sealing allows for measurements over time which allows the DSCs to experience a ripening effect.
- Seven layers of screen printed TiO₂ layers lead to more efficient DSCs compared to doctor bladed DSCs with a comparable TiO₂ layer thickness of 12-15 μm. Additionally, screen printed electrodes are more uniform than doctor bladed electrodes and more reproducible cells can be produced.
- The use of 25 μm thick sealing foils in completely sealed DSCs improved the global solar cell efficiency compared to the application of 60 and 100 μm thick sealing foils.
- UV-O₃ cleaning of the FTO-coated glass prior to screen printing of the TiO₂ layers improved the solar cell's efficiency.
- DSCs filled with Standard II electrolyte (0.1 M LiI, 0.05 M I₂, 0.5 M MBI and 0.6 M BMII in 3-methoxypropionitrile) outperformed DSCs that were filled with Standard I electrolyte (0.5 M LiI, 0.05 M I₂ and 0.5 M MBI in 3-methoxypropionitrile).
- 4-wire measurements lead to an increase in ff and hence the efficiency compared to 2-wire measurements.

8 Anchoring Ligands

Unlike the ruthenium dye N719 which contains a carboxylic acid and carboxylate anchor, the *homoleptic* copper(I) complexes discussed in section 5.4 have no suitable functional groups to bind to the TiO₂ surface. However, due to their lability towards ligand exchange,⁴⁷ they offer a convenient and simple *in situ* synthesis of *heteroleptic* copper(I) complexes through ligand exchange with TiO₂-bound anchoring ligands. This method has been published by our group and has been successfully tested for different copper(I) dyes.⁴³⁻⁴⁶ This quasi solid-phase synthesis (better described as an 'on-surface' approach) enables the straightforward synthesis of *heteroleptic* copper(I) complexes bound to TiO₂ that would be very challenging to synthesize by solution chemistry as the exchange of ligands and equilibration of products leads to a statistical mixture of the *heteroleptic* and *homoleptic* complexes. Consequently, this method profits from all the advantages of the on-surface synthesis such as high yields by using of an excess of the *homoleptic* copper(I) complex and easy workup by washing off the unreacted copper(I) complexes. Furthermore this method allows for a wide screening of different anchoring ligands and is thereby a fast method for the synthesis of *heteroleptic* copper(I) dyes. The reactions occur almost instantaneously at room temperature, observable by a color change from colorless or pale yellow to orange-red. The highest efficiencies in DSCs were obtained after soaking the working electrodes in the dye solution for three days.

However, as a consequence of the *in situ* synthesis of the *heteroleptic* complexes, they can only be analyzed on the TiO₂ surface. This reduces the number of techniques that can be used to study these complexes. Usually quantification of the amount of adsorbed dye is done by desorption of the dye by mild acid or base treatment and determination of the concentration by UV-Vis spectroscopy. However, the lability of the *heteroleptic* copper(I) complexes does not allow this method to be used since once released from the surface, the dyes will equilibrate to a mixture of *homoleptic* and *heteroleptic* species. Ultimately, for the DSC development, the dye on the semiconductor and its performance in a working DSC is important.

In this chapter the results obtained with copper(I) sensitized solar cells is outlined. As described earlier (see Chapter 7) the fabrication process of the DSCs was changed and improved over the period of this doctoral research. Therefore it is meaningless to compare early cells with ones using more developed procedures later in the thesis. Furthermore, as mentioned earlier, DSCs from doctor bladed TiO₂ electrodes are less reproducible than screen printed or commercial (also screen-printed) ones. However, the comparisons to an N719 reference cell and differences between Cu(I) cells should not be affected strongly by this. Therefore, the data are still valid

and significant trends can be seen. In this chapter the screening of different anchoring ligands is outlined using DSCs containing doctor-bladed TiO₂ electrodes.

The stepwise *in situ* synthesis of the *heteroleptic* copper(I) complexes allows for a fast screening of anchoring ligands. In Section 5.2 all anchoring ligands tested in this thesis are described. All anchoring ligands are based on 6,6'-dimethyl-2,2'-bipyridines and consist of either carboxylic or phosphonic acid anchoring groups (Figure 64). **ALC1**, **ALP1** and **ALP1 TBA** have an additional phenyl spacer to increase the distance from the donating ligand to the acid anchors as the accepting groups. Increasing distance of the charge separation has been shown to be beneficial for the performance of DSCs.¹⁰⁷ Labeling of the anchoring ligands follows a logical concept with **AL** standing for anchoring ligand, **P** for phosphonic acid, **C** for carboxylic acid, and **1** for one phenyl spacer. **ALP1 TBA** stands for the tetrakis(tetra-*n*-butyl)ammonium salt of the respective acid **ALP1**.

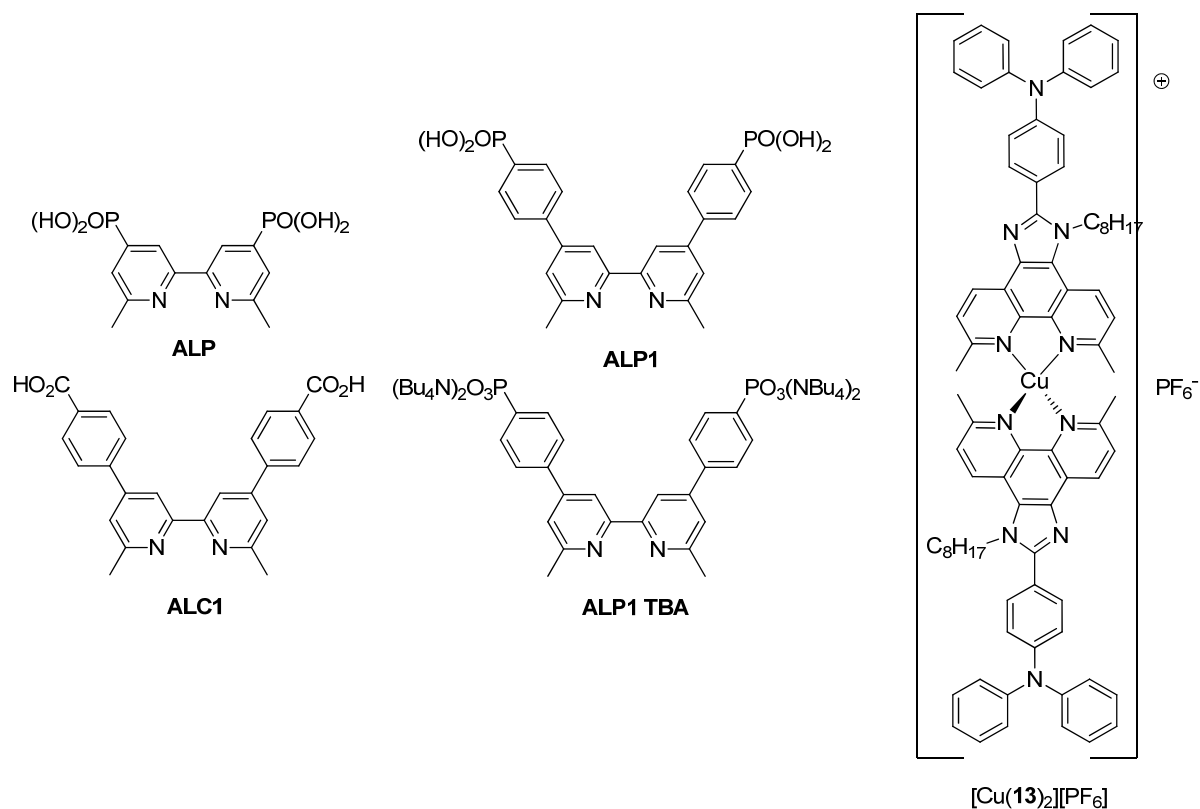


Figure 64 Anchoring Ligands **ALP**, **ALP1**, **ALP1 TBA** and **ALC1** used in this section together with **[Cu(13)₂][PF₆]**.

For the experiments in this section, the *homoleptic* complex **[Cu(13)₂][PF₆]** (Figure 64) was used as a representative dye to form *heteroleptic* Cu(I) complexes of the type **[Cu(13)(AL)]⁺** on the TiO₂ surface by ligand exchange with TiO₂-bound anchoring ligands. For this, the TiO₂

electrodes were first functionalized by dipping into a solution of the respective anchoring ligand for 24 h. After cleaning, the electrodes were dipped into a solution of the *homoleptic* dye to obtain *heteroleptic* Cu(I) sensitized electrodes (Figure 65).

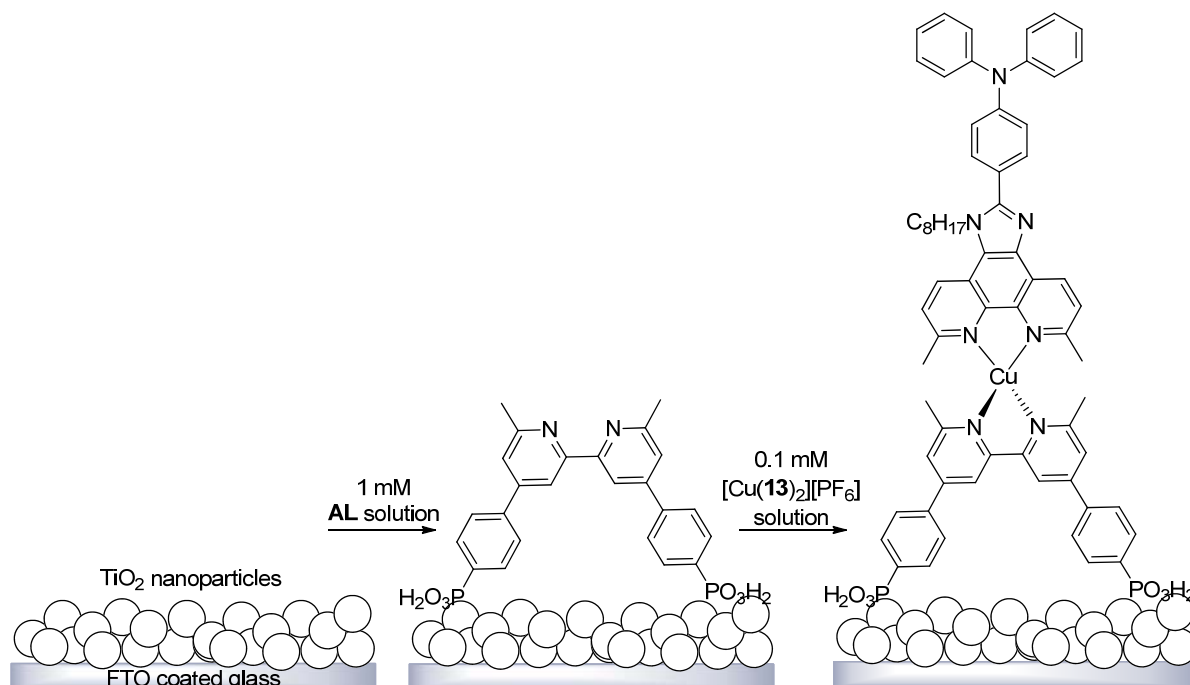


Figure 65 On-surface synthesis of a *heteroleptic* Cu(I) complex using the example of ALP1 and $[\text{Cu}(\mathbf{13})_2][\text{PF}_6]$.

For the experiments, a 1 mM solution of the anchoring ligands was prepared. Due to their poor solubility, all anchoring ligands except for **ALP1 TBA** were dissolved in DMSO. **ALP1 TBA** was synthesized to improve the solubility and to investigate the anchoring properties of the **TBA** salt analogue of **ALP1**. **ALP1 TBA** is soluble in polar organic solvents such as ethanol, which is also used for the N719 dye solutions. Consequently, a 1 mM solution of **ALP1 TBA** was prepared in ethanol.

As mentioned above, for these experiments DSCs with doctor bladed TiO_2 electrodes were used. The N719 reference cells had an efficiency of 6.25% and 6.57% on day 1, respectively, and 8.38% and 9.17%, on day 5, respectively. As for the N719 cells (see Chapter 7), the Cu(I) sensitized ones show an improvement in efficiency over time. This ripening effect is shown in Figure 66 by plotting the efficiency of DSCs versus time after sealing the cells. For each anchoring ligand, 2, 4 or 5 duplicate cells were prepared to confirm reproducibility of the measurements. It is evident that the maximum efficiencies are reached within a week, with the main improvements occurring within the first few days after cell assembly. The ripening effect

is more distinctive for the phosphonate anchoring groups than for the carboxylate. The phosphonate anchors show an increase of roughly 100%, which is also significantly more than for the N719 reference cells (compare Figure 57 with Figure 66).

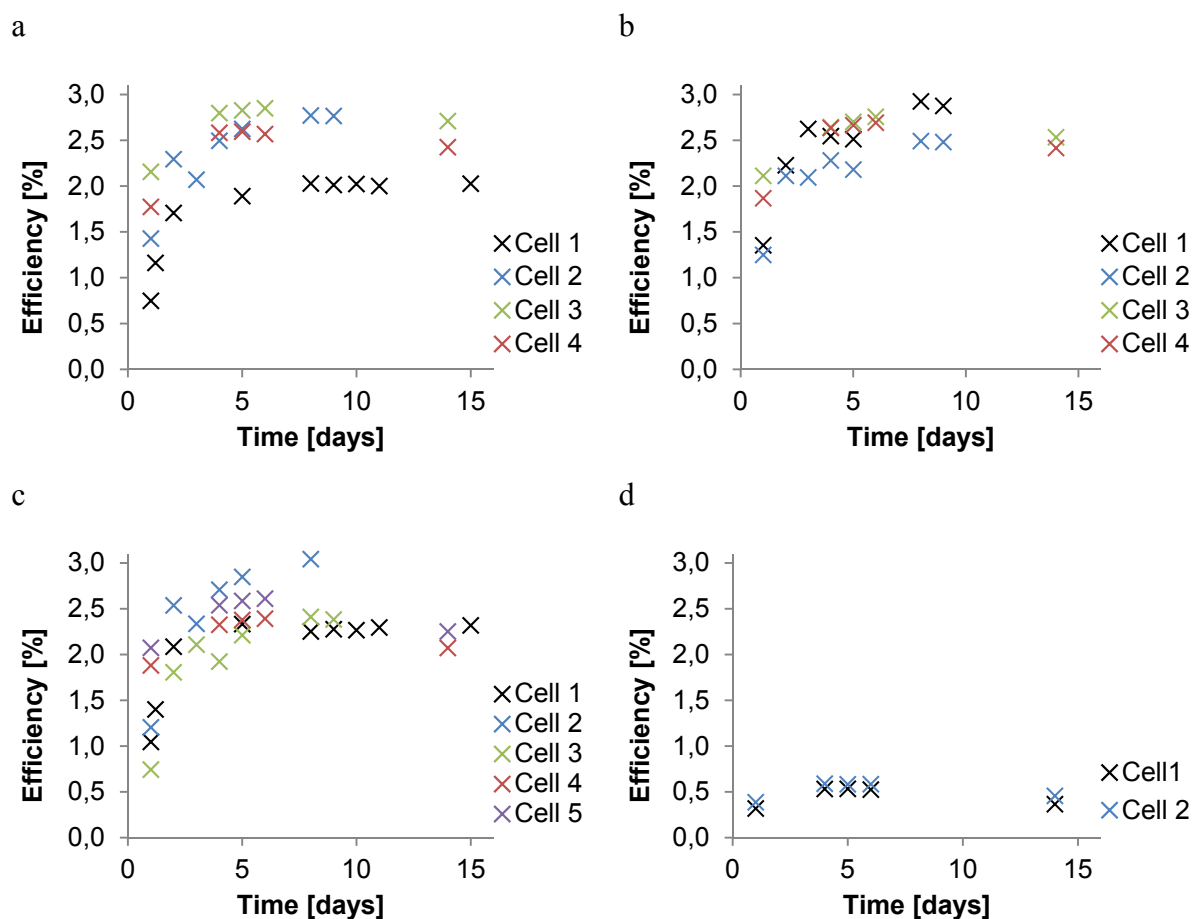


Figure 66 Different sets of DSCs with the respective anchoring ligands and the efficiencies plotted versus time. DSCs are sensitized with $[\text{Cu}(\mathbf{13})(\text{AL})]^+$ with AL= ALP in a, ALP1 in b, ALP1 TBA in c and ALC1 in d.

Table 18 shows the photovoltaic parameters and the J/V curves of $[\text{Cu}(\mathbf{13})(\text{AL})]$ sensitized solar cells with AL = ALP, ALP1, ALP1 TBA and ALC1. The results are shown both on the day of assembly and on day 5 to illustrate the ripening effect. As all the DSCs reach a plateau in efficiency after about 5-8 days, it is sensible to discuss the influence of the anchoring ligand based on the results on day 5 in Table 18. It is obvious that the anchoring group itself has a tremendous impact on the overall performance of the DSCs. ALP, ALP1 and ALP1 TBA clearly outperform the DSCs prepared with ALC1. The use of phosphonic acid anchors or their respective salts seems to be strongly beneficial for the overall solar-to-electrical energy conversion of copper bis-diimine sensitized solar cells. The phosphonic acid-based anchoring groups lead to both higher J_{sc} and higher V_{oc} values but have similar ff values as the carboxylic

acid anchor **ALC1**. In the literature, this trend is also described for both *homoleptic*⁴² and *heteroleptic*^{46,92} Cu(I) complexes using 2,2'-bipyridine-based ancillary ligands. Furthermore, Grätzel¹⁰⁸ found that the adhesion of a ruthenium complex with a phosphonate anchor is superior to that of a carboxylate anchor and the stability towards desorption is higher due to a stronger binding to the TiO₂. Ambrosio *et al.*¹⁰⁹ showed in a computational study that phosphonic acid anchors should exhibit an intrinsically better charge injection and stronger binding to TiO₂ than the commonly used carboxylic acid anchoring group.

In contrast to Cu(I)bpy-dyes reported by our group⁴⁵, the data in Table 18 show no apparent influence on the performance by insertion of a phenyl spacer into the anchoring ligand on going from **ALP** to **ALP1** on day 5. However, Figure 66 shows that a higher efficiency is achieved more quickly after sealing the cells for **ALP1** versus **ALP**. The average and maximum efficiencies are very similar to each other and the same is true for J_{sc} , V_{oc} and ff .

Again, comparison of **ALP1** and **ALP1 TBA** shows that the parameters are very similar. However, **ALP1 TBA** shows slightly higher V_{oc} values and somewhat lower J_{sc} values. Indeed, the overall performances are the same within the error of the measurements.

In Figure 67 the J/V curves of the best performing DSCs on day 5 for each anchoring ligand are shown to visualize the results and trends. The best performing DSC in the measured time period for every anchoring group is listed in Table 19. Again **ALP**, **ALP1** and **ALP1 TBA** have very close maximum efficiencies and differ only in the day the maximum was reached. All DSCs with phosphonate anchors clearly outperform the DSC using a carboxylic acid anchor, reaching about 5 times the efficiency of **ALC1**.

Anchoring Ligand	Day	Cell	J _{sc} [mAcm ⁻²]	V _{oc} [mV]	ff [%]	η [%]
ALP	1	1	1.58	725	66	0.75
		2	3.18	730	60	1.43
		3	4.99	658	66	2.16
		4	4.82	648	57	1.77
	5	1	4.04	673	70	1.89
		2	6.40	658	62	2.63
		3	6.19	674	68	2.83
		4	5.65	669	69	2.60
ALP1	1	1	3.52	730	53	1.36
		2	2.80	730	61	1.25
		3	4.96	651	65	2.11
		4	4.30	655	66	1.87
	5	1	6.61	650	58	2.51
		2	5.65	649	60	2.18
		3	5.77	666	70	2.70
		4	5.89	651	69	2.67
ALP1 TBA	1	1	2.07	708	71	1.05
		2	2.55	730	65	1.21
		3	1.49	700	71	0.74
		4	4.19	659	68	1.88
		5	4.61	658	68	2.07
	5	1	4.76	691	71	2.33
		2	6.69	672	63	2.85
		3	5.06	674	65	2.21
		4	5.17	662	69	2.38
		5	5.53	659	71	2.59
ALC1	1	1	1.00	508	63	0.32
		2	1.16	522	64	0.39
	5	1	1.47	535	68	0.53
		2	1.61	534	68	0.58

Table 18 Photovoltaic parameters of [Cu(13)(AL)] sensitized solar cells on the day of assembly and day 5, with AL= ALP, ALP1, ALP1 TBA and ALC1, respectively. 2, 4 or 5 duplicate DSCs were fabricated for each anchoring ligand for reproducibility.

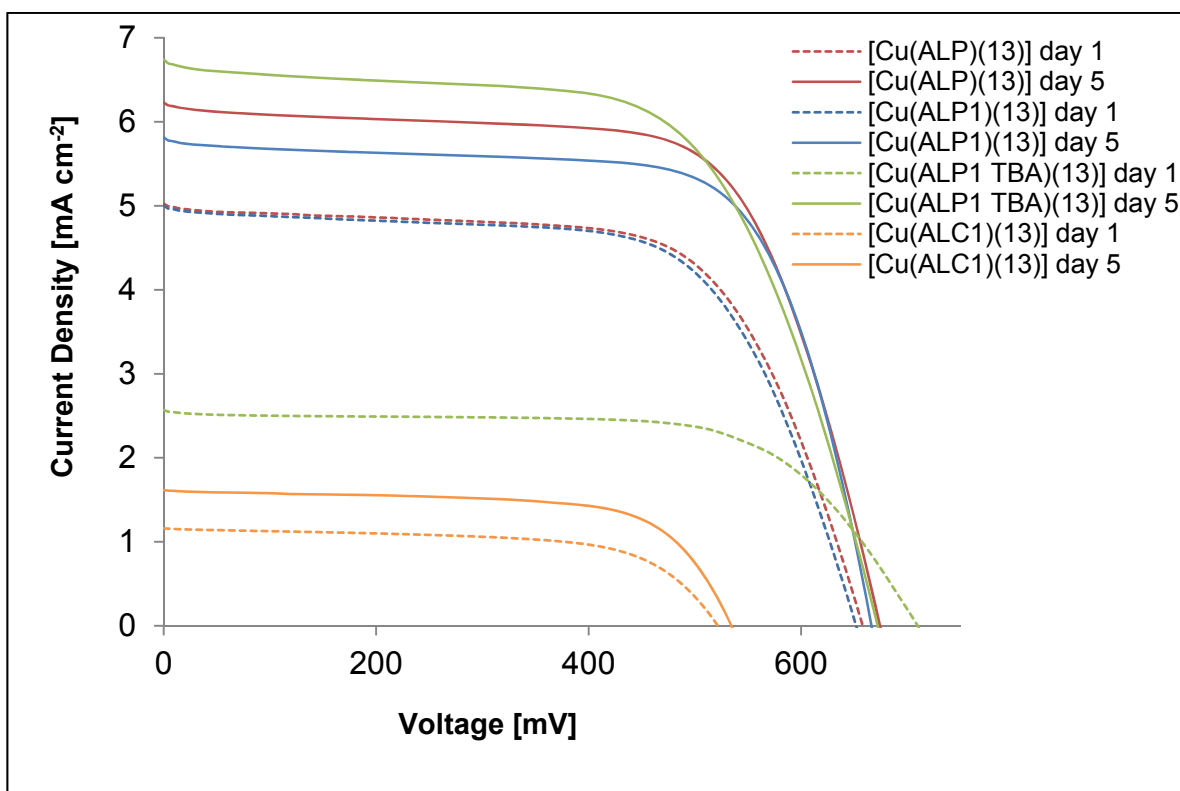


Figure 67 J/V curves of the *heteroleptic* complexes [Cu(ALP)(13)], [Cu(ALP1)(13)], [Cu(ALP1 TBA)(13)] and [Cu(ALC1)(13)] on days 1 and 5, respectively.

Anchoring Ligand	Cell	Day	J_{sc} [mAcm ⁻²]	V_{oc} [mV]	ff [%]	η [%]
ALP	3	6	6.26	670	68	2.85
ALP1	1	8	6.74	648	67	2.93
ALP1 TBA	2	9	6.75	679	68	3.10
ALC1	2	6	1.65	520	68	0.59

Table 19 Maximum efficiencies for [Cu(13)(AL)] sensitized solar cells using anchoring ligands ALP, ALP1, ALP1 TBA and ALC1.

9 Phenanthroline Based Copper Dyes

In this chapter, the DSC performances of the *heteroleptic* Cu(I) dyes (shown in Figure 68) are discussed. The first section compares the performances of the different Cu(I) dyes in DSCs and outlines the influence of 5,6-substitution versus 4,7-substitution in the phenanthroline ancillary ligands. Furthermore the different behaviours of carbazole and diarylamine donors are illustrated. In the second section of this chapter, the necessity of methyl substituents in the 2- and 9-positions of the phenanthroline ancillary ligand together with an alternative assembly of the *heteroleptic* Cu(I) dyes on the TiO₂ surface are presented.

9.1 Investigation of Different 2,9-Dimethylphenanthroline Ancillary Ligands

The complexes in this section were synthesized by the *on-surface* synthesis described in Chapter 8 and shown in Scheme 1 from *homoleptic* Cu(I) complexes (see Section 5.4). For the ease of comparison, only one anchoring ligand was used in these experiments. As anchoring ligand **ALP1** turned out to be beneficial for Cu(I) dyes incorporating 6,6'-dimethyl-2,2'-bipyridine ancillary ligands⁴⁵ and because the performance in [Cu(**13**)(**AL**)]⁺ sensitized DSCs was shown to be similar for **ALP**, **ALP1** and **ALP1 TBA** (Chapter 8), **ALP1** was chosen for these experiments. Furthermore, this allows for comparison with previously reported dyes of our group.

Solid state UV-Vis absorption spectra of the *heteroleptic* Cu(I) dyes on the TiO₂ surface were measured. Commercial transparent TiO₂ electrodes were prepared in a similar fashion to the TiO₂ working electrodes for DSCs, by soaking in an **ALP1** solution in DMSO for 24 hours followed by soaking in a solution of the *homoleptic* complex [Cu(L_{ancillary})₂][PF₆] for 72 hours. Thereby, a TiO₂ electrode is prepared that is analogous to the working electrode in DSCs but without a scattering layer. Figure 69 shows the solid state UV-Vis absorption spectra of the adsorbed dyes [Cu(**6**)(**ALP1**)]⁺, [Cu(**13**)(**ALP1**)]⁺, [Cu(**15**)(**ALP1**)]⁺, [Cu(**17**)(**ALP1**)]⁺ and [Cu(**28**)(**ALP1**)]⁺, and N719 for comparison. The spectra are cut off at 370 nm as the TiO₂ electrode absorbs up to this wavelength and the measured absorbance below 370 nm would interfere with that of the adsorbed dye. It is important to mention that the spectra are plotted as absorbance (and not extinction coefficient ϵ) versus wavelength because the absolute amount of adsorbed dye is unknown. Therefore, these spectra can only show how strongly a sensitized TiO₂ electrode absorbs but do not distinguish between a stronger absorption of the dye and a higher amount of adsorbed dye molecules. Provided that the dye molecules do not aggregate,

the origin for the increase in absorption of an electrode is not relevant for the performance in a DSC as, generally, a higher absorption will lead to a better performance. However, for the improvement of the DSCs this would be valuable information. Unfortunately, due to the fact that *heteroleptic* Cu(I) complexes rapidly equilibrate in solution with the two respective *homoleptic* complexes, the amount of dye could not be determined by desorption in mild base and determination by solution UV-Vis absorption spectroscopy as it is commonly described in the literature.¹¹⁰

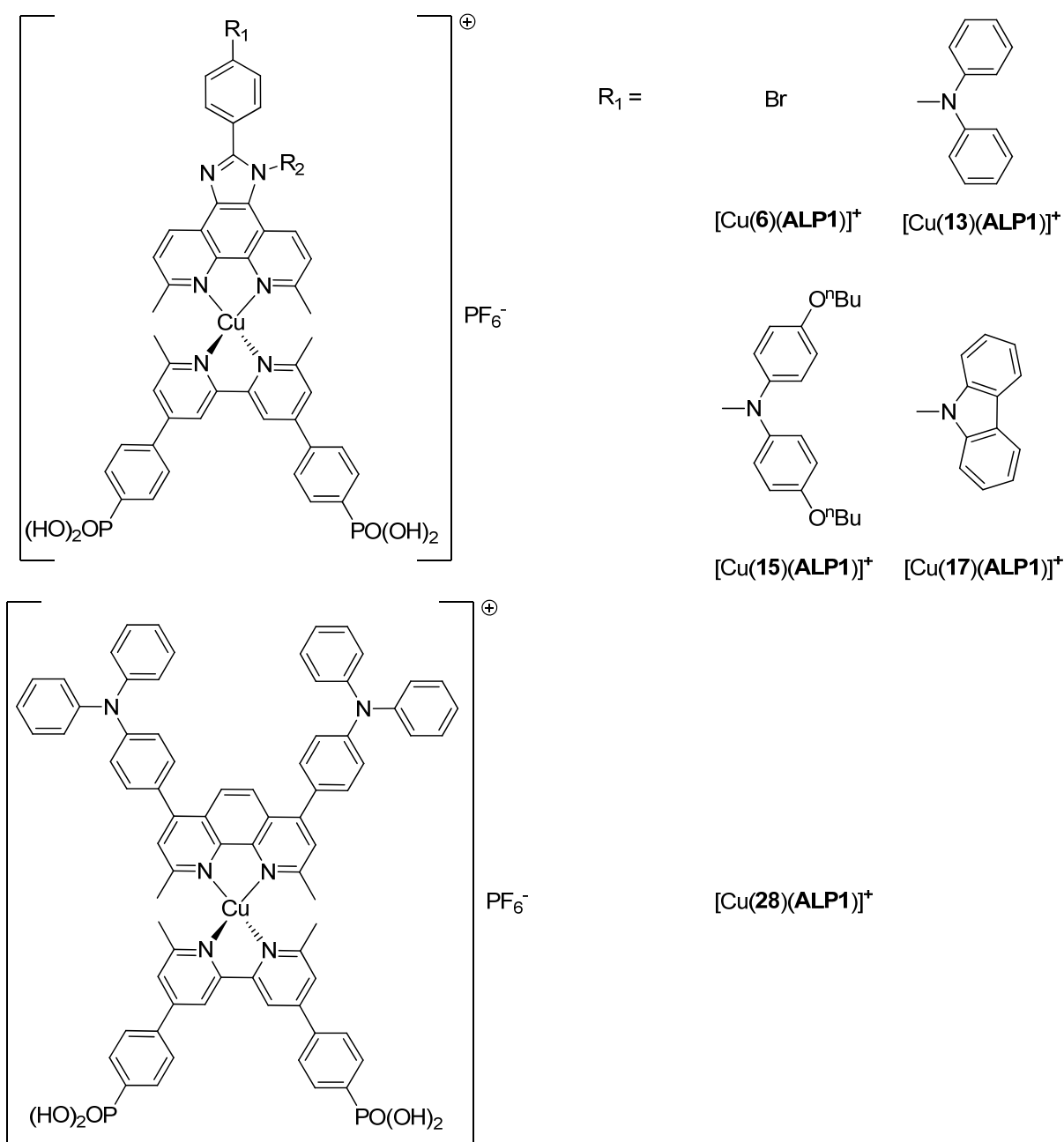


Figure 68 On-surface synthesized *heteroleptic* complexes whose performances in DSCs were tested.

From Figure 69, it can be concluded that, between 370 nm and 499 nm, the $[\text{Cu}(\mathbf{28})(\text{ALP1})]^+$ sensitized electrode shows the strongest absorption. In ligand **28**, substitution in the 4- and 7-positions of the *phen* unit allows the introduction of two donating groups. With both being diaryl units, the π -system is extended and leads to the superior absorption. The absorption of the other dyes between wavelengths of 370-499 nm generally decreases in the order of N719 > $[\text{Cu}(\mathbf{17})(\text{ALP1})]^+ \approx [\text{Cu}(\mathbf{13})(\text{ALP1})]^+ > [\text{Cu}(\mathbf{6})(\text{ALP1})]^+ > [\text{Cu}(\mathbf{15})(\text{ALP1})]^+$. Above 499 nm, the N719 sensitized electrode shows a much more intense absorption than $[\text{Cu}(\mathbf{28})(\text{ALP1})]^+$ followed by the other copper complexes in the same order as before. The electrodes sensitized with N719, $[\text{Cu}(\mathbf{6})(\text{ALP1})]^+$, $[\text{Cu}(\mathbf{13})(\text{ALP1})]^+$ and $[\text{Cu}(\mathbf{17})(\text{ALP1})]^+$ have MLCT maxima at 537 nm, 460 nm, 460 nm and 461 nm, respectively. $[\text{Cu}(\mathbf{15})(\text{ALP1})]^+$ and $[\text{Cu}(\mathbf{28})(\text{ALP1})]^+$ show shoulders at ≈ 470 nm and ≈ 480 nm, respectively. By eye, a red shift is visible going from $[\text{Cu}(\mathbf{15})(\text{ALP1})]^+$ to $[\text{Cu}(\mathbf{17})(\text{ALP1})]^+$ and finally to $[\text{Cu}(\mathbf{28})(\text{ALP1})]^+$ (Figure 70) while $[\text{Cu}(\mathbf{6})(\text{ALP1})]^+$, $[\text{Cu}(\mathbf{13})(\text{ALP1})]^+$ and $[\text{Cu}(\mathbf{15})(\text{ALP1})]^+$ are difficult to distinguish. However, for a maximum performance in a solar cell, the dyes should preferably absorb further into the red part of the solar spectrum as the intensity of the sunlight is significantly higher in this region (see Figure 8).

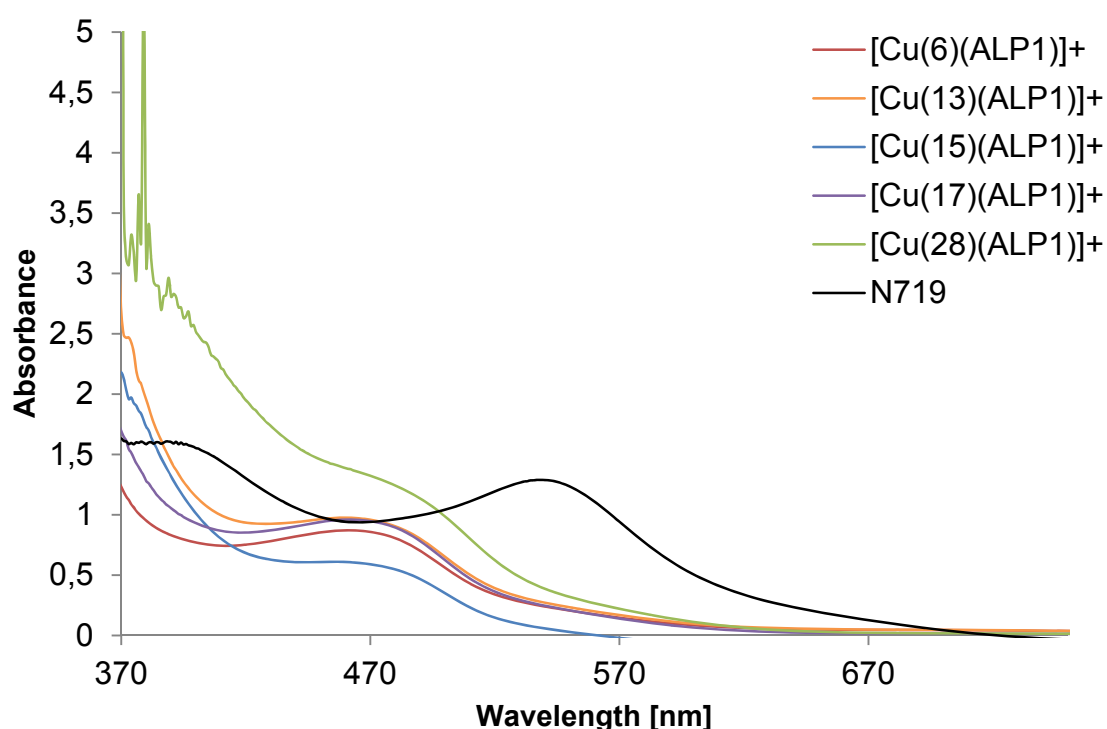


Figure 69 Solid state UV-Vis absorption spectra of the *heteroleptic* dyes $[\text{Cu}(\mathbf{6})(\text{ALP1})]^+$ (red), $[\text{Cu}(\mathbf{13})(\text{ALP1})]^+$ (orange), $[\text{Cu}(\mathbf{15})(\text{ALP1})]^+$ (blue), $[\text{Cu}(\mathbf{17})(\text{ALP1})]^+$ (purple) and $[\text{Cu}(\mathbf{28})(\text{ALP1})]^+$ (green) adsorbed on TiO_2 electrodes.

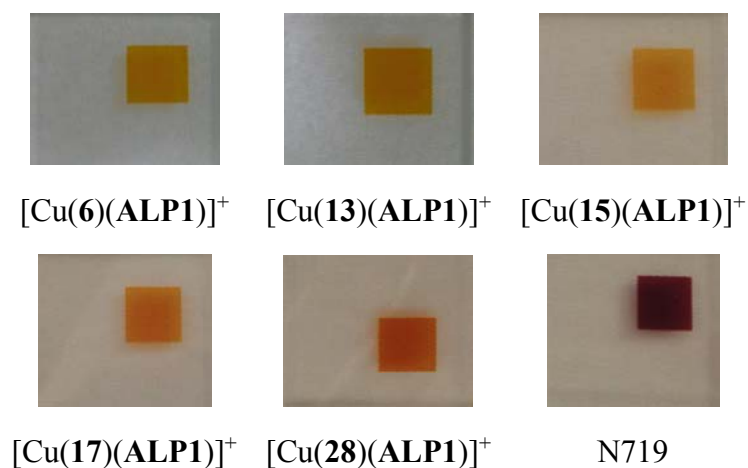


Figure 70 Photographs of the *heteroleptic* Cu(I) complexes on a TiO₂ surface and the ruthenium dye N719 for comparison.

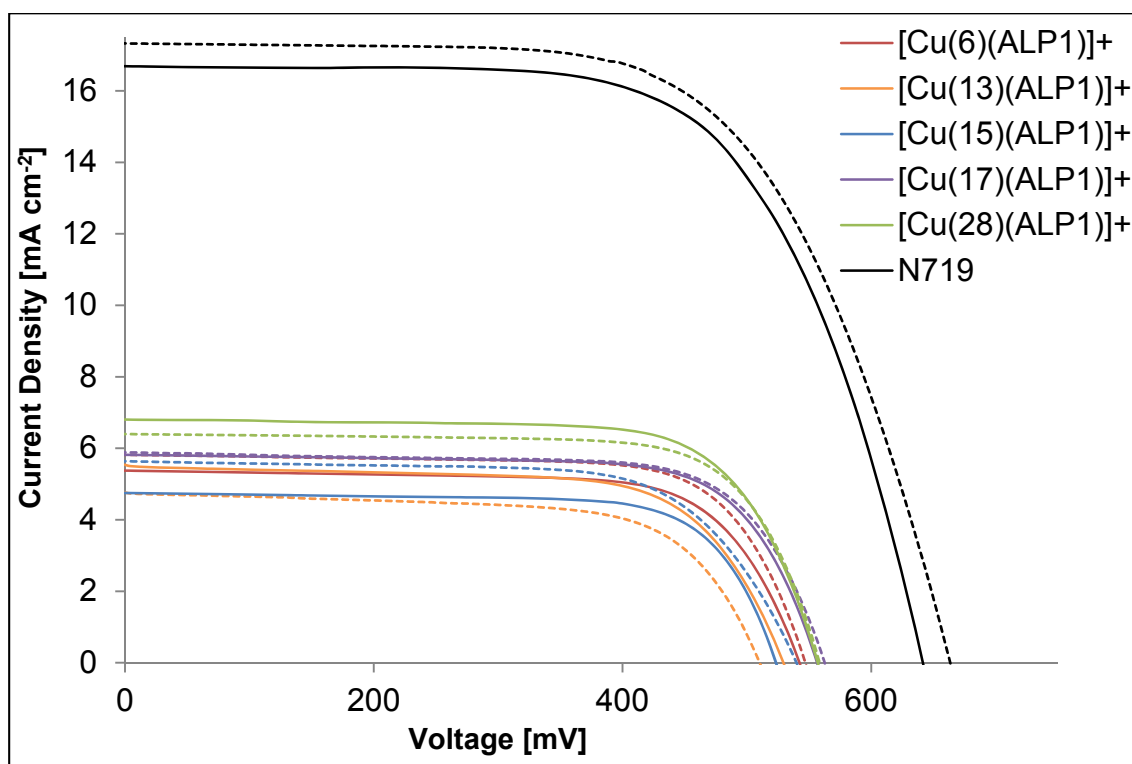


Figure 71 Photocurrent density/voltage (J/V) characteristics of duplicate DSCs sensitized with the *heteroleptic* Cu(I) complexes shown in Figure 68 on the day of assembly.

Table 20 gives the photovoltaic parameters of duplicate DSCs containing [Cu(6)(ALP1)]⁺, [Cu(13)(ALP1)]⁺, [Cu(15)(ALP1)]⁺, [Cu(17)(ALP1)]⁺ and [Cu(28)(ALP1)]⁺ on the day of assembly (day 1) and day 4 and the J/V curves recorded on day 1 are shown in Figure 71. DSCs sensitized with [Cu(28)(ALP1)]⁺, which is the only 4,7-substituted phenanthroline dye, clearly outperform the other solar cells. The main factor for this superior performance is the higher J_{sc} values with respect to the other copper sensitized DSCs. This is consistent with the higher

absorption shown in Figure 69 and the higher external quantum efficiencies (EQE) plotted in Figure 72. The EQE (in the solar cell community, often referred to as the incident photon to current efficiency, IPCE) shows the current output of a solar cell as a function of wavelength. Hence, the EQE shows how efficiently a DSC converts the incoming monochromatic light into electrical current. By comparison of the EQE spectra with the solid state UV-Vis spectra, the amount of absorbed light that is actually converted to electrical current can be estimated. Although $[\text{Cu}(\mathbf{28})(\text{ALP1})]^+$ shows the strongest absorption in the solid state UV-Vis spectrum, it does not have the highest maximum EQE of the copper sensitized solar cells. However, the higher EQEs at longer wavelengths (≈ 570 nm) lead to higher J_{SC} values with respect to the other investigated dyes in this set. The V_{OC} values of $[\text{Cu}(\mathbf{28})(\text{ALP1})]^+$ are in the same range as for $[\text{Cu}(\mathbf{13})(\text{ALP1})]^+$ and $[\text{Cu}(\mathbf{17})(\text{ALP1})]^+$ and are higher than the values measured for $[\text{Cu}(\mathbf{6})(\text{ALP1})]^+$, and $[\text{Cu}(\mathbf{15})(\text{ALP1})]^+$, respectively. All DSCs show similar ffs , with the highest values measured for DSCs containing $[\text{Cu}(\mathbf{13})(\text{ALP1})]^+$. Comparison of the DSC performances of $[\text{Cu}(\mathbf{6})(\text{ALP1})]^+$ with $[\text{Cu}(\mathbf{13})(\text{ALP1})]^+$, $[\text{Cu}(\mathbf{15})(\text{ALP1})]^+$ and $[\text{Cu}(\mathbf{17})(\text{ALP1})]^+$ shows the influence of the donating group in 5,6-substituted phenanthroline dyes. On going from $[\text{Cu}(\mathbf{6})(\text{ALP1})]^+$ to $[\text{Cu}(\mathbf{13})(\text{ALP1})]^+$ and $[\text{Cu}(\mathbf{15})(\text{ALP1})]^+$, a diaryl unit is introduced to improve the donating character of the ancillary ligand. This leads to an extension of the π -system and hence an increase in absorption of the *heteroleptic* complex on the TiO_2 surface for $[\text{Cu}(\mathbf{13})(\text{ALP1})]^+$ and $[\text{Cu}(\mathbf{17})(\text{ALP1})]^+$ but not for $[\text{Cu}(\mathbf{15})(\text{ALP1})]^+$ (Figure 69). The quantum efficiency is similar in DSCs containing $[\text{Cu}(\mathbf{17})(\text{ALP1})]^+$ and reduced in DSCs containing $[\text{Cu}(\mathbf{13})(\text{ALP1})]^+$ and $[\text{Cu}(\mathbf{15})(\text{ALP1})]^+$ with respect to DSCs containing $[\text{Cu}(\mathbf{6})(\text{ALP1})]^+$ (Figure 72). In principle, integration over the whole EQE spectra gives J_{SC} . However, it should be noted that EQE spectra are usually collected at lower light intensities. Even so, the obtained trends should be reflected in the J_{SC} values. Consequently, DSCs with $[\text{Cu}(\mathbf{13})(\text{ALP1})]^+$ and $[\text{Cu}(\mathbf{15})(\text{ALP1})]^+$ show lower J_{SC} values and similar values are obtained for DSCs containing $[\text{Cu}(\mathbf{17})(\text{ALP1})]^+$ with respect to $[\text{Cu}(\mathbf{6})(\text{ALP1})]^+$ (Table 20). These trends lead to the assumption that the absorbed light cannot be sufficiently transferred to the anchoring ligand to inject the excited electrons into the semiconductor. The V_{OC} values decrease in the order $[\text{Cu}(\mathbf{13})(\text{ALP1})]^+ \approx [\text{Cu}(\mathbf{17})(\text{ALP1})]^+ > [\text{Cu}(\mathbf{6})(\text{ALP1})]^+ > [\text{Cu}(\mathbf{15})(\text{ALP1})]^+$. This results in a trend for the overall DSC efficiencies on day 1 of $[\text{Cu}(\mathbf{17})(\text{ALP1})]^+ > [\text{Cu}(\mathbf{6})(\text{ALP1})]^+ \approx [\text{Cu}(\mathbf{13})(\text{ALP1})]^+ > [\text{Cu}(\mathbf{15})(\text{ALP1})]^+$. In summary, introduction of a carbazole unit as the donating group in $[\text{Cu}(\mathbf{17})(\text{ALP1})]^+$ leads to superior J_{SC} and V_{OC} and similar ffs with respect to the other 5,6-substituted copper(I) dyes (including the unsubstituted ligand **6**) and consequently results in the highest efficiencies for these types of

dyes. This leads to the conclusion that carbazole donors are more efficient donating groups for 5,6-substituted-2,9-dimethyl-phenanthroline ancillary ligands in Cu(I) dyes with respect to diarylamines. The best DSC performance was obtained with DSCs containing the 4,7-substituted phenanthroline dye [Cu(28)(ALP1)]⁺.

Dye	Day	Cell	J _{sc}	V _{oc}	ff	η	relative η
			[mA cm ⁻²]	[mV]	[%]	[%]	[%]
[Cu(6)(ALP1)] ⁺	1	1	5.38	542	71	2.08	25.8
		2	5.82	547	72	2.30	28.6
	4	1	5.32	548	71	2.06	24.3
		2	5.57	555	72	2.23	26.3
[Cu(13)(ALP1)] ⁺	1	1	5.41	562	75	2.29	28.4
		2	4.71	558	73	1.92	23.9
	4	1	4.84	570	75	2.06	24.3
		2	4.24	567	72	1.74	20.4
[Cu(15)(ALP1)] ⁺	1	1	4.75	523	73	1.81	22.5
		2	5.65	540	68	2.07	25.7
	4	1	4.47	539	72	1.73	20.4
		2	5.11	546	68	1.88	22.2
[Cu(17)(ALP1)] ⁺	1	1	5.82	556	73	2.35	29.1
		2	5.89	562	72	2.38	29.5
	4	1	5.54	558	72	2.22	26.1
		2	5.26	570	71	2.14	25.2
[Cu(28)(ALP1)] ⁺	1	1	6.81	557	72	2.73	33.9
		2	6.40	558	73	2.62	32.5
	4	1	6.47	567	71	2.59	30.5
		2	6.17	564	73	2.54	30.0
N719	1	1	17.94	642	70	8.06	100.0
N719	4	1	17.77	700	68	8.49	100.0

Table 20 Photovoltaic parameters of DSCs containing the *heteroleptic* Cu(I) dyes [Cu(6)(ALP1)]⁺, [Cu(13)(ALP1)]⁺, [Cu(15)(ALP1)]⁺, [Cu(17)(ALP1)]⁺, [Cu(28)(ALP1)]⁺ on day 1 and 4 with respect to N719. The last column shows the relative efficiency with respect to the N719 reference cell on the respective day.

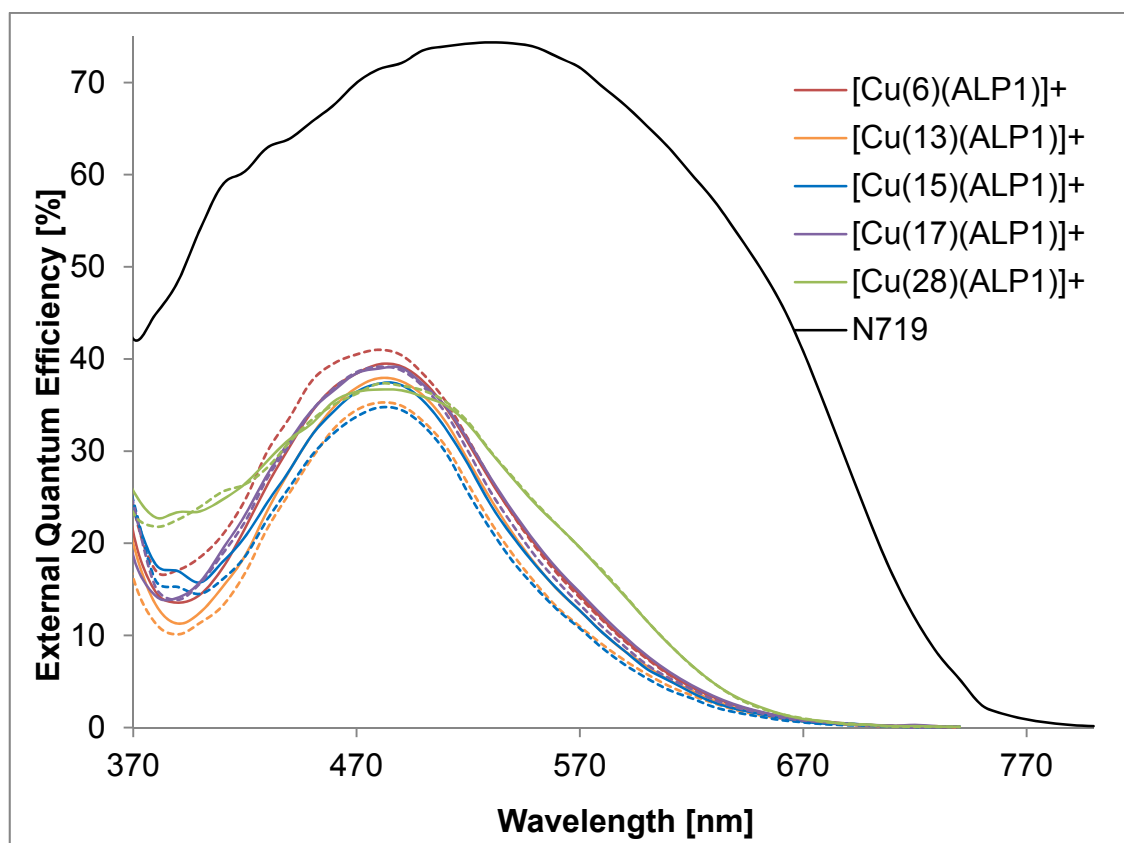


Figure 72 EQE spectra of DSCs containing the *heteroleptic* Cu(I) complexes $[\text{Cu}(6)(\text{ALP1})]^+$, $[\text{Cu}(15)(\text{ALP1})]^+$, $[\text{Cu}(17)(\text{ALP1})]^+$, $[\text{Cu}(28)(\text{ALP1})]^+$ in DSCs on day 4 with respect to N719.

Figure 73 shows the efficiencies of duplicate cells containing all the investigated dyes over time. The efficiencies change only marginally over the measured five days. The efficiency of the best performing dye $[\text{Cu}(28)(\text{ALP1})]^+$ slightly decreases in this period. The same trend is seen for $[\text{Cu}(17)(\text{ALP1})]^+$ and $[\text{Cu}(13)(\text{ALP1})]^+$ while no consistent trend was observed for the duplicate cells with $[\text{Cu}(6)(\text{ALP1})]^+$ and $[\text{Cu}(15)(\text{ALP1})]^+$.

Figure 74 shows the J/V curves on day 1 and day 4 together with the dark current measurement on day 4. For the sake of clarity, only the better performing cell of each set of the duplicates is shown. Together with the photovoltaic parameters of day 1 and day 4 in Table 20, this gives more information about the origin of the observed trends. Dark current measurements¹¹¹ is a technique to estimate the recombination loss in DSCs. Surface recombination of electrons from the TiO_2 lower the V_{oc} of DSCs significantly.¹¹² The dark current measurement on day 4 shows a shift in onset towards higher potential for $[\text{Cu}(13)(\text{ALP1})]^+$ with respect to $[\text{Cu}(15)(\text{ALP1})]^+$ and $[\text{Cu}(6)(\text{ALP1})]^+$, indicating a reduced recombination loss, and may explain the difference in V_{oc} . $[\text{Cu}(13)(\text{ALP1})]^+$ also shows a reduced dark current with respect to $[\text{Cu}(17)(\text{ALP1})]^+$ and $[\text{Cu}(28)(\text{ALP1})]^+$. However, DSCs from these dyes show similar V_{oc} to $[\text{Cu}(13)(\text{ALP1})]^+$ sensitized DSCs. This is attributed to the higher J_{sc} values measured for these DSCs which

increases the number of electrons in the semiconductor, resulting in a conduction band edge shift and lower V_{OC} values.¹¹³

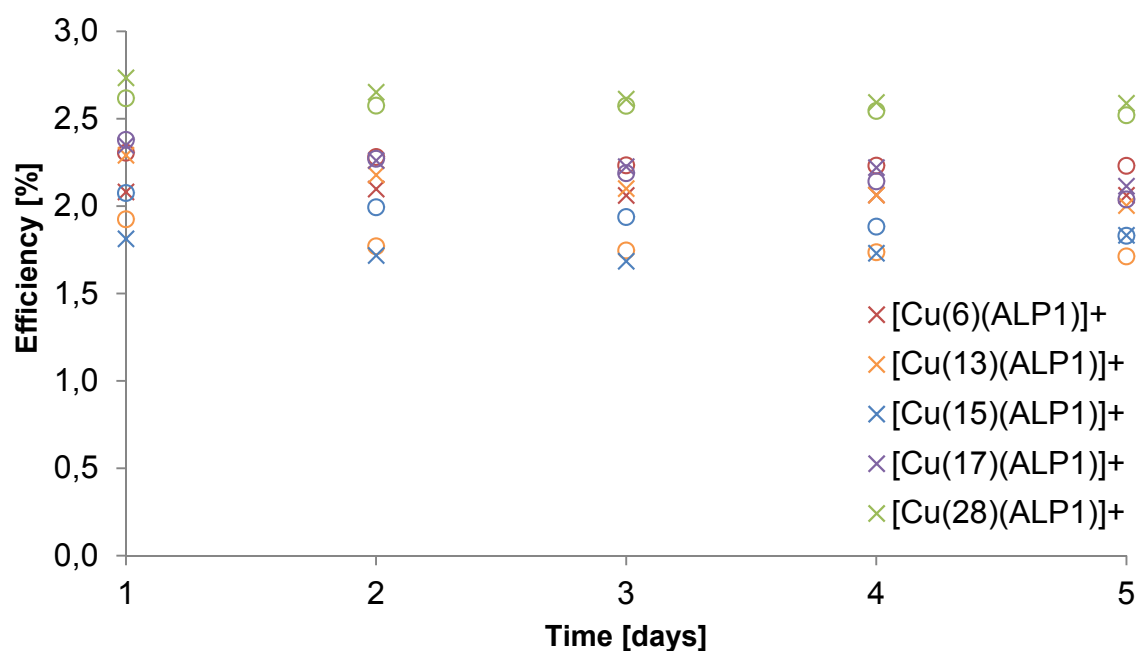


Figure 73 Efficiency over time for duplicate DSCs containing the *heteroleptic* Cu(I) dyes [Cu(6)(ALP1)]⁺, [Cu(13)(ALP1)]⁺, [Cu(15)(ALP1)]⁺, [Cu(17)(ALP1)]⁺ and [Cu(28)(ALP1)]⁺.

Figure 74 and Table 20 illustrate that [Cu(28)(ALP1)]⁺ sensitized DSCs show a decrease in J_{SC} and an increase in V_{OC} from day 1 to day 4 with constant ff over this period. This results in a lower overall performance from 2.73% to 2.59% and 2.62% to 2.54%, respectively, for the two cells. A similar decrease in J_{SC} and an increase in V_{OC} is found for [Cu(17)(ALP1)]⁺ causing a decrease in efficiency from 2.35% to 2.22% and 2.38% to 2.14%. In both duplicate cells of [Cu(6)(ALP1)]⁺, all three characteristic parameters stay nearly unaffected over four days and consequently show no change within the investigated period. The duplicate cells sensitized with [Cu(13)(ALP1)]⁺ decrease in J_{SC} and marginally in V_{OC} from day 1 to 4, resulting in a decrease in efficiency from 2.29% to 2.06%, and 1.92% to 1.74%, respectively. Finally, [Cu(15)(ALP1)]⁺ shows a decrease in J_{SC} and an increase in V_{OC} resulting in a decrease of η , similar to [Cu(17)(ALP1)]⁺ and [Cu(28)(ALP1)]⁺. However, although duplicate cells were used to help validate DSC performance data, a greater number of DSCs for each dye should ideally be used to confirm trends on going from one dye to the next.

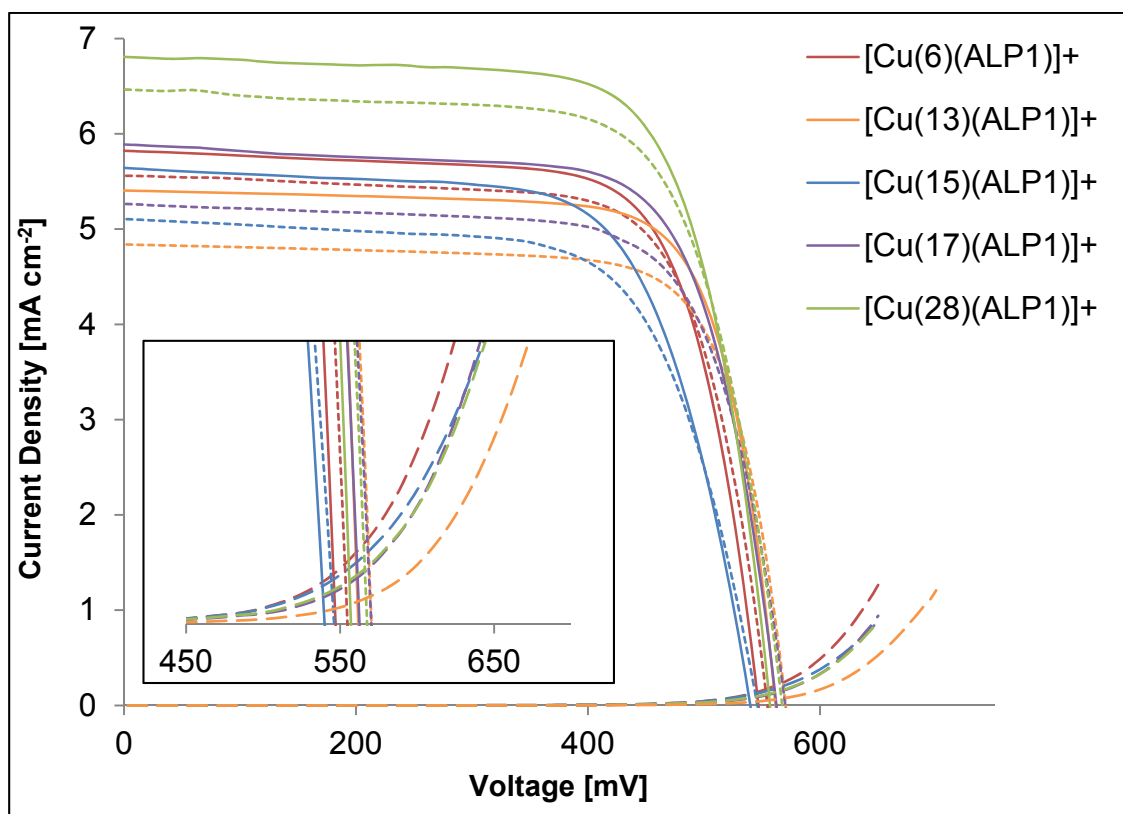


Figure 74 Photocurrent density/voltage (J/V) on day 1 (solid lines) and 4 (dotted lines) and dark current (dashed lines) characteristics of DSCs sensitized with $[\text{Cu}(6)(\text{ALP1})]^+$, $[\text{Cu}(13)(\text{ALP1})]^+$, $[\text{Cu}(15)(\text{ALP1})]^+$, $[\text{Cu}(17)(\text{ALP1})]^+$ and $[\text{Cu}(28)(\text{ALP1})]^+$. For the sake of clarity only the better performing DSC of each set of duplicates in Figure 71 are shown.

In summary it can be said that of all investigated *heteroleptic* Cu(I) dyes in this section, $[\text{Cu}(28)(\text{ALP1})]^+$ with its 4,7-substituted phenanthroline ancillary ligand, shows the best performance in DSCs. From the Cu(I) dyes based on 5,6-substituted phenanthroline ancillary ligands, $[\text{Cu}(17)(\text{ALP1})]^+$ with its carbazole donor outperforms the other three dyes. Introduction of diaryl units as a donating group in $[\text{Cu}(13)(\text{ALP1})]^+$ and $[\text{Cu}(15)(\text{ALP1})]^+$ resulted in similar and poorer overall DSC performances, respectively, with respect to the unsubstituted analogue $[\text{Cu}(6)(\text{ALP1})]^+$.

*Brauchli*¹¹⁴ reported a *heteroleptic* Cu(I) dye composed of **ALP1** and an ancillary ligand similar to **28** but based on 2,2'-bipyridine (Figure 75). DSCs were prepared from *Solaronix* TiO₂ electrodes by using the same *on-surface* strategy as discussed above. An overall power conversion efficiency of 1.61% on the day of assembly was reported with J_{sc} of 4.55 mA cm⁻², a V_{oc} of 489 mV and a ff of 72%. Because the measurement conditions are not perfectly reproducible the comparison of the relative efficiency to N719 sensitized solar cells may give a better picture of the relative performance of the two dyes. However, with an efficiency of 8.15% on the day of assembly, the relative efficiency to N719 of 19.7 % on day 1 for the dye

shown in Figure 75 is still significantly lower than the values obtained for the dyes investigated in this section (Table 20). For example, for the best performing DSC containing $[\text{Cu}(\mathbf{28})(\text{ALP1})]^+$, a relative efficiency of 33.9% was obtained on day 1. This leads to the assumption that ancillary ligands based on phenanthroline rather than 2,2'-bipyridine lead to superior efficiencies in DSCs. However, with 6,6'-dimethyl-2,2'-bipyridine¹¹⁵ or 4,4'-bis(4-iodophenyl)-6,6'-dimethyl-2,2'-bipyridine⁴⁸ as ancillary ligands relative efficiencies to N719 cells of 27.9% and 38.9% were obtained, respectively. For a better understanding of the different behavior of 2,2'-bipyridine and 1,10-phenanthroline ancillary ligands, 1,10-phenanthroline ligands with a 4-iodophenyl substituent in the 4- and 7-positions would be necessary.

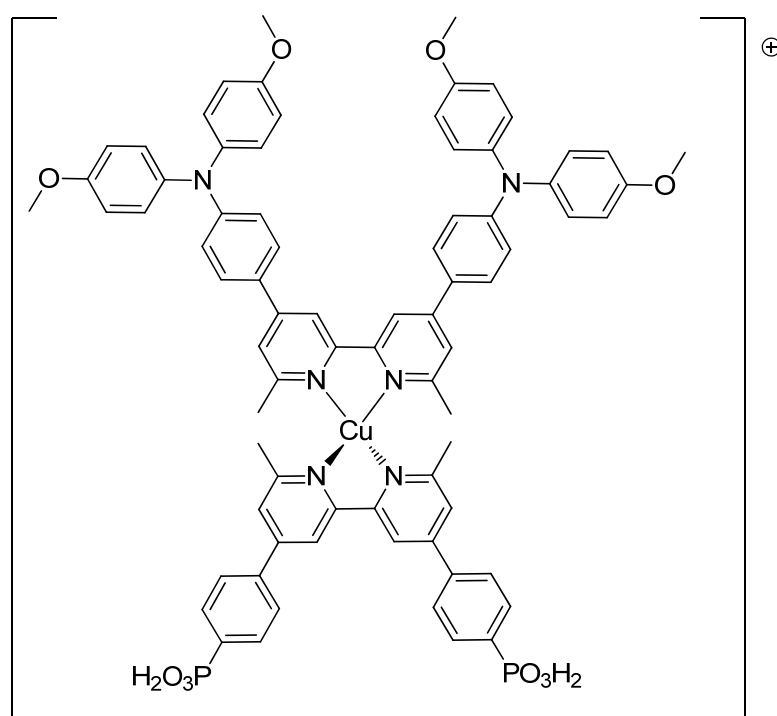
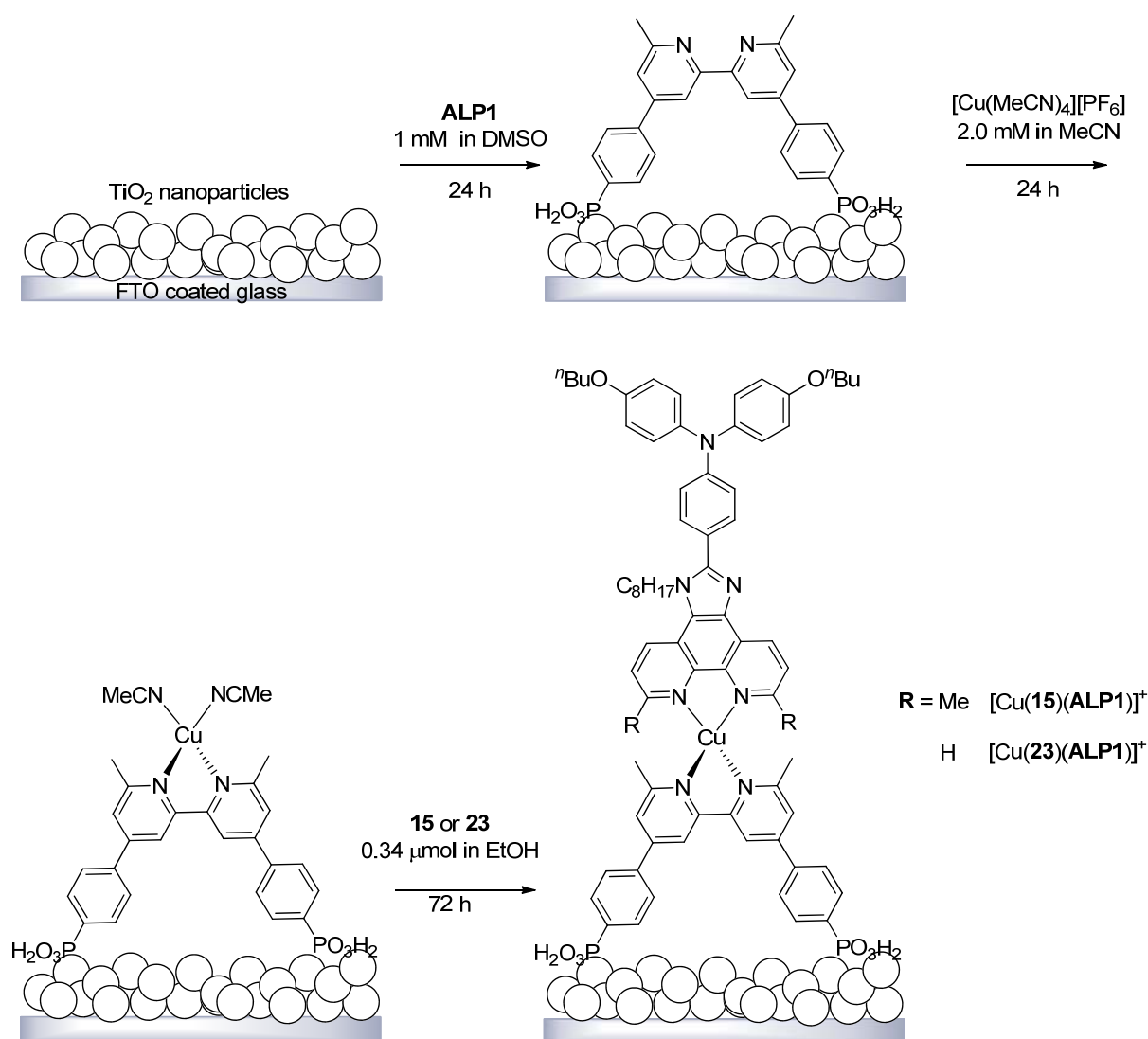


Figure 75 Heteroleptic Cu(I) dye reported by *Brauchli* using ALP1 as an anchoring ligand and an ancillary ligand similar to **28** but based on 2,2'-bipyridine.

9.2 Stepwise assembly

In this section the necessity of methyl groups in the 2,9-positions of the phenanthroline ancillary ligand is investigated. Cu(I) complexes are sensitive towards nucleophilic attack and oxidation to Cu(II) by O_2 .¹¹⁶ Therefore it would be expected that steric protection by the methyl groups is necessary for the stability of the dye on the surface. However, it has been shown that *homoleptic* Cu(I) 2,2'-bipyridine complexes with only one methyl group in the 6-position are

stable with respect to oxidation and can form *heteroleptic* complexes with 6,6'-dimethyl-2,2'-bipyridine anchoring ligands for use in DSCs.⁹² For this experiment, ancillary ligand **15** and its non-methylated analogue **23** were tested (structure bottom right in Scheme 3). Since *homoleptic* Cu(I) complexes without any steric protection are unstable towards oxidation, the *on-surface* synthesis of the *heteroleptic* Cu(I) complexes had to be adjusted. *Hostettler*¹¹⁷ introduced a stepwise assembly by adsorbing a terpyridine anchoring ligand on a TiO₂ surface followed by metallation with a Zn(II) salt and subsequent capping with a donating ancillary terpyridine ligand. This was later adapted by *Brauchli*¹¹⁸ and *Schönhofer*¹¹⁹ for copper(I) dyes with 2,2'-bipyridine ligands using [Cu(MeCN)₄][PF₆] for the metallation step. Scheme 3 shows the stepwise assembly of *heteroleptic* Cu(I) complexes using **ALP1** as the anchoring ligand and **15** and **23** as ancillary ligands, respectively.



Scheme 3 Stepwise assembly of the surface-bound copper complexes [Cu(**15**)(ALP1)]⁺ and [Cu(**23**)(ALP1)]⁺.

Figure 76 shows the solid state UV-Vis absorption spectra of both $[\text{Cu}(\mathbf{15})(\text{ALP1})]^+$ and $[\text{Cu}(\mathbf{23})(\text{ALP1})]^+$ prepared by the stepwise assembly and compares them to the absorption spectra of N719 and $[\text{Cu}(\mathbf{15})(\text{ALP1})]^+$ prepared by the classical assembly. The absorbance of $[\text{Cu}(\mathbf{15})(\text{ALP1})]^+$ shows only little dependence on the method of assembly with both absorption spectra nearly overlaying with each other. The methyl groups in the 2,9-positions of phenanthroline lead to a slight flattening of the absorption curve and minor affect on the absorption up to 450 nm with a more intense absorbance in this region.

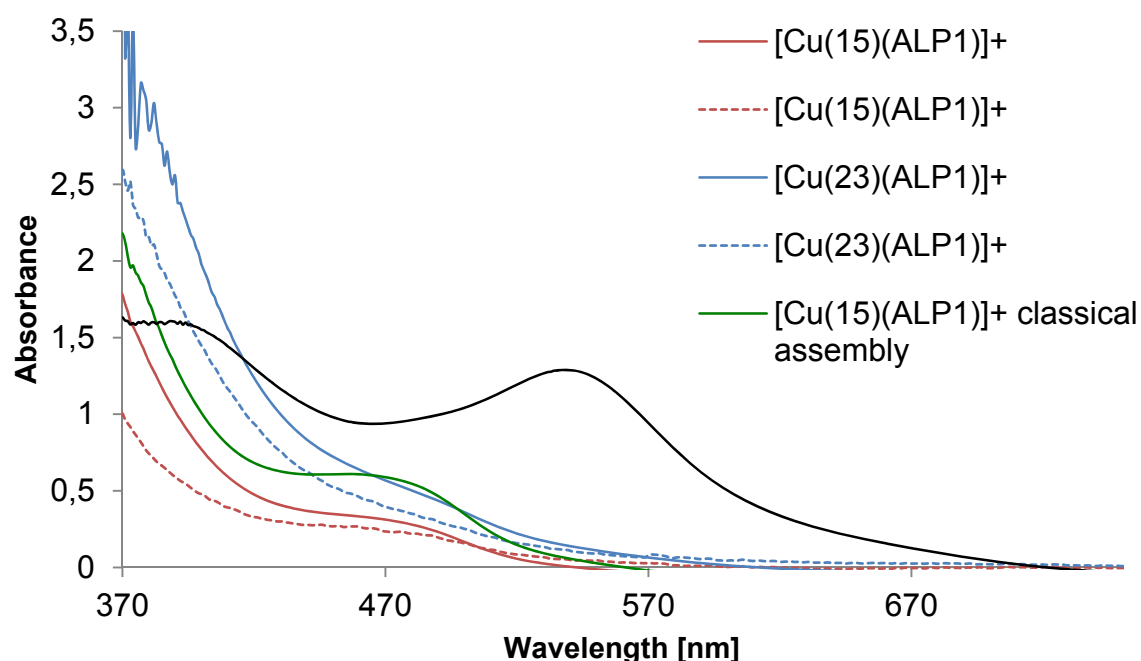


Figure 76 Solid state UV-Vis absorption spectra of the *heteroleptic* dyes $[\text{Cu}(\mathbf{15})(\text{ALP1})]^+$ and $[\text{Cu}(\mathbf{23})(\text{ALP1})]^+$ prepared by the stepwise assembly and adsorbed on TiO_2 electrodes. Dashed lines are after soaking in the electrolyte solution for 7 hours. For comparison, the absorption spectrum of $[\text{Cu}(\mathbf{15})(\text{ALP1})]^+$ prepared by the classical ligand exchange assembly is shown.

In Figure 77, the J/V curves of DSCs containing $[\text{Cu}(\mathbf{15})(\text{ALP1})]^+$ and $[\text{Cu}(\mathbf{23})(\text{ALP1})]^+$ prepared by the stepwise assembly are presented and compared to the J/V measurements of a DSC with $[\text{Cu}(\mathbf{15})(\text{ALP1})]^+$ prepared by the classical assembly. Another electrolyte (labeled **E7**) was used for this measurement, which showed an improved performance with $[\text{Cu}(\mathbf{15})(\text{ALP1})]^+$ sensitized solar cells prepared by the classical assembly (see Chapter 10). The electrolyte consists of 0.03 M I_2 , 0.6 M 1-butyl-3-methyl imidazolium iodide (BMII), 0.4 M 4-*tert*-butyl pyridine (TBP), and 0.1 M guanidinium thiocyanate (GNCS) in 3-methoxypropionitrile (MPN). J/V curves of an N719 sensitized solar cell using Standard II electrolyte are also included for comparison. The detailed photovoltaic parameters of these

DSCs are listed in Table 21. The $[\text{Cu}(\mathbf{15})(\mathbf{ALP1})]^+$ sensitized solar cell clearly outperforms the $[\text{Cu}(\mathbf{23})(\mathbf{ALP1})]^+$ DSC with an efficiency of 1.76% versus 0.17% on day 1. This huge difference arises from a significantly increased J_{SC} with more than 14-fold higher values for the $[\text{Cu}(\mathbf{15})(\mathbf{ALP1})]^+$ cell. This is also reflected in the EQE spectra (Figure 78) which show that the DSC with $[\text{Cu}(\mathbf{23})(\mathbf{ALP1})]^+$ has a very low quantum efficiency over the whole spectrum with respect to $[\text{Cu}(\mathbf{15})(\mathbf{ALP1})]^+$. This is in contrast to the solid state UV-Vis spectra shown in Figure 76 in which both copper dyes show similar absorbances. This leads to the conclusion that either $[\text{Cu}(\mathbf{23})(\mathbf{ALP1})]^+$ does not inject the excited electrons into the semiconductor or is destroyed (e.g. by ligand dissociation) by the electrolyte. However, no visible change was detected by eye when filling the DSC with electrolyte; “bleaching” is the usual sign that a copper(I) bis(diamine) dye is destroyed. This was confirmed by a solid state UV measurement in which the absorbance of $[\text{Cu}(\mathbf{15})(\mathbf{ALP1})]^+$ and $[\text{Cu}(\mathbf{23})(\mathbf{ALP1})]^+$ sensitized electrodes were compared before and after soaking in an electrolyte solution for 7 hours. Both dyes showed a similar behaviour with a slight decrease in absorbance after the electrolyte treatment. However, this cannot explain the significant difference in DSC performance. Therefore either the electron injection of $[\text{Cu}(\mathbf{23})(\mathbf{ALP1})]^+$ is significantly lower or the dye performance is hindered under working solar cell conditions. *Ashbrook et al.*⁵⁰ found TBP to reversibly form adducts with Cu(II) centres, leaving a significant fraction of the dye inactive for a while. This may be an explanation for the significant difference of the two dyes in DSCs since the lack of methyl groups in the 2 and 9 position of the phenanthroline in $[\text{Cu}(\mathbf{23})(\mathbf{ALP1})]^+$ facilitates attack from TBP.

The other characteristic photovoltaic parameters, namely V_{OC} and ff , are both increased on going from $[\text{Cu}(\mathbf{15})(\mathbf{ALP1})]^+$ to $[\text{Cu}(\mathbf{23})(\mathbf{ALP1})]^+$. Due to the series resistance, low J_{SC} values usually cause higher ff s.¹²⁰ The increase in V_{OC} can be explained by a reduced recombination of electrons from the TiO_2 semiconductor to the electrolyte.^{82,113,121} This is shown in Figure 79 for the stepwise assembled DSCs sensitized with $[\text{Cu}(\mathbf{15})(\mathbf{ALP1})]^+$ and $[\text{Cu}(\mathbf{23})(\mathbf{ALP1})]^+$ and an N719 cell as a reference. In the OCVD measurement (Figure 79a), the speed of the V_{OC} decay increases in the order of $\text{N719} < [\text{Cu}(\mathbf{23})(\mathbf{ALP1})]^+ < [\text{Cu}(\mathbf{15})(\mathbf{ALP1})]^+$. This indicates a higher recombination rate for $[\text{Cu}(\mathbf{15})(\mathbf{ALP1})]^+$ versus $[\text{Cu}(\mathbf{23})(\mathbf{ALP1})]^+$ and N719, respectively, and hence a lower V_{OC} . Dark current measurements (shown in Figure 79b) show the same trend with an onset difference of ≈ 160 mV from $[\text{Cu}(\mathbf{15})(\mathbf{ALP1})]^+$ to $[\text{Cu}(\mathbf{23})(\mathbf{ALP1})]^+$.

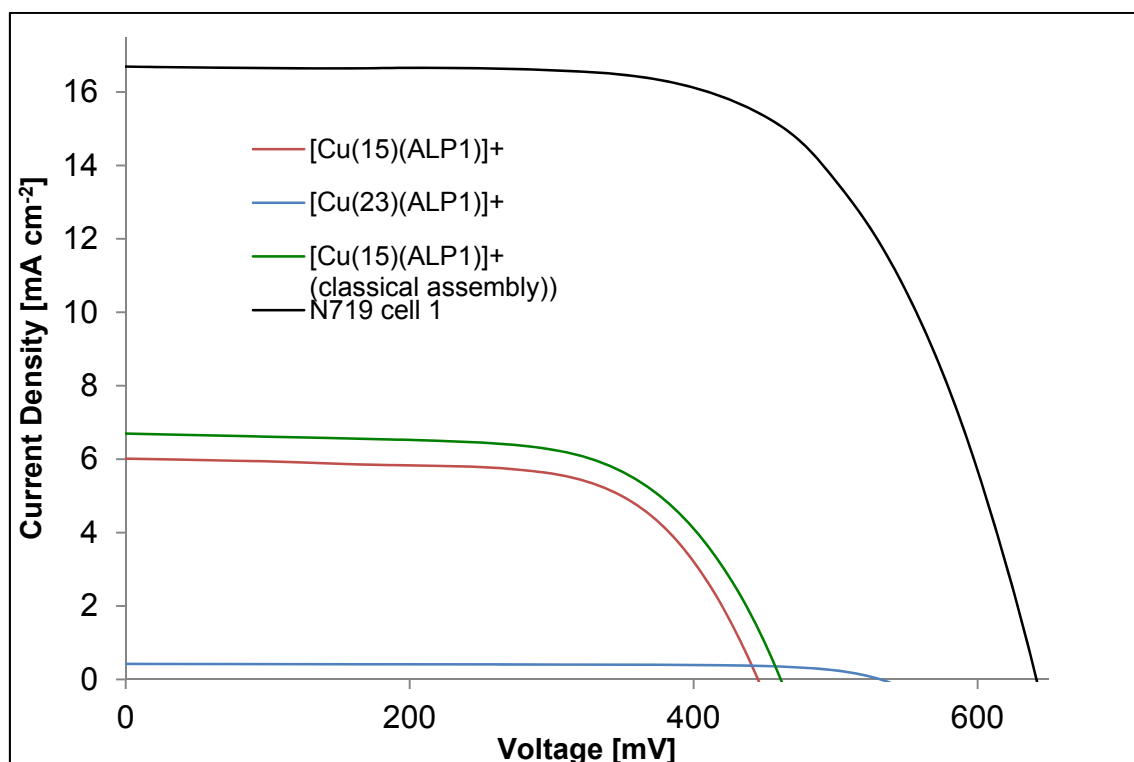


Figure 77 Photocurrent density/voltage (J/V) characteristics of DSCs sensitized with the *heteroleptic* Cu(I) complexes $[Cu(15)(ALP1)]^+$ and $[Cu(23)(ALP1)]^+$ prepared by the stepwise assembly on day 1 with respect to DSCs of $[Cu(15)(ALP1)]^+$ prepared by the classical assembly. All three cells were filled with an electrolyte labeled E7 that consists of 0.03 M I_2 , 0.6 M BMII, 0.4 M TBP 0.1 M GNCS in MPN. For comparison a N719 sensitized DSC with Standard II electrolyte is shown.

Dye	Day	Cell	J_{sc} [mA cm ⁻²]	V_{oc} [mV]	FF [%]	η [%]	η relative [%]
$[Cu(15)(ALP1)]^+$	1	1	6.01	445	66	1.76	25.25
		2	4.57	503	71	1.62	23.29
$[Cu(23)(ALP1)]^+$	1	1	0.42	534	74	0.17	2.37
		2	0.27	564	74	0.11	1.60
$[Cu(15)(ALP1)]^+$ (classical assembly)	1	1	6.70	461	64	1.98	28.46
N719	1	1	16.70	641	65	6.97	100.00
		2	17.33	663	63	7.26	-

Table 21 Photovoltaic parameters of duplicate cells of $[Cu(15)(ALP1)]^+$ and $[Cu(23)(ALP1)]^+$ fabricated by the stepwise assembly on the day of assembly.

The comparison of the $[Cu(15)(ALP1)]^+$ DSCs assembled with the two different methods shows that the solar cell fabricated by the classical assembly exhibits higher characteristic photovoltaic parameters leading to a superior efficiency. This conclusion is similar to the results

of *Brauchli*, who found the efficiencies to be equal or worse for the stepwise assembly with respect to the classical assembly depending on the dye investigated.¹¹⁸

In summary, methyl groups in the 2- and 9-positions of phenanthroline ligands are vital for the performance of Cu(I) dyes in DSCs. Omitting these substituents results in a drastic drop of the J_{SC} and leads to a poor overall performance of the DSCs. A stepwise assembly instead of classical assembly appears to be disadvantageous for the performance of 5,6-substituted 2,9-dimethylphenanthroline Cu(I) dyes in DSCs.

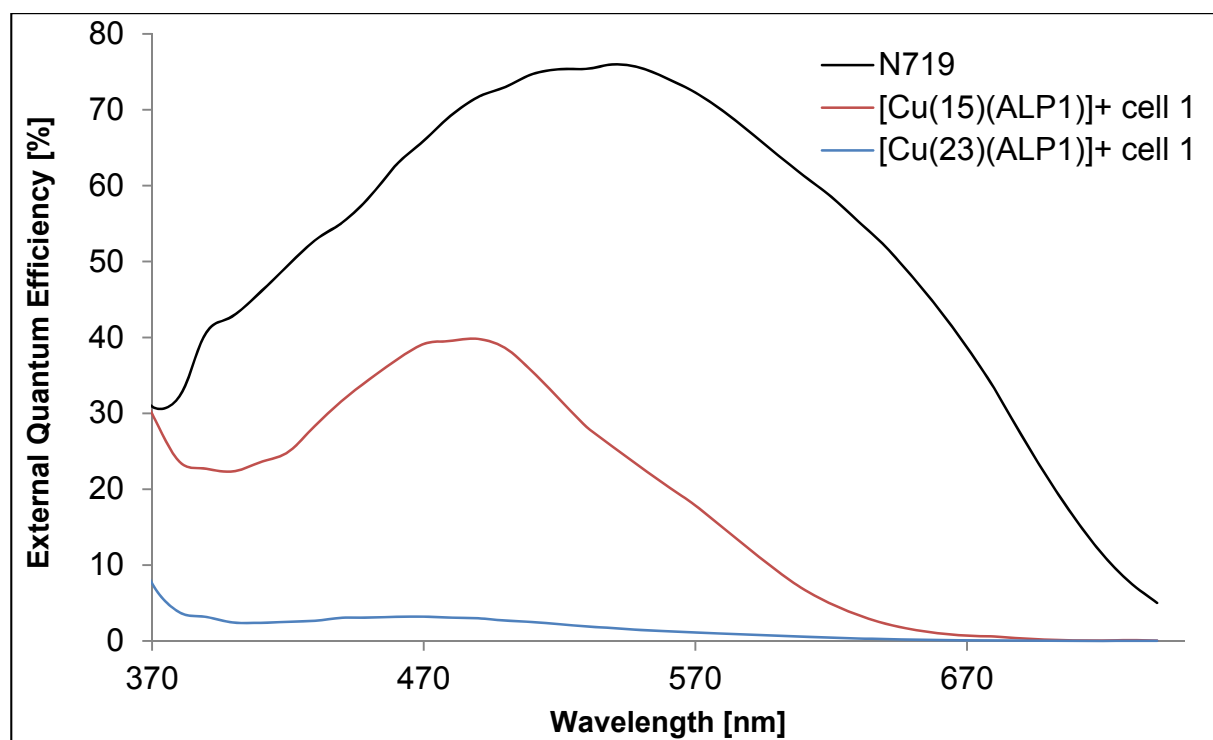


Figure 78 EQE spectra of DSCs containing the *heteroleptic* Cu(I) complexes $[\text{Cu}(17)(\text{ALP1})]^+$ and $[\text{Cu}(23)(\text{ALP1})]^+$ in DSCs fabricated by the stepwise assembly on day 2 with N719 as a reference.

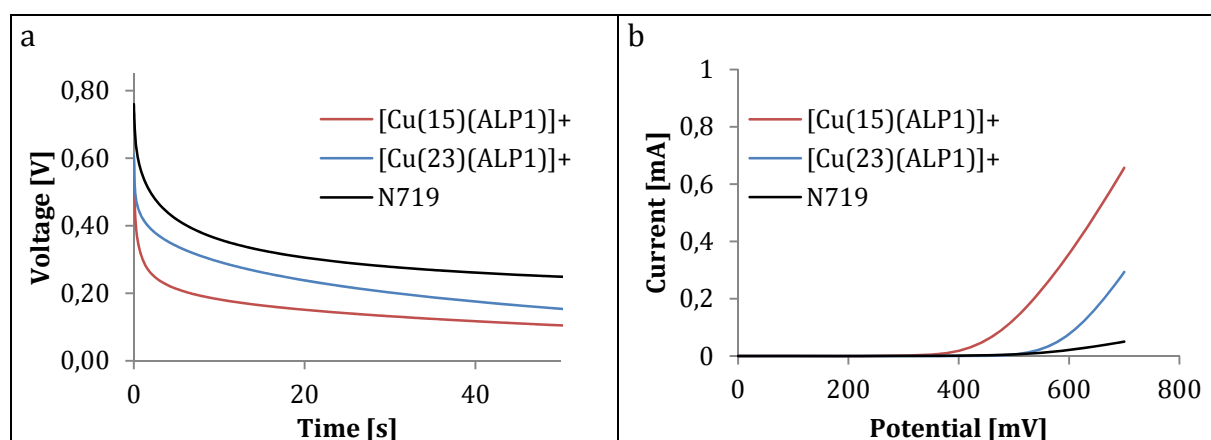


Figure 79 Recombination characteristics of DSCs in Figure 77 both measured on day 2. OCVD measurement is shown in a and a dark current measurement in b.

10 Optimization of the I^-/I_3^- Electrolyte for the Performance of Copper(I) Dyes in DSCs

The I^-/I_3^- electrolyte is one of the most commonly used in DSCs. Originally the composition of the electrolyte was optimized to work as a redox shuttle combined with ruthenium(II)-containing dyes in n-type DSCs. A number of additives are typically combined with the redox couple (composed of LiI and I_2) in an ionic liquid, such as 1-butyl-3-methylimidazolium iodide (BMII). Commonly used additives are 4-*tert*-butylpyridine and guanidinium thiocyanate.

In this chapter, the optimization of the I^-/I_3^- electrolyte for copper(I) bis(diimine) dyes is presented. The first section of this chapter (10.1 Screening of I^-/I_3^- electrolytes) was done in collaboration with *Laura Luu* as part of her ‘Wahlpraktikum’ (internship). In the first section, the results of screening different I^-/I_3^- electrolytes reported in the literature are shown. For a fast screening, DSCs with the Cu(I) dye $[Cu(15)(ALP1)]^+$ were prepared with an electrode soaking time in a solution of the *homoleptic* dye $[Cu(15)_2][PF_6]$ for 24 hours. In a second step, a selection of electrolytes was tested in DSCs with an increased soaking time of 72 hours and the results were compared to the measurements from the 24 hours soaking time. The photovoltaic parameters were measured over a period of one week to evaluate ripening effects. In the second section, the best electrolyte was systematically optimized by varying the components of the electrolyte solution.

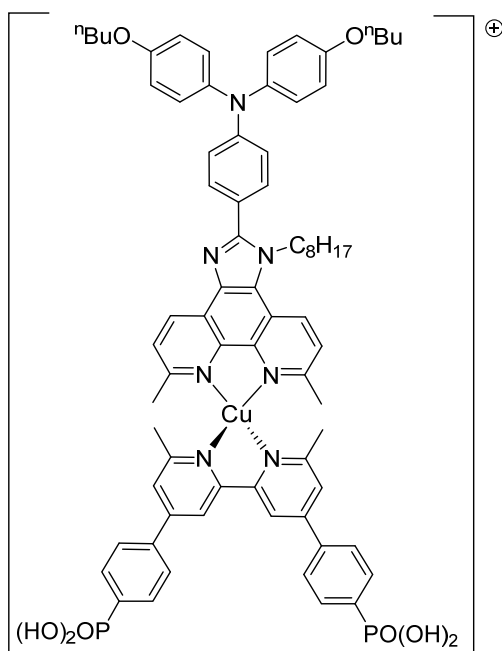


Figure 80 The *heteroleptic* Cu(I) dye $[Cu(15)(ALP1)]^+$ investigated in this chapter.

10.1 Screening of I⁻/I₃⁻ electrolytes

Table 22 shows the compositions of the electrolytes screened in this section. The electrolyte compositions were taken from literature reports or are electrolytes used in our research group. To the best of our knowledge, the only investigation of electrolytes for Cu(I) dyes was done by *Colombo et al.*¹²² who found **E8** (Table 22) to perform the best in their devices with DSCs which contained the *homoleptic* [Cu(6,6'-dimethyl-2,2'-bipyridine-4,4'-dibenzoic acid)₂]⁺ ([Cu(**ALC1**)₂]⁺ in the terminology of this thesis). They concluded that Li⁺ ions are vital for the good performance of Cu(I) sensitized solar cells and also that including the additive guanidinium thiocyanate (GNCS) lowers the efficiency. However, from the data they published, on going from one electrolyte to another more than one component was changed and their best performing DSCs had a significantly smaller active area with respect to other published DSCs. Other electrolytes presented in Table 22 that were used in combination with Cu(I) dyes are **E2**, **E3**, **E9** and the Standard II electrolyte **E10**, which is the electrolyte used mainly throughout this thesis. The other electrolytes from Table 22, namely **E1**¹²³, **E4**, **E5**¹²⁴ and **E6** are optimized for ruthenium(II) dyes and were reported by the group of *Grätzel*. **E7** consists of the same components as **E6** but uses an 85:15 mixture of acetonitrile (MeCN) and valeronitrile (VN) instead of 3-methoxypropionitrile (MPN) as a solvent. In summary, several characteristic components in the electrolyte solution are changed across the series of electrolytes investigated in this section: (i) the concentration of the iodine (I₂) and iodide sources (LiI and ionic liquid) as well as their ratio to each other, (ii) additives like 4-*tert*-butylpyridine (TBP), *n*-butylbenzimidazole (NBB) or guanidinium thiocyanate (GNCS) and (iii) the solvent which was either MeCN, an 85:15 mixture of MeCN and VN or MPN, respectively. Historically, a mixture of MeCN and VN has been used to keep the vapour pressure of the electrolytes as low as possible and was later replaced by MPN as it shows similar properties but superior performance in DSCs. MPN was especially important when working with partially sealed cells.

Name	LiI	I ₂	Ionic liquid	Additive	GNCS	Solvent
	[M]	[M]	[M]	[M]	[M]	(v/v)
E1 ¹²⁵	0.02	0.03	0.6 M DMII	0.5 M TBP	0.1	MeCN/VN (4.25/0.75)
E2	0.05	0.03	1 M DMII	0.5 M TBP	0.1	MeCN/VN (4.25/0.75)
E3	0.1	0.03	0.6 M DMII	0.5 M TBP	0.1	MeCN/VN (4.25/0.75)
E4	0.05	0.15	1 M DMII	0.5 M NBB	0.1	MPN
E5 ¹²⁴	0.1	0.04	0.7 M DMPI	0.125 M TBP		MeCN
E6	-	0.03	0.6 M BMII	0.4 M TBP	0.1	MeCN/VN (4.25/0.75)
E7	-	0.03	0.6 M BMII	0.4 M TBP	0.1	MPN
E8 ¹²²	0.025	0.04	0.65 M BMII	0.28 M TBP	-	MeCN/VN (4.25/0.75)
E9	0.5	0.03	-	0.5 M NBB	-	MPN
E10	0.1	0.05	0.6 M BMII	0.5 M MBI	-	MPN

Table 22 Electrolytes screened in this section. BMII = 1-butyl-3-methylimidazolium iodide; DMII = 1,3-dimethylimidazolium iodide; DMPI = 1,2-dimethyl-3-propylimidazolium iodide; GNCS = guanidinium thiocyanate; NBB = *n*-butylbenzimidazole; TBP = 4-*tert*-butylpyridine; VN = valeronitrile.

To allow for the ripening effect sometimes observed with DSCs (see above), the cells were measured over the course of one week. For consistency, duplicate cells were prepared with commercial TiO₂ electrodes for comparable results. For a fast screening of the electrolytes, DSCs were fabricated by soaking the commercial TiO₂ electrodes for 24 hours in a solution of **ALP1** and 24 hours in a solution of the *homoleptic* Cu(I) dye [Cu(**15**)₂][PF₆]. It was assumed that the relative performances of the electrolytes in DSCs should not depend on the soaking time. To confirm this hypothesis, measurements of selected electrolytes were made with a longer soaking time, and the results are shown and discussed later in this section. Figure 81 shows the efficiencies over one week with only a small ripening effect for all of the cells over the measured time period. One of each duplicate cells of electrolyte **E5** and **E8** showed faulty results so the data was ignored. **E7**, **E8** and **E6** show superior performance in [Cu(**15**)(**ALP1**)]⁺ sensitized solar cells with respect to Standard II electrolyte **E10**. Clearly, the highest efficiency was reached using electrolyte **E7**, followed by **E8** and **E6**. Interestingly, **E6** and **E7** are the only electrolytes that do not include any lithium ions, which is in contrast to the results by *Colombo*

*et al.*¹²² discussed above. The only source of I^- for these electrolytes is the ionic liquid BMII. The huge improvement from **E6** to **E7** was obtained by a change in the solvent from an 85:15 ratio of MeCN and VN to MPN. Figure 82 shows the J/V curves for DSCs using **E6-E8** in comparison to those with **E10** on day 1 (solid line) and day 6 (dotted line) and the photovoltaic parameters are presented in Table 23. For the sake of clarity, only the better performing DSC of each pair of duplicates for every electrolyte is shown. It is apparent that the improved performance of **E7** with respect to the other three electrolytes arises from an increase in J_{sc} . On day 1, the J_{sc} for **E7** is 7.85 mA cm^{-2} compared to 4.30 mA cm^{-2} for **E10** on the same day. The other two electrolytes (**E6** and **E8**) outperform electrolyte **E10**, and also profit from higher J_{sc} values and additionally from higher V_{oc} values on day 1. The highest V_{oc} measured on the day of assembly of the DSCs filled with **E6-8** and **E10** was reached with electrolyte **E6** with a V_{oc} of 527 mV followed by **E8** with 519 mV, **E10** with 496 mV and **E7** with 489 mV. The ff measured for these cells is comparable for all of the cells and is in the range of 69-71 % on the first day.

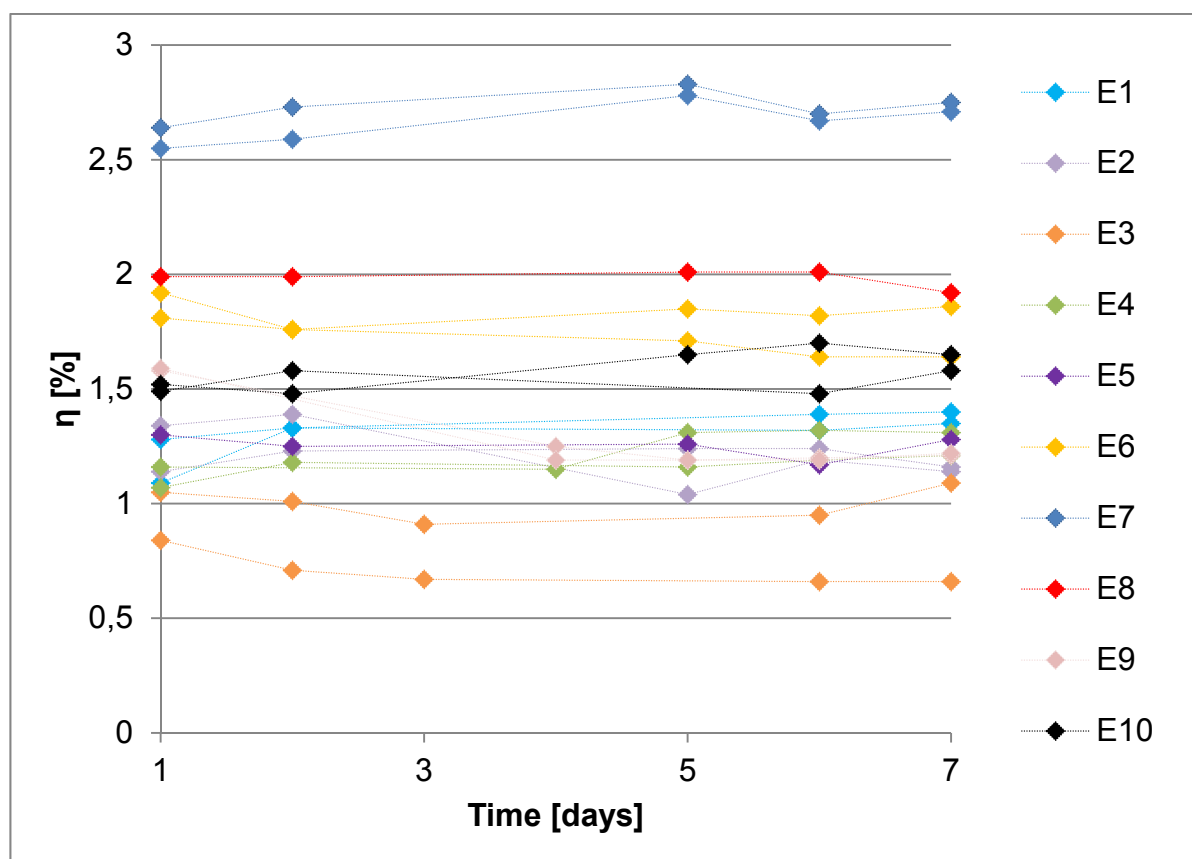


Figure 81 Efficiencies of duplicate DSCs filled with electrolytes E1-E10 and measured over the course of one week. The DSCs were prepared by soaking the TiO_2 electrodes in a solution of ALP1 and $[\text{Cu}(15)_2][\text{PF}_6]$ for 24 hours each. One DSC with each of E5 and E8 had to be discarded due to problems with the cells.

The ripening effect differs between the investigated electrolytes. While for **E6** a lower η was obtained after five days, DSCs filled with **E7**, **E8** and **E10** improved or were constant. For **E10** the best improvement from 1.52% to 1.70% was found. DSCs incorporating **E10** are the only cells for which both J_{SC} and V_{OC} improve within five days. DSCs with **E7** and **E8** show both lowered J_{SC} and increased V_{OC} values while DSCs with **E6** show a drop in J_{SC} and a marginal decrease in V_{OC} .

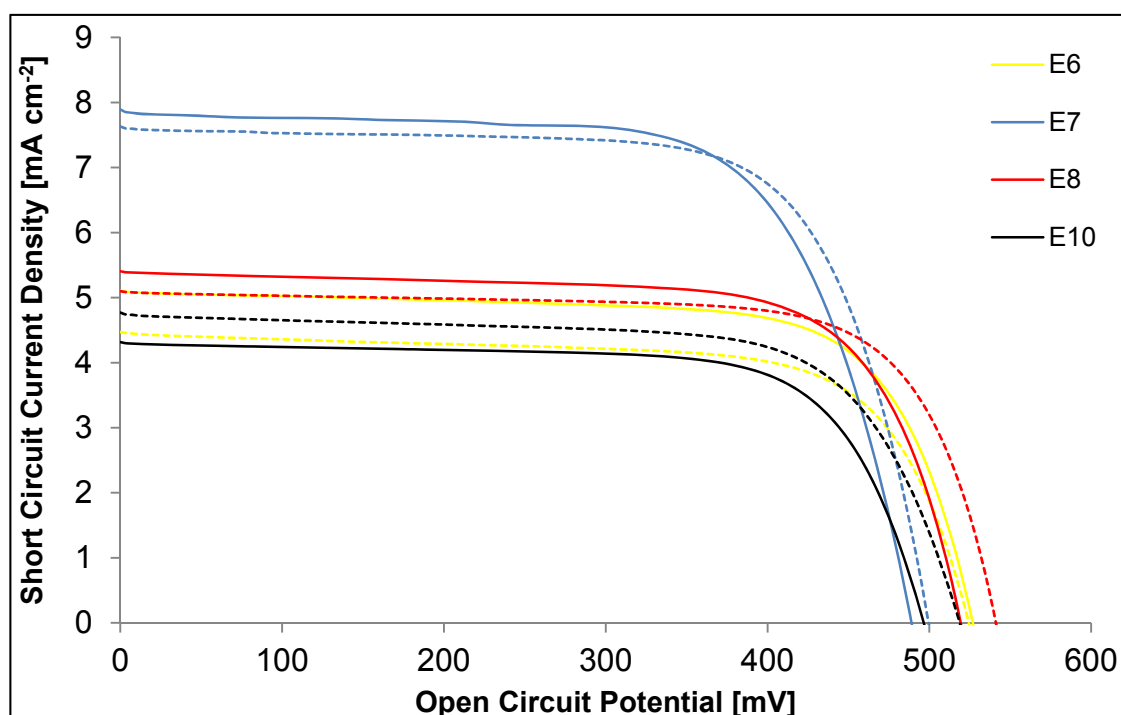


Figure 82 J/V curves on day 1 (solid line) and day 6 (dotted line) of E6-E10 in comparison to E10 (Standard II electrolyte). For the sake of clarity, only the better performing cell of the duplicate cells is shown for each electrolyte.

Electrolyte	Day	J_{sc}	V_{oc}	ff	η	η (relative)
		[mA cm^{-2}]	[mV]	[%]	[%]	[%]
E6	1	5.09	527	72	1.92	29.3
	6	4.45	524	70	1.64	26.8
E7	1	7.85	489	69	2.64	40.3
	6	7.60	499	71	2.70	44.2
E8	1	5.39	519	71	1.99	30.4
	6	5.08	541	73	2.01	32.9
E10	1	4.30	496	71	1.52	23.2
	6	4.74	518	69	1.70	27.9
N719	1	15.29	616	70	6.56	100.0
	6	14.74	596	70	6.11	100.0

Table 23 Photovoltaic parameters of the DSCs shown in Figure 82 on day 1 and day 6.

To confirm the hypothesis that the trends in performances of the DSCs obtained are not dependent on the soaking time in the *homoleptic* $[\text{Cu}(\mathbf{15})_2][\text{PF}_6]$ solution, selected electrolytes were tested in DSCs with an extended soaking time of 72 hours. For this, all electrolytes that outperformed **E10** in the 24 hours experiment were selected. Figure 83 shows the efficiencies of duplicate DSCs with a soaking time of 72 hours in a solution of $[\text{Cu}(\mathbf{15})_2][\text{PF}_6]$ using electrolytes **E6-E8** and **E10** measured over the course of one week. The DSCs filled with **E10** show relatively big differences between the duplicate cells. The general trend appears to be the same as in the 24 hour measurements. Clearly, the best results were obtained with electrolyte **E7**, followed by **E6**, **E8** and **E10**; however, the order between electrolytes **E8** and **E10** is ambiguous. In comparison with DSCs prepared with a 24 hour soaking time, the 72 hour soaked DSCs show the same or better performances. The best performing electrolyte **E7** starts with a marginally lower efficiency after soaking for 72 hours versus 24 hours on the day of assembly, but shows roughly the same efficiencies after a few days within the error of the measurement.

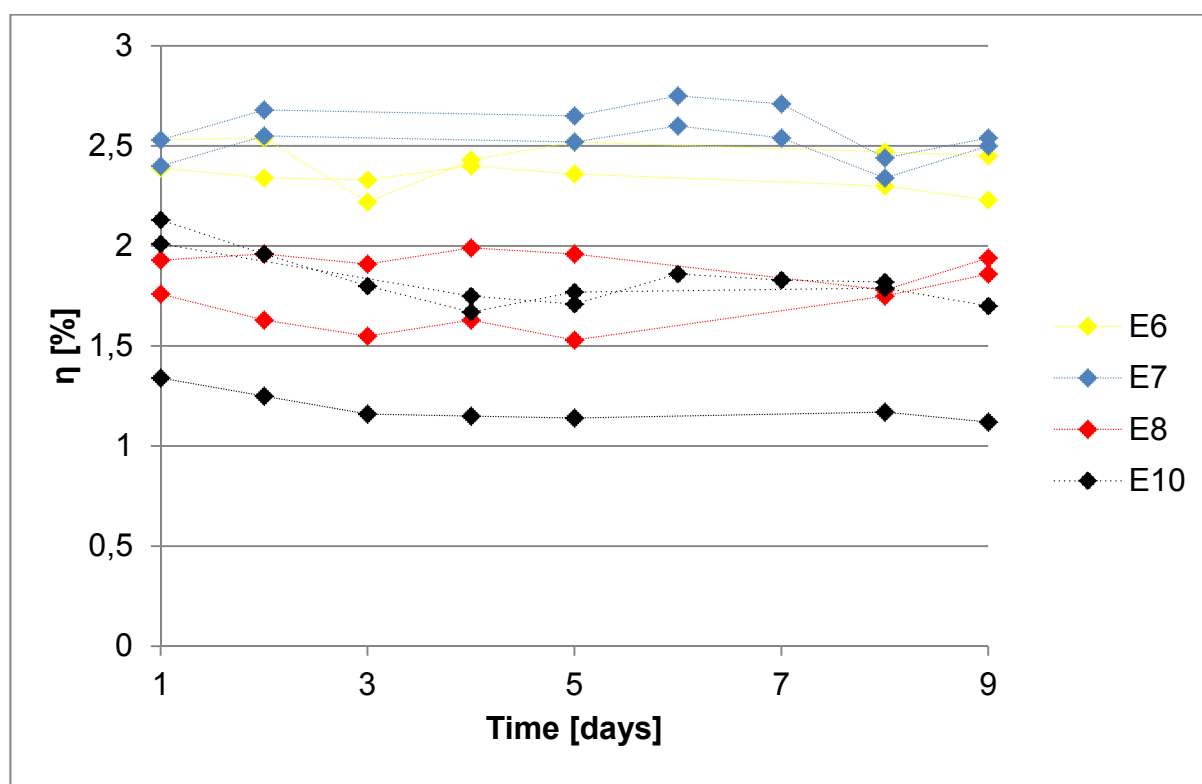


Figure 83 Efficiencies of duplicate DSCs filled with electrolytes E1-E10 and measured over the course of one week. The DSCs were prepared by soaking the TiO_2 electrodes in a solution of ALP1 for 24 hours and $[\text{Cu}(\mathbf{15})_2][\text{PF}_6]$ for 72 hours.

Table 24 shows the photovoltaic parameters of duplicate DSCs containing the best performing electrolyte **E7** on the day of assembly. The relative efficiencies compared to an N719 reference cell are shown and confirm the excellent performance of DSCs using this electrolyte.

Electrolyte	Cell	J_{sc} [mA cm ⁻²]	V_{oc} [mV]	ff [%]	η [%]	η (relative) [%]
E7	1	7.71	499	66	2.53	37.3
	2	7.49	490	65	2.40	35.4
N719	1	17.05	619	64	6.78	100.0

Table 24 Photovoltaic parameters of duplicate DSCs filled with electrolyte E7 on day 1 with respect to a N719 reference cell. The DSCs were prepared by soaking the TiO₂ electrodes in a solution of ALP1 for 24 hours and [Cu(15)₂][PF₆] for 72 hours.

In conclusion, **E7** was shown to be the best performing electrolyte in DSCs with a soaking time of both 24 and 72 hours. An increased soaking time leads to similar or higher efficiencies depending on the electrolyte used. Hence, for the optimization of the I⁻/I₃⁻ electrolytes for [Cu(15)(ALP1)]⁺ sensitized solar cell, **E7** was used as a starting point and a soaking time of 72 hours was applied.

10.2 Optimization of the I⁻/I₃⁻ electrolyte for [Cu(15)(ALP1)]⁺ sensitized solar cells

Based on the results of screening different electrolytes in the previous section, the four components of electrolyte **E7** were systematically varied to find the optimal composition for a maximum performance in DSCs. At first, the optimal ratio and concentrations of I₂ and BMII were investigated. From the optimized conditions, the influence of a change in concentration of the additives TBP and GNCS was investigated. TBP is generally known to increase the V_{oc} . *Boschloo* and *Hagfeldt*¹⁰² found that TBP changes the surface charge of TiO₂ by decreasing the amount of protons and Li⁺ ions on the surface and this shifts the band edge of TiO₂ to more negative potentials. Furthermore, TBP leads to an increase in electron lifetime in the semiconductor¹⁰² and is attributed to a reduced accessibility of the surface for I₃⁻ due to adsorbed TBP on the TiO₂ surface. Both effects lead to an increase in V_{oc} . *Ashbrook et al.*⁵⁰ found that TBP interacts with Cu(II) to form Cu(II)-TBP adducts that are stable with respect to reduction by the mediator on a timescale of minutes. Absence of TBP in their Co^{2+/3+} mediator significantly increased their J_{sc} values in DSCs.

The mechanism for the improvement of DSC efficiency upon addition of GNCS to the electrolyte solution is still under debate. *Kopidakis et al.*¹²⁶ showed that GNCS in the electrolyte leads to a slower recombination by a factor of 20 and simultaneously shifts the band edge to more positive potential. Since a reduction in electron recombination increases V_{OC} but a band edge shift to more positive potential lowers V_{OC} , these effects oppose each other. However, the net result is an overall improvement in the open-circuit potential. *Zhang et al.*¹²⁷ reported an increase in J_{SC} upon addition of GNCS to the electrolyte and this was attributed to an increase in the electron injection. However, *O'Regan et al.*¹²⁸ recently proposed a different mechanism for the improvement of the DSC efficiency upon treatment with GNCS. They disagree with passivation of the TiO_2 surface by GNCS since they found that GNCS only binds weakly to the semiconductor surface. In contrast, they showed that GNCS competes with iodine to bind to N719 and D131 dyes and therefore decreases the surface concentration of dye- I_2 complexes. By reducing recombination loss, a higher collection efficiency and thus photocurrent is achieved.

Name	I₂ [M]	BMII [M]	TBP [M]	GNCS [M]
E7	0.030	0.605	0.396	0.010
Ea	0.300	0.600	0.396	0.010
Eb	0.060	0.600	0.396	0.010
Ec	0.015	0.600	0.396	0.010
Ed	0.005	0.600	0.396	0.010
Ee	0.300	0.302	0.399	0.010
Ef	0.060	0.302	0.396	0.010
Eg	0.015	0.302	0.396	0.010
Uh	0.300	0.100	0.396	0.010
Ei	0.060	0.100	0.396	0.010
Ej	0.015	0.100	0.396	0.010
Ek	0.015	0.600	0.396	0.100
El	0.015	0.600	0.396	-
Em	0.015	0.600	3.960	0.010
En	0.015	0.600	-	0.010

Table 25 Investigated electrolyte compositions, starting from electrolyte E7.

Table 25 shows the electrolyte compositions for the optimization of electrolyte **E7**. To understand the influence of each component, only one parameter was changed at a time. Electrolytes **Ea-Ed** were prepared to investigate the effect of a change in I_2 concentration on

the performance in DSCs. All other concentrations were kept constant. The concentration of I_2 is calculated by the weight per volume. The actual I_2 concentration in the electrolyte after equilibration with the other electrolyte components was not determined. In electrolytes **Ee-Ef**, the concentration of BMII is reduced by half with respect to electrolytes **Ea-Ed** and again the I_2 concentration is varied. In electrolytes **Eh-Ej**, the concentration of BMII is further diluted to a sixth of the initial concentration in electrolytes **Ea-Ed** and again three different I_2 concentrations were prepared. Figure 84 shows the 3D-plot of efficiencies of duplicate DSCs sensitized with $[Cu(15)(ALP1)]^+$ with electrolytes with I_2 concentrations of 0.3 M, 0.06 M or 0.015 M and BMII concentrations of 0.6 M, 0.3 M or 0.1 M in MPN. The highest efficiencies in DSCs were obtained using electrolytes **Ec** and **Eg**. It appears that increasing the BMII concentration at higher I_2 concentrations (0.3 M) significantly increases the efficiency. However, at lower I_2 concentrations the influence of the BMII concentration does not seem to significantly affect the DSC efficiency. On the other hand, the efficiency improves with decreasing concentrations of I_2 . However, even lower concentrations of I_2 do not lead to a further improvement of the DSC efficiency as is shown in the example of electrolytes **Ea-Ed** and **E7** in Figure 85. All electrolytes in Figure 85 have a BMII concentration of 0.6 M and the I_2 concentration is lowered from 0.3 M to 0.005 M. The best efficiencies were still obtained for electrolytes **E7** and **Ec** with I_2 concentrations of 0.03 M and 0.015 M.

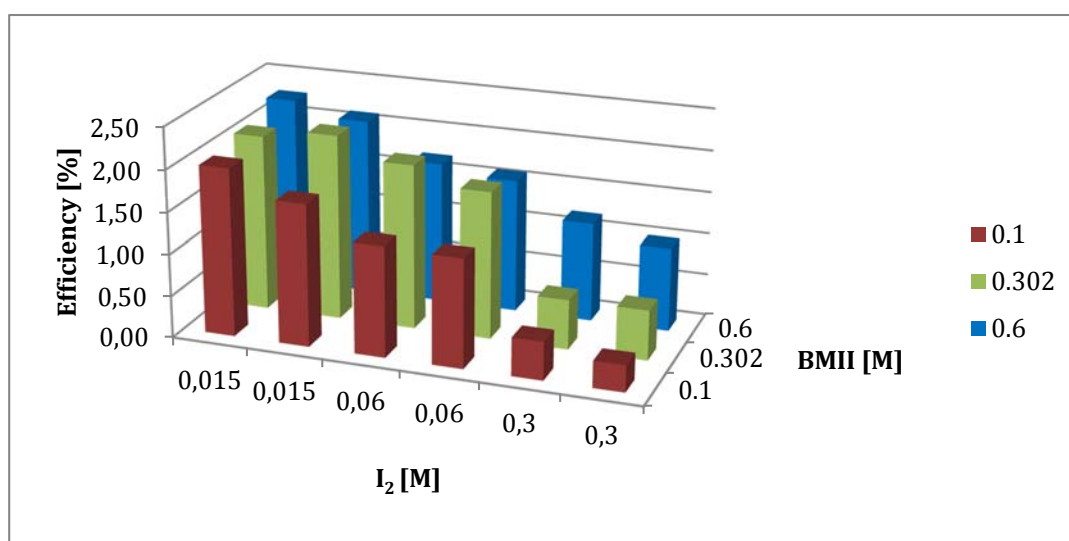


Figure 84 3D-plot of the efficiencies of duplicate DSCs sensitized with $[Cu(15)(ALP1)]^+$ and varying I_2 and BMII concentrations.

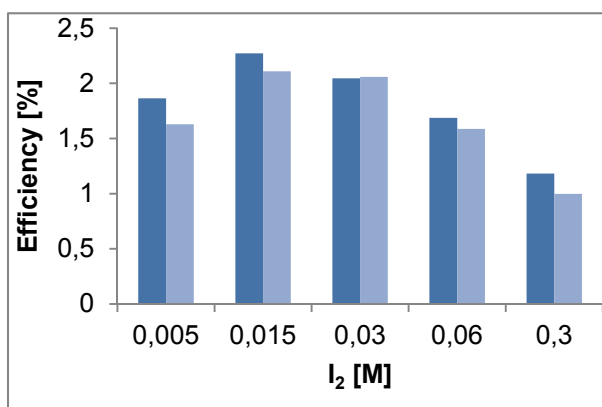


Figure 85 Efficiencies of duplicate DSCs sensitized with $[Cu(15)(ALP1)]^+$ and containing 0.6 M BMII.

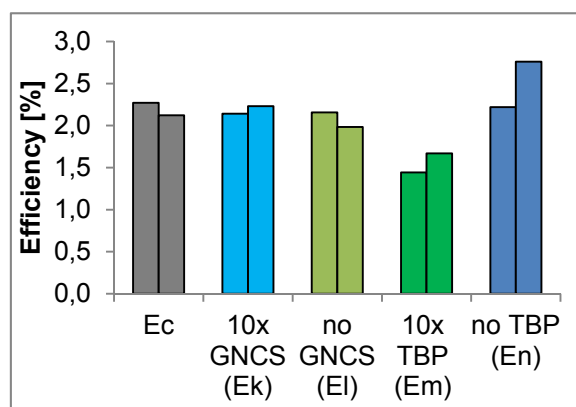


Figure 86 Influence of a change in concentration of the additives GNCS and TBP, respectively, on the performance in $[Cu(15)(ALP1)]^+$ sensitized solar cells.

In the last step, the influence of the additives TBP and GNCS was investigated. For this, the best performing electrolyte from the previous experiments, electrolyte **Ec**, was used as a starting point. Electrolytes **Ek** and **El** have a 10-fold increased concentration of GNCS and no GNCS at all, respectively. Electrolytes **Em** and **En** comprise a 10-fold amount of TBP and no TBP, respectively. Figure 86 shows the results of these experiments with respect to electrolyte **Ec**. GNCS does not seem to have a significant influence on the performance of the Cu(I) sensitized solar cells. Approximately the same efficiency was obtained for a 10-fold increase in concentration or the complete absence of GNCS. On the other hand, a 10-fold increase of the TBP concentration led to inferior efficiencies for the duplicate DSCs. The highest efficiency was measured without TBP.

Electrolyte	Cell	J_{sc} [mA cm ⁻²]	V_{oc} [mV]	ff [%]	η [%]	η [%]
Ek	1	5.83	561	65	2.14	31.8
	2	5.69	566	69	2.23	33.2
El	1	5.51	559	70	2.16	32.1
	2	5.17	560	69	1.98	29.5
Em	1	4.25	576	59	1.44	21.5
	2	4.53	579	64	1.67	24.8
En	1	6.95	483	66	2.22	33.0
	2	7.80	501	71	2.76	41.0
Ec	1	6.16	549	67	2.27	33.8
	2	6.01	547	64	2.11	31.4
N719	1	15.32	664	66	6.72	100.0

Table 26 Photovoltaic parameters of DSCs containing [Cu(15)(ALP1)]⁺ and electrolytes Ek-En on the day of assembly.

Table 26 shows the influence of the additives on the photovoltaic parameters to study the origin of the changes in efficiency discussed above. Comparison of electrolytes **Ek**, **EI** and **Ec** shows the influence of GNCS. As discussed above, GNCS lowers the conduction band edge of TiO₂ and reduces surface electron recombination. These two contrary effects lead to a complicated response of the DSCs upon a change in GNCS concentration. The complete absence of GNCS in **EI** leads to lower J_{SC} values consistent with reduced charge injection from the dye into the semiconductor as a consequence of the higher conduction band edge of TiO₂ as reported by *Zhang*¹²⁷. By adding GNCS to the electrolyte solution (**Ec**), J_{SC} is improved with a simultaneous decrease in V_{OC} . A 10-fold increase in the concentration of GNCS in **Ek** increases the V_{OC} with respect to **Ec** due to a reduced surface recombination confirmed by V_{OC} decay measurements (discussed later). The origin of the loss in current density is unclear; however, it may arise from a negative influence of a high GNCS concentration on the electrolyte diffusion.

Electrolytes **Em** and **En** with respect to **Ec** reveal the impact of TBP on the photovoltaic parameters of [Cu(15)(ALP1)]⁺ sensitized solar cells. It was found that the absence of TBP significantly lowers the V_{OC} values with respect to DSCs from electrolyte **Ec**. This is mainly attributed to an increased recombination rate found by V_{OC} decay measurements and is consistent with the absence of surface passivation by TBP as reported by *Boschloo* and *Hagfeldt*¹⁰². A 10-fold increase in the concentration of TBP in **Em** with respect to **Ec** shows the opposite effect with the highest V_{OC} measured (579 mV) for these types of DSCs due to a reduced recombination rate. This is related to an opposite impact on the J_{SC} , which may arise from reduced ion mobility since more TBP significantly increases the viscosity of the electrolyte solution. Based on the findings of *Ashbrook et al.*⁵⁰, the inferior J_{SC} values may also be attributed to formation of a Cu(II)-TBP adduct to temporarily⁵⁰ remove some of the dye molecules from participation in photoinjection.

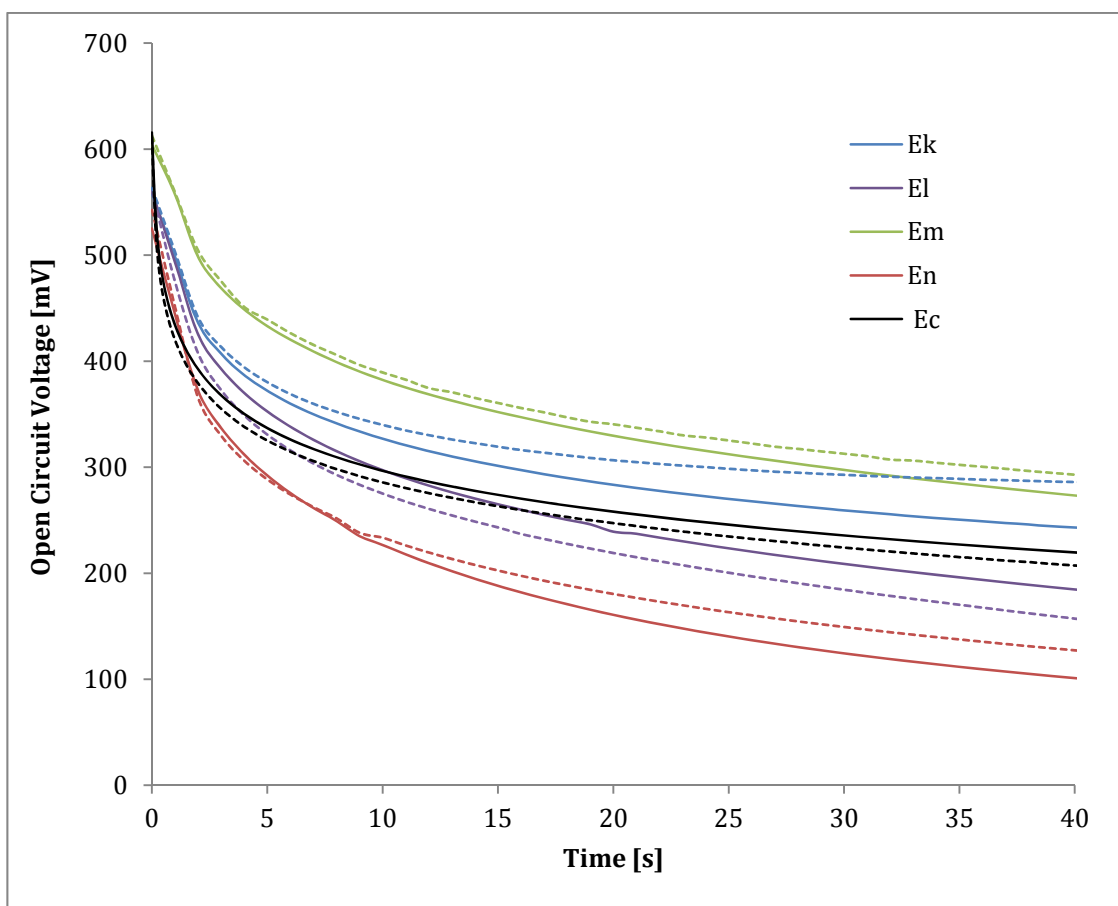


Figure 87 Open circuit voltage decay (OCVD) measurements of cells containing electrolytes **Ek-En** with respect to **Ec**.

Figure 87 shows V_{oc} decay curves of duplicate DSCs containing electrolytes **Ek-En** with respect to **Ec**. All duplicate cells show consistent results and still have a V_{oc} of 110 mV or higher after 40 seconds. However, the differences in the V_{oc} after 40 seconds as well as the initial decay within the first 5-10 seconds are significant between the different electrolytes. In agreement with the literature (discussed above), the incorporation of GNCS and TBP significantly reduces the surface recombination rate. **Ek** and **Em**, having a 10-fold increase of GNCS and TBP with respect to **Ec**, respectively, both show a reduced recombination rate. In contrast, the absence of either of the two in **El** and **Eo** increases the recombination rate significantly.

In conclusion, the efficiency of **E7** was optimized by reducing the I_2 concentration by half and completely removing TBP. This gave an optimized I^-/I_3^- electrolyte consisting of 0.015 M I_2 , 0.6 M BMII and 0.01 M GNCS labelled as electrolyte **En**. GNCS in the electrolyte did not show a significant influence on the overall DSC performance. However, testing the dependence

of the GNCS concentration in the absence of TBP will be part of further investigations. Based on the results obtained, an ideal additive would lower the conduction band edge of TiO_2 , thereby slightly increasing the charge injection yield (as observed for GNCS) and simultaneously efficiently suppress the surface recombination at the semiconductor-electrolyte interface and the dye layer-electrolyte interface (as observed for TBP).

11 Co(II/III) electrolytes for Cu(I) Sensitized Solar Cells

In dye sensitized solar cells, the V_{OC} is determined by the Fermi level and the redox potential of the electrolyte. The V_{OC} can be significantly increased upon changing the redox couple from I^-/I_3^- to $Co^{2+}/3+$ due to the more positive redox potentials of the cobalt complexes with respect to the I^-/I_3^- redox couple.¹²⁹ However, cobalt electrolytes were long thought to be limited by recombination and mass transport.⁷⁰ Recently, it was found that by adjusting the thickness, particle size, pore size and porosity of TiO_2 layers, diffusion problems of cobalt electrolytes can be eliminated and DSC efficiencies improved.²⁶ *Feldt et al.* have previously shown that the introduction of butoxy chains to organic sensitizers lowers the recombination at the TiO_2 surface. When these sensitizers were combined with $Co^{2+}/3+$ redox complexes containing unsubstituted ligands such as 2,2'-bipyridine, superior performances were observed with respect to systems in which the steric hindrance of the ligands in the cobalt electrolyte was increased to suppress recombination.²² Based on these results, *Yella et al.* developed a donor-acceptor zinc(II) porphyrin sensitizer that showed a record efficiency of 12% for DSCs based on $[Co(bpy)_3]^{2+}/3+$ electrolyte.¹³

In this chapter, the replacement of I^-/I_3^- electrolyte by the Co(II/III) mediator in copper(I) sensitized solar cells is shown. In the first section, the optimization of the TiO_2 electrode for the use of cobalt electrolytes is shown. In the second part, the *heteroleptic* Cu(I) dyes $[Cu(\mathbf{13})(ALP1)]^+$ and $[Cu(\mathbf{15})(ALP1)]^+$ are compared in DSCs containing $[Co(bpy)_3][PF_6]_{2/3}$ electrolyte. Finally, in the last section of this chapter, the influence of the counter ion in $[Co(bpy)_3]^{2+}/3+$ electrolytes is investigated.

For all the measurements in this chapter, the cobalt electrolytes consist of 0.2 M $[Co(bpy)_3][PF_6]_2$, 0.05 M $[Co(bpy)_3][PF_6]_3$, 0.1 M $LiClO_4$ and 0.2 M TBP in MeCN.

11.1 Optimization of the TiO₂ working electrode for DSCs incorporating [Co(bpy)₃][PF₆]_{2/3} electrolytes

This section was carried out in collaboration with *Lukas J. Troxler* as part of his ‘Wahlpraktikum’ (internship).

Based on the report of *Tsao et al.*, who showed that through the optimization of the TiCl₄ post-treatment step, diffusion problems with a [Co(bpy)₃]^{2+/3+} electrolyte could be eliminated²⁶, the post-treatment with aqueous TiCl₄ of screen printed TiO₂ electrodes was optimized for our system. By variation of the TiCl₄ concentration in the post-treatment step, the porosity and the overall surface of the TiO₂ semiconductor can be influenced. The increase in surface area allows for adsorption of a higher amount of dye molecules but reduces the porosity. For the cobalt redox mediator, the porosity has a crucial influence on the performance as mass transport through the nanoporous layer and surface recombination play a more important role for this redox couple. For the same reason, the thickness of the TiO₂ layer needs to be optimized for the use of cobalt electrolytes.

We first investigated DSCs from 3+1 layer TiO₂ electrodes (3+1 meaning 3 layers TiO₂ + 1 TiO₂ scattering layer). This is 1 layer thinner compared to the DSCs based on I⁻/I₃⁻ discussed earlier and was implemented to avoid mass transport problems with the [Co(bpy)₃]^{2+/3+} electrolyte. Table 27 shows the photovoltaic parameters of cells containing [Co(bpy)₃][PF₆]_{2/3} electrolyte and [Cu(**13**)(**ALP1**)]⁺ sensitized 3+1 layer TiO₂ electrodes. The TiCl₄ concentration in the post-treatment step was varied from 0-60 mM. Since dye uptake is expected to depend on the dipping time in the dye solution, DSCs with soaking times of 24 and 64 hours are compared in Table 27. Independent of the soaking time, higher TiCl₄ concentrations in the post-treatment step led to superior efficiencies. This trend generally arises from an increase in J_{SC} , V_{OC} and ff . Higher efficiencies were obtained with 64 hours soaking time (compared to 24 hours) mainly due to higher J_{SC} values, consistent with a higher dye uptake. In summary, the results presented in Table 27 suggest that a longer soaking time of 64 h and post-treatment with a TiCl₄ concentration >15 mM leads to improved power conversion efficiencies in DSCs incorporating [Co(bpy)₃][PF₆]_{2/3} electrolyte.

Soaking time [h]	[TiCl ₄] [mM]	J _{sc} [mA cm ⁻²]	V _{oc} [mV]	ff [%]	η [%]
24	0	1.15	380	49	0.22
	5	1.75	535	53	0.50
	15	1.62	564	56	0.51
	30	1.56	590	61	0.56
	40	2.20	542	55	0.66
	60	3.17	596	63	1.19
64	0	2.28	586	55	0.73
	5	1.83	611	62	0.69
	15	3.15	621	63	1.24
	30	3.44	628	70	1.50
	40	3.48	619	70	1.51
	60	2.87	621	68	1.21

Table 27 Photovoltaic parameters of [Cu(13)(ALP1)]⁺ sensitized solar cells with [Co(bpy)₃][PF₆]_{2/3} electrolyte and 3+1 TiO₂ layer electrodes on the day of assembly. The electrodes were soaked in the *homoleptic* Cu(I) dye solution for 24 hours and 64 hours. The TiCl₄ post-treatment was varied from 0 to 60 mM.

To investigate if the concentration of the TiCl₄ post-treatment is a general effect or depends on the electrolyte, analogous DSCs were prepared incorporating Standard II electrolyte, (i.e. the conventional I⁻/I₃⁻ redox couple). Table 28 shows the photovoltaic parameters of DSCs containing the [Cu(13)(ALP1)]⁺ sensitizer with a soaking time of 24 hours. Post-treatment with a 5 mM TiCl₄ solution leads to an increase in *J*_{sc} and *V*_{oc} resulting in a higher efficiency with respect to an untreated DSC. However, in contrast to the results obtained for the DSCs containing the cobalt electrolyte (Table 27), further increase of the TiCl₄ concentration has little or no effect on the DSC performance.

[TiCl ₄] [mM]	J _{sc} [mA cm ⁻²]	V _{oc} [mV]	ff [%]	η [%]
0	1.99	588	69	0.80
5	2.73	612	70	1.18
15	2.00	608	67	0.81
30	2.25	599	65	0.88
40	2.11	591	64	0.80
60	2.34	592	64	0.89

Table 28 Photovoltaic parameters of [Cu(13)(ALP1)]⁺ sensitized solar cells using Standard II electrolyte 3+1 TiO₂ layer electrodes on the day of assembly. The electrodes were soaked in the *homoleptic* Cu(I) dye solution for 24 hours. The TiCl₄ post-treatment was varied from 0 to 60 mM.

A further gain in efficiency was obtained by increasing the TiO₂ layer thickness from 3+1 to 4+1 layers and increasing the soaking time to 110 hours (Table 29). Duplicate cells were

prepared to validate the data and a general trend towards higher efficiencies with increasing concentration of the TiCl₄ post-treatment up to 60 mM was found. A maximum efficiency of 2.02% was obtained with a DSC from a 60 mM TiCl₄ treated TiO₂ electrode, which is similar to the efficiency achieved with the reference DSC filled with Standard II electrolyte on the day of assembly. No concentrations greater than 80 mM TiCl₄ solutions were tested as the increasing acidity was expected to have a negative impact on the DSC performance. An additional duplicate cell was prepared for each of the 15 mM, 30 mM and 40 mM TiCl₄ post-treated DSCs but these data were discarded as they were not consistent with the other two prepared cells for each concentration. This indicates that for better validation, a higher number of duplicate cells should be prepared.

[TiCl ₄] [mM]	Cell	J _{sc} [mA cm ⁻²]	V _{oc} [mV]	ff [%]	η [%]
0	1	2.70	467	51	0.65
	2	3.01	545	51	0.83
15	1	2.49	389	50	0.48
	2	2.39	391	51	0.48
30	1	3.16	517	55	0.89
	2	3.39	427	52	0.75
40	1	5.05	578	59	1.73
	2	3.56	573	55	1.12
60	1	4.00	607	66	1.60
	2	4.95	610	67	2.02
80	1	3.42	607	62	1.29
	2	2.94	546	64	1.02
40	1	5.30	551	68	1.98
Standard II	2	5.11	574	71	2.08
40	1	15.78	690	63	6.90
N719	2	13.61	699	64	6.04

Table 29 Photovoltaic parameters of duplicate [Cu(13)(ALP1)]⁺ sensitized solar cells with [Co(bpy)₃][PF₆]_{2/3} electrolyte on the day of assembly. The 4+1 layer electrodes were soaked in the *homoleptic* Cu(I) dye solution for 110 hours. TiCl₄ post-treatment was varied from 0-80 mM. For comparison a DSC containing [Cu(13)(ALP1)]⁺ and Standard II electrolyte and a N719 reference cell with a soaking time of 64 hours is shown.

The stability of DSCs containing [Cu(13)(ALP1)]⁺ and either [Co(bpy)₃][PF₆]_{2/3} or the I⁻/I₃⁻ Standard II electrolyte was investigated by continuous irradiation and measurement over a period of 30 hours. For this, a different measuring setup had to be used that allowed for simultaneous measurement of two independent DSCs. A homemade source meter (prepared by the workshop in the Department of Physics) was controlled via a *Labview* interface

programmed by *Dr. Gino Günzburger* to measure J/V curves every 5 minutes. As in our usual setup, the cells were fully masked and the temperature was kept at 25 °C throughout the measurements. Due to different measuring resistances, this measuring setup leads to lower photovoltaic parameters with respect to our standard setup. The differences are shown in Table 30 and indicate that all photovoltaic parameters are lower but a significant difference is found for J_{SC} and ff . However, the error is systematic and has no influence on the stability of the cell itself and the trends from the long-term measurement are valid. The two best performing cells in Table 29 (60 mM $TiCl_4$ post-treated cell 2 with $[Co(bpy)_3][PF_6]_{2/3}$ and 40 mM $TiCl_4$ post-treated cell 2 with Standard II electrolyte) were chosen for this experiment. The difference of the photovoltaic parameters from Table 29 to Table 30 are due to ageing processes of the DSCs.

Measuring setup	Electrolyte	$[TiCl_4]$ [mM]	J_{sc} [mA cm ⁻²]	V_{oc} [mV]	ff [%]	η [%]
normal	$[Co(bpy)_3][PF_6]_{2/3}$	60	4.28	594	71	1.80
	I^-/I_3^-	40	4.55	596	71	1.93
long-term	$[Co(bpy)_3][PF_6]_{2/3}$	60	3.73	581	61	1.33
	I^-/I_3^-	40	3.83	571	62	1.35

Table 30 Comparison of the standard measuring setup with the one used for long-term measurements. The same two cells were measured under the same conditions other than the sourcemeter and the controlling software.

Figure 88 shows the long-term measurement of the $[Cu(13)(ALP1)]^+$ sensitized solar cells for the two electrolytes. After an initial small decrease within the first 10-15 hours, both DSCs are surprisingly stable for the next 15 hours. The observed stability of the DSC containing Standard II electrolyte towards nucleophilic attack by iodide ion is in contrast to earlier reports by our group when *heteroleptic* Cu(I) complexes are sometimes found to be labile towards attack by I^- in DSCs.⁴⁷

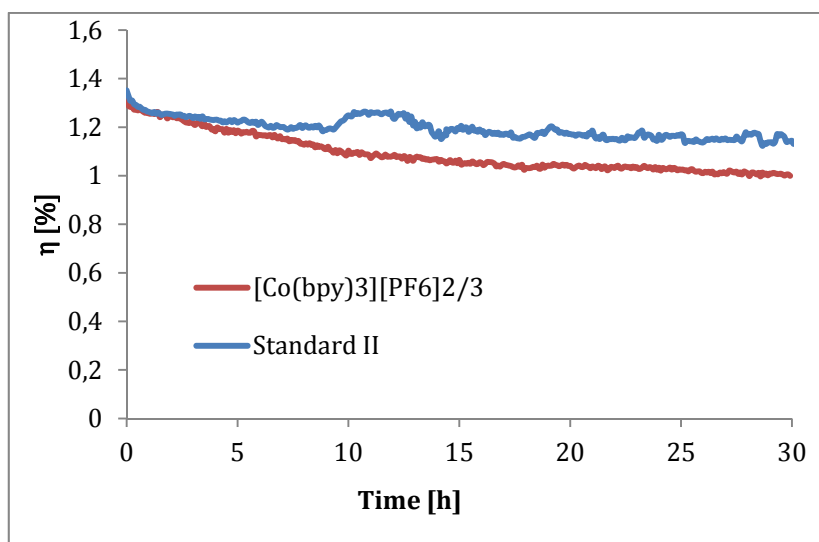


Figure 88 Long-term measurement of $[\text{Cu}(\mathbf{13})(\text{ALP1})]^+$ sensitized solar cells with either $[\text{Co}(\text{bpy})_3][\text{PF}_6]_{2/3}$ or Standard II electrolyte, respectively.

11.2 DSCs Containing $[\text{Cu}(\mathbf{13})(\text{ALP1})]^+$ or $[\text{Cu}(\mathbf{15})(\text{ALP1})]^+$ Dyes with $[\text{Co}(\text{bpy})_3][\text{PF}_6]_{2/3}$ Electrolyte

The work in this section was carried out in collaboration with *Tatjana Kosmalski* as part of her ‘Wahlpraktikum’ (internship).

11.2.1 Comparison of $[\text{Cu}(\mathbf{13})(\text{ALP1})]^+$ and $[\text{Cu}(\mathbf{15})(\text{ALP1})]^+$ Sensitized Solar Cells

In this section, the performance of DSCs using $[\text{Co}(\text{bpy})_3][\text{PF}_6]_{2/3}$ electrolyte with the *heteroleptic* Cu(I) dyes $[\text{Cu}(\mathbf{13})_2][\text{PF}_6]$ and $[\text{Cu}(\mathbf{15})_2][\text{PF}_6]$ was investigated. The initial idea behind the introduction of butoxy chains to the diarylunit in $[\text{Cu}(\mathbf{15})_2][\text{PF}_6]$ with respect to $[\text{Cu}(\mathbf{13})_2][\text{PF}_6]$ was to increase the donating character of the ancillary ligand as well as the steric hindrance for a consequent reduction in recombination in DSCs with $\text{Co}^{2+/3+}$ electrolytes.¹³⁰ Butoxy chains have been found to significantly improve the performance of triphenylamine based organic sensitizers in DSCs containing cobalt electrolytes.²² Due to the steric hindrance of the butoxy chains, electron recombination with the electrolyte, which previously was reported to be one of the main issues with this kind of mediator,⁷⁰ was significantly reduced.

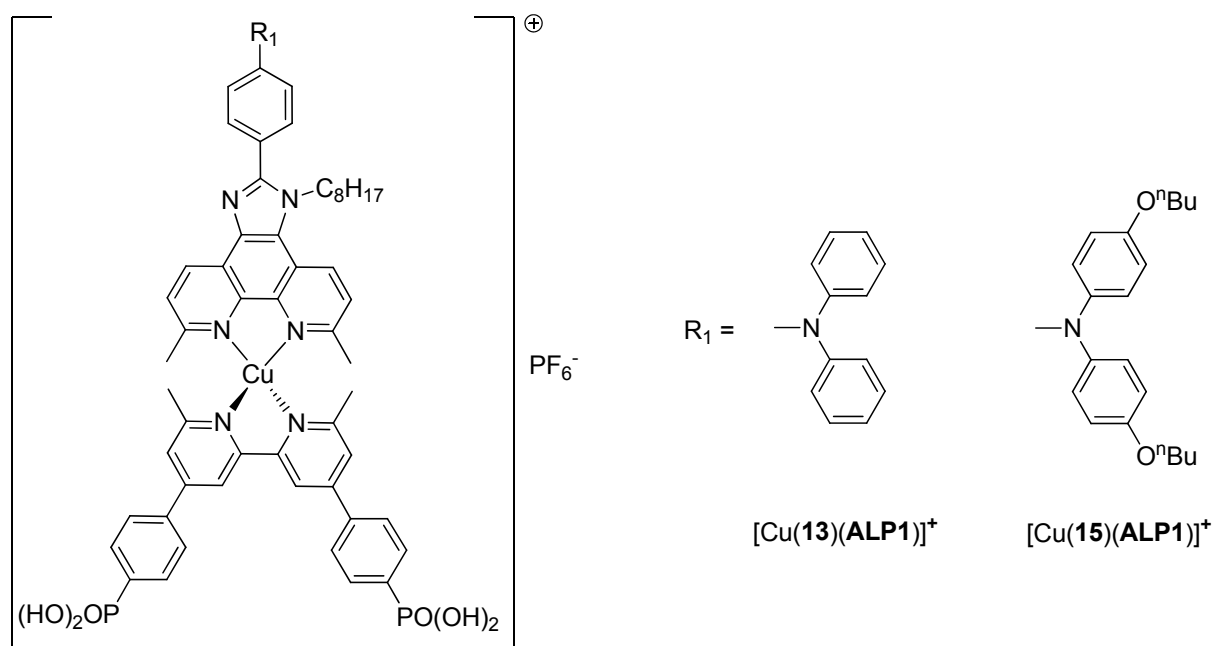


Figure 89 The *heteroleptic* Cu(I) dyes $[\text{Cu}(\mathbf{13})_2][\text{PF}_6]$ and $[\text{Cu}(\mathbf{15})_2][\text{PF}_6]$ investigated in this section.

For the experiments in this section, the optimized conditions for the use of $[\text{Co}(\text{bpy})_3][\text{PF}_6]_{2/3}$ electrolyte with $[\text{Cu}(\mathbf{13})(\mathbf{ALP1})]^+$ sensitized solar cells were applied: 4+1 screen-printed layers of TiO_2 , post-treatment with 60 mM TiCl_4 solution and 68 hours soaking time in the *homoleptic* dye solution. Table 31 shows the photovoltaic parameters of duplicate DSCs containing $[\text{Cu}(\mathbf{13})(\mathbf{ALP1})]^+$ and $[\text{Cu}(\mathbf{15})(\mathbf{ALP1})]^+$, respectively, and $[\text{Co}(\text{bpy})_3][\text{PF}_6]_{2/3}$ electrolyte on the day of assembly. All Cu(I) DSCs reach efficiencies higher than 2% on the day of assembly and the highest efficiency of 2.6% was obtained with a $[\text{Cu}(\mathbf{15})(\mathbf{ALP1})]^+$ sensitized solar cell. The maximum efficiency arises from an increase in V_{OC} and J_{SC} with respect to the $[\text{Cu}(\mathbf{13})(\mathbf{ALP1})]^+$ sensitized cells. While the V_{OC} values are comparable for the four cells, the J_{SC} values are significantly higher with DSCs containing $[\text{Cu}(\mathbf{15})(\mathbf{ALP1})]^+$. The efficiencies for DSCs containing $[\text{Cu}(\mathbf{13})(\mathbf{ALP1})]^+$ are higher than the values obtained in Table 29 in Section 11.1. This may arise from a change of the counter electrode from self-made to commercial ones (Solaronix Test Cell kit). However, the duplicate cells are fairly consistent on the day of assembly.

A comparison of the photovoltaic parameters in Table 31 obtained for DSCs containing $[\text{Co}(\text{bpy})_3][\text{PF}_6]_{2/3}$ electrolyte with the results obtained by using the I^-/I_3^- Standard II electrolyte in Table 20, shows that for both ($[\text{Cu}(\mathbf{13})(\mathbf{ALP1})]^+$ and $[\text{Cu}(\mathbf{15})(\mathbf{ALP1})]^+$) dyes, higher conversion efficiencies were obtained using the cobalt electrolyte. The best DSC containing $[\text{Cu}(\mathbf{13})(\mathbf{ALP1})]^+$ and Standard II electrolyte had a J_{SC} of 5.41 mA cm^{-2} , a V_{OC} of 562 mV, a ff

of 75%, an η of 2.29% and a relative η of 28.4% with respect to the N719 reference cell. The best DSC containing [Cu(15)(ALP1)]⁺ and Standard II electrolyte had a J_{SC} of 5.65 mA cm⁻², a V_{OC} of 540 mV, a ff of 68%, an η of 2.07% and a relative η of 25.7% with respect to the N719 reference cell. Comparison with the data from Table 31 shows that both dyes have significantly higher J_{SC} and V_{OC} values and only the ff s are reduced with cobalt electrolyte, resulting in slightly improved overall conversion efficiencies. If the relative efficiencies with respect to the N719 reference cells are taken into account, DSCs containing cobalt electrolyte clearly outperform cells using I⁻/I₃⁻ electrolyte.

Dye	Electrolyte	Cell	J_{sc} [mA cm ⁻²]	V_{oc} [mV]	ff [%]	η [%]	η^a [%]	η^b [%]
[Cu(13)(ALP1)] ⁺	[Co(bpy) ₃][PF ₆] _{2/3}	1	5.85	635	64	2.37	37.4	33.0
		2	5.99	634	62	2.35	37.1	32.7
[Cu(15)(ALP1)] ⁺	[Co(bpy) ₃][PF ₆] _{2/3}	1	6.83	609	55	2.28	35.9	31.6
		2	6.71	647	61	2.65	41.8	36.8
N719	Standard II	1	16.05	667	59	6.34	100.0	-
		2	16.06	680	66	7.20	-	100.0

Table 31 Photovoltaic parameters of duplicate [Cu(13)(ALP1)]⁺ and [Cu(15)(ALP1)]⁺ sensitized solar cells with [Co(bpy)₃][PF₆]_{2/3} electrolyte on the day of assembly. For comparison duplicate N719 reference cells are shown. ^a relative to N719 cell 1, ^b relative to N719 cell 2.

Figure 90 shows the efficiencies of the four cells over time. There is no general trend for each set of duplicate cells. However, all cells undergo a ripening effect within the first 4 days and show a constant behaviour until day 8. The [Cu(15)(ALP1)]⁺ sensitized cell 1 shows a strong ripening effect over the first 4 days with a maximum efficiency of 2.79%. On the contrary, [Cu(13)(ALP1)]⁺ sensitized cell 1 decreases within the first days to 1.54% on day 4. Since the behaviour of one cell is contrary to the other three cells (including the duplicate cell), this indicates a fabrication problem; however, by eye, no electrolyte leakage was detected and the origin of the problem was not confirmed.

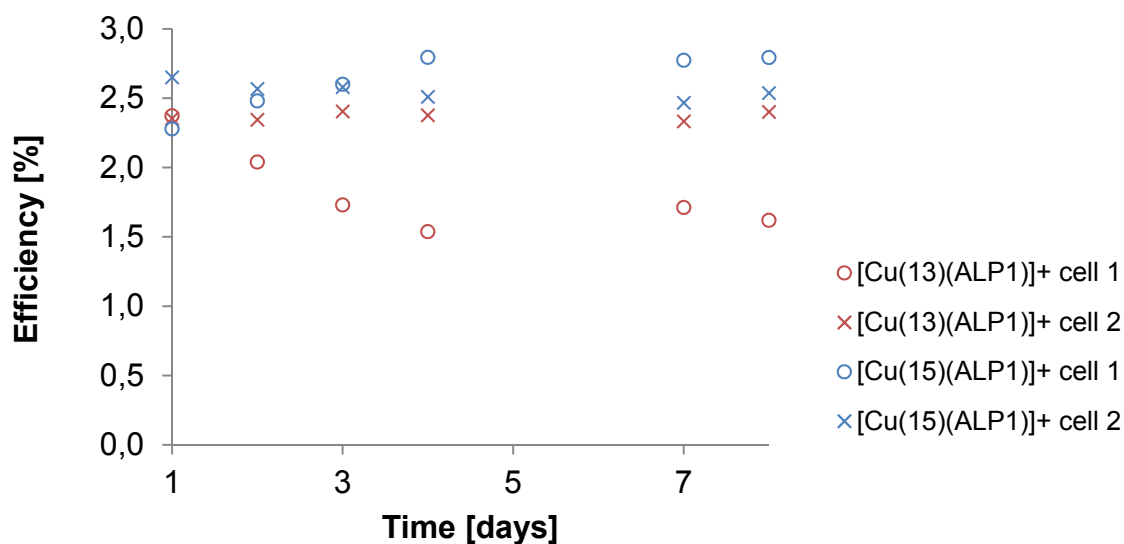


Figure 90 Efficiencies over time for $[\text{Cu}(13)(\text{ALP1})]^+$ and $[\text{Cu}(15)(\text{ALP1})]^+$ sensitized solar cells and $[\text{Co}(\text{bpy})_3][\text{PF}_6]_{2/3}$ electrolyte.

Figure 91 shows the external quantum efficiency of the DSCs presented in Table 31 on day 2. Consistent with the higher J_{SC} values obtained for the DSCs containing $[\text{Cu}(15)(\text{ALP1})]^+$, the quantum efficiencies are significantly higher over the whole spectral width. A maximum around 490 nm is seen for all the investigated cells with a maximum EQE of 48% obtained for $[\text{Cu}(15)(\text{ALP1})]^+$.

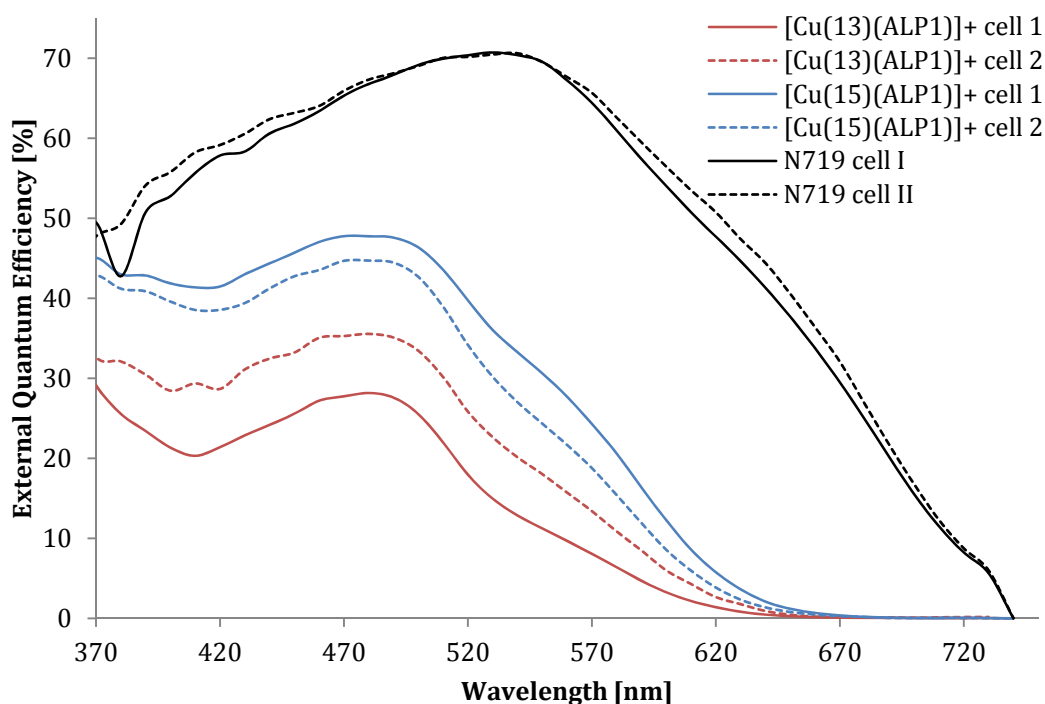


Figure 91 External quantum efficiencies of the DSCs in Table 31 on day 2.

The J/V curves in Figure 92 measured on day 2 graphically summarize the trends discussed above for the photovoltaic parameters. The dark current measurement in the same figure shows that the lower V_{OC} measured for $[\text{Cu}(\mathbf{15})(\text{ALP1})]^+$ cell 1 arises from a higher surface recombination indicated by an onset at lower potential in the dark current measurement. The other three cells have similar onset values consistent with the similar V_{OC} measured. However, this shows that the initial idea of introduction of butoxy chains when designing the dyes did not lead to a reduced surface recombination. This may arise from the large distance between the butoxy substituents and the TiO_2 surface if a binding through two $-\text{P}(\text{O})(\text{OH})_2$ groups is assumed. Organic sensitizers usually only consist of one anchoring group, typically cyanoacrylic acid, allowing for more flexibility of the sensitizer and the butyloxy chains coming closer to the semiconductor surface.

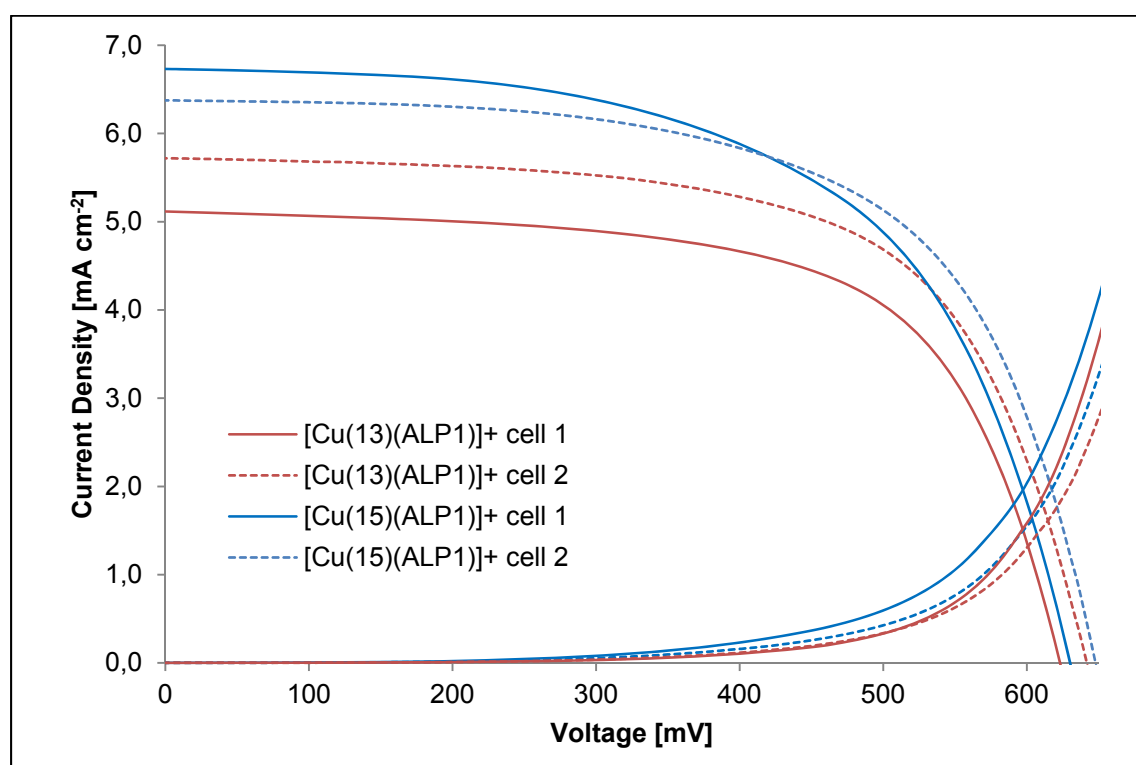


Figure 92 J/V curves and dark current measurements of duplicate $[\text{Cu}(\mathbf{13})(\text{ALP1})]^+$ and $[\text{Cu}(\mathbf{15})(\text{ALP1})]^+$ sensitized solar cells with $[\text{Co}(\text{bpy})_3][\text{PF}_6]_{2/3}$ electrolyte on day 2.

In conclusion, the *heteroleptic* Cu(I) dyes $[\text{Cu}(\mathbf{13})(\text{ALP1})]^+$ and $[\text{Cu}(\mathbf{15})(\text{ALP1})]^+$ show superior efficiencies by changing the electrolyte from the I^-/I_3^- based Standard II electrolyte to $[\text{Co}(\text{bpy})_3][\text{PF}_6]_{2/3}$ arising from a significant increase in V_{OC} and J_{sc} . $[\text{Cu}(\mathbf{15})(\text{ALP1})]^+$ sensitized solar cells outperformed DSCs containing $[\text{Cu}(\mathbf{13})(\text{ALP1})]^+$ dye with a maximum efficiency of 2.79% reached on day 4 following a ripening effect.

11.2.2 Silane Additives as a Recombination Blocking Layer

An alternative to modifying the sensitizer for an efficient blocking of the surface recombination is the addition of coadsorbents. Addition of coadsorbents was shown to efficiently reduce recombination, shift the conduction band edge, and avoid performance losses due to dye aggregation.^{131–134} The most commonly used coadsorbant is chenodeoxycholic acid and it has been shown to induce a negative shift of the semiconductor Fermi level, which reduces recombination through passivation of the surface, reduce aggregation of dye molecules and lead to more efficiently bound dye molecules to the TiO₂ surface.^{23,133,135,136} Other coadsorbents such as 3-phenylpropionic acid or stearic acid¹³¹ have also been successfully implemented in DSCs. Furthermore, silanes were found to strongly bind to the TiO₂ surface and form insulating films on the semiconductor surface, significantly reducing the recombination process^{137,138} or increasing the amount of strongly bound dyes on the surface with concomitant improved conversion efficiencies.¹³⁹ Carli *et al.* found the alkoxysilanes APTES and TMAS effectively passivate the TiO₂ surface, thereby reducing surface recombination with Co^{2+/3+} electrolytes in ruthenium(II) sensitized solar cells.¹⁴⁰

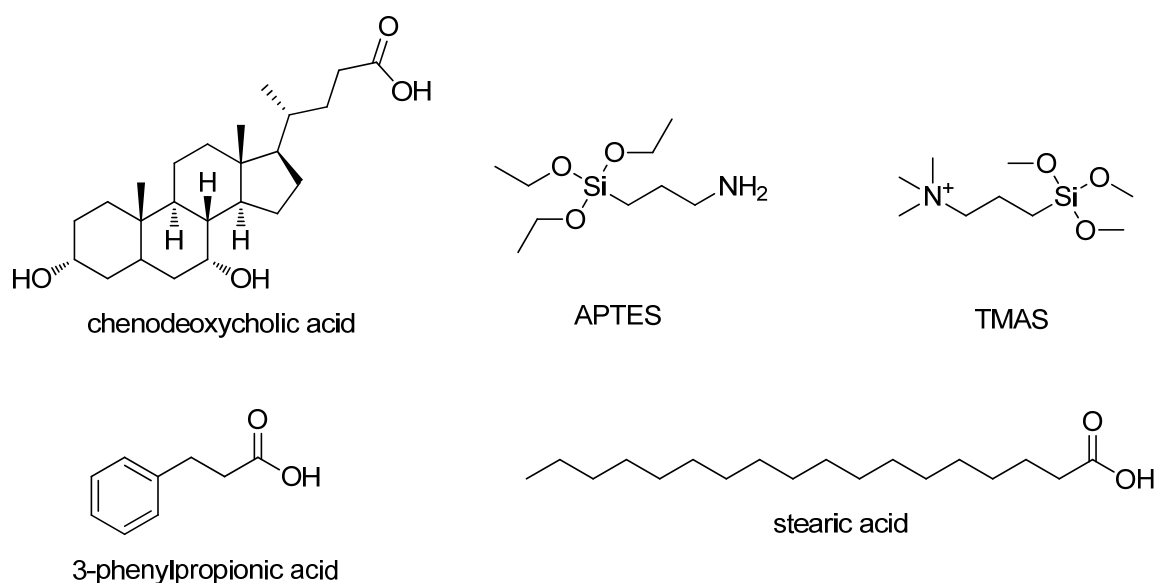


Figure 93 Chemical structure of the coadsorbents chenodeoxycholic acid, APTES, TMAS, 3-phenylpropionic acid and stearic acid.

In this section, the influence of coadsorbants 3-(aminopropyl)triethoxysilane (APTES) and trimethylammoniumpropyltrimethoxysilane (TMAS) on the overall conversion efficiency in DSCs is shown. For this, the dye-sensitized 4+1 layer TiO₂ electrodes were dipped into a 0.1% v/v solution of APTES in toluene at 55–60 °C for 1 hour (i.e. the APTES treatment was *after*

the on-surface dye assembly). After rinsing with toluene and drying in N₂ the cells were assembled as usual.

Table 32 shows the photovoltaic parameters of DSCs containing [Cu(13)(ALP1)]⁺ and [Cu(15)(ALP1)]⁺ and a subsequent APTES treatment. By eye, the APTES treatment leads to a slight bleaching of the electrodes, which is consistent with an exchange of the surface bound dye by APTES. This results in lower current densities and hence lower conversion efficiencies of the APTES treated cells shown in Table 32 with respect to untreated cells (Table 31). However, a 50-60 mV increase in V_{OC} along with an improved ff of 5-10% was obtained for DSCs from both Cu(I) dyes.

Dye	Electrolyte	Cell	J _{sc} [mA cm ⁻²]	V _{oc} [mV]	ff [%]	η [%]	η ^a [%]	η ^b [%]
[Cu(13)(ALP1)] ⁺	[Co(bpy) ₃][PF ₆] _{2/3}	1	3.08	692	73	1.55	24.5	21.6
		2	2.65	688	70	1.27	20.0	17.6
[Cu(15)(ALP1)] ⁺	[Co(bpy) ₃][PF ₆] _{2/3}	1	2.40	661	70	1.11	17.5	15.4
		2	2.69	697	69	1.30	20.6	18.1
N719	Standard II	1	16.05	667	59	6.34	100.0	-
		2	16.06	680	66	7.20	-	100.0

Table 32 Photovoltaic parameters of duplicate [Cu(13)(ALP1)]⁺ and [Cu(15)(ALP1)]⁺ sensitized solar cells with [Co(bpy)₃][PF₆]_{2/3} electrolyte on the day of assembly. The sensitized TiO₂ electrodes were treated with a 0.1% V/V solution of APTES in toluene at 55-60°C for 1 hour. ^a relative to N719 cell 1, ^b relative to N719 cell 2

The gain in V_{OC} is consistent with the concept of blocking the recombination at the TiO₂ surface. To confirm that the APTES treatment reduces the recombination rate of electrons from the semiconductor with the electrolyte, V_{OC} decay (OCVD) measurements were carried out and are compared with measurements of untreated cells in Figure 94. The APTES treated cells show a significantly reduced recombination rate with respect to the untreated cells for both dyes. This is consistent with V_{OC} values obtained from the J/V measurements and shows that the concept of surface passivation using silanes with alkyl tails is valid.

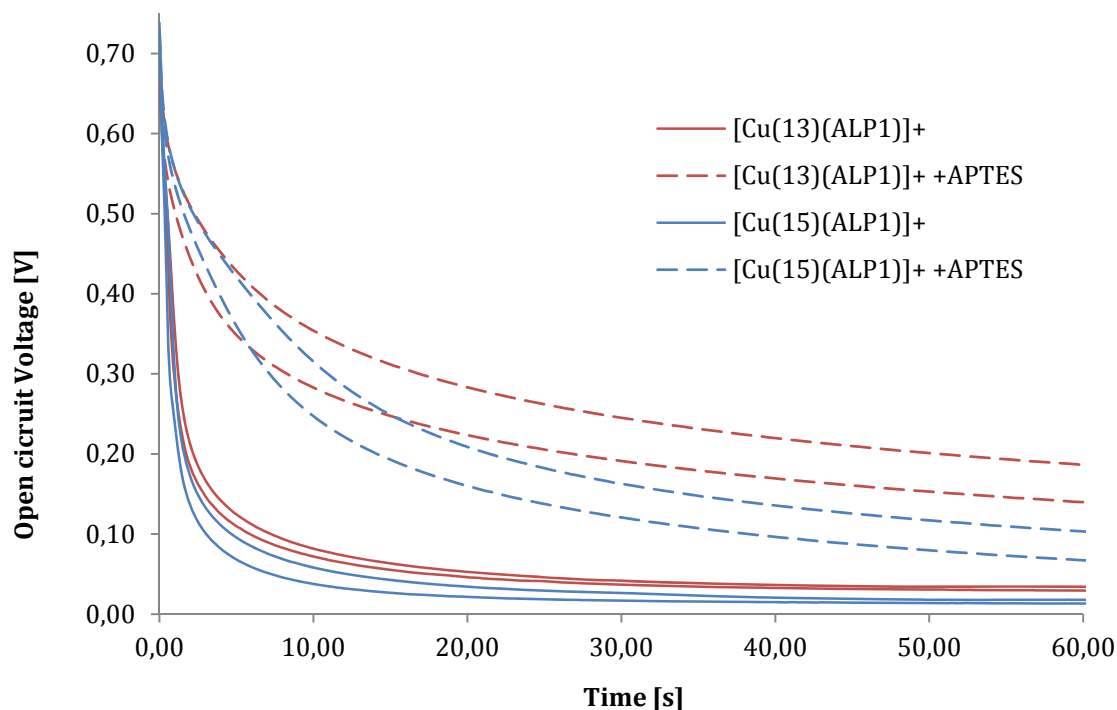


Figure 94 Comparison of OCVD measurements of APTES treated and untreated DSCs containing [Cu(13)(ALP1)]⁺ and [Cu(15)(ALP1)]⁺ dyes, respectively.

Based on the results obtained by *Carli et al.*¹⁴⁰ who also found TMAS to efficiently reduce recombination with $\text{Co}^{2+/3+}$ electrolytes through steric and additional electronic repulsion of Co^{3+} , DSCs from TMAS post-treated TiO_2 electrodes were prepared. For this, sensitized electrodes were immersed in a 0.2 % v/v solution of trimethylammoniumpropyl-trimethoxysilane chloride (TMAS Cl) in methanol at 55-60 °C for one hour. However, the electrodes were visibly bleached during this process, indicating a desorption of the sensitizer from the surface. An additional dipping cycle in the *homoleptic* Cu(I) dye solutions did not lead to a recovery of the dye on the surface. This leads to the assumption that the bleaching is caused by a complete desorption of the dye, including the anchoring ligand. Table 33 shows the photovoltaic parameters obtained with the TMAS treated DSCs. Consistent with the observed bleaching, the J_{sc} values are significantly lower than with untreated cells (Table 31). This results in lower V_{oc} values and, consequently, in low efficiencies.

Dye	Electrolyte	Cell	J _{sc}	V _{oc}	ff	η	η ^a	η ^b
			[mA cm ⁻²]	[mV]	[%]	[%]	[%]	[%]
[Cu(13)(ALP1)] ⁺	[Co(bpy) ₃][PF ₆] _{2/3}	1	1.38	495	68	0.47	7.4	6.5
		2	1.37	498	67	0.46	7.2	6.4
[Cu(15)(ALP1)] ⁺	[Co(bpy) ₃][PF ₆] _{2/3}	1	1.59	512	70	0.57	9.0	7.9
		2	2.61	532	69	0.96	15.1	13.3
N719	Standard II	1	16.05	667	59	6.34	100.0	-
		2	16.06	680	66	7.20	-	100.0

Table 33 Photovoltaic parameters of duplicate [Cu(13)(ALP1)]⁺ and [Cu(15)(ALP1)]⁺ sensitized solar cells with [Co(bpy)₃][PF₆]_{2/3} electrolyte on the day of assembly. The sensitized TiO₂ electrodes were treated with a 0.2% v/v solution of TMAS Cl in methanol at 55-60°C for 1 hour.

In conclusion, it is possible to passivate the TiO₂ surface using APTES to significantly reduce the recombination rate from electrons in the semiconductor to the electrolyte species. However, these experiments are a proof-of-concept and further investigations on the optimum conditions for the passivation are required to convert the reduced recombination into an improvement of the overall conversion efficiency. Shorter soaking times in the APTES solution, lower APTES concentrations, or passivation at room temperature may lead to superior results.

11.3 Influence of the Counterion of the Co(II/III) Electrolyte on the DSC Performance

The work in this section was done in collaboration with *Fabienne Thommen* as part of her “Wahlpraktikum” (internship).

As discussed earlier, cobalt electrolytes have been extensively used in DSCs with a wide range of dyes. However, different counter ions for Co(II/III) complexes have been reported but only little focus has been given to their influence. *Nusbaumer et al.*⁶⁷ showed that there is only very little change in the redox potentials of [Co(dmbip)₂]²⁺ (dmbip = [2,6-bis(1'-methylbenzimidazol-2'-yl)pyridine]) with DDS⁻ (dodecylsulfate), PF₆⁻ and ClO₄⁻ as the counterions and, consequently, no change in *V*_{oc} in solar cells. However, they found a significant difference in *J*_{sc} and *η* upon change of the counterion of [Co(dmbip)₂]²⁺ when being used in DSCs. While in most studies PF₆⁻ is used as the counterion for Co(II/III) electrolytes, recently [B(CN)₄]⁻ has been used for DSCs showing record efficiencies of over 12%.¹³ Therefore, the influence of the counterion, which is either PF₆⁻ or [B(CN)₄]⁻, was investigated in this section using DSCs containing [Cu(13)(ALP1)]⁺ and [Cu(15)(ALP1)]⁺, respectively. The electrolytes consisted of 0.2 M [Co(bpy)₃][X]₂, 0.05 M [Co(bpy)₃][X]₃, 0.1 M LiClO₄, and 0.2 M TBP in MeCN, with X⁻ being either PF₆⁻ or [B(CN)₄]⁻. Table 34 shows the photovoltaic

parameters of duplicate DSCs for each dye and electrolyte on day 1. For DSCs containing [Cu(13)(ALP1)]⁺ and [Co(bpy)₃][PF₆]_{2/3}, only one cell gave usable results. All cells show efficiencies between 2.53% and 3.38% on the day of assembly with all having remarkably high relative efficiencies of 32-43% with respect to the best performing N719 reference cell 1. The outstandingly high efficiency of 3.38% obtained for a DSC containing [Cu(15)(ALP1)]⁺ and Co(bpy)₃][B(CN)₄]_{2/3} is the highest measured efficiency in this thesis and arises from a *J*_{sc} of 7.01 mA cm⁻², a *V*_{oc} of 670 mV, a *ff* of 72%, an *η* of 3.38% and shows a remarkable relative efficiency of 43% with respect to an N719 reference cell. These correspond to the best performing DSC with a copper(I) dye reported to date. The *V*_{oc} values obtained for the DSCs containing [Cu(15)(ALP1)]⁺ and using either of the two cobalt electrolytes are now in the range of the N719 reference cells. However, the errors between duplicate cells are relatively large (compared to previous measurements) and more duplicate cells are required to get more insight into the influence of the counterion. In conclusion, no general trend was found for any of the characteristic parameters on going from PF₆⁻ to [B(CN)₄]⁻ based on the results shown in Table 34.

Dye [mM]	Electrolyte	Cell	<i>J</i> _{sc} [mA cm ⁻²]	<i>V</i> _{oc} [mV]	<i>ff</i> [%]	<i>η</i> [%]	<i>η</i> ^a [%]
[Cu(13)(ALP1)] ⁺	[Co(bpy) ₃][PF ₆] _{2/3}	1	6.95	629	70	3.04	38.9
	[Co(bpy) ₃][B(CN) ₄] _{2/3}	1	6.20	664	69	2.84	36.4
[Cu(15)(ALP1)] ⁺	[Co(bpy) ₃][PF ₆] _{2/3}	2	5.69	647	69	2.53	32.4
		1	6.28	678	71	3.02	38.7
	[Co(bpy) ₃][B(CN) ₄] _{2/3}	2	6.36	685	72	3.14	40.2
		1	7.01	670	72	3.38	43.3
N719	Standard II	2	5.75	681	70	2.75	35.2
		1	17.33	682	66	7.81	100.0
		2	15.73	689	67	7.27	-
		3	16.85	693	64	7.49	-
		4	17.82	679	64	7.73	-

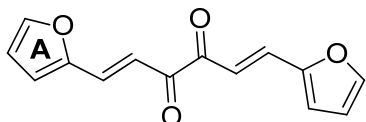
Table 34 Photovoltaic parameters of DSCs containing [Cu(13)(ALP1)]⁺ or [Cu(15)(ALP1)]⁺ dyes and either [Co(bpy)₃][PF₆]_{2/3} or [Co(bpy)₃][B(CN)₄]_{2/3} electrolyte on the day of assembly. ^a relative to the N719 reference cell 1.

12 Experimental Part

12.1 Anchoring Ligands

12.1.1 (1*E*,5*E*)-1,6-Di(furan-2-yl)hexa-1,5-diene-3,4-dione (2)

SF78



This synthesis was done according to a literature procedure.¹⁸

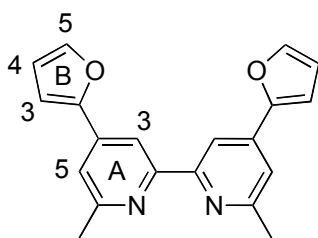
2-Furaldehyde (21.0 ml, 24.4 g, 254 mmol, 2.0 eq) and 2,3-butanedione (11.1 ml, 10.9 g, 127 mmol, 1.0 eq) were dissolved in 20 ml of EtOH to give a dark brown solution. 12 drops of piperidine were added and the mixture was stirred at rt for 9 days. The orange precipitate was filtered off and was washed with EtOH to yield the product as an orange solid (2.66 g, 11.0 mmol, 8.7%).

¹H NMR (400 MHz, CDCl₃) δ/ppm: 7.61 (d, *J* = 15.9 Hz, 1H, H^{CH-CO}), 7.57 (dd, *J* = 1.8, 0.7 Hz, 1H, H^{A5}), 7.31 (d, *J* = 15.9 Hz, 1H, H^{CH=CH-CO}), 6.80 (dd, *J* = 3.5, 0.6 Hz, 1H, H^{A3}), 6.53 (dd, *J* = 3.5, 1.8 Hz, 1H, H^{A4}).

The data matches well the literature values.¹⁸

12.1.2 1*E*,5*E*-1,6-Di(2-furyl)hexa-1,5-diene-3,4-dione

SF25



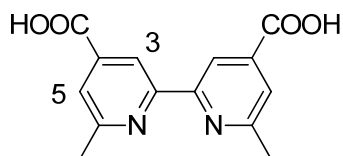
Acetylpyridinium chloride (2.84 g, 16.53 mmol, 2.0 eq) was dissolved in 70 ml of methanol. (1*E*,5*E*)-1,6-Di(furan-2-yl)hexa-1,5-diene-3,4-dione (2.00 g, 8.26 mmol, 1.0 eq) and ammonium acetate (4.00 g, 51.9 mmol, 6.3 eq) were added to the colourless solution and the orange solution was stirred and heated. The solution immediately turned brown and was refluxed over night. A beige solid was filtered off and washed with cold methanol and dried in the desiccator to give a grey-beige solid (1.25 g, 48%).

¹H-NMR (400 MHz, CDCl₃, δ/ppm): 8.44 (d, *J* = 1.0 Hz, 2H, H^{3A}), 7.56 (dd, *J* = 1.7, 0.6 Hz, 2H, H^{5B}), 7.45 (d, *J* = 1.3 Hz, 2H, H^{5A}), 6.98 (dd, *J* = 3.4, 0.6 Hz, 2H, H^{3B}), 6.54 (dd, *J* = 3.5, 1.8 Hz, 2H, H^{4B}), 2.69 (s, 6H, CH₃).

The $^1\text{H-NMR}$ spectrum agrees well with that given in literature ¹⁴¹.

12.1.3 6,6'-Dimethyl-2,2'-bipyridine-4,4'-dicarboxylic acid (ALC)

SF79



This synthesis was done according to a literature procedure.¹⁸

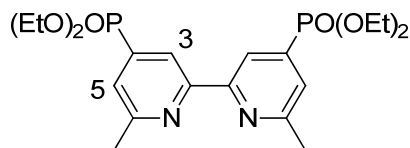
1*E*,5*E*-1,6-Di(2-furyl)hexa-1,5-diene-3,4-dione (1.40 g, 4.43 mmol, 1.0 eq.) was dissolved in 300 ml of a warm *t*-BuOH/water mixture (5:1) and KMnO_4 (7.00 g, 44.3 mmol, 10.0 eq.) was added. The mixture was refluxed at 90 °C for 3h and left standing to cool down to room temperature. The dark brown mixture was filtered through celite and the filter cake was washed with water (~150 ml), 30 ml of a 1:3 *t*-BuOH/water mixture and with 30 ml of CHCl_3 . The light brown compound was refluxed in CHCl_3 for 1 h and was filtered hot. The product was isolated as a beige solid (543 mg, 1.99 mmol, 45.0%).

$^1\text{H NMR}$ (400 MHz, DMSO) δ /ppm: 13.72 (s, 2H, H^{COOH}), 8.64 (d, $J = 1.4$ Hz, 2H, H^3), 7.77 (d, $J = 1.4$ Hz, 2H, H^5), 2.67 (s, 6H, H^{Me}).

The $^1\text{H-NMR}$ agrees well with the literature.¹⁸

12.1.4 Tetraethyl 6,6'-dimethyl-2,2'-bipyridine-4,4'-diylbisphosphonate (4)

SF63



This synthesis was done according to a literature procedure.¹⁸

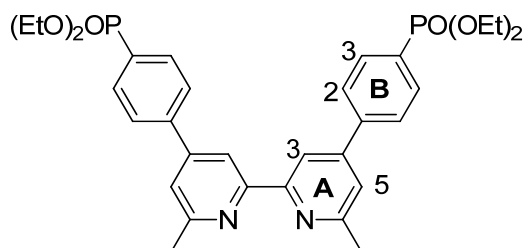
4,4'-Dibromo-6,6'-dimethyl-2,2'-bipyridine (100 mg, 0.292 mmol, 1.0 eq.), Pd(PPh₃)₄ (30.7 mg, 0.0266 mmol, 0.091 eq.) and Cs₂CO₃ (208 mg, 0.638 mmol, 2.2 eq.) were added to a 2-5 ml microwave vial and the vial flushed with N₂. 2 ml THF and diethyl phosphite (0.07 ml, 80.8 mg, 0.585 mmol, 2.0 eq.) were added and the reaction mixture was heated to 110 °C for 20 min. in the microwave reactor. The yellow mixture was filtered and the solvent was removed. The brown residue was redissolved in CH₂Cl₂ and washed with water. The organic layer was dried over Na₂SO₄ and the solvent was removed to obtain a brown oil. The product was purified by column chromatography on silica eluting with CH₂Cl₂ /MeOH 95:5 to obtain beige crystals which were recrystallized from hexane to yield the product as white crystals (73 mg, 0.160 mmol, 54.8%).

¹H NMR (250 MHz, CDCl₃) δ/ppm: 8.58 (d, *J*_{PH} = 14.0 Hz, 2H, H^{A3}), 7.56 (d, *J*_{PH} = 14.3 Hz, 2H, H^{A5}), 4.18 (m, 8H, H^{CH2}), 2.69 (s, 6H^{Me}), 1.37 (t, *J* = 7.1 Hz, 12H, H^{CH2CH3}).

The values agree well with the literature.¹⁸

12.1.5 tetraethyl ((6,6'-dimethyl-[2,2'-bipyridine]-4,4'-diyl)bis(4,1-phenylene))bis(phosphonate) (5)

SF64



4,4'-Bis(4-bromophenyl)-6,6'-dimethyl-2,2'-bipyridine⁴⁴ (100 mg, 0.202 mmol, 1.0 eq.), Pd(PPh₃)₄ (21.3 mg, 0.0184 mmol, 0.091 eq.) and Cs₂CO₃ (144 mg, 0.442 mmol, 2.2 eq.) were added to a 2-5 ml microwave vial and the vial flushed with N₂. 2 ml THF and diethyl phosphite (0.05 ml, 55.9 mg, 0.405 mmol, 2.0 eq.) were added and the reaction mixture was heated to 110 °C for 20 min. in the microwave reactor. The yellow mixture was filtered and the solvent was

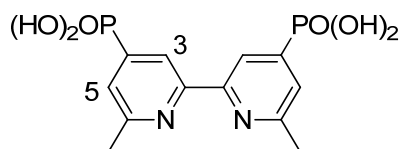
removed. The brown residue was redissolved in CH_2Cl_2 and washed with water. The organic layer was dried over Na_2SO_4 and the solvent was removed to obtain a brown oil. The product was purified by column chromatography on silica eluting with CH_2Cl_2 / MeOH 95:5 to obtain a beige, sticky oil (98 mg, 0.161 mmol, 79.7%).

^1H NMR (250 MHz, CDCl_3) δ /ppm: 8.51 (d, $J = 1.2$ Hz, 2H, $\text{H}^{\text{A}3}$), 8.02 – 7.89 (m, 4H, $\text{H}^{\text{B}2/\text{B}3}$), 7.85 (m, 4H, $\text{H}^{\text{B}2/\text{B}3}$), 7.41 (d, $J = 1.5$ Hz, 2H, $\text{H}^{\text{A}5}$), 4.17 (m, 8H, H^{Et}), 2.72 (s, 6H, H^{Me}), 1.36 (t, $J = 7.1$, 12H, $\text{H}^{\text{Et-CH}3}$).

This compound was made prior to the published work but agrees well with the data in the literature.⁴⁵

12.1.6 (6,6'-dimethyl-[2,2'-bipyridine]-4,4'-diyl)diphosphonic acid (ALP)

SF65



This synthesis was done according to a literature procedure.¹⁸

4 (73.0 mg, 0.160 mmol, 1.0 eq.) was dissolved in CH_2Cl_2 in an atmosphere of N_2 . BrSiMe_3 (0.21 ml, 245 mg, 1.60 mmol, 10.0 eq.) was added dropwise and the solution was stirred at room temperature for 5 h. The solvent was removed and the orange residue was redissolved in MeOH to give a yellow solution that was stirred at rt overnight. As no precipitate was obtained, 5 ml of water and a few drops of 1M HCl were added and the solution was extracted with CH_2Cl_2 . The aqueous phase was separated and the water removed. The extraction was evaporated to obtain an orange solid. The residue was redissolved in 2.5 ml of MeOH cooled with an ice bath and was stirred overnight. A white precipitate was obtained, which was filtered, washed with MeOH and diethyl ether and dried in vacuo (18 mg, 0.052 mmol, 32.7%).

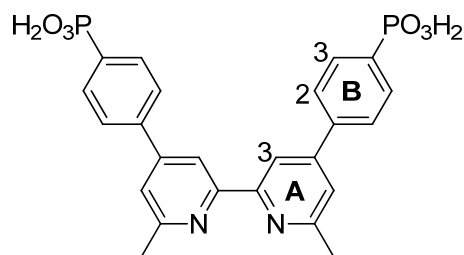
^1H NMR (250 MHz, D_2O) δ /ppm: 8.35 (d, $J_{\text{PH}} = 12.0$ Hz, 2H, $\text{H}^{\text{A}3/\text{A}5}$), 7.92 (d, $J_{\text{PH}} = 12.2$ Hz, 2H, $\text{H}^{\text{A}3/\text{A}5}$), 2.80 (s, 6H, H^{Me}).

^1H NMR (400 MHz, TFA) δ /ppm: 9.39 (d, $J_{\text{PH}} = 12.3$ Hz, 2H, $\text{H}^{\text{A}3}$), 8.54 (d, $J_{\text{PH}} = 12.6$ Hz, 2H, $\text{H}^{\text{A}5}$), 3.06 (s, 6H, H^{Me}).

The ^1H NMR spectrum matches the literature data.¹⁸

12.1.7 ((6,6'-dimethyl-[2,2'-bipyridine]-4,4'-diyl)bis(4,1-phenylene))diphosphonic acid (ALP1)

SF75



5 (280 mg, 0.460 mmol, 1.0 eq.) was dissolved in dry CH₂Cl₂ in an atmosphere of N₂. Bromotrimethylsilane (0.6 ml, 704 mg, 4.60 mmol, 10.0 eq.) was added dropwise and the mixture was stirred at room temperature for 47 h. The solvent was removed and the remaining yellow solid was redissolved in MeOH (15 ml) and stirred at room temperature to form a white precipitate which was filtered off and was washed with MeOH and diethyl ether (204 mg, 0.411 mmol, 89.3%).

¹H NMR (500 MHz, TFA) δ/ppm: 8.66 (s, 2H, H^{A3}), 8.29 (s, 2H, H^{A5}), 8.12 (dd, *J*_{PH} = 14.0, *J*_{HH} = 8.0 Hz, 4H, H^{B3}), 8.02 – 7.97 (m, 4H, H^{B2}), 3.03 (s, 6H, H^{Me}).

¹H NMR (400 MHz, DMSO-*d*₆) δ 8.62 (s, 2H, H^{A3}), 8.01 (dd, *J* = 7.8, 2.6 Hz, 4H, H^{A5/B2/B3}), 7.94 – 7.78 (m, 6H, H^{A5/B2/B3}), 2.73 (s, 6H, H^{Me}).

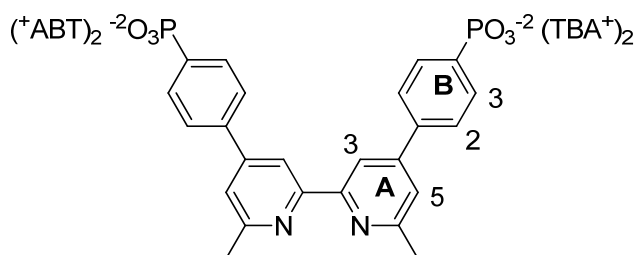
MALDI MS: *m/z* 497.0 [M+H]⁺ (calc. 497.1).

ESI MS *m/z*: 497.1 [M+H]⁺ (calc. 497.1).

The protonated form measured in TFA matches the literature data well but the measurement in DMSO is shifted with respect to the literature probably due to the protonation state or water content.⁴⁵ Addition of basic alumina to the NMR-tube didn't lead to any change.

12.1.8 ALP1 TBA

SF101



ALP1 (100 mg, 0.201 mmol, 1.0 eq.) was suspended in ~2 ml of EtOH and N^iBu_4OH (40% sol. in H_2O) was added till everything was dissolved. The solvent was removed and the slightly yellow residue was dried in vacuo to yield the product as a beige solid (24.9 mg, 17.0 mmol, 8.5 %).

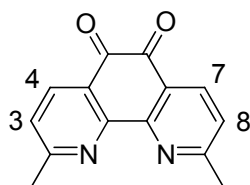
1H NMR (400 MHz, MeOD) δ 8.43 (m, 2H, H^{A3}), 7.97 (dd, $J = 12.0, 8.3$ Hz, 4H, $H^{B2/B3}$), 7.84 (dd, $J = 8.3, 2.9$ Hz, 4H, $H^{B2/B3}$), 7.64 (m, 2H, H^{A5}), 3.30 (dt, $J = 3.2, 1.6$ Hz, 32H, H^{NCH_2}), 3.22 (m, 32H), 2.71 (s, 6H, H^{bpyMe}), 1.64 (dt, $J = 15.9, 7.8$ Hz, 32H, $H^{NCH_2CH_2}$), 1.40 (h, $J = 7.4$ Hz, 32H, $H^{NCH_2CH_2CH_2}$), 1.06 – 0.95 (t, $J = 7.3$ Hz, 48H, H^{Me}).

1H NMR (250 MHz, $CDCl_3$) δ/ppm : 8.21 (s, 2H, H^{A3}), 7.75 (m, 4H, $H^{B2/B3}$), 7.45 – 7.32 (m, 4H, $H^{B2/B3}$), 7.12 (s, 2H, H^{A5}), 3.39 – 3.04 (m, 32H, H^{NCH_2}), 2.37 (s, 6H, H^{bpyMe}), 1.55 (s, 32H, $H^{NCH_2CH_2}$), 1.36 (h, $J = 6.9$ Hz, 32H, $H^{NCH_2CH_2CH_2}$), 0.92 (t, $J = 7.2$ Hz, 48H, H^{Me}).

12.2 Ligand Synthesis

12.2.1 2,9-Dimethyl-1,10-phenanthroline-5,6-dione (1)

SF120, SF148



This synthesis was done according to a literature procedure.⁸⁵ Neocuproine (10.0 g, 46.0 mmol, 1 eq) was dissolved in 107 ml of 60% aqueous sulfuric acid. Potassium bromate (8.47 g, 50.6 mmol, 1.1 eq) was added portionwise over a period of 1.5 h to give an orange solution. The mixture was stirred at rt overnight. After 20h the orange mixture

was poured into ice and was neutralized with 8 M NaOH solution. The yellow precipitate was collected and recrystallized from methanol to yield the product as a yellow solid (8.70 g, 36.5 mmol, 79%).

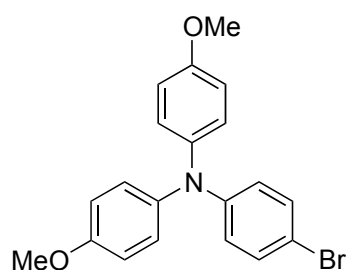
^1H NMR (500 MHz, CDCl_3) δ /ppm: 8.41 – 8.32 (d, $J = 8.0$ Hz, 2H, H^4), 7.45 – 7.36 (d, $J = 8.0$ Hz, 2H, H^3), 2.99 – 2.63 (s, 6H, H^{Me}).

^{13}C NMR (126 MHz, CDCl_3) δ /ppm: 178.98 (2C, C^5), 167.25 (2C, C^2), 152.74 (2C, $\text{C}^{10\text{a}}$), 137.60 (2C, C^4), 126.17 (2C, $\text{C}^{4\text{a}}$), 125.65 (2C, C^3), 26.13 (2C, C^{Me}).

The ^1H -NMR spectrum agrees well with the literature.⁸⁵

12.2.2 4-bromo-*N,N*-bis(4-methoxyphenyl)aniline (2)

SF23



This synthesis was made according to reference ¹⁴².

Under an atmosphere of N_2 sodium (598 mg, 26.0 mmol, 2.5 eq) was carefully dissolved in MeOH and 2,4,6-collidine (32.0 ml, 29.1 g, 240 mmol, 23.1 eq) was added to obtain a pale yellow solution. CuI (1.98 g, 10.4 mmol, 1.0 eq) and tris(4-bromophenyl)amine (5.01 g, 10.4 mmol, 1.0 eq) was added. The mixture was refluxed for 2 hours and was allowed to cool to room temperature and the solvent was removed. The residue was dissolved in TBME and washed with 1M HCl and water. The combined organic fractions were dried over Na_2SO_4 and the solvent was removed. The dark green oil was purified by column chromatography on alumina eluting with cyclohexane/TBME 60:1 to yield the product as a white solid (1.11 g, 2.88 mmol, 28%).

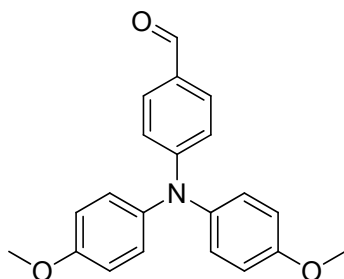
^1H NMR (400 MHz, CDCl_3) δ / ppm: 9.75 (s, 1H), 7.63 (d, $J = 8.9$ Hz, 2H), 7.13 (d, $J = 8.9$ Hz, 4H), 6.89 (m, 4H), 6.85 (d, $J = 8.8$ Hz, 2H), 3.82 (s, 6H).

ESI MS m/z : 334.2 [$\text{M}+\text{H}$]⁺ (calc. 334.1).

The ^1H -NMR spectrum agrees well with the literature.¹⁴²

12.2.3 Di-4-anisyl-4-bromophenylamine (3)

SF27



This synthesis was made according to reference ¹⁴².

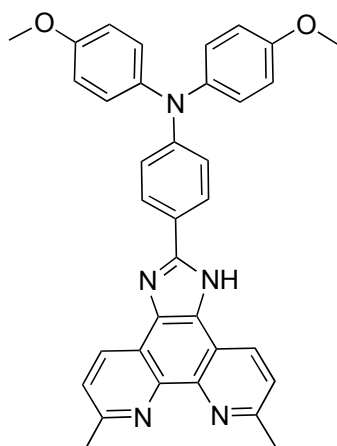
In an atmosphere of N₂, a solution of **2** (1.10 g, 2.85 mmol, 1.0 eq) in 15 ml of dry THF was cooled to -70 °C with an acetone/CO₂ cooling bath. A 1.6 M solution of *tert*-butyl lithium (3.56 ml, 2.46 g, 5.70 mmol, 2.0 eq) was added dropwise over a period of 15 min. The solution was stirred for 1 h and 4-formylmorpholine (0.43 ml, 492 mg, 4.28 mmol, 1.5 eq) was added and the solution was allowed to warm up to rt. After quenching with 1 ml of conc. HCl, the solution was diluted with 10 ml of water and extracted with TBME three times. The combined organic fractions were washed with saturated NaHCO₃ solution and water and the solvent was removed. After purification with column chromatography on silica eluting with cyclohexane/TBME 2:1 the product was isolated as a yellow oil (480 mg, 1.44 mmol, 51%).

¹H NMR (400 MHz, CDCl₃) δ / ppm: 7.62 (dt, *J* = 9.0 Hz, 2.2 Hz, 2H), 7.12 (dt, 4H, *J* = 9.0 Hz, 2.2 Hz), 6.88 (dt, *J* = 9.1 Hz, 2.2 Hz, 4H), 6.84 (dt, *J* = 9.1 Hz, 2.2 Hz, 2H), 3.81 (s, 6H).

The ¹H-NMR spectrum agrees well with the literature.¹⁴²

12.2.4 4-(6,9-dimethyl-1H-imidazo[4,5-f][1,10]phenanthrolin-2-yl)-N,N-bis(4-methoxyphenyl)aniline (4)

SF32, SF202



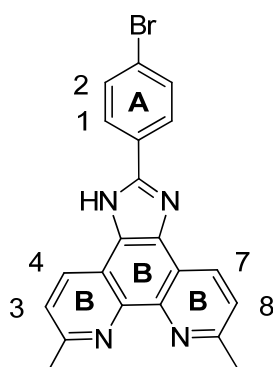
3 (586 mg, 1.76 mmol, 1.0 eq.), **1** (428 mg, 1.80 mmol, 1.02 eq.) and an excess of NH_4OAc (4.49 g, 58.3 mmol, 33.2 eq.) were mixed with 100 ml of EtOH. The light brown solution was refluxed overnight after which time the solvent was removed. The dark orange residue was dissolved in CH_2Cl_2 (50 ml) and washed with water. A yellow precipitate had formed between the phases. The organic layer was separated, dried over Na_2SO_4 and the solvent was removed to obtain a brown solid. The yellow precipitate was collected and washed with water and diethyl ether and was collected by dissolving in CH_2Cl_2 and EtOH. The product was isolated as a yellow solid by column chromatography on alumina using $\text{CH}_2\text{Cl}_2 + 3\% \text{ MeOH}$ as an eluent (282 mg, 0.575 mmol, 29.2%).

$^1\text{H NMR}$ (250 MHz, CDCl_3) δ / ppm: 9.06 (d, $J = 8.3$ Hz, 1H), 8.22 (d, $J = 7.7$ Hz, 2H), 7.50 (d, $J = 8.1$ Hz, 1H), 6.99 (d, $J = 8.8$ Hz, 4H), 6.76 (d, $J = 8.8$ Hz, 8H), 3.73 (s, 6H, H^{OMe}), 2.51 (s, 3H, $\text{H}^{\text{Me-phen}}$), 2.10 (s, 3H, $\text{H}^{\text{Me-phen}}$).

ESI MS m/z : 552.5 $[\text{M}+\text{H}]^+$ (calc. 552.2).

12.2.5 2-(4-bromophenyl)-6,9-dimethyl-1H-imidazo[4,5-f][1,10]phenanthroline (5)

SF121



Under an atmosphere of argon, 4-bromobenzaldehyde (1.30 g, 7.01 mmol), 2,9-dimethyl-1,10-phenanthroline-5,6-dione (2.00 g, 8.40 mmol) and an excess of NH_4OAc (7.40 g, 96 mmol) were added to EtOH (45 mL). The yellow mixture was heated at reflux for 3 d, after which time the solvent was removed under reduced pressure. The brown residue was dissolved in CH_2Cl_2 and the organic layer was washed with water. A yellow precipitate formed, was separated by filtration and dried *in vacuo*. **5** was isolated as a yellow solid (2.57 g, 6.38 mmol, 91%).

^1H NMR (400 MHz, DMSO-d_6) δ / ppm 13.70 (v br, H^{NH}), 8.76 (d, $J = 8.2$ Hz, 2H, $\text{H}^{\text{B}3}$), 8.21 (d, $J = 8.7$ Hz, 2H, $\text{H}^{\text{A}3}$), 7.82 (d, $J = 8.5$ Hz, 2H, $\text{H}^{\text{A}2}$), 7.68 (d, $J = 8.7$ Hz, 2H, $\text{H}^{\text{B}4}$), 2.79 (s, 6H, H^{Me}).

^{13}C NMR (126 MHz, CDCl_3) δ / ppm 156.2 ($\text{C}^{\text{B}2}$), 149.0 ($\text{C}^{\text{A}1}$), 142.9 (2C^{Q}), 132.0 ($\text{C}^{\text{A}2}$), 129.9 ($\text{C}^{\text{B}3}$), 129.4 (C^{Q}), 128.0 ($\text{C}^{\text{A}3}$), 123.3 ($\text{C}^{\text{B}4}$), 122.7 ($\text{C}^{\text{A}4}$), 25.1 (C^{Me}); one C^{Q} not observed.

ESI MS m/z : 405.1 [$\text{M}+\text{H}$] $^+$ (calc. 405.1).

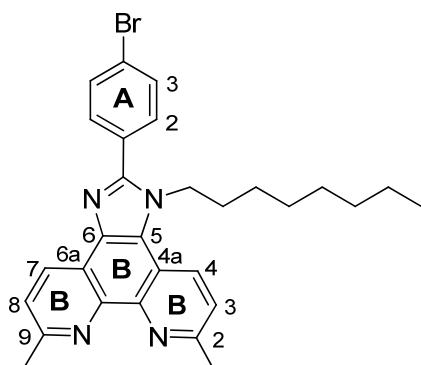
IR (solid, v/cm^{-1}): 3360 (w), 3121 (w), 2915 (w), 1549 (w), 1475 (m), 1439 (m), 1370 (w), 1009 (m), 832 (s), 748 (m), 734 (m), 724 (m).

UV-VIS (MeOH, 1.0×10^{-5} mol dm^{-3}) λ / nm 276 (ϵ / $\text{dm}^3 \text{mol}^{-1} \text{cm}^{-1}$ 37200), 293 (37200), 317 sh (32600), 324 sh (28700).

The synthesis and characterization of **5** was published in⁴³.

12.2.6 2-(4-bromophenyl)-6,9-dimethyl-1-octyl-1*H*-imidazo[4,5-*f*][1,10]phenanthroline (6)

SF136, SF213



This reaction was done in analogy to reference ¹⁴³.

NaH (60% oil dispersion, 255 mg, 6.38 mmol) were suspended in DMF (15 mL) under an atmosphere of argon. **5** (857 mg, 2.13 mmol) was added and the brown suspension was heated to 40 °C. A 10-fold excess of 1-bromooctane (3.7 ml, 2.13 mmol) was added and the mixture was heated at reflux for 68 h. The black mixture was poured into an ice bath and a yellow precipitate formed. This was collected by filtration and purified by column chromatography (basic alumina, toluene/ethyl acetate 2:1) and recrystallized from toluene/ethyl acetate (3:1 by volume) to yield **6** as white needles (225 mg, 0.436 mmol, 21%).

¹H NMR (500 MHz, CDCl₃) δ / ppm 8.93 (d, J = 8.2 Hz, 1H, H^{B4/B7}), 8.45 (d, J = 8.5 Hz, 1H, H^{B4/B7}), 7.71 (m, 2H, H^{A2/A3}), 7.60 (m, 2H, H^{A2/A3}), 7.57 (m, 2H, H^{B3+B8}), 4.54 (m, 2H, H^{NCH2}), 2.98 (s, 3H, H^{Me-phen}), 2.96 (s, 3H, H^{Me-phen}), 1.91 (m, 2H, H^{CH2}), overlapping 1.24 and 1.18 (m, 10H, H^{CH2}), 0.85 (t, J = 7.0 Hz, 3H, H^{Me}).

¹³C NMR (126 MHz, CDCl₃) δ / ppm 158.1 (C^{B2/B9}), 156.9 (C^{B2/B9}), 152.3 (C^{NCN}), 144.2 (C^Q), 143.5 (C^Q), 136.5 (C^Q), 132.3 (C^{A2/A3}), 131.6 (C^{A2/A3}), 130.8 (C^{B4/B7}), 129.7 (C^Q), 128.5 (C^{B4/B7}), 124.9 (C^{B6}), 124.4 (C^{A1}), 124.0 (C^{B3/B8}), 123.0 (C^{B3/B8}), 122.1 (C^{A4}), 117.9 (C^{B5}), 46.9 (C^{NCH2}), 31.8 (C^{CH2}), 30.3 (C^{CH2}), 29.2 (C^{CH2}), 29.0 (C^{CH2}), 26.5 (C^{CH2}), 26.1 (C^{Me-phen}), 25.9 (C^{Me-phen}), 22.7 (C^{CH2}), 14.2 (C^{Me}).

ESI MS *m/z*: 515.2 [M+H]⁺ (calc. 515.2).

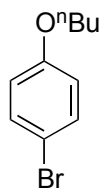
IR (solid, v/cm⁻¹): 2952 (w), 2925 (m), 2854 (m), 1585 (w), 1585 (w), 1533 (m), 1466 (m), 1402 (m), 1357 (m), 1185 (w), 1149 (w), 1008 (m), 837 (s), 817 (m), 748 (m), 719 (m).

UV-VIS (CH₂Cl₂, 1.0 × 10⁻⁵ mol dm⁻³) λ / nm 249 (ε / dm³ mol⁻¹ cm⁻¹ 40012), 276 (41370), 292 (40950), 370 sh (2380).

The synthesis and characterization of **6** was published in⁴³.

12.2.7 1-bromo-4-butoxybenzene (7)

SF122



This reaction was done in analogy to reference ⁸⁶.

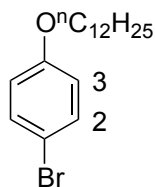
4-Bromophenol (5.00 g, 28.9 mmol, 1.0 eq.) was dissolved in 60 ml of acetone and 1-bromobutane (3.7 ml, 4.75 g, 34.7 mmol, 1.2 eq.) was added and the white suspension was stirred for 5 min. K₂CO₃ (7.99 g, 57.8 mmol, 2.0 eq.) was added and the mixture was refluxed for 3 days. The white suspension was filtered off and washed with acetone (4.76 g, 20.8 mmol, 71.9%).

¹H NMR (400 MHz, CDCl₃) δ/ppm: 7.35 (m, 2H, H²), 6.77 (m, 2H, H³), 3.92 (t, *J* = 6.5 Hz, 2H, H^{CH2}), 1.75 (m, 2H, H^{CH2}), 1.48 (m, 2H, H^{CH2}), 0.97 (t, *J* = 7.4 Hz, 3H, H^{Me}).

The ¹H NMR matches the literature data.¹⁴⁴

12.2.8 1-bromo-4-(dodecyloxy)benzene (8)

SF143



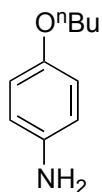
8 was synthesized in analogy to **7** using 4-bromophenol (5.00 g, 28.9 mmol, 1.0 eq.), 1-bromododecane (8.6 ml, 8.82 g, 34.7 mmol, 1.2 eq.) and K₂CO₃ (7.99 g, 57.8 mmol, 2.0 eq.) to yield the product as white crystals (6.74 g, 19.7 mmol, 68.3%).

¹H NMR (400 MHz, CDCl₃) δ/ppm: 7.36 (d, *J* = 8.9 Hz, 2H, H²), 6.77 (d, *J* = 8.9 Hz, 2H, H³), 3.91 (t, *J* = 6.5 Hz, 2H, H^{OCH2}), 1.74 (m, 2H, H^{OCH2CH2}), 1.44 (m, 2H, H^{OCH2CH2CH2}), 1.38-1.22 (m, 16 H, H^{CH2}), 0.88 (t, *J* = 6.9 Hz, 3H, H^{CH3}).

The ¹H NMR matches the literature data.¹⁴⁵

12.2.9 4-butoxyaniline (**9**)

SF124



This reaction was done in analogy to reference ⁸⁶.

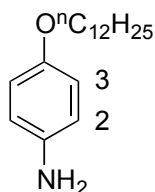
4-Acetamidophenol (5.00 g, 33.1 mmol, 1.0 eq.) was suspended in 60 ml of acetone. K_2CO_3 (9.15 g, 66.2 mmol, 2.0 eq.) was added and the white suspension was stirred for 5 min. 1-Bromobutane (4.3 ml, 5.44 g, 39.7 mmol, 1.2 eq.) was added and the mixture was refluxed overnight. Because not all 4-acetamidophenol was consumed, another 2 ml of 1-bromobutane was added. After 3 days the mixture was poured into 250 ml of water and was stirred for 10 min. at room temperature. The white precipitate was filtered off and dried in vacuo. More product was isolated by extracting the mother liquor with ethyl acetate. The organic phase was separated, dried over Na_2SO_4 and the solvent was removed to yield the product as a white solid that turns slightly brown in air after a while (3.45 g, 20.9 mmol, 63.1%).

1H NMR (400 MHz, $CDCl_3$) δ /ppm: 6.79 (m, 4H, H^{2+3}), 3.89 (t, $J = 6.5$ Hz, 2H, H^{OCH_2}), 1.72 (m, 2H, $H^{OCH_2CH_2}$), 1.47 (m, 2H, $H^{OCH_2CH_2CH_2}$), 0.96 (t, $J = 7.4$ Hz, 3H, H^{CH_3}).

The 1H NMR matches the literature data. ¹⁴⁶

12.2.10 4-dodecyloxyaniline (**10**)

SF144



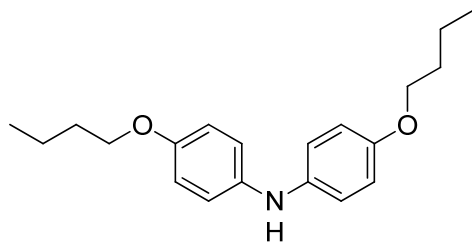
10 was synthesized in analogy to **9** using 4-acetamidophenol (5.00 g, 33.1 mmol, 1.0 eq.), 1-bromododecane (9.8 ml, 10.1 g, 39.7 mmol, 1.2 eq.) and K_2CO_3 (9.14 g, 66.2 mmol, 2.0 eq.) to yield the product as a light brown solid (5.6950 g, 20.6 mmol, 62.1%).

1H NMR (400 MHz, $CDCl_3$) δ /ppm: 6.78 – 6.67 (m, 4H, H^{arene}), 3.88 (t, $J = 6.6$ Hz, 2H, H^{OCH_2}), 1.73 (m, 2H, $H^{OCH_2CH_2}$), 1.50 – 1.38 (m, 2H, $H^{OCH_2CH_2CH_2}$), 1.37 – 1.18 (m, 16H, H^{CH_2}), 0.88 (t, $J = 6.7$ Hz, 3H, H^{CH_3}).

The 1H NMR matches the literature data. ¹⁴⁷

12.2.11 Bis(4-butoxyphenyl)amine (11)

SF125



This synthesis was made following reference ⁸⁶ for the hexoxy analogue.

4-(Butyloxy)benzeneamine (1.42 g, 8.58 mmol, 1.0 eq) and K_2CO_3 (3.56 g, 25.8 mmol, 3.0 eq) were mixed in 20 ml of DMSO in an atmosphere of nitrogen. After stirring for 20 min., 1-bromo-4-butyloxybenzene (2.95 g, 12.9 mmol, 1.5 eq), CuI (0.163 g, 0.858 mmol, 0.1 eq) and L(-)-proline (0.198 g, 1.72 mmol, 0.2 eq) were added and the black mixture was refluxed at 90 °C for ~36 h. After letting the solution cool down to rt 100 ml of water were added and the mixture was extracted with ethyl acetate. The organic layer was washed with brine (2x100 ml) and water (1x100 ml) and dried over Na_2SO_4 . The solvent was removed and the product crystallized out of the oily residue (258 mg, 9.59 %).

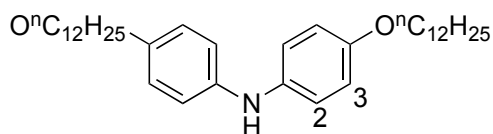
1H NMR (400 MHz, $CDCl_3$) δ / ppm: 6.98 – 6.93 (m, 2H, H^{arene}), 6.84 – 6.78 (m, 2H, H^{arene}), 3.92 (t, $J = 6.4$ Hz, 2H, H^{OCH_2}), 1.78 – 1.63 (m, 2H, $H^{OCH_2CH_2}$), 1.56 – 1.42 (m, 2H, $H^{OCH_2CH_2CH_2}$), 0.96 (t, $J = 7.4$ Hz, 3H, H^{CH_3}).

^{13}C NMR (101 MHz, $CDCl_3$) δ / ppm: 154.2 (C^{arene}), 139.3 (C^{arene}), 119.5 (C^{arene}), 116.1 (C^{arene}), 68.6 (C^{OCH_2}), 32.3 ($C^{OCH_2CH_2}$), 19.9 ($C^{OCH_2CH_2CH_2}$), 14.1 (C^{CH_3}).

The ^{13}C NMR spectra agrees well with the literature values.¹⁴⁸ 1H NMR spectrum is published in benzene only.

12.2.12 Bis(4-dodecyloxyphenyl)amine (12)

SF145



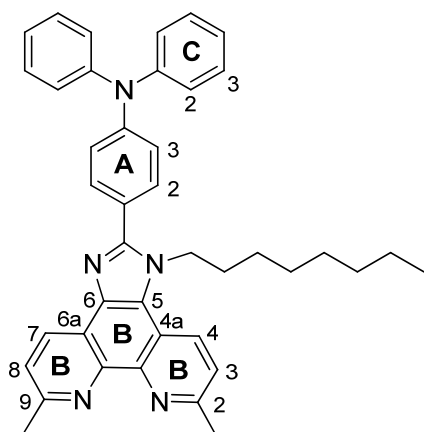
12 was synthesized in analogy to **11** using **10** (2.71 g, 9.77 mmol, 1.0 eq), **8** (5.00 g, 14.6 mmol, 1.5 eq.), K₂CO₃ (2.70 g, 19.5 mmol, 2.0 eq.), CuI (0.186 g, 0.977 mmol, 0.1 eq.) and L(-)-prolin (0.225 g, 1.95 mmol, 0.2 eq.).

The product was yielded as a brown solid (6.25 g) and was used for the next step without further purification.

¹H NMR (400 MHz, CDCl₃) δ/ppm: 7.35 (m, 4H, H^{arene}), 6.77 (m, 4H, H^{arene}), 3.91 (t, *J* = 6.5 Hz, 4H, H^{OCH₂}), 1.76 (m, 4H, H^{OCH₂CH₂}), 1.42 (m, 4H, H^{OCH₂CH₂CH₂}), 1.38 – 1.19 (m, 32H, H^{CH₂}), 0.88 (t, *J* = 6.7 Hz, 6H, H^{CH₃}).

12.2.13 4-(6,9-dimethyl-1-octyl-1*H*-imidazo[4,5-*f*][1,10]phenanthrolin-2-yl)-*N,N*-diphenylaniline (13)

SF140



6 (119 mg, 0.231 mmol), Ph₂NH (43.0 mg, 0.254 mmol) and NaO^tBu (55.4 mg, 0.577 mmol) were added to toluene (10 mL) under an atmosphere of N₂. Bis(dibenzylideneacetone) palladium(0) (6.64 mg, 0.0115 mmol) and a 1.0 mol dm⁻³ solution of ^tBu₃P in toluene (0.012 ml, 0.0115 mmol) was added to the reaction mixture which was then heated at reflux overnight. The reaction mixture was filtered hot, the solvent removed and the remaining brown solid

purified by column chromatography (basic alumina, toluene/ethyl acetate 2:1). **13** was isolated as a yellow solid (52.4 mg, 0.121 mmol, 52%).

M. pt. 121 °C.

¹H NMR (500 MHz, CDCl₃) δ / ppm 8.97 (d, *J* = 8.2 Hz, 1H, H^{B4/B7}), 8.46 (d, *J* = 8.5 Hz, 1H, H^{B4/B7}), 7.57 (m, 4H, H^{B3+B8+A2}), 7.31 (m, 4H, H^{C3}), 7.21 (d, *J* = 8.6 Hz, 2H, H^{A3}), 7.18 (m, 4H, H^{C2}), 7.10 (m, 2H, H^{C4}), 4.60 (m, 2H, H^{NCH2}), 2.97 (s, 3H, H^{Me-phen}), 2.95 (s, 3H, H^{Me-phen}), 1.95 (m, 2H, H^{CH2}), overlapping 1.28 and 1.22 (m, 10H, H^{CH2}), 0.84 (t, *J* = 7.0 Hz, 3H, H^{Me}).

¹³C NMR (126 MHz, CDCl₃) δ / ppm 157.8 (C^{B2/B9}), 156.5 (C^{B2/B9}), 153.6 (C^{NCN}), 149.3 (C^Q), 147.3 (C^{C1}), 143.9 (C^Q), 143.3 (C^Q), 136.4 (C^Q), 130.8 (C^{A2}), 130.75 (C^{B4/B7}), 129.6 (C^{C3}), 128.5 (C^{B4/B7}), 125.3 (C^{C2}), 124.7 (C^Q), 124.0 (C^{B3/B8}), 123.9 (C^{C4}), 123.5 (C^Q), 122.9 (C^{B3/B8}), 122.5 (C^{A3}), 122.1 (C^Q), 118.0 (C^{B5}), 46.8 (C^{NCH2}), 30.3 (C^{CH2}), 29.8 (C^{CH2}), 29.2 (C^{CH2}), 29.0 (C^{CH2}), 26.4 (C^{CH2}), 26.0 (C^{Me-phen}), 25.8 (C^{Me-phen}), 22.7 (C^{CH2}), 14.2 (C^{Me}).

ESI MS *m/z*: 604.3 [M+H]⁺ (calc. 604.3).

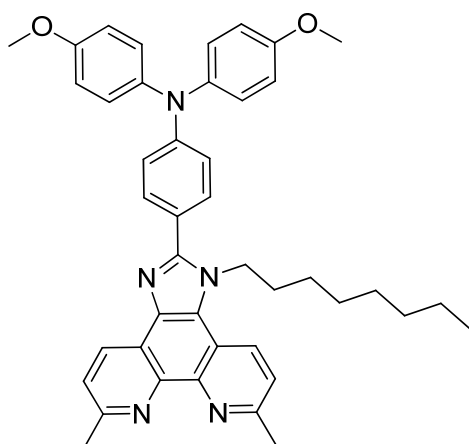
IR (solid, v/cm⁻¹): 2923 (w), 2854 (w), 1588 (m), 1520 (w), 1488 (m), 1467 (m), 1316 (w), 1280 (m), 1180 (w), 820 (w), 749 (m), 695 (m).

UV-VIS (CH₂Cl₂, 1.0 × 10⁻⁵ mol dm⁻³) λ / nm 240 (ε / dm³ mol⁻¹ cm⁻¹ 35850), 258 (31800), 295 (42300), 335 (29900).

The synthesis and characterization of **13** was published in⁴³.

12.2.14 4-(6,9-dimethyl-1-octyl-1*H*-imidazo[4,5-*f*][1,10]phenanthrolin-2-yl)-*N,N*-bis(4-methoxyphenyl)aniline (**14**)

SF199, SF161



A 2-5 ml microwave vial was charged with **6** (101 mg, 0.196 mmol, 1.0 eq.) and was flushed with N₂ for 10 min. 4,4'-dimethoxyphenylamine (281 mg, 1.20 mmol, 6.1 eq.) and NaO^tBu (57.8 mg, 0.601 mmol, 3.1 eq.) were added and the vial was flushed for another 10 min. Toluene

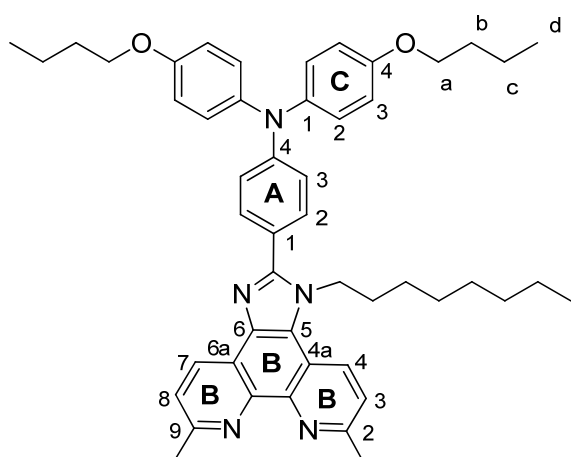
(4.5 ml) was added and N₂ was bubbled through the solution for 5 min. Pd(PPh₃)₄ (27.8 mg, 0.0241 mmol, 0.1 eq.) was added and the mixture was heated to 130 °C in the microwave reactor for 20 min. The dark brown mixture was filtered, the solvent removed and purified by column chromatography eluting with CH₂Cl₂.

¹H NMR (400 MHz, CDCl₃) δ / ppm: 9.05 (d, *J* = 8.3 Hz, 1H), 8.99 (d, *J* = 8.2 Hz, 1H), 8.46 (m, 1H), 7.74 – 7.68 (m, 1H), 7.62 – 7.54 (m, 4H), 7.53 – 7.47 (m, 2H), 7.17 – 7.10 (m, 4H), 7.04 (d, *J* = 8.8 Hz, 2H), 6.92 – 6.84 (m, 4H), 4.64 – 4.53 (m, 2H, H^{NCH₂}), 3.82 (s, 6H, H^{OMe}), 2.98 (s, 6H, overlying H^{Me-phen}), 1.93 (d, *J* = 7.6 Hz, 2H, H^{CH₂}), 1.19 (d, *J* = 14.2 Hz, 16H), 0.89 – 0.79 (m, 3H, H^{CH₃}).

ESI MS *m/z*: 664.7 [M+H]⁺ (calc. 664.4).

12.2.15 4-butoxy-N-(4-butoxyphenyl)-N-(4-(6,9-dimethyl-1-octyl-1H-imidazo[4,5-f][1,10]phenanthrolin-2-yl)phenyl)aniline (15)

SF159



A 50 ml flask was charged with **6** (300 mg, 0.582 mmol, 1.0 eq), **11** (279 mg, 0.873 mmol, 1.5 eq), NaO^tBu (140 mg, 1.45 mmol, 2.5 eq.) and Pd(dba)₂ (18.4 mg, 0.0291 mmol, 0.05 eq) and was evacuated for 15 min. Toluene (20 ml) and PtBu₃ (0.03 ml of a 0.1 M sol. in toluene, 23.9 mg, 0.0291 mmol, 0.05 eq.) were added and the reddish brown mixture was heated to 95 °C for 8 days. The mixture was allowed to cool to room temperature, filtered and the solvent was removed. The remaining brown solid was purified by column chromatography on alumina eluting with CH₂Cl₂ to yield the product as a yellow solid (223 mg, 298 μmol, 51.2%).

¹H NMR (500 MHz, CDCl₃) δ / ppm: 9.24 (s, br, 1H, H^{B^{4/7}}), 8.48 (d, *J* = 8.6 Hz, 1H, H^{B^{4/7}}), 7.66 (d, *J* = 8.2 Hz, 1H, H^{B^{3/8}}), 7.62 (d, *J* = 8.4 Hz, 1H, H^{B^{3/8}}), 7.54 (d, *J* = 8.2 Hz, 2H, H^{A^{2/3}}), 7.13 (d, *J* = 8.8 Hz, 4H, H^{C²}), 7.03 (d, *J* = 8.7 Hz, 2H, H^{A^{2/3}}), 6.88 (d, *J* = 9.0 Hz, 4H, H^{C³}), 4.78 – 4.25 (m, 2H, H^{NCH₂}), 3.96 (t, *J* = 6.5 Hz, 4H, H^a), 3.07 (s, 3H, H^{Me-phen}), 3.01 (s, 3H, H^{Me-}

^{phen}), 2.04 – 1.80 (s, 2H, H^{CH2}), 1.78 (m, 4H, H^b), 1.51 (m, 4H, H^c), 1.38 – 1.10 (m, 12H, H^{CH2}), 0.99 (t, *J* = 7.4 Hz, 6H, H^d), 0.85 (t, *J* = 6.9 Hz, 3H, H^{Me}).

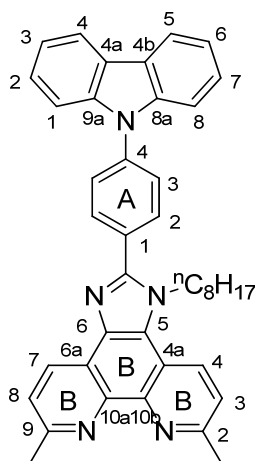
¹³C NMR (126 MHz, CDCl₃) δ / ppm: 157.2 (C^{B2/9}), 156.2 (C^{C4}), 139.4 (C^{C1}), 130.6 (C^{A2/3}), 128.6 (C^{B4/7}), 127.4 (C^{C2}), 124.5 (C^{B3/8}), 123.6 (C^{B3/8}), 118.6 (C^{A2/3}), 117.7 (C^q), 115.4 (C^{C3}), 67.9 (C^{CH2}), 46.9 (C^{CH2}), 31.8 (C^{CH2}), 31.5 (C^{CH2}), 30.2, (C^{CH2}), 29.8 (C^{CH2}), 29.2 (C^{CH2}), 28.9 (C^{CH2}), 26.4 (C^{CH2}), 25.3 (C^{phen-Me}), 25.1 (C^{phen-Me}), 22.7 (C^{CH2}), 19.5 (C^{CH2}), 14.2 (C^{CH2}).

Found C 78.52, H 7.51, N 8.96; C₄₉H₅₇N₅O₂ requires C 78.68, H 7.68, N 9.36%.

HRMS *m/z*: 748.4582 [M+H]⁺ (calc. 748.4585).

12.2.16 2-(4-(9*H*-carbazol-9-yl)phenyl)-6,9-dimethyl-1-octyl-1*H*-imidazo[4,5-*f*][1,10]phenanthroline (17)

SF204



NaH (60% oil dispersion, 122 mg, 3.05 mmol, 7.5 eq.) was suspended and stirred vigorously for 1.5 h in 5 ml of DMF under an atmosphere of N₂. **19** (200 mg, 0.409 mmol, 1.0 eq.) was added and the suspension was stirred for 10 min. and 1-bromooctane (0.711 ml, 789 mg, 4.09 mmol, 10.0 eq.) was added and the mixture was heated to 70 °C for 3 days. The black mixture was allowed to cool down to room temperature and was diluted with water to form a suspension that was extracted with CH₂Cl₂ (25 ml). The organic layer was washed with water (5x40 ml), dried over Na₂SO₄ and the solvent was removed. The remaining DMF was removed by azeotrope distillation with toluene five times. The remaining brown solid was washed with petroleum ether. The brown foam obtained after drying in vacuo was cleaned by column chromatography on alumina CH₂Cl₂ --> CH₂Cl₂ + 2% MeOH, followed by one on alumina with toluene / ethyl acetate 4:1 --> 1:1 and a final one on alumina using CH₂Cl₂ + 0.25% MeOH to yield the product as a beige solid (45 mg, 0.075 mmol, 18.3 %).

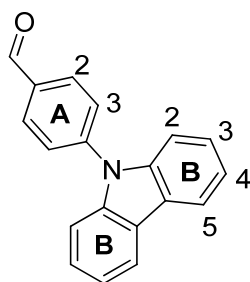
^1H NMR (500 MHz, DMSO) δ / ppm: 8.85 (d, $J = 8.3$ Hz, 1H, $\text{H}^{\text{B}7}$), 8.78 (d, $J = 8.6$ Hz, 1H, $\text{H}^{\text{B}4}$), 8.30 (d, $J = 7.9$ Hz, 2H, $\text{H}^{\text{C}4/5}$), 8.10 (d, $J = 7.9$ Hz, 2H, $\text{H}^{\text{A}2/3}$), 7.91 (d, $J = 7.9$ Hz, 2H, $\text{H}^{\text{A}2/3}$), 7.77 (d, $J = 8.3$ Hz, 1H, $\text{H}^{\text{C}3/8}$), 7.73 (d, $J = 8.0$ Hz, 1H, $\text{H}^{\text{C}3/8}$), 7.56 (d, $J = 8.2$ Hz, 2H, $\text{H}^{\text{C}1/8}$), 7.50 (t, $J = 7.6$ Hz, 2H, $\text{H}^{\text{C}2/7}$), 7.35 (t, $J = 7.3$ Hz, 2H, $\text{H}^{\text{C}3/6}$), 4.82 (m, 2H, $\text{H}^{\text{CH}2}$), 2.84 (s, 3H, $\text{H}^{\text{Me-phen}}$), 2.83 (s, 3H, $\text{H}^{\text{Me-phen}}$), 1.93 – 1.75 (m, 2H, $\text{H}^{\text{CH}2}$), 1.24 – 0.94 (m, 10H, $\text{H}^{\text{CH}2}$), 0.76 – 0.61 (m, 3H, H^{Me}).

^{13}C NMR (126 MHz, CDCl_3) δ / ppm: 156.2 ($\text{C}^{\text{B}2/9}$), 155.7 ($\text{C}^{\text{B}2/9}$), 152.4 ($\text{C}^{\text{imidazole}}$), 139.7 ($\text{C}^{\text{C}8\text{a}/\text{C}9\text{a}}$), 137.8 ($\text{C}^{\text{A}1/4}$), 131.6 ($\text{C}^{\text{A}2/3}$), 130.1 ($\text{C}^{\text{B}4/7}$), 129.3 ($\text{C}^{\text{B}4/7}$), 129.2 ($\text{C}^{\text{A}1/4}$), 126.7 ($\text{C}^{\text{A}2/3}$), 126.3 ($\text{C}^{\text{C}2/7}$), 124.4 ($\text{C}^{\text{B}5}$), 123.7 ($\text{C}^{\text{B}3/8}$), 123.1 ($\text{C}^{\text{B}3/8}$), 122.8 ($\text{C}^{\text{C}4\text{a}/\text{C}4\text{b}}$), 121.3 (C^{q}), 120.5 ($\text{C}^{\text{C}4/5}$), 120.3 ($\text{C}^{\text{C}3/6}$), 117.4 (C^{q}), 109.6 ($\text{C}^{\text{C}1/8}$), 24.6 (overlapping $\text{C}^{\text{Me-phen}}$).

ESI MS m/z : 602.6 $[\text{M}+\text{H}]^+$ (calc. 602.3).

12.2.17 5-(9H-carbazol-9-yl)thiophene-2-carbaldehyde (18)

SF201



This synthesis was made according to reference ⁸⁷ with the difference of a shorter reaction time. Under an atmosphere of N_2 , 4-bromobenzaldehyde (1.80 g, 9.73 mmol, 3.3 eq.), carbazole (0.526 g, 2.99 mmol, 1.0 eq.), copper (0.991 g, 15.6 mmol, 5.2 eq.), 18-crown-6 (0.163 g, 0.617 mmol, 0.2 eq.) and potassium carbonate (0.998 g, 7.22 mmol, 2.42 eq.) were mixed with 1,2-dichlorobenzene (12 ml) and the mixture was degassed for 30 min. by bubbling through N_2 . The mixture was heated to 180 °C and was refluxed overnight. The mixture was allowed to cool down to room temperature and was filtered. The brown solution was purified by column chromatography on silica using petroleum ether / ethyl acetate 1:0 --> 20:1 as an eluent. The product was collected as a pale yellow solid (535 mg, 1.97 mmol, 65.9 %).

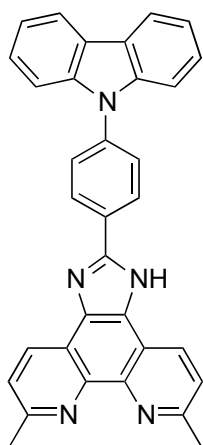
^1H NMR (400 MHz, CDCl_3) δ / ppm: 10.13 (s, 1H, $\text{H}^{\text{aldehyde}}$), 8.16 – 8.13 (m, 4H, H), 7.81 (d, $J = 8.4$ Hz, 2H), 7.52 – 7.50 (m, 2H), 7.46 – 7.42 (m, 2H), 7.36 – 7.32 (m, 2H).

ESI MS m/z : 490.4 $[\text{M}+\text{H}]^+$ (calc. 490.2).

The ^1H -NMR spectrum agrees well with the literature data.

12.2.18 2-(4-(9*H*-carbazol-9-yl)phenyl)-6,9-dimethyl-1*H*-imidazo[4,5-*f*][1,10]phenanthroline (19)

SF203



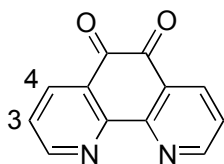
18 (535 mg, 1.97 mmol, 1.0 eq.), **1** (481 mg, 2.02 mmol, 1.02 eq.) and an excess of NH₄OAc (5.04 g, 65.4 mmol, 33.2 eq.) were mixed with EtOH (100 ml). The yellow mixture was refluxed overnight after which time the solvent was removed. The remaining orange solid was washed with water and diethyl ether. The product was isolated as a yellow solid by column chromatography on alumina using CH₂Cl₂ + 3% MeOH as an eluent (282 mg, 0.575 mmol, 29.2%).

¹H NMR (500 MHz, DMSO) δ / ppm: 13.81 (s, 1H), 8.84 (d, *J* = 8.2 Hz, 2H), 8.56 (d, *J* = 8.5 Hz, 2H), 8.29 (dt, *J* = 7.8, 1.0 Hz, 2H), 7.91 (d, *J* = 8.6 Hz, 2H), 7.78 – 7.65 (m, 2H), 7.58 – 7.52 (m, 2H), 7.49 (m, 2H), 7.34 (m, 1.1 Hz, 2H), 2.82 (s, 6H).

ESI MS *m/z*: 490.4 [M+H]⁺ (calc. 490.2).

12.2.19 1,10-phenanthroline-5,6-dione (20)

SF167



This synthesis was done according to a literature procedure.⁸⁵

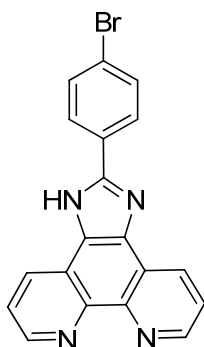
Phenanthroline (1.00 g, 5.04 mmol, 1 eq) was dissolved in 12 ml of 60% aqueous sulfuric acid. Potassium bromate (0.929 g, 5.55 mmol, 1.1 eq) was added portionwise over a period of 30 minutes to give an orange solution. The mixture was stirred at rt overnight. After 20h the orange mixture was poured into ice and was neutralized with 8 M NaOH solution. The yellow precipitate was collected and recrystallized from methanol to yield the product as a yellow solid (0.914 g, 4.35 mmol, 86%).

¹H-NMR (400 MHz, CDCl₃) δ /ppm: 9.12 (dd, $J = 4.7, 1.8$ Hz, 2H), 8.50 (dd, $J = 7.9, 1.9$ Hz, 2H), 7.59 (dd, $J = 7.9, 4.7$ Hz, 2H).

The ¹H-NMR spectrum agrees well with the literature.⁸⁵

12.2.20 2-(4-bromophenyl)-1H-imidazo[4,5-f][1,10]phenanthroline (21)

SF175



This procedure was adapted from ⁸⁸.

20 (4.00 g, 19.0 mmol, 1.0 eq.), 4-bromobenzaldehyde (4.98 g, 26.9 mmol, 1.41 eq.), and an excess of NH₄OAc (29.3 g, 381 mmol, 20.0 eq.) were suspended in glacial acetic acid. The orange mixture was heated 115 °C for 5 d, after which time the mixture was allowed to cool down to room temperature. The mixture was poured into 200 ml of water and was neutralized with aqu. ammonia to pH 6 and the yellow precipitate was filtered off, washed with water and

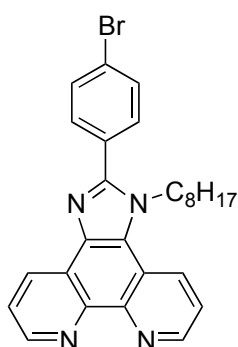
was dried with diethyl ether. The filter cake was collected by dissolving in a $\text{CHCl}_3/\text{EtOH}$ mixture and the solvent was removed (0.369g, 0.983 mmol, 85.5 %).

$^1\text{H NMR}$ (400 MHz, DMSO) δ / ppm: 13.82 (s, 1H), 9.04 (dd, $J = 4.4, 1.7$ Hz, 2H), 8.89 (d, $J = 8.0$ Hz, 2H), 8.22 (m, 2H), 7.83 (m, 2H).

The NH-signal is shifted with respect to the literature values in DMSO, the other signals agree well with it.⁸⁸

12.2.21 2-(4-bromophenyl)-1-octyl-1H-imidazo[4,5-f][1,10]phenanthroline (22)

SF185



This reaction was done in analogy to reference .

21 (1.00 g, 2.53 mmol, 1.0 eq.) was dissolved in 25 ml of DMF at 50 °C in an atmosphere of N_2 . NaH (60% oil dispersion, 546 mg, 13.7 mmol, 5.4 eq.) was added and the black mixture was stirred for 40 min. to heat it to 120 °C for 2 days. The mixture was poured into 20 ml of water and was extracted with CH_2Cl_2 (3x10 ml). The organic layer was washed with water and brine, dried over Na_2SO_4 and the solvent was removed. The orange residue was suspended in acetone and filtered to yield the product as a beige solid (300 mg, 0.615 mmol, 24.3%).

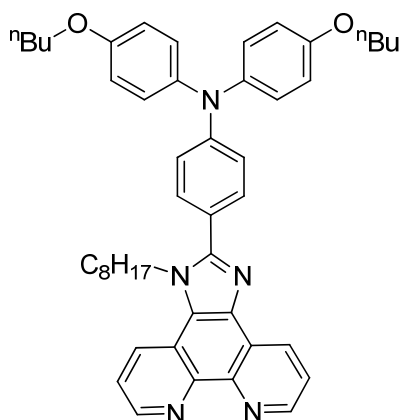
$^1\text{H NMR}$ (400 MHz, CDCl_3) δ / ppm: 9.20 (m, 2H, H^{arene}), 9.07 (dd, $J = 8.1, 1.8$ Hz, 1H, H^{arene}), 8.56 (dd, $J = 8.5, 1.6$ Hz, 1H, H^{arene}), 7.77 – 7.69 (m, 4H, H^{arene}), 7.66 – 7.58 (m, 2H, H^{arene}), 4.59 (t, 2H, H^{NCH_2}), 1.92 (p, $J = 7.5$ Hz, 2H, $\text{H}^{\text{NCH}_2\text{CH}_2}$), 1.30 – 1.12 (m, 10H, H^{CH_2}), 0.85 (t, $J = 7.0$ Hz, 3H, H^{CH_3}).

MALDI MS m/z : 487.9 $[\text{M}+\text{H}]^+$ (calc. 487.2).

The $^1\text{H NMR}$ signals of the aromatic peaks are shifted with respect to the literature data.¹⁴⁹

12.2.22 4-butoxy-*N*-(4-butoxyphenyl)-*N*-(4-(1-octyl-1*H*-imidazo[4,5-*f*][1,10]phenanthrolin-2-yl)phenyl)aniline (23)

SF187



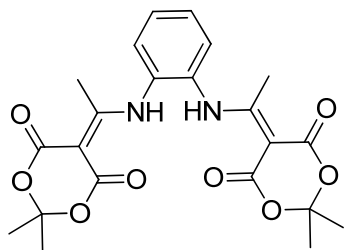
Under an atmosphere of N₂, a 50 ml three-neck flask was charged with **22** (50.0 mg, 0.103 mmol, 1.0 eq.), **11** (164 mg, 0.513 mmol, 5.0 eq.) and NaOtBu (24.6 mg, 0.256 mmol, 2.5 eq.) and the mixture was evacuated for 30 min. Pd(dba)₂ (5.9 mg, 0.0103 mmol, 0.1 eq.) was added and the mixture was evacuated for 15 min. Degassed toluene (6 ml) were added and P^tBu₃ (0.01 ml of a 0.1 M solution in toluene, 8.2 mg, 0.01 mmol, 0.05 eq.) was added and the dark brown mixture was heated to 110 °C for three days. The mixture was filtered through cotton and celite and the solvent was removed. The dark brown solid was purified by column chromatography on basic alumina eluting with cyclohexane/acetone 1:0→1:1→1:2→0:1 and was finally flushed with EtOH. The product was isolated as a yellow solid (14 mg, 0.019 mmol, 19%).

¹H-NMR (400 MHz, Acetone-*d*₆) δ / ppm: 9.10 – 8.97 (m, 2H), 8.97 – 8.91 (m, 1H), 8.85 – 8.71 (m, 1H), 7.82 (s, 1H), 7.78 – 7.70 (m, 2H), 7.67 – 7.57 (m, 2H), 7.21 – 7.11 (m, 3H), 7.02 – 6.89 (m, 4H), 4.84 – 4.68 (m, 2H, H^{NCH₂}), 4.00 (t, *J* = 6.4 Hz, 3H, H^{OCH₂}), 1.98 – 1.86 (m, 2H, H^{NCH₂CH₂}), 1.83 – 1.67 (m, 4H, H^{OCH₂CH₂}), 1.58 – 1.42 (m, 4H, H^{OCH₂CH₂CH₂}), 1.27 – 1.05 (m, 12H, H^{CH₂}), 0.97 (t, *J* = 7.4 Hz, 6H, H H^{OCH₂CH₂CH₂CH₃}), 0.92 – 0.86 (m, 1H), 0.84 – 0.73 (m, 3H, H^{CH₃}).

ESI MS *m/z*: 720.8 [M+H]⁺ (calc. 720.4).

12.2.23 5,5'-((1,2-phenylenebis(azanediy))bis(ethan-1-yl-1-ylidene))bis(2,2-dimethyl-1,3-dioxane-4,6-dione) (25)

SF217



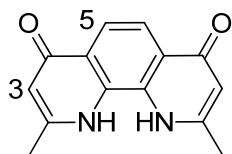
This synthesis is adapted from ¹⁵⁰.

A 250 ml 2 necked flask equipped with a reflux condenser was charged with 2,2-dimethyl-1,3-dioxane-4,6-dione (4.00 g, 27,8 mmol, 2.17 eq) and trimethyl orthoacetate (100 ml, 94.0 g, 782 mmol, 61.1 eq) to give a colorless solution that was heated to a gentle reflux at 115 °C for 15 min.. The pale yellow solution was further heated to 120 °C for another 15 min. to obtain a yellow solution that was allowed to cool down to 80 °. *ortho*-Phenylenediamine (1.38 g, 12.8 mmol, 1.00 eq) was added in portions and the solution turned slightly darker. The mixture was heated to 125 °C and refluxed for 2 h, allowed to cool down to rt and stirred overnight. A white precipitate formed that was filtered off and washed with diethyl ether (4x25 ml) to yield the product as a white powder (1.17 g, 2.47 mmol, 19.3 %).

¹H NMR (400 MHz, CDCl₃) δ / ppm: 12.80 (s, 2H, H^{NH}), 7.52-7.50 (m, 2H, H^{arene}), 7.37-7.35 (m, 2H, H^{arene}), 2.54 (s, 6H^{Me}), 1.72 (s, 12H^{Me}).

12.2.24 2,9-dimethyl-1,10-phenanthroline-4,7(1H,10H)-dione (26)

SF218



This synthesis is adapted from ¹⁵⁰.

Diphenyl ether (30 ml) was gently refluxed at 230 °C. **25** (1.16 g, 2.44 mmol, 1.0 eq) was added portionwise and the suspension was refluxed at 240 °C for 45 min. After letting the suspension cool down to 70 °C and a precipitate was filtered off and washed with acetone, pentane and diethyl ether (2x10 ml each) to obtain **26** as an off white powder (517 mg, 2.15 mmol, 88.2 %).

^1H NMR (400 MHz, DMSO) δ / ppm: 11.47 (s, br, 2H, H^{NH}), 7.88 (s, 2H, H^5), 6.37 (s, br, 2H, H^3), 2.56 (s, 6H).

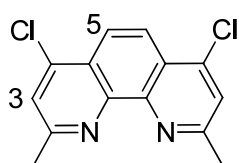
^1H NMR (400 MHz, $\text{D}_2\text{O} + \text{K}_2\text{CO}_3$) δ / ppm: 7.57 (2H, H^5), 6.15 (2H, H^3), 2.23 (6H, H^{Me}).

ESI MS m/z : 241.1 [$\text{M}+\text{H}$] $^+$ (calc. 241.1).

The ^1H -NMR spectrum agrees well with the literature.¹⁵⁰

12.2.25 4,7-dichloro-2,9-dimethyl-1,10-phenanthroline (27)

SF219



This synthesis is adapted from ¹⁵⁰.

26 (0.500 g, 2.08 mmol, 1.0 eq.) was suspended in phosphorous oxychloride (10.0 ml, 16.5 g, 108 mmol, 51.9 eq.) under an atmosphere of N_2 . After heating at 90 °C for 5.5 h the brown solution was poured slowly into 100 ml of an ice-water mixture and was stirred for 15 min. CHCl_3 (25 ml) were added and the pH was adjusted to pH 14 using an aqueous 8 M NaOH solution to form a white precipitate. The mixture was extracted with CHCl_3 (4x ~50 ml) and the organic layer was washed with 1M NaOH solution. The organic layer was separated, dried over Na_2SO_4 and the solvent was removed to obtain **27** as a light brown solid (363 mg, 1.31 mmol, 63.0 %).

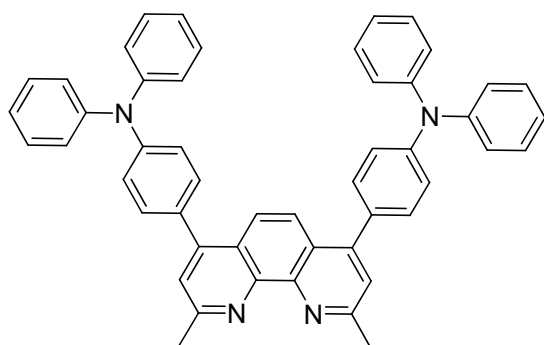
^1H NMR (400 MHz, CDCl_3) δ / ppm: 8.27 (s, 2H, H^5), 7.67 (s, 2H, H^3), 2.99 (s, 6H).

ESI MS m/z : 277.1 [$\text{M}+\text{H}$] $^+$ (calc. 277.0).

The ^1H -NMR spectrum agrees well with the literature.¹⁵⁰

12.2.26 4,4'-(2,9-dimethyl-1,10-phenanthroline-4,7-diyl)bis(*N,N*-diphenylaniline) (28)

SF220



This synthesis is adapted from the phenanthroline analogue reported in ¹⁵¹.

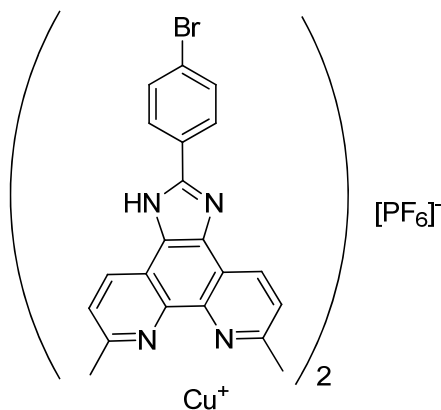
Under a N₂ inert atmosphere, potassium phosphate (343 mg, 1.62 mmol, 4.48 eq.) was dissolved in 2 ml of water and N₂ was bubbled through the solution for 10 min. In another 2-necked round bottomed flask, N₂ was bubbled through 1,4-dioxane (5 ml) for 10 min. **27** (100 mg, 0.361 mmol, 1 eq), 4-(diphenylamino)phenylboronic acid (230 mg, 0.794 mmol, 2.2 eq.), Pd(dba)₃ (24.7 mg, 0.0238 mmol, 6.6 mol%, 0.066 eq.) and tricyclohexylphosphine (15.2 mg, 0.0542 mmol, 0.15 eq.) were added. The aqueous solution was added and the brown mixture was heated to reflux at 95 °C over night. The orange mixture was allowed to cool down to room temperature and 10 ml of water were added. The mixture was extracted with CH₂Cl₂ (5x15 ml) and the organic layer was dried over Na₂SO₄ and the solvent was removed. After recrystallization from a 1:1 mixture of CH₂Cl₂ /MeOH the product was obtained as a yellow solid (97.0 mg, 0.140 mmol, 38.7 %).

¹H-NMR (400 MHz, CDCl₃) δ / ppm: 7.95 (s, 1H), 7.49 (s, 1H), 7.41 (d, J = 8.5 Hz, 4H), 7.32 (dd, J = 8.5, 7.3 Hz, 8H), 7.21 – 7.18 (m, 12H), 7.11 – 7.07 (m, 4H), 3.05 (s, 6H).

12.3 Copper Complex Synthesis

12.3.1 [Cu(5)₂][PF₆]

SF212



A solution of [Cu(NCMe)₄][PF₆] (18.5 mg, 0.0496 mmol, 1 eq.) in MeCN (5 mL) was added dropwise to a solution of **5** (40.0 mg, 0.0992 mmol) in CH₂Cl₂. The dark red solution was stirred for 4h and was left overnight. The solvent was removed and the dark red solid was purified by column chromatography on alumina using CH₂Cl₂ with 3% MeOH as an eluent to yield [Cu(**5**)₂][PF₆] as a dark red solid (20.8 mg, 0.0240 mmol, 48.2%).

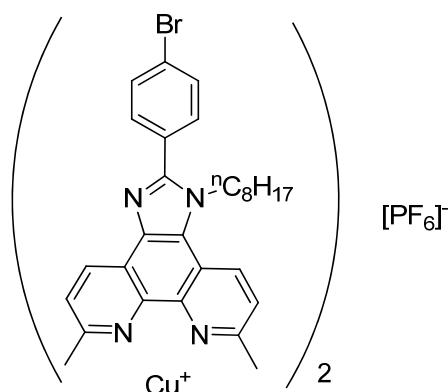
¹H NMR (400 MHz, CD₂Cl₂) δ / ppm: 8.97 (d, *J* = 8.2 Hz, 2H), 8.23 (d, *J* = 8.0 Hz, 2H), 7.62 (t, *J* = 9.5 Hz, 4H), 2.38 (s, 3H).

¹H NMR (400 MHz, Methanol-*d*₄) δ / ppm: 9.13 (d, *J* = 7.4 Hz, 2H), 8.23 (d, *J* = 8.4 Hz, 2H), 7.99 (d, *J* = 8.3 Hz, 2H), 7.83 (d, *J* = 8.4 Hz, 2H), 2.50 (s, 6H).

ESI MS *m/z*: 869.4 [M-PF₆]⁺ (calc. 869.0).

12.3.2 [Cu(6)₂][PF₆]

SF215



A solution of [Cu(NCMe)₄][PF₆] (16.2 mg, 0.0435 mmol, 1 eq.) in MeCN (2 mL) was added dropwise to a solution of **6** (44.8 mg, 0.0870 mmol) in CHCl₃ (1 mL). The dark red solution was stirred for 3h and the solvent was removed. The dark red solid was purified by column chromatography on alumina using CH₂Cl₂ with 1% MeOH as an eluent to yield [Cu(**6**)₂][PF₆] as a dark red solid (38.0 mg, 0.0310 mmol, 70.5%).

¹H NMR (500 MHz, CD₃CN) δ: 9.10 (d, *J* = 8.2 Hz, 1H, H^{B4}), 8.91 (d, *J* = 8.7 Hz, 1H, H^{B7}), 7.91 (d, *J* = 8.6 Hz, 2H, H^{B8}), 7.89 (d, *J* = 10.5, 8.3 Hz, 2H, H^{B3}), 7.85 – 7.80 (m, 2H, H^{A3}), 7.73 (d, *J* = 8.4 Hz, 2H, H^{A2}), 4.73 (t, *J* = 7.3 Hz, 2H, H^{NCH2}), 2.44 (s, 3H, H^{Me-phen}), 2.43 (s, 3H, H^{Me-phen}), 1.24 – 1.09 (m, 12H, H^{CH2}), 0.83 (t, *J* = 7.2 Hz, 3H, H^{Me}).

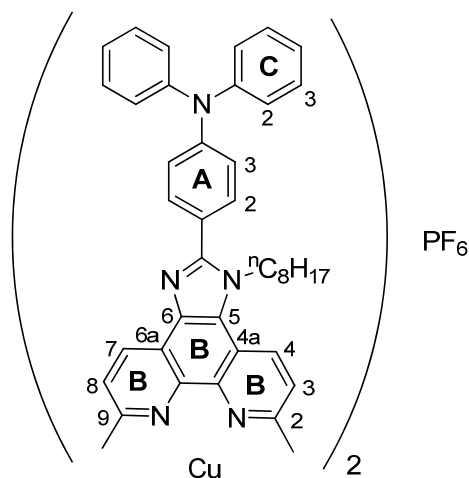
¹³C NMR (126 MHz, CDCl₃) δ / ppm: 157.1 (C^{B2}), 156.6 (C^{B9}), 154.6 (C^{imidazole}), 142.5 (C^q), 142.0 (C^q), 137.3 (C^q), 133.1 (C^{A3}), 132.8 (C^{A2}), 131.4 (C^{B7}), 130.6 (C⁴), 126.9 (C^{B3}), 126.3 (C^{B8}), 124.9 (C¹), 123.1 (C^{B4}), 120.0 (C^q), 47.5 (C^{NCH2}), 32.3 (C^{CH2}), 29.6 (C^{CH2}), 29.5 (C^{CH2}), 26.5 (C^{CH2}), 25.9 (C^{CH2}), 23.2 (C^{CH2}), 14.3 (C^{Me}).

ESI MS *m/z*: 1093.7 [M-PF₆]⁺ (calc. 1093.3).

Found C 57.02, H 5.38, N 9.01; C₅₈H₆₂Br₂CuF₆N₈P requires C 56.20, H 5.04, N 9.04%.

12.3.3 [Cu(**13**)₂][PF₆]

SF141



A solution of [Cu(NCMe)₄][PF₆] (17.3 mg, 0.0464 mmol) in MeCN (2 mL) was added dropwise to a solution of **13** (56.0 mg, 0.0927 mmol) in CHCl₃ (2 mL). The dark red solution was stirred for 1h and then solvent was removed. The dark red solid was purified by filtration through silica to yield [Cu(**3**)₂][PF₆] as a dark red solid (65.0 mg, 0.0459 mmol, 99%).

¹H NMR (500 MHz, CDCl₃) δ / ppm 9.22 (d, *J* = 8.2 Hz, 1H, H^{B⁴/B⁷}), 8.85 (d, *J* = 8.6 Hz, 1H, H^{B⁴/B⁷}), 7.95 (d, *J* = 8.5 Hz, 1H, H^{B³/B⁸}), 7.79 (d, *J* = 8.4 Hz, 1H, H^{B³/B⁸}), 7.61 (d, *J* = 8.6 Hz, 2H, H^{A²}), 7.34 (m, 4H, H^{C³}), 7.24 (d, *J* = 8.7 Hz, 2H, H^{A³}), 7.20 (m, 4H, H^{C²}), 7.13 (m, 2H, H^{C⁴}), 4.78 (m, 2H, H^{N^{CH₂}}), 2.46 (s, 3H, H^{Me-phen}), 2.43 (s, 3H, H^{Me-phen}), 2.01 (m, 2H, H^{CH₂}), overlapping 1.32 and 1.23 (m, 10H, H^{CH₂}), 0.84 (t, *J* = 7.0 Hz, 3H, H^{Me}).

¹³C NMR (126 MHz, CDCl₃) δ / ppm 155.3 (C^{B²/B⁹}), 155.1 (C^{B²/B⁹}), 154.9 (C^{N^{CN}}), 149.6 (C^Q), 147.0 (C^{C¹}), 141.2 (C^Q), 141.0 (C^Q), 136.1 (C^Q), 131.7 (C^{B⁴/B⁷}), 130.8 (C^{A²}), 130.1 (C^{B⁴/B⁷}), 129.7 (C^{C³}), 125.7 (C^{B³/B⁸}), 125.4 (C^{B³/B⁸}), 125.2 (C^{C²}), 124.9 (C^Q), 124.1 (C^{C⁴}), 123.1 (C^Q), 122.3 (C^{A³}), 121.8 (C^Q), 119.2 (C^{B⁵}), 46.7 (C^{N^{CH₂}}), 31.8 (C^{CH₂}), 30.1 (C^{CH₂}), 29.2 (C^{CH₂}), 28.9 (C^{CH₂}), 26.1 (C^{CH₂}), 25.8 (C^{Me-phen}), 25.6 (C^{Me-phen}), 22.5 (C^{CH₂}), 14.2 (C^{Me}).

MALDI MS: *m/z* 1271.6 [M-PF₆]⁺ (calc. 1269.6), 666.9 [M - **13** - PF₆]⁺ (calc. 666.3).

IR (solid, v/cm⁻¹): 2924 (w), 2854 (w), 1588 (m), 1489 (m), 1468 (m), 1282 (m), 836 (s), 746 (m), 695 (s), 557 (s).

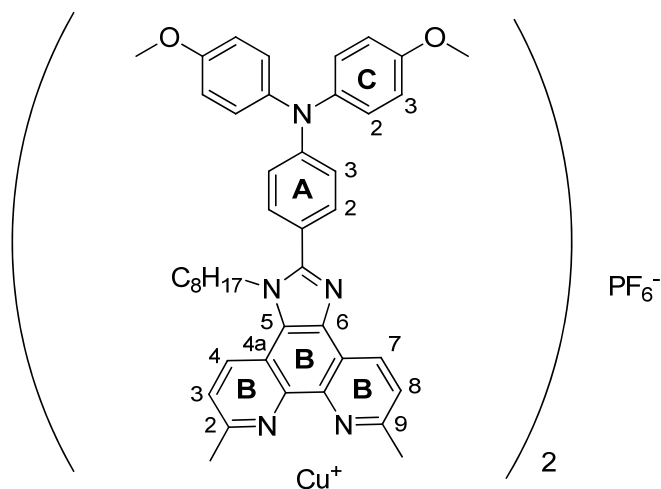
UV-VIS (CH₂Cl₂, 1.0 × 10⁻⁵ mol dm⁻³) λ / nm 266 (ε / dm³ mol⁻¹ cm⁻¹ 74200), 299 (89300), 342 (61700), 476 (15150).

Found C 69.61, H 6.17, N 9.42; C₈₂H₈₂CuF₆N₁₀P requires C 69.55, H 5.84, N 9.89%.

The synthesis and characterization of [Cu(**13**)₂][PF₆] was published in⁴³.

12.3.4 [Cu(14)₂][PF₆]

SF163



A solution of [Cu(MeCN)₄][PF₆] (7.0 mg, 0.0188 mmol, 1.0 eq.) in 2 ml of MeCN was added dropwise to a solution of **14** (25 mg, 0.0377 mmol, 2.0 eq.) in 2 ml of CHCl₃. The solution turned red immediately and was stirred at room temperature for 40 min. The solvent was removed and the remaining red solid purified by column chromatography on alumina eluting with CH₂Cl₂ + 1% MeOH. The main red band was collected to yield the product as a red solid (16.5 mg).*

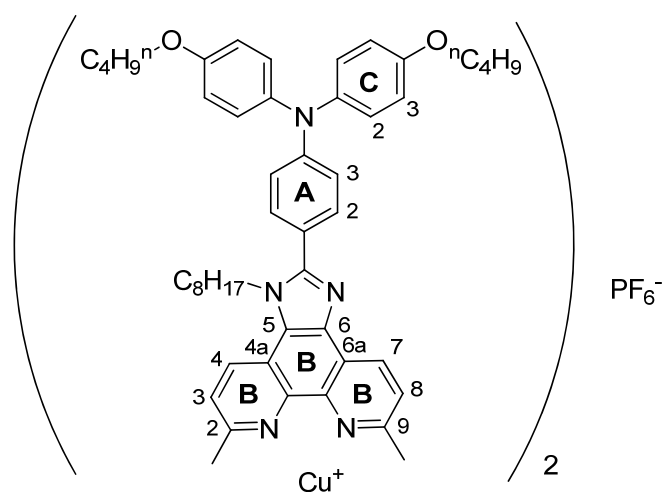
¹H NMR (500 MHz, CDCl₃) δ / ppm: 9.30 – 9.16 (m, 1H), 8.90 – 8.81 (m, 1H), 7.97 – 7.90 (m, 1H), 7.81 – 7.75 (m, 1H), 7.71 – 7.63 (m, 2H), 7.59 – 7.50 (m, 3H), 7.50 – 7.42 (m, 2H), 7.16 (d, *J* = 8.8 Hz, 4H), 7.07 (d, *J* = 8.5 Hz, 2H), 6.90 (d, *J* = 8.9 Hz, 4H), 4.84 – 4.70 (m, 2H, HN^{CH2}), 3.83 (s, 6H, H^{OMe}), 2.49 – 2.40 (s, 6H, overlaying H^{phen-Me}), 2.05 – 1.93 (m, 2H, H^{CH2}), 1.37 – 1.12 (m, 12H, H^{CH2}), 0.83 (t, *J* = 6.7 Hz, 3H, H^{CH3}).

HRMS: *m/z* 1389.6438 [M-PF₆]⁺ (calc.1389.6437).

* small impurities left. Therefore this dye was not used in DSCs

12.3.5 [Cu(15)₂][PF₆]

SF163



A solution of [Cu(MeCN)₄][PF₆] (12.5 mg, 0.0334 mmol, 1.0 eq.) in 2 ml of MeCN was added dropwise to a solution of **15** (50 mg, 0.0668 mmol, 2.0 eq.) in 2 ml of CHCl₃. The solution turned red immediately and was stirred at room temperature for 40 min. The solvent was removed and the remaining red solid purified by column chromatography on alumina eluting with CH₂Cl₂ + 1% MeOH. The main red fraction was collected to yield the product as a red solid (41.4 mg, 24.3 μmol, 72.7%).

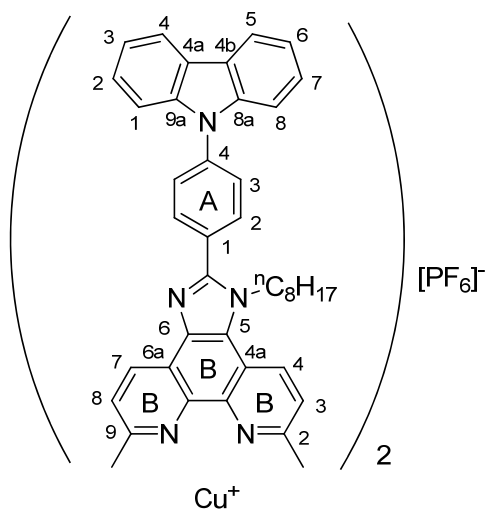
¹H NMR (500 MHz, CDCl₃) δ / ppm: 9.24 (s, 1H, H^{B7}), 8.85 (d, *J* = 8.6 Hz, 1H, H^{B4}), 7.94 (d, *J* = 8.5 Hz, 1H, H^{B3}), 7.78 (d, *J* = 8.3 Hz, 1H, H^{B8}), 7.54 (d, *J* = 8.2 Hz, 2H, H^{A2}), 7.15 (d, *J* = 8.4 Hz, 4H, H^{C2/C3}), 7.07 (d, *J* = 8.4 Hz, 2H, H^{A3}), 6.89 (m, 4H, H^{C2/C3}), 4.78 (t, *J* = 6.8 Hz, 2H, H^{NCH2}), 3.97 (t, *J* = 6.4 Hz, 4H, H^{CH2}), 2.45 (s, 3H, H^{Me-phen}), 2.43 (s, 3H, H^{Me-phen}), 2.00 (m, 2H, H^{CH2}), 1.79 (m, 4H, H^{CH2}), 1.52 (m, 4H, H^{CH2}), 1.31 (m, 2H, H^{CH2}), 1.27 – 1.14 (m, 10H, H^{CH2}), 0.99 (t, *J* = 7.4 Hz, 6H, H^{Me}), 0.84 (t, *J* = 6.8 Hz, 3H, H^{Me}).

¹³C NMR (126 MHz, CDCl₃) δ / ppm: 156.1 (C^{C4}), 155.3 (C^{B9}), 155.2 (C^{A1}), 154.8 (C^{B2}), 150.4 (C^{A4}), 141.1 (C^q), 139.7 (C^{C1}), 131.7 (C^{B7}), 130.5 (C^{A2}), 129.9 (C^{B4}), 127.3 (C^{C2/C3}), 125.6 (C^{B3}), 125.4 (C^{B8}), 124.9 (C^q), 124.7 (C^{imidazole}), 123.1 (C^{6a}), 119.1 (C^{B4a}), 118.9 (C^{A3}), 115.4 (C^{C2/C3}), 67.8 (C^{CH2}), 46.7 (C^{NCH2}), 31.6 (C^{CH2}), 31.2 (C^{CH2}), 30.0 (C^{CH2}), 28.8 (C^{CH2}), 26.0 (C^{CH2}), 25.8 (overlapping C^{Me-phen}), 22.4 (C^{CH2}), 18.9 (C^{CH2}), 13.9 (overlapping C^{Me}).

HRMS *m/z*: 1557.8334 [M-PF₆]⁺ (calc. 1557.8315).

12.3.6 [Cu(17)₂][PF₆]

SF210



A solution of [Cu(NCMe)₄][PF₆] (12.4 mg, 0.0332 mmol, 1 eq.) in MeCN (5 mL) was added dropwise to a solution of **17** (40.0 mg, 0.0665 mmol) in CH₂Cl₂ (5 ml). The dark red solution was stirred for 4h and poured into 40 ml of diethyl ether. The solvent was removed and the dark red solid was purified by column chromatography on alumina using CH₂Cl₂ with 1% MeOH as an eluent to yield [Cu(**17**)₂][PF₆] as a dark red solid (46.9 mg, 0.0330 mmol, 100%).

¹H NMR (500 MHz, CDCl₃) δ / ppm: 9.16 (d, *J* = 8.2 Hz, 1H, H^{B7}), 8.97 (d, *J* = 8.6 Hz, 1H, H^{B4}), 8.25 (dt, *J* = 7.8, 1.0 Hz, 2H, H^{C4/5}), 8.09 (m, 2H, H^{A3}), 7.97-7.89 (m, 4H, overlapping H^{A2+B3/B8}), 7.61 (m, 2H, H^{C1/8}), 7.51 (ddd, *J* = 8.3, 7.0, 1.2 Hz, 2H, H^{C2/7}), 7.36 (ddd, *J* = 8.0, 7.0, 0.9 Hz, 2H, H^{C3/6}), 4.88 (t, *J* = 7.2 Hz, 2H, H^{CH2}), 2.48 (s, 6H, overlapping H^{Me-Phen}), 1.35 – 1.25 (m, 2H, H^{CH2}), 1.25 – 1.11 (m, 10H, H^{CH2}), 0.76 (t, *J* = 6.9 Hz, 3H, H^{Me}).

¹³C NMR (126 MHz, CDCl₃) δ / ppm: 157.1 (C^{B2/9}), 156.5 (C^{B2/9}), 154.9 (C^q imidazole), 142.1 (C^q), 142.4 (C^q), 139.8 (C^{A1}), 137.1 (C^q), 132.7 (C^{A3}), 132.1 (C^{B7}), 131.4 (C^{B4}), 128.2 (C^{A2}), 127.3 (C^{C2/7}), 126.5 (C^{B3/8}), 126.2 (C^{B5}), 124.4 (C^q), 124.0 (C^q), 121.4 (C^q), 120.5 (C^{C4/5}), 120.3 (C^{C3/6}), 120.2 (C^q), 110.8 (C^{C1/8}), 47.6 (C^{CH2}), 32.3 (C^{CH2}), 29.5 (C^{CH2}), 25.9 (overlapping C^{Me-Phen}), 23.2 (C^{CH2}), 14.2 (C^{Me}).

¹⁹F {¹H} NMR (376 MHz, CD₃CN) δ / ppm: -72.97 (d, *J* = 706.3 Hz).

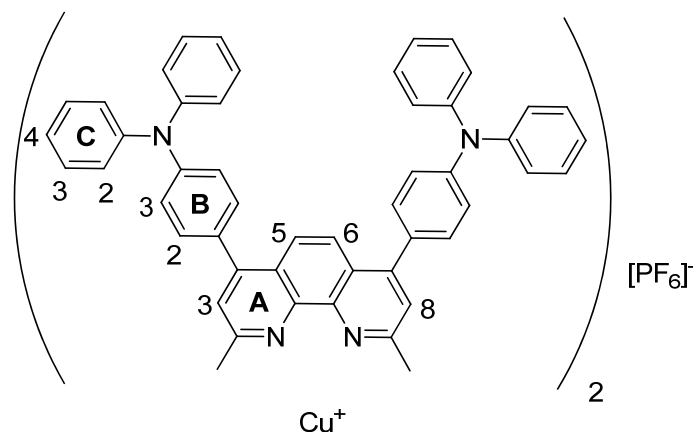
ESI MS *m/z*: 1266.0 [M-PF₆]⁺ (calc. 1265.6).

HRMS: *m/z* 1265.5687 [M-PF₆]⁺ (calc. 1265.5701).

Found C 69.00, H 5.78, N 9.74; C₈₂H₇₈CuF₆N₁₀P + 0.5 H₂O requires C 69.30, H 5.60, N 9.86%.

12.3.7 [Cu(28)₂][PF₆]

SF221



A solution of [Cu(NCMe)₄][PF₆] (22.8 mg, 0.0612 mmol) in MeCN (2 mL) was added dropwise to a solution of **28** (85.0 mg, 0.122 mmol) in CHCl₃ (2 mL). The dark red solution was stirred for 0.5 h and the solvent was removed. The residue was suspended in water and filtered off. The filter cake was collected by dissolving it in acetonitrile and chloroform and filtering through a P3 filter. After removing the solvent in vacuo the product was obtained as a red solid (91.0 mg, 0.057 mmol, 93.0 %).

¹H NMR (500 MHz, CDCl₃) δ / ppm: 8.26 – 8.17 (m, 1H), 7.72 (s, 1H, H^{A3/A8}), 7.55 – 7.47 (m, 2H), 7.40 – 7.27 (m, 6H), 7.27 – 7.19 (m, 7H), 7.18 – 7.11 (m, 2H), 7.11 – 7.03 (m, 1H), 2.57 – 2.47 (s, 3H).

¹H NMR (400 MHz, acetone-*d*₆) δ / ppm: 8.29 (s, 2H, H^{A5}), 7.96 (s, 2H, H^{A3}), 7.68 – 7.62 (m, 4H, H^{B2}), 7.44 – 7.36 (m, 8H, H^{C2}), 7.26 – 7.20 (m, 12H, overlaying H^{B3+C3}), 7.20 – 7.14 (m, 4H, H^{C4}), 2.63 (s, 6H, H^{Me}).

¹³C NMR (126 MHz, acetone-*d*₆) δ / ppm: 158.4 (C^{A2}), 150.1 (C^{A4/A10b}), 150.0 (C^{B1/B4}), 148.15, 131.7 (C^{B2}), 130.6 (C^{A4a}), 130.5 (C^{C2}), 126.5 (C^{A3}), 126.1 (C^{C3}), 125.0 (C^{C4}), 124.7 (C^{A5}), 122.9 (C^{B3}), 26.13 (C^{Me}).

ESI MS *m/z*: 1452.1 [M-PF₆]⁺ (calc. 1452.6).

Found C 72.47, H 4.79, N 7.01; C₁₀₀H₇₆CuF₆N₈P·3H₂O requires C 72.69, H 5.00, N 6.78%.

13 Conclusion

In conclusion, a state-of-the-art N719 reference cell was developed and could be significantly improved from 2.18% in a partially sealed doctor bladed cell to 9.66% in a fully optimized, completely sealed, screen printed DSC. Due to the ripening effect in completely sealed DSCs this efficiency even improved to 9.92% on day 8. The main achievements leading to this significant improvement were: (i) the complete sealing of the cells, which also allows for measurements over time, (ii) screen-printing of the TiO₂ films rather than doctor blading; with 7 layers of screen-printing was found to be the optimum, (iii) use of 25 μm thick sealing foils rather than 60 or 100 μm, (iv) UV-O₃ cleaning of the FTO-coated glass prior to screen printing of the TiO₂ layers, (v) choice of the electrolyte with Standard II electrolyte (with a lower concentration of LiI but also consisting of BMII) was found to outperform Standard I. (vi) 4-wire rather than 2-wire measurements lead to an increase in ff and hence the efficiency. Furthermore, it was found, that complete masking of DSCs is essential to overcome overestimation of the incident light and that masking typically reduces the efficiencies by a 20-40%.

The performances of DSCs containing *heteroleptic* Cu(I) complexes made from [Cu(**13**)₂][PF₆] and four different anchoring ligands with carboxylic acid (**ALC1**) or phosphonic acid (**ALP**, **ALP1** and **ALP1 TBA**) anchors were investigated. It was found that DSCs containing phosphonic acid anchoring ligands show clearly improved efficiencies over carboxylic acid anchors. The performance using either of the three phosphonic acid anchoring ligands was shown to be similar.

A series of five *homoleptic* copper(I) dyes was synthesized, characterized and implemented to DSCs as *heteroleptic* Cu(I) dyes in combination with **ALP1**. The performance of these cells was compared and [Cu(**28**)(**ALP1**)]⁺ with its 4,7-substituted phenanthroline ancillary ligand, was found to perform best in DSCs with a maximum efficiency of 2.73% (33.9% relative to N719). From the Cu(I) dyes based on 5,6-substituted phenanthroline ancillary ligands, [Cu(**17**)(**ALP1**)]⁺ with its carbazole donor was found to outperform the other three dyes. Introduction of diaryl units as a donating group as in [Cu(**13**)(**ALP1**)]⁺ and [Cu(**15**)(**ALP1**)]⁺ resulted in similar and poorer, respectively, overall DSC performance with respect to the unsubstituted analogue [Cu(**6**)(**ALP1**)]⁺.

Methyl groups in the 2- and 9-positions of phenanthroline ligands were confirmed to be vital for the performance of Cu(I) dyes in DSCs. Omitting these substituents resulted in a drastic drop of the J_{SC} and this led to a poor overall performance of the DSCs. A stepwise assembly

instead of classical assembly appeared to be disadvantageous for the performance of 5,6-substituted 2,9-dimethylphenanthroline Cu(I) dyes in DSCs.

By screening of Γ^-/I_3^- electrolytes from different compositions, Li^+ ions were found to be unfavourable for the performance of $[Cu(\mathbf{15})(ALP1)]^+$ sensitized solar cells. Successive optimization of the electrolyte composition resulted in an optimized Γ^-/I_3^- electrolyte consisting of 0.015 M I_2 , 0.6 M BMII and 0.01 M GNCS in MPN labeled as electrolyte **En**. Use of this electrolyte resulted in a maximum efficiency for a $[Cu(\mathbf{15})(ALP1)]^+$ sensitized solar cell of 2.76% (41.0% relative to N719). Omitting of TBP was found to be beneficial for the DSC performance while there was no significant influence on the overall conversion efficiency detected for GNCS.

Superior efficiencies of the *heteroleptic* Cu(I) dyes $[Cu(\mathbf{13})(ALP1)]^+$ and $[Cu(\mathbf{15})(ALP1)]^+$ were obtained upon changing the electrolyte from the Γ^-/I_3^- based Standard II electrolyte to $[Co(bpy)_3][PF_6]_{2/3}$ arising from a significant increase in V_{OC} and J_{SC} . $[Cu(\mathbf{15})(ALP1)]^+$ sensitized solar cells outperformed DSCs containing $[Cu(\mathbf{13})(ALP1)]^+$ dye. Upon change of the counter ion in the electrolyte species from $[PF_6]^-$ to $[B(CN)_4]^-$ an outstandingly high efficiency of 3.38% was measured for a DSC containing $[Cu(\mathbf{15})(ALP1)]^+$ and $Co(bpy)_3[B(CN)_4]_{2/3}$. This efficiency resulted from a J_{SC} of 7.01 mA cm^{-2} , a V_{OC} of 670 mV, a *ff* of 72%, and an η of 3.38%. This corresponds to a relative efficiency of 43% with respect to a N719 reference cell and for the first time, V_{OC} values in the range usually measured for our N719 reference cells were obtained. These correspond to the best performing DSC with a copper(I) dye reported to date. However, no general trend for the influence of the counter ion in the redox shuttle was found.

It was shown that the rate of surface recombination at the TiO_2 surface can be significantly reduced by passivating the TiO_2 film using APTES. However, these experiments were proof-of-concept and further investigations on the optimum conditions for the passivation are required to convert the reduced recombination into an improvement of the overall conversion efficiency.

Future work will focus on 4,7-substituted phenanthroline ancillary ligands since they showed the best performance of all investigated Cu(I) under comparable conditions. Changing the donor group to carbazole- or 4-halo-phenyl-moieties may lead to even higher power conversion efficiencies. Combining this type of dyes, in particular $[Cu(\mathbf{28})(ALP1)]^+$, with $[Co(bpy)_3]^{2+/3+}$ electrolyte will be another important focus of future investigations. Optimization of the Co(II/III) electrolytes by changing the additive concentrations may also improve the performance; notably omitting of Li^+ ions since this has been found to be beneficial in Γ^-/I_3^-

electrolytes. Concerning the Γ^-/I_3^- electrolytes testing of the dependence of the DSC performance on the GNCS concentration in the absence of TBP should be part of further investigations. Based on the results obtained, an ideal additive would lower the conduction band edge of TiO_2 , thereby slightly increasing the charge injection yield (as observed for GNCS) and simultaneously efficiently suppress the surface recombination at the semiconductor-electrolyte interface and the dye layer-electrolyte interface (as observed for TBP).

14 References

- (1) Stocker, T. F.; Qin, D.; Plattner, G.-K.; Tignor, M.; Allen, S. K.; Boschung, J.; Nauels, A.; Xia, Y.; Bex, V.; Midgley, P. M. *Climate Change 2013: The Physical Science Basis. Contribution of Working Group I to the fifth Assessment Report of the Intergovernmental Panel on Climate Change*; Cambridge University Press: Cambridge, United Kingdom and New York, NY, USA, 2013.
- (2) Botschaft zum ersten Massnahmenpaket der Energiestrategie 2050 (Revision des Energierechts) und zur Volksinitiative «Für den geordneten Ausstieg aus der Atomenergie (Atomausstiegsinitiative)» <https://www.admin.ch/opc/de/federal-gazette/2013/7561.pdf> (accessed May 3, 2015).
- (3) European Commission. The 2020 climate and energy package http://ec.europa.eu/clima/policies/package/index_en.htm (accessed May 3, 2015).
- (4) Becquerel, A. E. *Comptes Rendues Acad. Sci.* **1839**, 145.
- (5) Wu, J.; Lan, Z.; Lin, J.; Huang, M.; Huang, Y.; Fan, L.; Luo, G. *Chem. Rev.* **2015**, *115*, 2136.
- (6) Kalyanasundaram, K.; Hagfeldt, A.; Boschloo, G.; Sun, L.; Kloo, L.; Pettersson, H. *Chem. Rev.* **2010**, *110*, 6595.
- (7) Green, M. A.; Emery, K.; Hishikawa, Y.; Warta, W.; Dunlop, E. D. *Prog. Photovoltaics Res. Appl.* **2015**, *23*, 55.
- (8) De Wild-Scholten, M. J. *Sol. Energy Mater. Sol. Cells* **2013**, *119*, 296.
- (9) Anderson, S.; Constable, E. C.; Dare-Edwards, M. P.; Goodenough, J. B.; Hamnett, A.; Seddon, K. R.; Wright, R. D. *Nature* **1979**, *280*, 571.
- (10) Meyer, G. J. *ACS Nano* **2010**, *4*, 4337.
- (11) Desilvestro, J.; Graetzel, M.; Kavan, L.; Moser, J.; Augustynski, J. *J. Am. Chem. Soc.* **1985**, *107*, 2988.
- (12) O'Regan, B.; Grätzel, M. *Nature* **1991**, *353*, 737.
- (13) Yella, A.; Lee, H.-W.; Tsao, H. N.; Yi, C.; Chandiran, a. K.; Nazeeruddin, M. K.; Diao, E. W.-G.; Yeh, C.-Y.; Zakeeruddin, S. M.; Gratzel, M. *Science* **2011**, *334*, 629.
- (14) Yang, H.; Yu, C.; Song, Q.; Xia, Y.; Li, F.; Chen, Z.; Li, X.; Yi, T.; Huang, C. *Chem. Mater.* **2006**, *18*, 5173.
- (15) Berginc, M.; Opara Krašovec, U.; Jankovec, M.; Topič, M. *Sol. Energy Mater. Sol. Cells* **2007**, *91*, 821.

- (16) Zhang, D.; Yoshida, T.; Oekermann, T.; Furuta, K.; Minoura, H. *Adv. Funct. Mater.* **2006**, *16*, 1228.
- (17) Jin, H. Y.; Kim, J. Y.; Lee, J. A.; Lee, K.; Yoo, K.; Lee, D. K.; Kim, B.; Kim, J. Y.; Kim, H.; Jung Son, H.; Kim, J.; Lim, J. A.; Ko, M. J. *Appl. Phys. Lett.* **2014**, *104*.
- (18) Redondo Hernandez, A. Copper (I) polypyridine complexes: the sensitizers of the future for dye-sensitized solar cells (DSSCs), PhD thesis, University of Basel, 2009.
- (19) Clifford, J. N.; Martínez-Ferrero, E.; Palomares, E. *J. Mater. Chem.* **2012**, *22*, 12415.
- (20) Green, A. N. M.; Chandler, R. E.; Haque, S. a; Nelson, J.; Durrant, J. R. *J. Phys. Chem. B* **2005**, *109*, 142.
- (21) Feldt, S. M.; Wang, G.; Boschloo, G.; Hagfeldt, A. *J. Phys. Chem. C* **2011**, *115*, 21500.
- (22) Feldt, S. M.; Gibson, E. A.; Gabrielsson, E.; Sun, L.; Boschloo, G.; Hagfeldt, A. *J. Am. Chem. Soc.* **2010**, *132*, 16714.
- (23) Salvatori, P.; Marotta, G.; Cinti, A.; Mosconi, E.; Panigrahi, M.; Giribabu, L.; Nazeeruddin, M. K.; De Angelis, F. *Inorganica Chim. Acta* **2013**, *406*, 106.
- (24) Di Paola, A.; Bellardita, M.; Palmisano, L. *Catalysts* **2013**, *3*, 36.
- (25) Benkstein, K. D.; Kopidakis, N.; van de Lagemaat, J.; Frank, A. J. *MRS Proc.* **2003**, *789*, 7759.
- (26) Tsao, H. N.; Comte, P.; Yi, C.; Grätzel, M. *ChemPhysChem* **2012**, *13*, 2976.
- (27) Kislenko, S. a.; Amirov, R. K.; Popel', O. S.; Samoilov, I. S. *Therm. Eng.* **2010**, *57*, 969.
- (28) Nazeeruddin, M. K.; De Angelis, F.; Fantacci, S.; Selloni, A.; Viscardi, G.; Liska, P.; Ito, S.; Takeru, B.; Grätzel, M. *J. Am. Chem. Soc.* **2005**, *127*, 16835.
- (29) Snaith, H. J. *Adv. Funct. Mater.* **2010**, *20*, 13.
- (30) Hardin, B. E.; Snaith, H. J.; McGehee, M. D. *Nat. Photonics* **2012**, *6*, 162.
- (31) Li, C.; Wu, S.-J.; Wu, C.-G. *J. Mater. Chem. A* **2014**, *2*, 17551.
- (32) Polander, L. E.; Yella, A.; Curchod, B. F. E.; Ashari Astani, N.; Teuscher, J.; Scopelliti, R.; Gao, P.; Mathew, S.; Moser, J. E.; Tavernelli, I.; Rothlisberger, U.; Grätzel, M.; Nazeeruddin, M. K.; Frey, J. *Angew. Chemie - Int. Ed.* **2013**, *52*, 8731.
- (33) Klein, C.; Nazeeruddin, M. K.; Di Censo, D.; Liska, P.; Grätzel, M. *Inorg. Chem.* **2004**, *43*, 4216.
- (34) Siu, C. H.; Ho, C. L.; He, J.; Chen, T.; Cui, X.; Zhao, J.; Wong, W. Y. *J. Organomet. Chem.* **2013**, *748*, 75.

- (35) Wang, S.-W.; Wu, K.-L.; Ghadiri, E.; Lobello, M. G.; Ho, S.-T.; Chi, Y.; Moser, J.-E.; De Angelis, F.; Graetzel, M.; Nazeeruddin, M. K. *Chem. Sci.* **2013**, *4*, 2423.
- (36) Colombo, A.; Dragonetti, C.; Valore, A.; Coluccini, C.; Manfredi, N.; Abboto, A. *Polyhedron* **2014**, *82*, 50.
- (37) Grätzel, M. *Acc. Chem. Res.* **2009**, *42*, 1788.
- (38) Armaroli, N. *Chem. Soc. Rev.* **2001**, *30*, 113.
- (39) Flamigni, L.; Barbieri, A.; Sabatini, C.; Ventura, B.; Barigelletti, F. In *Bioelectrochemistry and Bioenergetics*; 2007; Vol. 281, pp. 143–203.
- (40) Alonso-Vante, N.; Nierengarten, J.-F.; Sauvage, J.-P. *J. Chem. Soc. Dalton Trans.* **1994**, 1649.
- (41) Sakaki, S.; Kuroki, T.; Hamada, T. *J. Chem. Soc. Dalton Trans.* **2002**, 840.
- (42) Bessho, T.; Constable, E. C.; Graetzel, M.; Hernandez Redondo, A.; Housecroft, C. E.; Kylberg, W.; Nazeeruddin, M. K.; Neuburger, M.; Schaffner, S. *Chem. Commun.* **2008**, 3717.
- (43) Bozic-Weber, B.; Constable, E. C.; Furer, S. O.; Housecroft, C. E.; Troxler, L. J.; Zampese, J. A. *Chem. Commun.* **2013**, *49*, 7222.
- (44) Bozic-Weber, B.; Brauchli, S. Y.; Constable, E. C.; Furer, S. O.; Housecroft, C. E.; Wright, I. A. *Phys. Chem. Chem. Phys.* **2013**, *15*, 4500.
- (45) Bozic-Weber, B.; Brauchli, S. Y.; Constable, E. C.; Furer, S. O.; Housecroft, C. E.; Malzner, F. J.; Wright, I. A.; Zampese, J. A. *Dalton Trans.* **2013**, *42*, 12293.
- (46) Bozic-Weber, B.; Chaurin, V.; Constable, E. C.; Housecroft, C. E.; Meuwly, M.; Neuburger, M.; Rudd, J. a; Schönhofer, E.; Siegfried, L. *Dalton Trans.* **2012**, *41*, 14157.
- (47) Hernandez Redondo, A.; Constable, E. C.; Housecroft, C. E. *Chimia* **2009**, *63*, 205.
- (48) Malzner, F. J.; Brauchli, S. Y.; Constable, E. C.; Housecroft, C. E.; Neuburger, M. *RSC Adv.* **2014**, *4*, 48712.
- (49) Hewat, T. E.; Yellowlees, L. J.; Robertson, N. *Dalton Trans.* **2014**, *43*, 4127.
- (50) Ashbrook, L. N.; Elliott, C. M. *J. Phys. Chem. C* **2013**, *117*, 3853.
- (51) Sandroni, M.; Kayanuma, M.; Planchat, A.; Szuwarski, N.; Blart, E.; Pellegrin, Y.; Daniel, C.; Boujtita, M.; Odobel, F. *Dalton Trans.* **2013**, 24.
- (52) Sandroni, M.; Favereau, L.; Planchat, A.; Akdas-Kilig, H.; Szuwarski, N.; Pellegrin, Y.; Blart, E.; Le Bozec, H.; Boujtita, M.; Odobel, F. *J. Mater. Chem. A* **2014**, *2*, 9944.

- (53) Schmittel, M.; Lüning, U.; Meder, M.; Ganz, A.; Michel, C.; Herderich, M. *Heterocycl. Commun.* **1997**, *3*, 493.
- (54) Clifford, J. N.; Martínez-Ferrero, E.; Viterisi, A.; Palomares, E. *Chem. Soc. Rev.* **2011**, *40*, 1635.
- (55) Yu, Z. Liquid Redox Electrolytes for Dye-Sensitized Solar Cells, PhD thesis, KTH: Stockholm, 2012.
- (56) Clifford, J. N.; Palomares, E.; Nazeeruddin, M. K.; Grätzel, M.; Durrant, J. R. *J. Phys. Chem. C* **2007**, *111*, 6561.
- (57) Boschloo, G.; Hagfeldt, A. *Acc. Chem. Res.* **2009**, *42*, 1819.
- (58) Hamann, T. W.; Ondersma, J. W. *Energy Environ. Sci.* **2011**, *4*, 370.
- (59) Schiffmann, F.; Vandevondele, J.; Hutter, J.; Urakawa, A.; Wirz, R.; Baiker, A. *Proc. Natl. Acad. Sci. U. S. A.* **2010**, *107*, 4830.
- (60) Wang, M.; Chamberland, N.; Breau, L.; Moser, J.-E.; Humphry-Baker, R.; Marsan, B.; Zakeeruddin, S. M.; Grätzel, M. *Nat. Chem.* **2010**, *2*, 385.
- (61) Daeneke, T.; Kwon, T.-H.; Holmes, A. B.; Duffy, N. W.; Bach, U.; Spiccia, L. *Nat. Chem.* **2011**, *3*, 211.
- (62) Kato, F.; Kikuchi, A.; Okuyama, T.; Oyaizu, K.; Nishide, H. *Angew. Chemie - Int. Ed.* **2012**, *51*, 10177.
- (63) Zhang, Z.; Chen, P.; Murakami, T. N.; Zakeeruddin, S. M.; Grätzel, M. *Adv. Funct. Mater.* **2008**, *18*, 341.
- (64) Hamann, T. W. *Dalton Trans.* **2012**, *41*, 3111.
- (65) Yu, Z.; Vlachopoulos, N.; Gorlov, M.; Kloo, L. *Dalton Trans.* **2011**, *40*, 10289.
- (66) Nusbaumer, H.; Moser, J.-E.; Zakeeruddin, S. M.; Nazeeruddin, M. K.; Grätzel, M. *J. Phys. Chem. B* **2001**, *105*, 10461.
- (67) Nusbaumer, H.; Zakeeruddin, S. M.; Moser, J. E.; Grätzel, M. *Chem. Eur. J.* **2003**, *9*, 3756.
- (68) Sapp, S. A.; Elliott, C. M.; Contado, C.; Caramori, S.; Bignozzi, C. A. *J. Am. Chem. Soc.* **2002**, *124*, 11215.
- (69) Nelson, J. J.; Amick, T. J.; Elliott, C. M. *J. Phys. Chem. C* **2008**, *112*, 18255.
- (70) Klahr, B. M.; Hamann, T. W. *J. Phys. Chem. C* **2009**, *113*, 14040.
- (71) Ito, S.; Murakami, T. N.; Comte, P.; Liska, P.; Grätzel, C.; Nazeeruddin, M. K.; Grätzel, M. *Thin Solid Films* **2008**, *516*, 4613.

- (72) Altomare, A.; Cascarano, G.; Giacobazzo, C.; Guagliardi, A. *J. Appl. Crystallogr.* **1994**, *27*, 1045.
- (73) Betteridge, P. W.; Carruthers, J. R.; Cooper, R. I.; Prout, K.; Watkin, D. J. *J. Appl. Crystallogr.* **2003**, *36*, 1487.
- (74) Bruno, I. J.; Cole, J. C.; Edgington, P. R.; Macrae, C. F.; Pearson, J.; Taylor, R. *Acta Crystallogr. Sect. B* **2002**, 389.
- (75) Macrae, C. F.; Bruno, I. J.; Chisholm, J. a.; Edgington, P. R.; McCabe, P.; Pidcock, E.; Rodriguez-Monge, L.; Taylor, R.; Van De Streek, J.; Wood, P. a. *J. Appl. Crystallogr.* **2008**, *41*, 466.
- (76) Snaith, H. J. *Nat. Photonics* **2012**, *6*, 337.
- (77) Zimmermann, E.; Ehrenreich, P.; Pfadler, T.; Dorman, J. A.; Weickert, J.; Schmidt-Mende, L. *Nat. Photonics* **2014**, *8*.
- (78) Snaith, H. J. *Energy Environ. Sci.* **2012**, *5*, 6513.
- (79) Ito, S.; Nazeeruddin, M. K.; Liska, P.; Comte, P.; Charvet, R.; Péchy, P.; Jirousek, M.; Kay, A.; Zakeeruddin, S. M.; Grätzel, M. *Prog. Photovoltaics Res. Appl.* **2006**, *14*, 589.
- (80) Yang, X.; Yanagida, M.; Han, L. *Energy Environ. Sci.* **2012**, *5*, 54.
- (81) Palomares, E.; Clifford, J. N.; Haque, S. A.; Lutz, T.; Durrant, J. R. *J. Am. Chem. Soc.* **2003**, *125*, 475.
- (82) Zaban, A.; Greenshtein, M.; Bisquert, J. *ChemPhysChem* **2003**, *4*, 859.
- (83) Kröhnke, F. *Synthesis* **1976**, *1*, 1.
- (84) Paw, W.; Eisenberg, R. *Inorg. Chem.* **1997**, *36*, 2287.
- (85) Zheng, R. H.; Guo, H. C.; Jiang, H. J.; Xu, K. H.; Liu, B. B.; Sun, W. L.; Shen, Z. Q. *Chinese Chem. Lett.* **2010**, *21*, 1270.
- (86) Shellaiah, M.; Rajan, Y. C.; Lin, H.-C. *J. Mater. Chem.* **2012**, *22*, 8976.
- (87) Guzow, K.; Czerwińska, M.; Ceszlak, A.; Kozarzewska, M.; Szabelski, M.; Czaplewski, C.; Łukaszewicz, A.; Kubicki, A.; Wiczak, W. *Photochem. Photobiol. Sci.* **2013**, *12*, 284.
- (88) Xu, H.; Zheng, K.-C.; Chen, Y.; Li, Y.-Z.; Lin, L.-J.; Li, H.; Zhang, P.-X.; Ji, L.-N. Effects of ligand planarity on the interaction of polypyridyl Ru(II) complexes with DNA. *Dalton Transactions*, 2003, 2260.
- (89) Eggleston, M. K.; McMillin, D. R.; Koenig, K. S.; Pallenberg, A. J. *Inorg. Chem.* **1997**, *36*, 172.

- (90) Bozic-Weber, B.; Chaurin, V.; Constable, E. C.; Housecroft, C. E.; Meuwly, M.; Neuburger, M.; Rudd, J. A.; Schönhofer, E.; Siegfried, L. *Dalton Trans.* **2012**, 14157.
- (91) Bondi, A. *J. Phys. Chem.* **1964**, *68*, 441.
- (92) Bozic-Weber, B.; Constable, E. C.; Housecroft, C. E.; Kopecky, P.; Neuburger, M.; Zampese, J. A. *Dalton Trans.* **2011**, *40*, 12584.
- (93) Schönhofer, E. Dye Sensitized Solar Cells : From Liquid Electrolytes to Solid State Hole Transport Materials, PhD thesis, University of Basel, 2015.
- (94) Barkhouse, D. A. R.; Gunawan, O.; Gokmen, T.; Todorov, T. K.; Mitzi, D. B. *Prog. Photovoltaics Res. Appl.* **2012**, *20*, 6.
- (95) Krüger, J. Interface Engineering in Solid-State Dye-Sensitized Solar Cells, PhD thesis, EPFL, 2003.
- (96) Kang, M.; Ryu, K.; Chang, S. *Bull. Korean Chem. Soc.* **2004**, *25*, 742.
- (97) Baglio, V.; Girolamo, M.; Antonucci, V.; Aricò, A. S. *In. J. Electrochem. Sci.* **2011**, *6*, 3375.
- (98) Hauch, A.; Georg, A. *Electrochim. Acta* **2001**, *46*, 3457.
- (99) Kuang, D.; Ito, S.; Wenger, B.; Klein, C.; Moser, J.-E.; Humphry-Baker, R.; Zakeeruddin, S. M.; Grätzel, M. *J. Am. Chem. Soc.* **2006**, *128*, 4146.
- (100) Hao, F.; Jiao, X.; Li, J.; Lin, H. *Nanoscale* **2013**, *5*, 726.
- (101) Jennings, J. R.; Wang, Q. *J. Phys. Chem. C* **2010**, *114*, 1724.
- (102) Boschloo, G.; Häggman, L.; Hagfeldt, A. *J. Phys. Chem. B* **2006**, *110*, 13144.
- (103) Redmond, G.; Fitzmaurice, D. *J. Phys. Chem.* **1993**, *97*, 1426.
- (104) Zhang, F.; Shi, F.; Ma, W.; Gao, F.; Jiao, Y.; Li, H.; Wang, J.; Shan, X.; Lu, X.; Meng, S. *J. Phys. Chem. C* **2013**, *117*, 14659.
- (105) Tachibana, Y.; Nazeeruddin, K.; Gr, M.; Klug, D. R.; Durrant, J. R. *Chem. Phys.* **2002**, *285*, 127.
- (106) Eliceiri, K. W.; Berthold, M. R.; Goldberg, I. G.; Ibáñez, L.; Manjunath, B. S.; Martone, M. E.; Murphy, R. F.; Peng, H.; Plant, A. L.; Roysam, B.; Sturmann, N.; Swedlow, J. R.; Tomancak, P.; Carpenter, A. E. *Nat. Methods* **2012**, *9*, 697.
- (107) Reynal, A.; Willkomm, J.; Muresan, N. M.; Lakadamyali, F.; Planells, M.; Reisner, E.; Durrant, J. *Chem. Commun.* **2014**, *50*, 12768.
- (108) Péchy, P.; Rotzinger, F. P.; Nazeeruddin, M. K.; Kohle, O.; Zakeeruddin, S. M.; Humphry-Baker, R.; Grätzel, M. *J. Chem. Soc., Chem. Commun.* **1995**, 65.

- (109) Ambrosio, F.; Martsinovich, N.; Troisi, A. *J. Phys. Chem. Lett.* **2012**, *3*, 1531.
- (110) Jiang, X.; Marinado, T.; Gabrielsson, E.; Hagberg, D. P.; Sun, L.; Hagfeldt, A. *J. Phys. Chem. C* **2010**, *114*, 2799.
- (111) Ito, S.; Liska, P.; Comte, P.; Charvet, R.; Péchy, P.; Bach, U.; Schmidt-Mende, L.; Zakeeruddin, S. M.; Kay, A.; Nazeeruddin, M. K.; Grätzel, M. *Chem. Commun.* **2005**, 4351.
- (112) Kroon, J. M.; Bakker, N. J.; Smit, H. J. P.; Liska, P.; Thampi, K. R.; Wang, P.; Zakeeruddin, S. M.; Grätzel, M.; Hinsch, A.; Hore, S.; Würfe, U.; Sastrawan, R.; Durrant, J. R.; Palomares, E.; Pettersson, H.; Gruszecki, T.; Walter, J.; Skupien, K.; Tulloch, G. E. *Prog. Photovoltaics Res. Appl.* **2007**, *15*, 1.
- (113) Bisquert, J.; Cahen, D.; Hodes, G.; Rühle, S.; Zaban, A. *J. Phys. Chem. B* **2004**, *108*, 8106.
- (114) Brauchli, S. Y.; Constable, E. C.; Housecroft, C. E. *Dye. Pigment.* **2015**, *113*, 447.
- (115) Malzner, F. J.; Brauchli, S. Y.; Schönhofer, E.; Constable, E. C.; Housecroft, C. E. *Polyhedron* **2014**, *82*, 116.
- (116) Goldstein, S.; Czapski, G. *Inorg. Chem.* **1985**, *24*, 1087.
- (117) Bozic-Weber, B.; Constable, E. C.; Hostettler, N.; Housecroft, C. E.; Schmitt, R.; Schönhofer, E. *Chem. Commun.* **2012**, *48*, 5727.
- (118) Brauchli, S. Y. How structural factors influence the performance of copper (I) bis(diimine) based DSCs, PhD thesis, University of Basel, 2014.
- (119) Schönhofer, E.; Bozic-Weber, B.; Martin, C. J.; Constable, E. C.; Housecroft, C. E.; Zampese, J. A. *Dye. Pigment.* **2015**, *115*, 154.
- (120) Ito, S.; Zakeeruddin, S. M.; Comte, P.; Liska, P.; Kuang, D.; Grätzel, M. *Nat. Photonics* **2008**, *2*, 693.
- (121) Bisquert, J.; Fabregat-Santiago, F.; Mora-Seró, I.; Garcia-Belmonte, G.; Giménez, S. *J. Phys. Chem. C* **2009**, *113*, 17278.
- (122) Colombo, A.; Dragonetti, C.; Roberto, D.; Valore, A.; Biagini, P.; Melchiorre, F. *Inorganica Chim. Acta* **2013**, *407*, 204.
- (123) Chandrasekharam, M.; Rajkumar, G.; Srinivasa Rao, C.; Suresh, T.; Anil Reddy, M.; Yella Reddy, P.; Soujanya, Y.; Takeru, B.; Jun-Ho, Y.; Nazeeruddin, M. K.; Grätzel, M. *Synth. Met.* **2011**, *161*, 1098.
- (124) Song, H.-K.; Park, Y. H.; Han, C.-H.; Jee, J.-G. *J. Ind. Eng. Chem.* **2009**, *15*, 62.

- (125) Chandrasekharam, M.; Rajkumar, G.; Srinivasa Rao, C.; Suresh, T.; Anil Reddy, M.; Yella Reddy, P.; Soujanya, Y.; Takeru, B.; Jun-Ho, Y.; Nazeeruddin, M. K.; Grätzel, M. *Synth. Met.* **2011**, *161*, 1098.
- (126) Kopidakis, N.; Neale, N. R.; Frank, A. J. *J. Phys. Chem. B* **2006**, *110*, 12485.
- (127) Zhang, C.; Huang, Y.; Huo, Z.; Chen, S.; Dai, S. *J. Phys. Chem. C* **2009**, *113*, 21779.
- (128) Jeanbourquin, X. a.; Li, X.; Law, C.; Barnes, P. R. F.; Humphry-Baker, R.; Lund, P.; Asghar, M. I.; Oregan, B. C. *J. Am. Chem. Soc.* **2014**, *136*, 7286.
- (129) Ohta, M.; Koumura, N.; Hara, K.; Mori, S. *Electrochem. commun.* **2011**, *13*, 778.
- (130) Hostettler, N.; Furer, S. O.; Bozic-Weber, B.; Constable, E. C.; Housecroft, C. E. *Dye. Pigment.* **2015**, *116*, 124.
- (131) Lim, J.; Kwon, Y. S.; Park, T. *Chem. Commun.* **2011**, *47*, 4147.
- (132) Zhang, Z.; Evans, N.; Zakeeruddin, S. M.; Humphry-Baker, R.; Gratzel, M. *J. Phys. Chem. C* **2007**, *111*, 398.
- (133) Neale, N. R.; Kopidakis, N.; van de Lagemaat, J.; Grätzel, M.; Frank, A. J. *J. Phys. Chem. B* **2005**, *109*, 23183.
- (134) Marinado, T.; Hahlin, M.; Jiang, X.; Quintana, M.; Johansson, E. M. J.; Gabrielsson, E.; Plogmaker, S.; Hagberg, D. P.; Boschloo, G.; Zakeeruddin, S. M.; Grätzel, M.; Siegbahn, H.; Sun, L.; Hagfeldt, A.; Rensmo, H. *J. Phys. Chem. C* **2010**, *114*, 11903.
- (135) Kay, A.; Graetzel, M. *J. Phys. Chem.* **1993**, *97*, 6272.
- (136) Hara, K.; Dan-oh, Y.; Kasada, C.; Ohga, Y.; Shinpo, A.; Suga, S.; Sayama, K.; Arakawa, H. *Langmuir* **2004**, *20*, 4205.
- (137) Gregg, B. a.; Pichot, F.; Ferrere, S.; Fields, C. L. *J. Phys. Chem. B* **2001**, *105*, 1422.
- (138) Feldt, S. M.; Cappel, U. B.; Johansson, E. M. J.; Boschloo, G.; Hagfeldt, A. *J. Phys. Chem. C* **2010**, *114*, 10551.
- (139) An, H.; Song, D.; Lee, J.; Kang, E.-M.; Jaworski, J.; Kim, J.-M.; Kang, Y. S. *J. Mater. Chem. A* **2014**, 2250.
- (140) Carli, S.; Casarin, L.; Caramori, S.; Boaretto, R.; Busatto, E.; Argazzi, R.; Bignozzi, C. *A. Polyhedron* **2014**, *82*, 173.
- (141) Mikkala, V.-M.; Kankare, J. J. *Helv. Chim. Acta* **1992**, *75*, 1578.
- (142) Bonho, P.; Moser, J.-E.; Humphry-baker, R.; Vlachopoulos, N.; Zakeeruddin, S. M.; Walder, L.; Gra, M.; Bonhôte, P.; Moser, J.-E.; Humphry-baker, R.; Vlachopoulos, N.; Zakeeruddin, S. M.; Walder, L.; Grätzel, M. *J. Am. Chem. Soc.* **1999**, *121*, 1324.

- (143) Shi, L.; Li, B. *Eur. J. Inorg. Chem.* **2009**, 2009, 2294.
- (144) Sevov, C. S.; Hartwig, J. F. *J. Am. Chem. Soc.* **2014**, 136, 10625.
- (145) Dutronc, T.; Terazzi, E.; Guénée, L.; Buchwalder, K. L.; Spoerri, A.; Emery, D.; Mareda, J.; Floquet, S.; Piguet, C. *Chem. Eur. J.* **2013**, 19, 8447.
- (146) Wolter, M.; Nordmann, G.; Job, G. E.; Buchwald, S. L. *Org. Lett.* **2002**, 4, 973.
- (147) Westphal, E.; Bechtold, I. H.; Gallardo, H. *Macromolecules* **2010**, 43, 1319.
- (148) Odom, S. A.; Lancaster, K.; Beverina, L.; Lefler, K. M.; Thompson, N. J.; Coropceanu, V.; Brédas, J.-L.; Marder, S. R.; Barlow, S. *Chemistry* **2007**, 13, 9637.
- (149) Mao, M.; Wang, J. B.; Xiao, Z. F.; Dai, S. Y.; Song, Q. H. *Dye. Pigment.* **2012**, 94, 224.
- (150) Larsen, A. F.; Ulven, T. *Org. Lett.* **2011**, 13, 3546.
- (151) Herron, Norman; Guidry, Mark A.; Rostovtsev, Vsevolod; Gao, Weiyang; Wang, Ying; Shen, Yulong; Merlo, Jeffrey A. Electronic Device Including Phenanthroline Derivative PCT/US2009/069184, **2010**.

Curriculum Vitae

Sebastian Fürer



Personal Data

Contact Sebastian Fürer
 Department of Chemistry
 University of Basel
 Spitalstrasse 51
 CH-4056 Basel, Switzerland
 Phone: +41 (0)61 267 10 64 Switzerland
 e-mail: s.fuerer@unibas.ch
 Private: Buchenstr. 45, 4054 Basel, Switzerland
Born April 7th 1986 in Basel, Switzerland
Citizenship Swiss

Education

Ph.D., Chemistry, <i>summa cum laude</i>	03/2011
Department of Chemistry, University of Basel , Switzerland	-
Supervisors: Prof. Dr. Edwin C. Constable, Prof. Dr. Catherine E. Housecroft	05/2015
Thesis Title: The application of Cu(I) phenanthroline dyes in DSCs with optimized I ⁻ /I ₃ ⁻ and Co(II/III) electrolytes.	
M.Sc., Chemistry	09/2010
Department of Chemistry, University of Basel , Switzerland	-
Supervisors: Prof. Dr. Edwin C. Constable, Prof. Dr. Catherine E. Housecroft	03/2011
Thesis Title: Cobalt based electrolytes for copper sensitized solar cells	

B.Sc.,		09/2006
Chemistry	09/	-
2006-06/2009		06/2009
Department of Chemistry, University of Basel , Switzerland		
Bachelor's Studies, Law	09/2005-06/2006	09/2005
University of Basel , Switzerland		-
		06/2006
Gymnasium Kirschgarten, Basel		08/1999
		-
		08/2004

Research Experience

Postdoctoral Researcher		05/201
		5-
		04/201
		6
Department of Chemistry, University of Basel , Switzerland		
Supervisors: Prof. Dr. Edwin C. Constable,		
Prof. Dr. Catherine E. Housecroft		
Ph.D. Researcher		03/201
		1-
		05/201
		5
Department of Chemistry, University of Basel , Switzerland		
Supervisors: Prof. Dr. Edwin C. Constable,		
Prof. Dr. Catherine E. Housecroft		
Master's Researcher		09/201
		0-
Department of Chemistry, University of Basel , Switzerland		
Supervisors: Prof. Dr. Edwin C. Constable,		
Prof. Dr. Catherine E. Housecroft		
		03/201
		1

Curriculum Vitae

Sebastian Fürer

Research Intern

03/201

BASF Switzerland, Basel, Switzerland

0-

Research Topic: Synthesis of hole-transport materials for OLEDs

05/201

0

Teaching Experience

University of Basel, Switzerland

Teaching assistant, Inorganic Chemistry practicum 2012-2014

Supervised and assisted undergraduate students in inorganic chemistry multi-step syntheses using Schlenk technique and basic analytical techniques

Teaching assistant, Introduction to Chemistry 2011-2014

Teaching of exercises (~400 students), helping in writing and correcting of exams, answering individual questions of students

Memberships

Swiss Chemical Society 2011-present

Publication List

1. "Improving performance of copper(I)-based dye sensitized solar cells through I-3/I- electrolyte manipulation"
S. O. Furer, L. Y. N. Luu, B. Bozic-Weber, E. C. Constable, C. E. Housecroft
Dyes and Pigments, **2016**, 132, 72-78.
2. "Heteroleptic copper(I) sensitizers with one versus two hole-transporting units in functionalized 2,9-dimethyl-1,10-phenanthroline ancillary ligands"
S. O. Furer, B. Bozic-Weber, M. Neuburger, E. C. Constable and C. E. Housecroft
RSC Advances, **2015**, 5, 69430-69440
3. "Alkyl chain-functionalized hole-transporting domains in zinc(II) dye-sensitized solar cells"
N. Hostettler, S. O. Furer, B. Bozic-Weber, E. C. Constable and C. E. Housecroft
Dyes and Pigments, **2015**, 116, 124-130.

4. "Copper(I) dye-sensitized solar cells with $[\text{Co}(\text{bpy})_3]^{2+/3+}$ electrolyte"
B. Bozic-Weber, E. C. Constable, S. O. Furer, C.E. Housecroft, L. J. Troxler and J. A. Zampese, *Chem. Commun.*, **2013**, 49(65), 7222-7224.
5. "Improving the photoresponse of copper(I) dyes in dye-sensitized solar cells by tuning ancillary anchoring ligand modules"
B. Bozic-Weber, S. Y. Brauchli, E. C. Constable, S. O. Furer, C. E. Housecroft, F. J. Malzner, I. A. Wright, J. A. Zampese, *Dalton Transactions*. **2013**, 42(34),12293-12308.
6. "Hole-transport functionalized copper(I) dye sensitized solar cells"
B. Bozic-Weber, S. Y. Brauchli, E. C. Constable, S. O. Furer, C. E. Housecroft, I. A. Wright, *Physical Chemistry Chemical Physics*, **2013**, 15(13), 4500-4504.

Presentations

"Pushing towards the red: The Performance of a Series of Copper(I) Phenanthroline Dyes in DSCs", poster presentation, 21st International Symposium on the Photophysics and Photochemistry of Coordination Compounds (ISPPCC), Kraków, Poland, July 5-9, 2015.

"Influence of Alkyl Chains in Neocuproine Copper(I) Dyes on the Performance in Dye Sensitized Solar Cells", poster presentation, International Conference on Coordination Chemistry (ICCC), Singapore, July 21-25, 2014.

"Neocuproine Based Copper Dye for DSCs with $[\text{Co}(\text{bpy})_3]^{2+/3+}$ electrolyte", poster presentation, 2nd Clariant Chemistry Day, University of Basel, Basel, April 10, 2014.

"Neocuproine Based Copper Dye for DSCs with $[\text{Co}(\text{bpy})_3]^{2+/3+}$ electrolyte", poster presentation, Fall Meeting 2013 of the Swiss Chemical Society, EPFL, Lausanne, September 6, 2013.

"Neocuproine Based Copper Dye for DSCs with $[\text{Co}(\text{bpy})_3]^{2+/3+}$ electrolyte", poster presentation, 20th International Symposium on the Photophysics and Photochemistry of Coordination Compounds (ISPPCC), Traverse City, Michigan, USA, July 7-11, 2013.

"A new Copper Dye for Dye Sensitized Solar Cells", poster presentation, Clariant Cleantech Day, University of Basel, Basel, November 15, 2012.

"A new Copper Dye for Dye Sensitized Solar Cells", Fall Meeting 2013 of the Swiss Chemical Society, ETH Zürich, Zürich, September 13, 2012.

"A new Copper Dye for Dye Sensitized Solar Cells", poster presentation and participation at the summer school, RSC Dalton Summer School: Electronic Structural Methods in Inorganic Chemistry, University of Edinburgh, School of Chemistry, Edinburgh, June 18-22, 2012.

"Cobalt based electrolytes for copper sensitized solar cells", poster presentation and participation at the summer school, VIII International Krutyn Summer School 2011, Krutyn, Poland, June 14-20, 2011.

Language skills

- German (native language)
- English (fluent)

References

Prof. Dr. Catherine E. Housecroft, Department of Chemistry, University of Basel, Switzerland
catherine.housecroft@unibas.ch, phone: +41 61 267 1008.

Prof. Dr. Edwin C. Constable, Department of Chemistry, University of Basel, Switzerland
Edwin.Constable@unibas.ch, phone: +41 (0)61 267 1001